UNIVERSIDADE DE LISBOA
FACULDADE DE CIÊNCIAS

Ciências
ULisboa

Nearshore hydrodynamics and morphology derived from video imagery

Doutoramento em Geologia
Especialidade de Geodinâmica Externa

Umberto Andriolo

Tese orientada por:
Professor Doutor Rui Pires de Matos Taborda
Doutora Fátima Cristina Gomes Ponte Lira

Documento especialmente elaborado para a obtenção do grau de doutor

2018

UNIVERSIDADE DE LISBOA

FACULDADE DE CIÊNCIAS

Ciências
ULisboa

Nearshore hydrodynamics and morphology derived from video imagery

Doutoramento em Geologia

Especialidade de Geodinâmica Externa

Umberto Andriolo

Tese orientada por:

Professor Doutor Rui Pires de Matos Taborda

Doutora Fátima Cristina Gomes Ponte Lira

Júri:

Presidente:

- Doutora Maria da Conceição Pombo de Freitas, Professora Catedrática da Faculdade de Ciências da Universidade de Lisboa

Vogais:Vogais:

- Doutor Rafael Vicent Almar, Charge de Recherche Laboratoire d'Etudes en Geophysique et Oceanographie Spatiales do Institut de Recherche pour le Developpement (France)
- Doutor Paulo Renato Enes Baganha Baptista, Investigador Auxiliar, Centro de Estudos do Ambiente e do Mar (CESAM) da Universidade de Aveiro
- Doutor Rui Pires de Matos Taborda, Professor Associado corn Agregação, Faculdade de Ciencias da Universidade de Lisboa, Orientador
- Doutora Ana Maria Almeida Nobre Silva, Professora Auxiliar Convidada Faculdade de Ciencias da Universidade de Lisboa

Documento especialmente elaborado para a obtenção do grau de doutor

Fundação para a Ciência e Tecnologia, Bolsa de Doutoramento SFRH/BD/52558/2014

2018

Acknowledgments

The present work was supported by the Fundação para a Ciência e Tecnologia (FCT) through grant SFRH/BD/52558/2014, within the EarthSystems Doctorate Program led by Instituto Dom Luiz. The work benefited from the facilities and equipment of the Instituto Don Luiz and the Department of Geology of the Faculty of Sciences, University of Lisbon.

The author is very grateful to Professor Rui Taborda and to Cristina Lira for their guidance and their careful and meticulous revision of the thesis.

A special gratitude goes to Luis Pedro Almeida, Alberto Azevedo, Diogo Mendes and Elena Sánchez-García for their fundamental help in the development of this work.

The author is also thankful to Pedro Almendra for the collaboration of Surftotal company which made possible the use of surfcam images of Ribeira d'Ilhas beach.

Acknowledgments to Rafael Almar for the hosting at Laboratoire d'Etudes en Geophysique et Oceanographie Spatiales do Institut de Recherche pour le Developpement (LEGOS-IRD), and for COASTVAR project data (French grant COASTVAR:ANR- 30214-ASTR-0019). Acknowledgments to Mounsef Sedrati (LGO UMR CNRS 6538 - University South Brittany, Vannes - France) and to Guillaume Brunier for the mission in French Guiana.

The author also thanks Ana Bastos, Andre Fortunato, Monica Ribeiro and Ana Nobre Silva for their help in fieldwork.

This thesis should be cited as: Andriolo, U. 2018. Nearshore hydrodynamics and morphology derived from video imagery. PhD thesis. University of Lisbon, Portugal, 197 pp.

Abstract

The coastal zone is the dynamic interface between the land and the ocean. Natural processes, including wave action, flooding and coastal erosion, often endanger human occupation and the use of the littoral. It is therefore essential to improve our understanding of the physical processes occurring at the coast, particularly those related with coastal morphodynamics. Due to the complexity of the coastal environment, littoral studies should be as comprehensive as possible, covering both hydrodynamic forcing and morphological response. However, conventional in-situ survey methods involve the use of instrumentation which, due to the logistical commitments, do not provide the required time-space scales.

Remote sensing methods emerge in this context as an interesting alternative solution to yield simultaneous high temporal frequency and high spatial resolution observations of the nearshore processes. Among others, shore-based video remote sensing systems have been proved, over the last three decades, as a cost-efficient and high-quality tool to support coastal scientists and managers. Video monitoring installations offer excellent spatio-temporal resolutions, in combination with cost-efficient long-term data acquisition.

This dissertation aims to present new conceptual models and video imagery tools to assess nearshore morphodynamics. This objective was accomplished through the development of a set of efficient computational tools to extract synoptic hydrodynamic and morphology information from video images.

Data used in this work were acquired at five different study sites located worldwide. At three sites, video data were collected from dedicated video systems installed for scientific purpose. Two more additional video data sets were derived from the acquisition of online-streaming surfcams, which are camera infrastructures installed at the coast to provide remote visual information of sea state to surf users.

A stand-alone set of algorithm was built to process and to geo-reference the acquired video sequence using already existing software. In addition, the automated processing is set to produce special images, namely Timex Variance and Timestack.

A first video-based technique exploited the pixel intensity variation of Timestack images to characterize nearshore hydrodynamics. The standard deviation of pixel intensity was successfully related to the spatial distribution of wave transformation domains. Therefore, shoaling, surf and swash zones could be clearly identified in the nearshore profile covered by the image. This technique provides a new tool to study the nearshore dynamics, as the extent of wave domains can be related with distinctive morphodynamic behaviour. The method can be also directly applied to Variance images, hence it offers the possibility of extending such studies to the alongshore dimension.

A second methodology developed in the scope of the present work exploited the use of pixel intensity average of Timestack images to estimate wave breaking height. Breakpoint locations and pixel intensity profiles were used to define the cross-shore breaking pattern length visible on a time-averaged image, here defined as the L_{Hs} parameter. A first approach coupled L_{Hs} to the available bathymetry to solve a simple conceptual model for finding breaker height. Wave breaking height estimates yield a Normalized Root Mean Square Error (NRMSE) of 14% when compared to numerical model results, for offshore wave heights ranging from 1.6 m to 3.5 m. A second approach proposed the relationship $L_{Hs}/24$ to replace water depth parameter on the simplest wave height calculation formula, which multiplies water depth by the breaker index. The technique can be directly applied on Timex, therefore images from four different sites were used to test its validity, obtaining an NRMSE of about 22% for a wide range of wave heights.

A third methodology aimed to investigate the possibility of combining two shore-based remote sensing techniques, 2D terrestrial LiDAR and video imagery to perform detailed beach intertidal topography. 2D LiDAR provided precise shoreline elevation along a cross-shore beach transect, while shoreline contour was detected on Timex images in the alongshore dimension. The dataset from both instruments were complemented to perform 3D beach intertidal topography mapping with a Root Mean Square Error (RMSE) of approximately 0.12 m.

Finally, a method to assess nearshore bathymetry was developed. The method is based on a depth inversion technique, where wave celerity was estimated using wave

trajectories visible on Timestacks. The procedure differentiates the waves in the shoaling and breaking zones and then estimates local depth from shallow or intermediate water equations. In the test case, bathymetry was mapped till a depth of 11 m with relative short time observations (5 hours), registering a RMSE of about 0.46 m when compared to ground truth data.

The techniques herein developed allow to extract from video images some of the key drivers of nearshore morphodynamics, such as wave breaking height and wave period, as well as the main morphological features, namely subtidal bathymetry and intertidal beach topography. The combination of the methodologies presented in this thesis provides a comprehensive coverage of nearshore processes, enabling a synoptic representation of hydrodynamics and morphology. These methodologies may foster the implementation of new video-based operational systems and support the quasi-real time determination of coastal indicators and early warning systems for coastal hazards.

Keywords: coast, wave, remote sensing, morphodynamics, bathymetry

Resumo

A zona costeira corresponde à interface dinâmica entre a terra e o oceano. Os processos naturais, incluindo a ação das ondas, inundações e erosão costeira, colocam muitas vezes em perigo a ocupação humana e o uso do litoral. Nesse sentido, é essencial melhorar o conhecimento sobre os processos físicos que ocorrem junto à costa, particularmente aqueles que se relacionam com a morfodinâmica do sistema costeiro. Devido à complexidade do ambiente costeiro, a aquisição de dados sobre o litoral deve ser o mais abrangente possível e cobrir simultaneamente o forçamento hidrodinâmico e a respetiva resposta morfológica. No entanto, os métodos convencionais de observação *in situ*, que envolvem o uso de instrumentação, devido à sua natureza e a limitações de caracter logístico, cobrem escalas de espaço-tempo geralmente reduzidas e que não são as mais adequadas para a correta compreensão da morfodinâmica costeira.

Os métodos de deteção remota emergem, neste contexto, como uma solução alternativa com grande potencial para produzir observações de alta frequência e elevada resolução espacial dos processos na zona *nearshore*. Os sistemas de vídeo-monitorização, em desenvolvimento nas últimas três décadas, têm-se revelado como uma ferramenta de elevada relação custo/qualidade na aquisição de dados sobre o sistema costeiro pelo que são utilizados cada vez com mais frequência para apoiar o trabalho de cientistas e gestores costeiros.

Esta dissertação tem como objetivo apresentar novos modelos conceptuais e ferramentas de processamento e análise de imagem vídeo para avaliar a morfodinâmica da zona costeira. Este objetivo foi concretizado através do desenvolvimento de um conjunto de ferramentas computacionais eficientes capazes de extrair informações sinópticas sobre a hidrodinâmica e a morfológica a partir de imagens de vídeo.

Os dados utilizados neste trabalho foram adquiridos em cinco locais de estudo diferentes localizados em diferentes partes do mundo. Em três locais, os dados vídeos foram adquiridos em estações dedicadas e instaladas para fins científicos. Dois conjuntos de dados adicionais utilizaram as imagens disponibilizadas on-line pelas

surfcams (infraestruturas instaladas na costa para cujo objetivo é fornecer informações visuais remotas do mar para a comunidade surfista).

No âmbito deste trabalho, foi elaborado um conjunto de algoritmos independentes para realizar o pré-processamento e georreferenciar as sequências de vídeo adquiridas a partir de aplicações informáticas pré-existentes. Este processamento incluiu a produção automática de imagens especiais, nomeadamente *Timex*, *Variance* e *Timestack*.

A primeira técnica desenvolvida no âmbito deste trabalho explorou a variação de intensidade do pixel das imagens *Timestack* para caracterizar a hidrodinâmica da zona *nearshore*. Para este efeito, relacionou-se o desvio padrão da intensidade do pixel com a distribuição espacial dos domínios de transformação das ondas, permitindo identificar com sucesso os domínios de empolamento, espalho e espraio no perfil *nearshore* coberto pela imagem. Esta técnica constitui uma nova ferramenta para estudar a evolução costeira, uma vez que os domínios das ondas estão diretamente relacionados com as características morfodinâmicas da praia. Acresce que, o facto deste método também poder ser aplicado a imagens *Variance* alarga esses estudos à dimensão longilitoral.

A segunda metodologia desenvolvida explorou a média da intensidade do pixel das imagens *Timestack* para estimar a altura de rebentação da onda. Neste contexto, foram identificados, nos perfis de intensidade, pontos de quebra notáveis que se relacionaram com o comprimento do padrão de rebentação visível (designado como parâmetro L_{Hs}). Numa primeira abordagem, a altura na rebentação foi estimada a partir da relação do parâmetro L_{Hs} com a informação batimétrica disponível. A altura da rebentação da onda estimada apresentou um Erro Quadrado Médio Normalizado (EQMN) de 14% quando comparado com os resultados de um modelo numérico, para alturas de onda ao largo que variaram entre 1.6 m e 3.5 m. Numa segunda abordagem propôs a relação $L_{Hs}/24$ para substituir o parâmetro de profundidade da água na fórmula mais simples de cálculo da altura da onda, que multiplica a profundidade da água pelo o índice de rebentação. Como a técnica pode ser aplicada diretamente a imagens *Timex*, foi possível utilizar imagens obtidas em quatro locais diferentes de forma a estender a respetiva validade. Nesta validação, obteve-se um EQMN de cerca de 22% para uma ampla gama de alturas de onda.

A terceira metodologia desenvolvida, teve como objetivo investigar a possibilidade de combinar a utilização de imagens vídeo com LiDAR terrestre 2D, para obter a topografia detalhada da zona intertidal da praia. O LiDAR 2D forneceu valores precisos de elevação, mas ao longo de um único perfil de praia, enquanto a variação longitudinal foi detetada nas imagens adquiridas pelo sistema vídeo (*Timex)*. Verificou-se que esta metodologia conseguia efetuar um levantamento 3D da topografia intertidal com um Erro Quadrático Médio (EQM) de aproximadamente 0.12 m.

Finalmente, foi desenvolvido um método para estimar a batimetria da praia submarina usando uma técnica de inversão batimétrica. A celeridade da onda foi estimada usando as trajetórias de onda extraídas de imagens *Timestack*, distinguindo as ondas na zona de empolamento e na zona de rebentação. A reconstituição batimétrica foi efetuada utilizando aproximações de águas pouco profundas e intermédias. O levantamento batimétrico efetuado até à profundidade de 11 m foi conseguido utilizando janelas de observação relativamente curtas (5 horas), obtendo-se um EQM de 0.46 m.

O conjunto de técnicas desenvolvidas no âmbito deste trabalho revelou-se uma ferramenta para o estudo da dinâmica costeira extremamente eficaz uma vez que possibilita a descrição simultânea do forçamento oceanográfico, como a altura da rebentação e o período da agitação incidente, bem como da respetiva resposta morfológica, nomeadamente a batimetria subtidal e a topografia intertidal. Estes métodos potenciam a adoção de sistemas de monitorização baseados em tecnologia vídeo de caracter operacional através da determinação em tempo quase real de indicadores costeiros, podendo ainda apoiar sistemas de aviso precoce de riscos costeiros.

Palavras chave: costa, onda**,** deteção remota**,** remote sensing, morfodinâmica costeira, batimetria

Table of Contents

List of Figures

3 – Study sites

4 – Identification of wave transformation domains

5 – Estimation of wave breaking height

6 – Intertidal beach topography assessment

7 – Subtidal bathymetry assessment

8 – Conclusions

List of Tables

1. INTRODUCTION

1.1 General context

The coastal zone is the interface between the land and the ocean. It is an extremely complex environment and one of the most dynamic regions on the Earth due to the numerous interactions of atmospheric, hydrodynamic and sedimentary processes.

A substantial proportion of the world population is concentrated in the coastal zone. For example, it is estimated that, in 2000, about 625 million people lived on low-lying (< 10 m) coastal areas worldwide (Neumann et al., 2015). In Europe, the population living on coastal municipalities reached 70 million inhabitants in 2001. In Portugal, about 60% of population resides within 10 km from the shore (Ferreira et al., 2008). Besides, the economic and social relevance of human activities taking place at the coast zone are also numerous. Leisure and sport, fishing and aquaculture, transportation and navigation, among others, generate economic incoming difficult to evaluate. Nevertheless, to cite some examples, the combined global value of goods and services from coastal ecosystems was estimated to $125 trillion/year (Costanza et al., 2014) in 2011. In Europe, the total value of economic assets located within 500 meters from the coastline was estimated in about 500-1000 billion euros in 2000 (Salman et al., 2004).

Natural processes, including wave action, flooding, storm surge, coastal erosion and sedimentation, often endanger human occupation and the use of the coastal zone (Davidson-Arnott, 2009; Ciavola et al., 2011a; Ciavola et al., 2011b). For example, all European coastal countries have been affected by coastal erosion over the last decades (Williams and Pranzini, 2013). The cost of mitigation against erosion and extreme wave events impacts along European coasts has been estimated to average 5400 million euro per year between 1990 and 2020 (Salman et al., 2004). Such threats to human life and economic activities are predicted to increase in the near future due to the occurring climate change worldwide (Stocker T., 2013).

Sea level rise will lead to more severe coastal storm impacts and will increment the number of floodings in the near future (Stocker T., 2013; Vousdoukas et al., 2017). In the perspective of population growth, with scenarios that project an increase till about 900 million by 2030, and over a 1100 million by 2060 of people living on the coast

worldwide (Neumann et al., 2015), there is a strong need to increase the resilience of coastal areas and communities to natural hazards.

It becomes therefore essential to improve our understanding of the physical processes occurring in the coastal zone, with particular attention to wave forcing and coastal morphodynamics.

1.2 The nearshore domain

A littoral profile is considered as a cross section taken perpendicular to the shoreline. It is generally composed of four sections: the offshore, the nearshore, the shore, and the coast (Dean and Dalrymple, 1984).

As a wave approaches from offshore into increasingly shallower waters, the depth where the seabed starts affecting the wave is defined as "offshore limit" (Svendsen, 2006), taken to be where the water depth is equal to half the deep-water wavelength ($\frac{h}{L} = 0.5$; Davies, 1973). In this work, nearshore coastal region is defined as the area between the offshore limit and the shoreline, which is defined as the edge between water and sand on the beach (Figure 1.1).

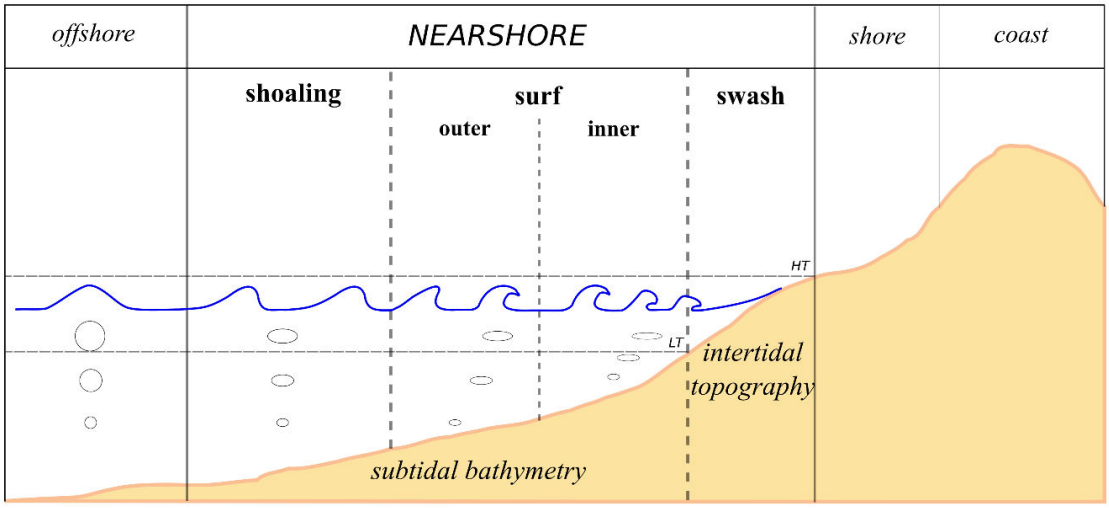

Figure 1.1 Idealised cross-section of a wave-dominated beach system. Nearshore area comprises shoaling, surf and swash zone. Subtidal bathymetry is defined as the beach slope under shoaling and surf zone, intertidal beach topography as the beach profile under swash zone.

Within the nearshore area, based on the wave properties, three distinct zones can be distinguished: shoaling, surf and swash zones.

In the shoaling zone, waves coming from deep sea start to alter their shape in response to sea bed interaction. In generally terms, wave height increases, wave speed decreases, and wave length decreases as wave orbits become asymmetrical.

When the wave crest becomes too steep, it becomes unstable, curling forward and breaking. This usually happens when the height of the wave becomes about the same size as the local water depth. The surf zone is the area comprised between the seaward and the landward wave breakpoint positions. The surf zone can be divided into 2 sub-regions: outer breaking surf zone, where only some waves are breaking, and inner breaking surf zone, or saturated breaker zone, where all waves have collapsed, and travel as bore.

Finally, the swash zone is the area in which the broken waves dissipate as swash on the beach foreshore slope. This is also called intertidal area, because the swash beach area zone is above water during low tide and under water at high tide.

1.3 Nearshore monitoring techniques

In order to analyse the complex interaction between coastal morphological processes, the coastal studies should be as much comprehensive as possible, covering both hydrodynamic and morphological measurements. The coverage in spatial and temporal scales of the forcing mechanisms controlling coastal evolution is also crucial to fully describe and understand their interaction.

Conventional surveys can provide high spatial resolution measurements of nearshore morphology, such as bathymetry (e.g., by vessel-based instrumentation) and beach topography (e.g., by RTK-GPS, Short and Trembanis, 2004). Nevertheless, they often lack the temporal resolution necessary for understanding the dynamic nature of the nearshore area due to logistical limitations and technical requirement (e.g., Mason et al., 2000). On the other hand, direct measurements of wave properties (e.g., wave height and wave period) are done with the use of oceanographic instruments, whose deployment is logistically difficult, and spatial and time-limited, especially at high energy environments with mobile sandy bottoms. As a consequence, description of wave transformation process as they approach the shoreline is often evaluated with hydrodynamic models and do not represent direct observations.

As many nearshore processes have a visible signature on the sea surface, remote sensing has emerged in this context as a valid technique for providing high spatio-temporal nearshore measurements. In contrast to in-situ sampling technique, remote sensing techniques (e.g., aerial photography, satellite imagery, wave radar, video monitoring, Light Detection And Ranging-LiDAR) offer the potential of a relative high resolution in time and space.

Among numerous remote sensing methodologies and approaches, shore-based coastal video monitoring has been proved as a cost-efficient and high-quality data collection tool to support coastal scientists and engineers over the last three decades (Holman and Stanley, 2007).

Coastal video monitoring uses images acquired by simple and common optical devices installed at the coast at an elevated position to collect frames of nearshore area at high frequency and continuously. Despite the lower spatial coverage, in comparison with other remote sensing technologies (e.g., satellite imagery, wave radar, LiDAR), video monitoring technique allows a high-frequency analysis of hydro- and mophodynamic processes of the beach system. Shore-based video system installations offer the advantages of excellent spatio-temporal resolutions (Figure 1.2), in combination with cost-efficient long-term data sampling.

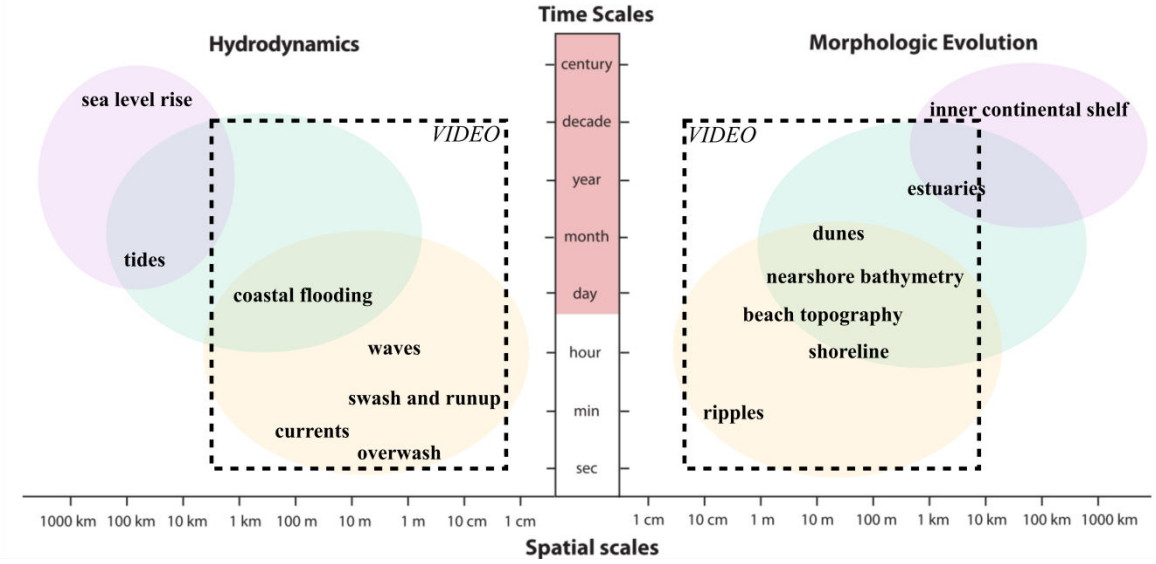

Figure 1.2. Conceptual representation of hydrodynamic processes and the morphologic evolution of coasts. The left side of the diagram indicates examples of fluid processes that influence changes in the morphologic features (shown on the right) in the time-space scales they occur. Dashed squares indicate the spatial and temporal range covered by coastal video monitoring technique application. (adapted from Elko et al., 2014)

As the study of natural processes requires continuous and quantitative observations, this work makes the use of the coastal video monitoring remote sensing technique the best compromise between spatial and temporal resolution, allowing the quantification of the hydro- and morphodynamic processes acting on the nearshore with unparalleled temporal resolution.

1.4 Motivation and Objectives

The main aim of this study is the development of new methodologies to achieve *synoptic hydrodynamic and morphology measurements in the nearshore through the exploitation of video monitoring technique*. With the achievement of this objective, it would be possible to combine nearshore hydrodynamic and morphology assessment to analyse in detail the coastal processes acting from the offshore limit to the shoreline.

A second aim is that such developed methodologies should be *simple and efficient*, *to overcome the complexity of image processing procedures and speed up digital signal operation.* The achievement of this objective aims to provide tools to sustain, for instance, quasi-real time measurements and early-warning systems.

A third aim of this work is *to investigate if and how existing data acquisition infrastructures (like "surfcams") can be exploited for coastal process studies*. For instance, coastal surfcams are online-streaming cameras installed at the coast to remotely providing visual information of sea state to surf users. A large amount of surfcams are streaming coastal images worldwide daily, therefore their image exploitation would be an attractive solution for supporting coastal monitoring and coastal management.

To achieve the three objectives of this thesis, *five major tasks* have been defined:

- identification of shoaling, surf and swash;
- estimation of wave breaking height;
- intertidal beach topography assessment;
- estimation of wave celerity;
- nearshore bathymetry retrieval.

1.5 Thesis outline

This thesis presents a wide range of novel techniques to improve and foster the use of video monitoring technique to measure hydrodynamics and morphological features in the nearshore. The work is structured in eight chapters.

1 - **Introduction**: describes the general context, the motivation and objectives of the study, along with listing the thesis outline.
2 - **Coastal Video monitoring technique**: gives an overview of coastal video monitoring technique, describing image processing techniques for rectification and special image generation. The exploitation of surfcam images for coastal studies is also introduced.
3 - **Study sites**: presents the sites considered in this study. It describes the heterogeneous hydrodynamics and morphological characteristics, along with the different video data collected and used in this work.
4 - **Identification of wave transformation domains**: describes a technique to identify wave transformation domains in the nearshore with the use of Timestack and Variance images.
5 - **Estimation of wave breaking height**: presents two developed methodologies to measure wave breaking height from Timestack and Timex images.
6 - **Intertidal beach topography assessment**: proposes an original approach based on coupling terrestrial LiDAR measurements and video-derived shoreline to accurately measure intertidal beach topography.
7 - **Subtidal bathymetry assessment**: presents a depth inversion technique that measures wave celerity on video imagery to assess nearshore subtidal bathymetry.
8 - **Conclusions**: summarizes the conclusions for each technique presented in the aforementioned chapters, adding suggestions for further improvement and future work.

2. COASTAL VIDEO MONITORING TECHNIQUE

2.1 Introduction

Video cameras are a powerful tool to monitor the coastal field. When these optical devices are installed on a fixed, shore-based platform composing a coastal video monitoring station, they offer the advantages of autonomous and non-intrusive collection of data observations, both short- and long-term acquisitions, with cost-efficiency and high spatial and temporal resolution. In this section, the characteristics of video coastal video monitoring stations and images are presented.

The pioneer ARGUS monitoring program (Holman and Stanley, 2007) was the first scientific program to install a shore-based video monitoring system and to support coastal studies through video-derived observations. The system was developed by the Coastal Imaging Lab at the Oregon State University in the early 90's, and it has been providing coastal image data worldwide for the last two decades. To 2007, approximately 30 Argus video-monitoring stations and 120 cameras were operating daily in 8 countries (Figure 2.1).

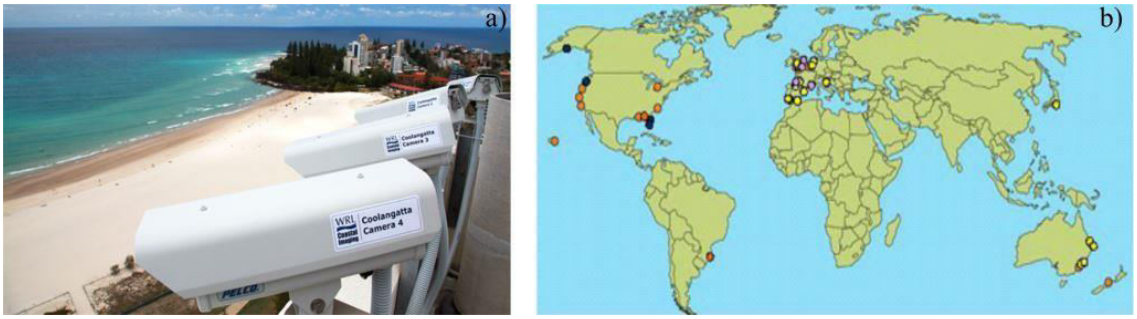

Figure 2.1. a) example of Argus system installation at Coolangatta, Australia (http://ci.wrl.unsw.edu.au/). b) locations of Argus stations over the world in 2003 (from Aarninkhof, 2003).

In the 2000's, the expansion of commercial video systems (e.g., CoastalComs, www.coastalcoms.com, Erdman www.video-monitoring.com) and the development of image processing tools (e.g., SIRENA - Nieto et al., 2010; COSMOS - Taborda and Silva, 2012, http://cosmos.fc.ul.pt; Beachkeeper plus - Brignone et al., 2012; ULISES - Simarro et al., 2017) promoted the installation of video monitoring stations for scientific purpose with the use of relatively cheap Internet Protocol (IP) video cameras to overcome the expensive installation and purchase of Argus system.

An IP camera is a type of digital video camera commonly employed for video surveillance. Such device can send data via a computer network and/or Internet protocol suite, both in form of images and video.

2.2 Video monitoring station

A video-monitoring station is usually composed by one (or more) video-camera connected to a personal computer, which has the functions of controlling the optical device and storing the video acquisitions (e.g., Vousdouskas et al., 2011). The optical device is usually installed stable at an elevated position looking at the emerged beach and the nearshore (Figure 2.2).

Data sampling interval can vary depending on the aim of the study and on the storage space capability. Image collection frequency is chosen based on camera properties and research objectives. In general, the choice should be based on the balance among data storage space, image quality, and image processing computational time. For instance, acquisition rate was found feasible at 1 frame per second (1 Hz) for long-term monitoring of shoreline change (e.g., Harley et al., 2013), 2 Hz for studying swash processes (e.g., Thuan et al., 2016), 10 Hz to video-measure high-frequency processes such as overwash (Matias et al., 2017).

Figure 2.2. Example of video monitoring stations. a) Praia de Faro, Portugal (Vousdoukas et al., 2011); b) Torre Canne, Italy, from Valentini et al. (2017a); c) Barreta Island, Portugal, from Matias et al. (2017).

Besides the relative long-term monitoring stations (Table 2.1), the portability of IP cameras has also promoted the temporary use of optical devices to support oceanographic field work (e.g., Senechal et al., 2011a) along with video monitoring application on physical modelling for a wide range of purposes such as wave hydrodynamics (e.g. Almar et al., 2011) wave runup measurements (e.g., Schimmels et al., 2012; González-Jorge et al., 2015) and overwash analysis (e.g., Matias et al., 2014).

Table 2.1. Coastal video monitoring systems deployed worldwide.

System	Site	City	Country	start date	Active /end	website	data online
Cam-era	New Brighton	New Brighton	NZ	1997	✓	www.niwa.co.nz/	
"	Pauanui	Pauanui	NZ	1997	✓	"	
"	Raglan	Raglan	NZ	1997	✓	"	
"	Tairua	Tairua	NZ	1997	✓	"	
Orasis	Faro beach	Faro	PRT	2009	2010	www.vousdoukas.com	
Casagec	Capbreton	Capbreton	FRA	2009	✓	www.casagec.fr	✓
COSMOS	Nazare station	Nazare	PRT	2009	2013	beachtocanyon.fc.ul.pt	
Horus	BocaGrande	Cartagena	COL	2009	2015	www.horusvideo.com	
SIRENA	Castelldefels	Barcelona	ESP	2010	✓	coo.icm.csic.es/	✓
"	Sisal	Merida	MEX	2011	✓	"	✓
"	Platja de Palma	Mallorca	ESP	2011	2018	socib.eu	✓
"	Cala Millor	Mallorca	ESP	2011	✓	"	✓
"	Son Bou	Menorca	ESP	2011	✓	"	✓
COSMOS	San Michele	Sirolo	ITA	2011	2013	-	
Orasis	Faro	Faro	PRT	2011	2012	www.vousdoukas.com	
"	Ammoudara beach	Creta	GRE	2012	✓	"	
"	Victoria beach	Cadiz	ESP	2012	✓	"	
"	Koutsounari beach	Creta	GRE	2012	2013	"	
"	Porto de Galinhas	Pernambuco	BRA	2013	✓	"	
"	Itapuama beach	Pernambuco	BRA	2013	✓	"	
"	Eressos Beach	Lesbos Island	GRE	2013	✓	"	
"	Kalo Livadi Beach	Mikonos	GRE	2014	✓	"	
"	Gerakas Beach	Zakynthos Island	GRE	2014	✓	"	
"	Katerini Beach	Central Macedonia	GRE	2014	✓	"	
Casagec	Le Barcares	Le Barcares	FRA	2014	✓	www.casagec.fr	✓
Poliba	Torre Canne	Fasano	ITA	2015	✓	http://91.121.30.84/	✓
Poliba	Torre Lapillo	Porto Cesareo	ITA	2015	✓	"	✓
Casagec	Angle	Biarritz	FRA	2017	✓	www.casagec.fr	✓
"	Lacanau	Lacanau	FRA	2017	✓	"	✓
"	La Salie	Biscarrosse	FRA	2017	✓	"	✓
"	Bidart	Biscarrosse	FRA	2017	✓	"	✓

2.2.1 Surfcam network

Despite the large exploitation of video imagery techniques, the use of online-streaming web-cam has been poorly investigated. For example, coastal "surfcams" are video cameras installed at the coast with the main aim of remotely providing visual information of sea state to surf users.

Two previous studies were conducted to investigate the possibility of using surfcam network for coastal studies (Mole et al., 2013; Bracs et al., 2016). Mole et al. (2013) used low-angle surfcam images to routinely monitor shoreline and inshore wave using a commercial software at seven different sites on the Australian coastline. In Bracs et al. (2016), a more detailed and accurate image geometry and shoreline extraction was presented, highlighting the potentiality for the surfcam systems to significantly expand coastal monitoring around the world's coastlines.

Due to the wide number of coastal surfcams present on the shore worldwide, it is a quite challenging task to quantify the numbers of such devices deployed. Over the Portuguese coast, three main companies have an operating surfcam network, namely Beachcam (www.beachcam.meo.pt), Surfline (www.surfline.com) and Surftotal (www.surftotal.com). To date, a total amount of 116 surfcams (Table 2.2) provides images of about 70 beaches spread all over the coast on real-time during daylights (Figure 2.3), with seven beaches in which all companies have installed surfcams, namely Costa da Caparica, Carcavelos, Guincho, Praia Grande, Ribeira d'Ilhas, Peniche and Nazare.

Table 2.2. Surfcam network at Portuguese coast (May 2018).

	Beachcam	***Surfline***	***Surftotal***
Number of cameras deployed	*63*	*33*	*20*

In this work, the feasibility of using surfcam images have been investigated. Video streamed online were retrieved using an automated Matlab-based algorithm developed for the purpose. The code read the video content at the specified Uniform Resource Locator (URL) and saved it to the specified filename. Details of the video properties are specified in the section dedicated to each singular study site (Chapter 3).

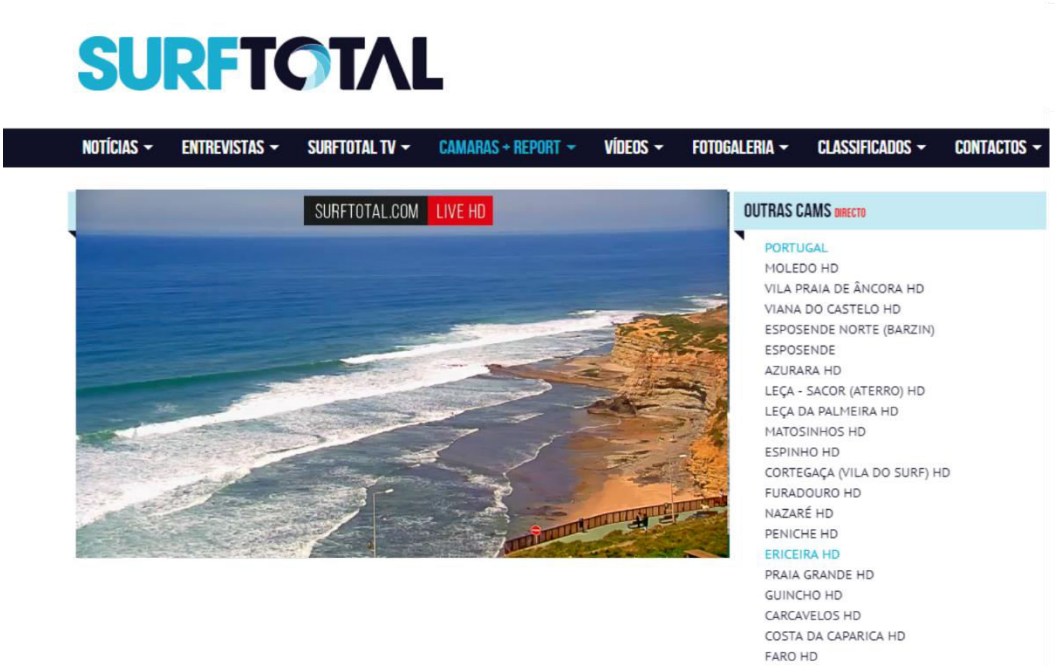

Figure 2.3. Screenshot example of Surftotal network web site.

2.3 Image processing

In order to exploit the images acquired by a coastal video-system for quantitative studies, an accurate procedure must be applied to raw video data to obtain geo-referenced images (e.g., Hartley and Zisserman, 2003). This section describes the necessary steps to obtain geo-referenced images from coastal video-monitoring system acquisitions.

2.3.1 Camera calibration

Camera calibration process, also called camera re-sectioning, is the process that estimates the intrinsic parameters of lens and image sensor of an optical device. Determination of camera internal parameters is necessary to correct the image distortion inducted by the lens curvature. Internal parameters are namely the focal length f, the position of the image center (u_c, v_c), radial and tangential distortion coefficients k_j. Focal length f is defined as the distance from the center of the lens to the focal points of the lens. It is a measure of how strongly the optical sensor converges or diverges light. It is usually specified in millimetres (mm) and it is inversely proportional to the field of view of a lens. The position of the image center (u_c,v_c) coincides around the center of the image in pixels. Finally, the distortion coefficients k_j quantify the deformation that might be inducted on the image by the lens curvature.

In this work, freely available Camera Calibration Toolbox for Matlab (Bouget, 2007) was used to perform camera calibration. The toolbox guides the user through the camera calibration process step-by-step to determine the camera intrinsic parameters.

2.3.2 Image rectification

The image rectification process is the procedure that transforms an originally oblique image into a plan view equivalent image, also known as rectified image (e.g., Taborda and Silva, 2012). Standard photogrammetric procedures (Holland et al., 1997) enable the transformation from Real World coordinates (X, Y, Z) to image coordinates (u, v) on the basis of the collinearity equations.

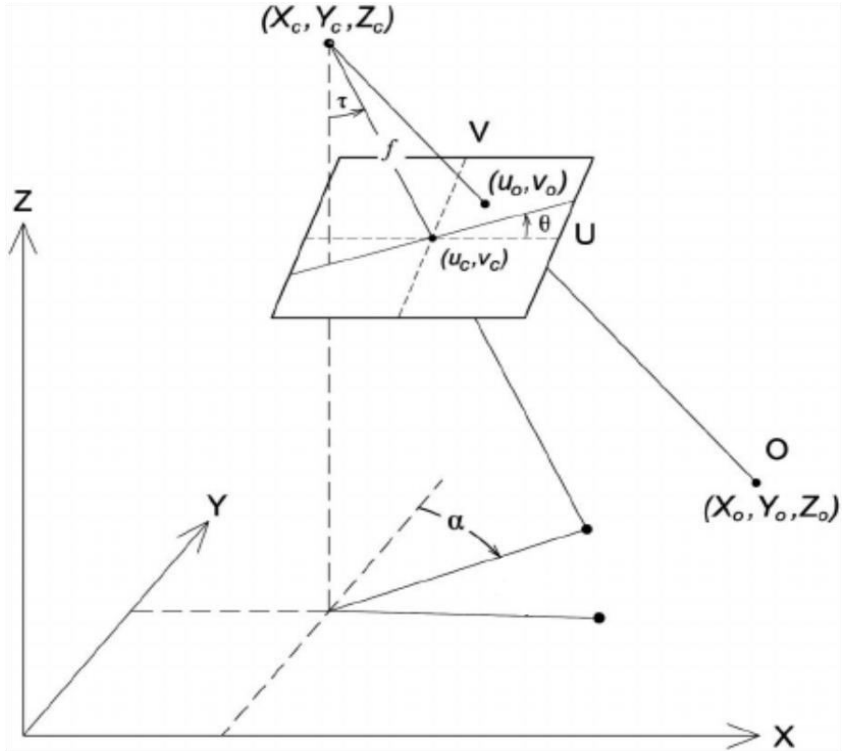

Figure 2.4. Pinhole camera model demonstrating the collinearity relationship between the object (X_o,Y_o,Z_o), the image point (u_o,v_o), the camera optical center (Xc,Yc,Zc) and camera rotation angles (azimuth α; tilt τ and roll θ). Adapted from Bechle et al. (2012).

Collinearity equations describe the physical model (Figure 2.4) representing the geometry between the projection center (u_c, v_c), the point on image coordinates (u_o, v_o) and the ground coordinates (X_o, Y_o, Z_o). These equations can be easily solved from the knowledge of camera internal and external parameters, i.e., principal point (u_c, v_c) and focal distance f computed in the calibration procedure, camera position (X_C, Y_C, Z_C) and camera orientation (azimuth α; tilt τ and roll θ):

$$u_O = u_C - f\left[\frac{m_{11}(X_O - X_C) + m_{12}(Y_O - Y_C) + m_{13}(Z_O - Z_C)}{m_{31}(X_O - X_C) + m_{32}(Y_O - Y_C) + m_{33}(Z_O - Z_C)}\right] \quad \text{Eq. 2.1}$$

and

$$v_O = v_C - f\left[\frac{m_{21}(X_O - X_C) + m_{22}(Y_O - Y_C) + 2_{13}(Z_O - Z_C)}{m_{31}(X_O - X_C) + m_{32}(Y_O - Y_C) + m_{33}(Z_O - Z_C)}\right] \quad \text{Eq. 2.2}$$

where (u_c, v_c) is the center of the image, f is the focal length and (X_C, Y_C, Z_C) is the camera location.

Parameters m_{nm} correspond to the parameters of the orientation matrix M (e.g., Wolf and Dewitt, 2000):

$$\begin{bmatrix} m_{11} & m_{12} & m_{13} \\ m_{21} & m_{22} & m_{23} \\ m_{31} & m_{32} & m_{33} \end{bmatrix} = \begin{bmatrix} cos(\alpha) & sin(\alpha) & 0 \\ sin(\alpha) & cos(\alpha) & 0 \\ 0 & 0 & 1 \end{bmatrix} \begin{bmatrix} 1 & 0 & 0 \\ 0 & cos(\tau) & -sin(\tau) \\ 0 & sin(\tau) & cos(\tau) \end{bmatrix} \begin{bmatrix} -cos(\theta) & -sin(\theta) & 0 \\ -sin(\theta) & cos(\theta) & 0 \\ 0 & 0 & 1 \end{bmatrix} \quad \textit{Eq. 2.3}$$

where azimuth α, tilt τ and roll θ.

For the purpose of solving the systems (Eq. 2.1 and Eq. 2.2), it is necessary to identify on the oblique undistorted image at least 6 reference Ground Control Points (GCPs) whose Real World coordinates are known. GCPs can be selected on fixed structure on the coast (such as breakwaters, houses, paths), installed in form of panels visible on the image (Harley et al., 2013), or be collected by GPS survey and later identified on the acquired image sequence.

While the two-dimensional coordinates transformation is solved by the process, the elevation value Z_o must be defined a priori. In this work, the third dimension Z_o was assumed equal to the tidal level correspondent to the image acquisition time.

COSMOS software (Taborda and Silva, 2012) was used for the rectification process in this work. COSMOS has a user-friendly interface which guides over the several photogrammetric steps for image rectification. COSMOS monitoring system has already been successfully applied to several coastal and estuarine sites with different objectives, illustrating its versatility and wide range of applicability (Harley et al., 2013; Silva, 2014). In order to automate and speed up the process, the series of algorithms used in COSMOS interface were joined to perform the rectification process with a single Matlab-based code.

2.3.3 Surfcam images rectification

The "standard" rectification procedure described above was not applicable to images acquired from surfcam streaming. In fact, the exact position and the internal parameters of the video surfcam were unknown.

Rectification procedure for surfcam images was performed using the semi-automatic photogrammetric tool *C-Pro* (Sánchez-García et al., 2017). Selecting a minimum of six GCPs, *C-Pro* algorithms achieved the preliminary camera calibration and repositioning by Direct Linear Transformation relation. Successively, the internal and external

photogrammetric orientation parameters were refined by an iterative collinearity adjustment to transform image data into Real-World coordinates. In order to optimize the procedure, *C-Pro* used the identified terrestrial horizon line in the image as a geometric computational constraint. Finally, image rectification was performed by inverse mapping and nearest neighbour interpolation methods.

Using the intrinsic and extrinsic camera parameters assessed by *C-Pro*, the rectified image sequence was obtained by the developed automatic COSMOS-based routine, which resulted much faster computing than *C-Pro* software for such purpose.

2.3.4 Spatial Resolution

The spatial resolution of a rectified image is the geometrical projection of the pixel dimension on the terrain. Therefore, the spatial dimension of the pixel is inversely proportional to the spatial resolution. Pixel dimension can be represented by two distinct components. The transversal component (Δc) corresponds to the dimension of the pixel along the rectified image x-axis, whereas the longitudinal component (Δr) is the pixel spatial dimension along the rectified image y-axis. Following Holman and Stanley (2007):

$$\Delta c = (dp * R)/f \qquad \textit{Eq. 2.4}$$

$$\Delta r = (\Delta c * R)/H \qquad \textit{Eq. 2.4}$$

where R is the radial distance from the camera, dp is the pixel dimension used for the rectification process and H is the elevation of the camera.

The spatial dimension of the pixel is a function of the camera position, field of view and angle of view. Therefore, spatial resolution of a rectified images decreases when the distance from the camera increases, while the camera elevation is directly proportional to the image resolution.

2.4 Secondary images product

Coastal video monitoring uses special images, namely Timex, Variance and Timestack, produced through the acquired image sequences. These specific images have been considered “standard” since the advent of coastal video-monitoring. In this section, these specific images and their use are described in detail below.

2.4.1 Timex

TIMe- EXposure images (Timex, Figure 2.5) are created by the mathematical average of RGB pixel intensity of the individual images collected over a period of sampling (Holman and Stanley, 2007), usually chosen of 10 minutes.

The averaging of pixel intensity smooth out variations in wave dissipation and swash movement on the shore, along with filtering out moving objects from the camera's field of view, such as ships, vehicles and people.

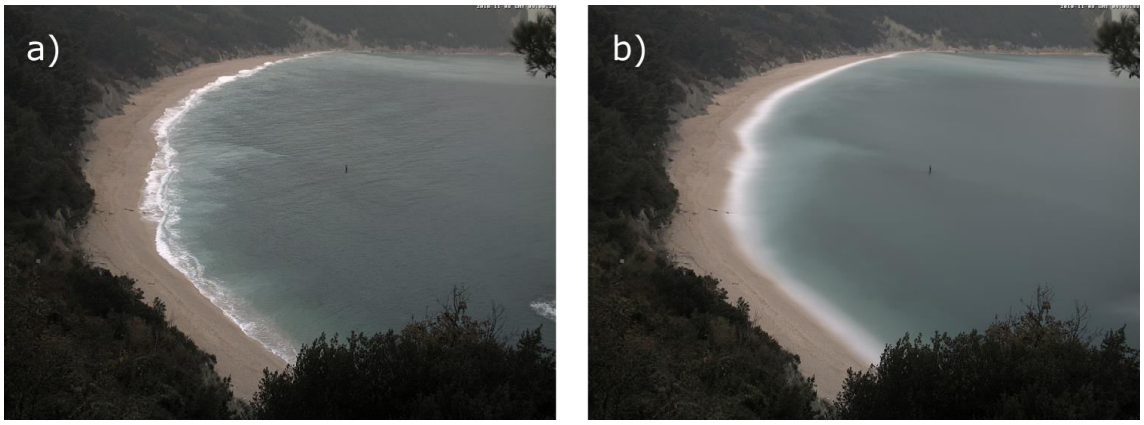

Figure 2.5. Original frame (a) and 10 minutes Timex image (b) of San Michele-Sassi Neri beach, Italy (from Harley et al., 2013)

The main characteristic of Timex is to underline the wave breaking process as white bright intensity pattern, which corresponds to the preferential location of wave breaking (e.g., Lippmann and Holman, 1989).

It has been shown that, since submerged sand bars cause preferential breaking over the bar crest, these images can be used to find the locations and morphology of submerged nearshore sand bars. This property has been exploited (Figure 2.6) for the study of nearshore sand bar migration (e.g., Armaroli and Ciavola, 2011; Angnuureng et al.,

2017), rip currents (e.g., Turner at al., 2007; Orzech et al., 2010; Gallop et al., 2011; Pitman et al., 2016), beach state characteristics (e.g., Ranashinke et al., 2004, Quartel et al., 2006; Ortega-Sánchez et al., 2008; Price and Ruessink, 2008; Masselink et al., 2014).

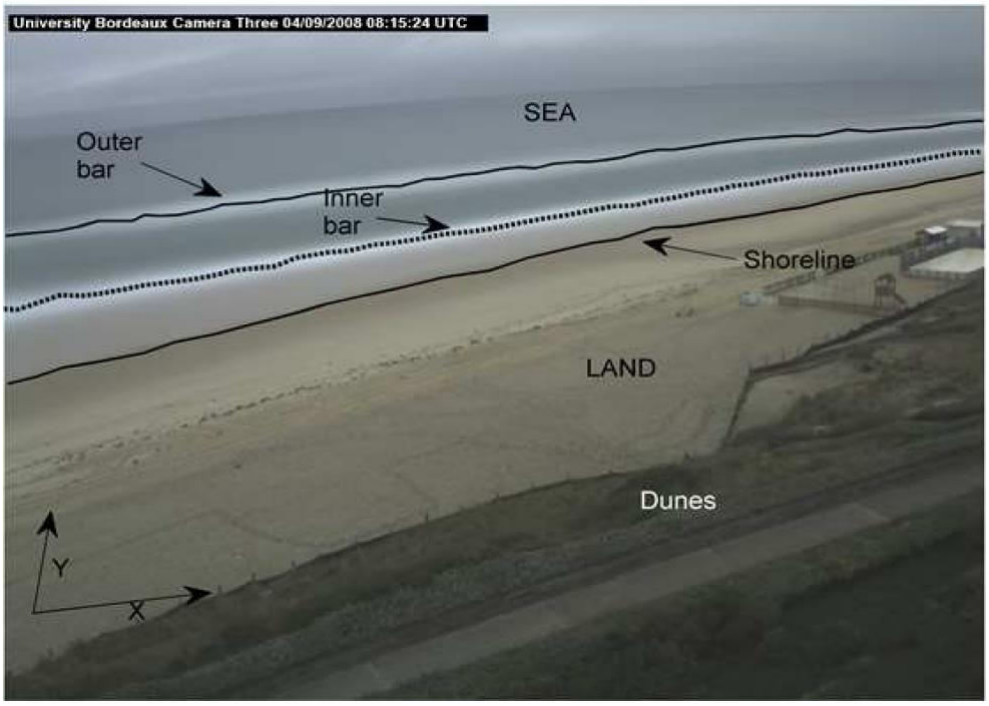

Figure 2.6. Coastal features detected on a 10-min Timex image from the camEra video system at Biscarrosse (from Angnuureng, 2016)

Since on Timex the pixel intensity is averaged on time, also swash movements on the foreshore slope are smoothed out and modulated. For this reason, several algorithms have been proposed for shoreline detection on Timex (e.g., Aarninkhof et al., 2003; Alvarez-Ellacuria et al., 2011; Osorio et al., 2012; Valentini et al., 2017b) and Timex have been widely used for a long-term monitoring of shoreline change (e.g., Ruiz de Alegria-Arzaburu and Masselink, 2010). Nevertheless, it has been observed that often shoreline detection on Timex might be affected by beach saturation color and misleading to a wrong shoreline position on low terrace and/or during low tide conditions (Huisman et al., 2011).

2.4.2 Variance

Variance images (Figure 2.7) are created by computing the standard deviation of the individual images that are collected over a period of sampling (Holman and Stanley, 2007). Variance images are bright on the areas with large temporal variability, while unchanged areas appear dark. Thus, a sandy beach is shown as dark in a Variance, while the surf zone appears very bright, due to the pixel intensity variation in relation to breaking waves (Holman and Stanley, 2007).

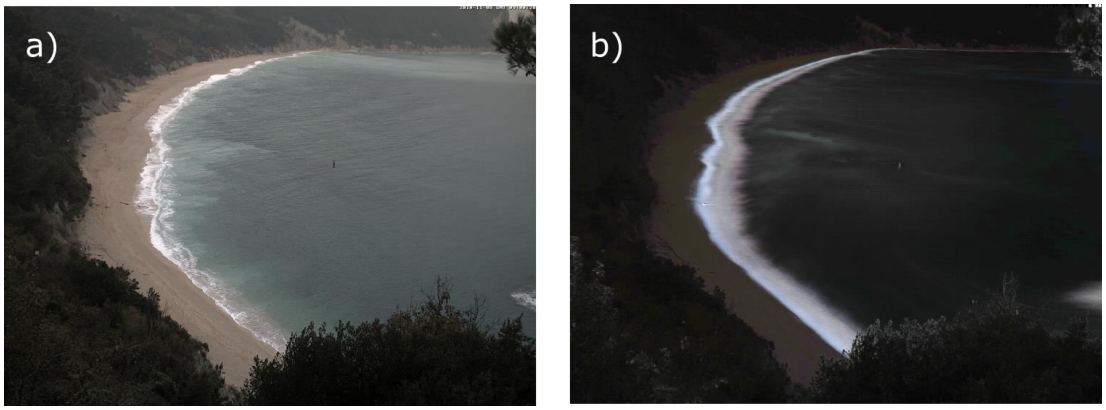

Figure 2.7. Original frame (a) and 10 minutes Variance image (b) of San Michele-Sassi Neri beach, Italy (from Harley et al., 2013)

Despite the fact that Argus stations and other video systems have been producing Variance for long time, this kind of images has been seldom used. Few examples of the use of Variance can be seen in Vousdoukas et al. (2011), in Simarro et al. (2015) and in Rigos et al. (2016), mainly regarding shoreline contour detection.

2.4.3 Timestacks

A Timestack image is generated by sampling a single line of pixels from each image over the period of acquisition and concatenating such array of pixel according to the frame acquisition frequency. Timestack is therefore composed by pixel intensity time series over a given image sequence. In general, a video data acquisition of 10 minutes is considered, however the chosen time interval can vary depending on the system set up or the main purposes of the study (e.g., from 7 mins to 34 mins in Stockdon et al., 2006; 20

mins in Almar et al., 2011). Depending on the sampled transect direction, can be produced cross-shore or along-shore.

Timestacks were firstly produced with the main purpose of measuring wave runup, as the camera acquisitions allowed the monitoring of the high-frequency waterline oscillation on the beach slope. The first appearance of a Timestack image (Figure 2.8-a) is dated to Aagaard and Holm (1989). A clearer image (Figure 2.8-b) was published in Holland and Holman (1993), originated from Argus images collected at Duck during DELILAH experiment (Birkemeier et al., 1997).

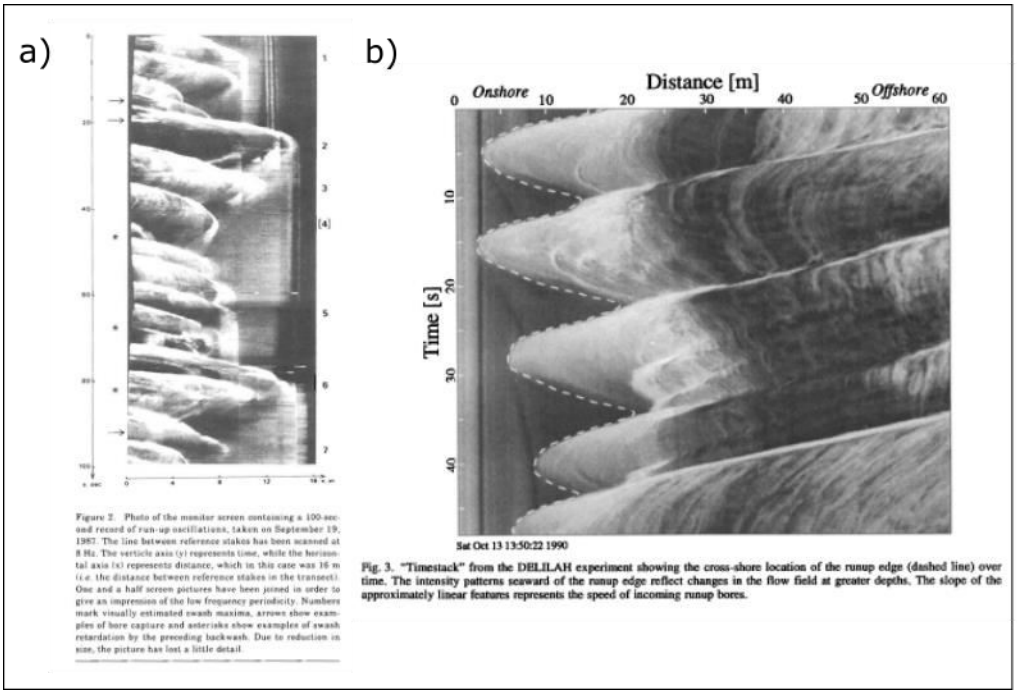

Figure 2. Photo of the monitor screen containing a 100-second record of run-up oscillations, taken on September 19, 1987. The line between reference stakes has been scanned at 8 Hz. The verticle axis (y) represents time, while the horizontal axis (x) represents distance, which in this case was 16 m (i.e. the distance between reference stakes in the transect). One and a half screen pictures have been joined in order to give an impression of the low frequency periodicity. Numbers mark visually estimated swash maxima, arrows show examples of bore capture and asterisks show examples of swash retardation by the preceding backwash. Due to reduction in size, the picture has lost a little detail.

Fig. 3. "Timestack" from the DELILAH experiment showing the cross-shore location of the runup edge (dashed line) over time. The intensity patterns seaward of the runup edge reflect changes in the flow field at greater depths. The slope of the approximately linear features represents the speed of incoming runup bores.

Figure 2.8. First representations of Timestack images. a) from Aagaard and Holm (1989). b) from Holland and Holman (1993).

Over the last decades, Timestack characteristic of clearly showing waterline variations (Figure 2.9) have been extensively applied to improve foreshore runup knowledge (Holland and Holman, 1993; Bailey and Shand, 1994; Holland et al., 1995; Ruggiero et al., 2004; Vousdoukas et al., 2009; Guedes et al, 2011a; Power et al., 2011; Senechal et al., 2011b; Brinkkemper et al, 2014; Stockdon et al, 2014; Vousdoukas et al., 2014) to improve runup measurements (Simarro et al., 2015; Blenkinsopp et al., 2016; Almar et al., 2017a) and to propose new wave runup parameterization (Stockdon et al., 2006; Vousdoukas et al., 2012; Poate et al., 2016; Atkinson et al., 2017).

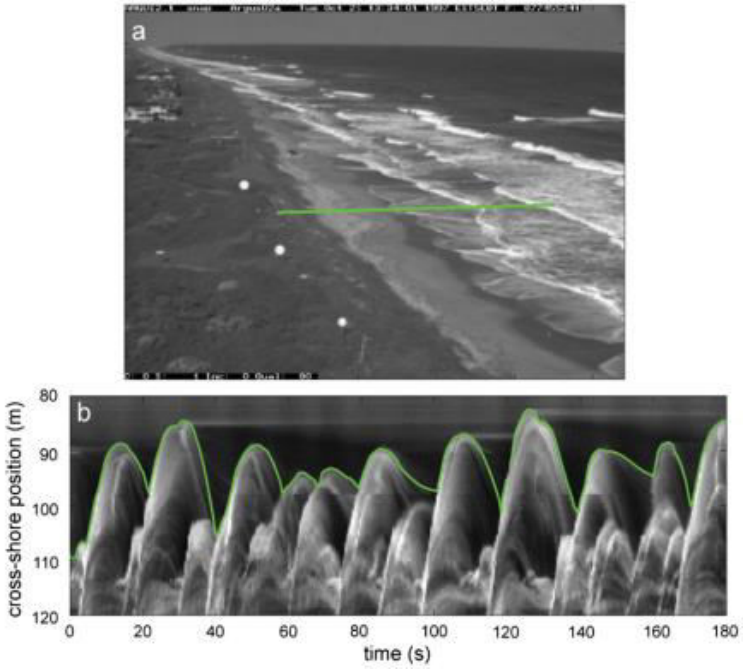

Figure 2.9. Timestack image for runup studies, from Stockdon (2014).

Besides the possibility of measuring wave runup, Lippmann and Holman (1990) related Timestack pixel intensity to temporal series of water surface elevation. Exploiting such property, authors measured the wave period applying frequency domain analysis (Lippman and Holman, 1989; Almar, 2009) or computing wave spectrum (Zikra, 2012) of pixel intensity timeseries.

Another Timestack application resides on the measurement of wave celerity (Almar et al, 2008; Tissier et al., 2011; Almar et al., 2014; Postacchini and Brocchini, 2014), which allowed to determine subtidal bathymetry using linear/non-linear wave theory and depth inversion technique (Stockdon and Holman, 2000; Yoo, 2007; Almar et al., 2011; Holman et al., 2013).

Finally, Timestack images were used to estimate wave breaking height (Gal et al., 2011; Almar et al., 2012a; Gal et al., 2014; Robertson et al., 2015), to measure overwash velocity (Matias et al., 2017), and along-shore Timestacks adopted to estimate longshore currents (Chickadel, 2007). In this work, used cross-shore Timestacks were generated by a Matlab code kindly provided by Almar (2009).

3. STUDY SITES

The present chapter is partially based on the works:

Andriolo, U., Herminio, J., Ribeiro, M., Taborda, R. (2015). Insights on run-up processes through high resolution video measurements. VIII International Symposium on the Iberian Atlantic Margin (MIA15). Malaga, Spain

Andriolo, U., Sanchez-Garcia, E., Taborda, R. (2016). Using surfcam online streaming images for nearshore hydrodynamics characterization. 4th Jornadas de Engenharia Hidrográfica, Lisbon, Portugal

Andriolo, U., Sedrati, M., Brunier, G., Gardel, A.,Taborda, R., Fargues, C., Furiga, J. (2018). Video monitoring for Guianese beach morphodynamics and management. EGU General Assembly 2018, Vienna, Austria

3.1 Introduction

This chapter describes the study sites considered in this thesis. Field measurements and video imagery data were collected at a wide range of beach environments that includes five different beaches from three continents, namely Europe, Asia and South America (Figure 3-1).

Three study sites are located on the Western Portuguese coast (Section 3.1.1), namely Praia Grande (Section 3.2), Costa da Caparica (Section 3.3), and Ribeira d'Ilhas (Section 3.4), exposed to the high-energy wave regime generated in the North Atlantic.

The fourth study site is a sector of Kourou beach (Section 3.5), located on the coast of French Guyana, along the South America coastline influenced by the Amazonian river.

The fifth study site is a sector of Nha Trang beach (Section 3.6), located in southeastern Vietnam coast facing the South China Sea.

The author participated in the installation of the video station at Praia Grande and Kourou, besides it implemented the standalone set of algorithms to process the acquired video data. Data processing comprehended image management, Timex and Variance production, image undistortion and rectification.

The online-streaming surfcam images at Costa da Caparica and Ribeira d'Ilhas were chosen to explore the feasibility of such devices for coastal videomonitoring.

Finally, the author had access and the possibility of using the video data acquired at Nha Trang within the COASTVAR project (Accompagnement spécifique des travaux de recherches et d'innovation défense , ASTRID-2014; ANR-14-ASTR-0019).

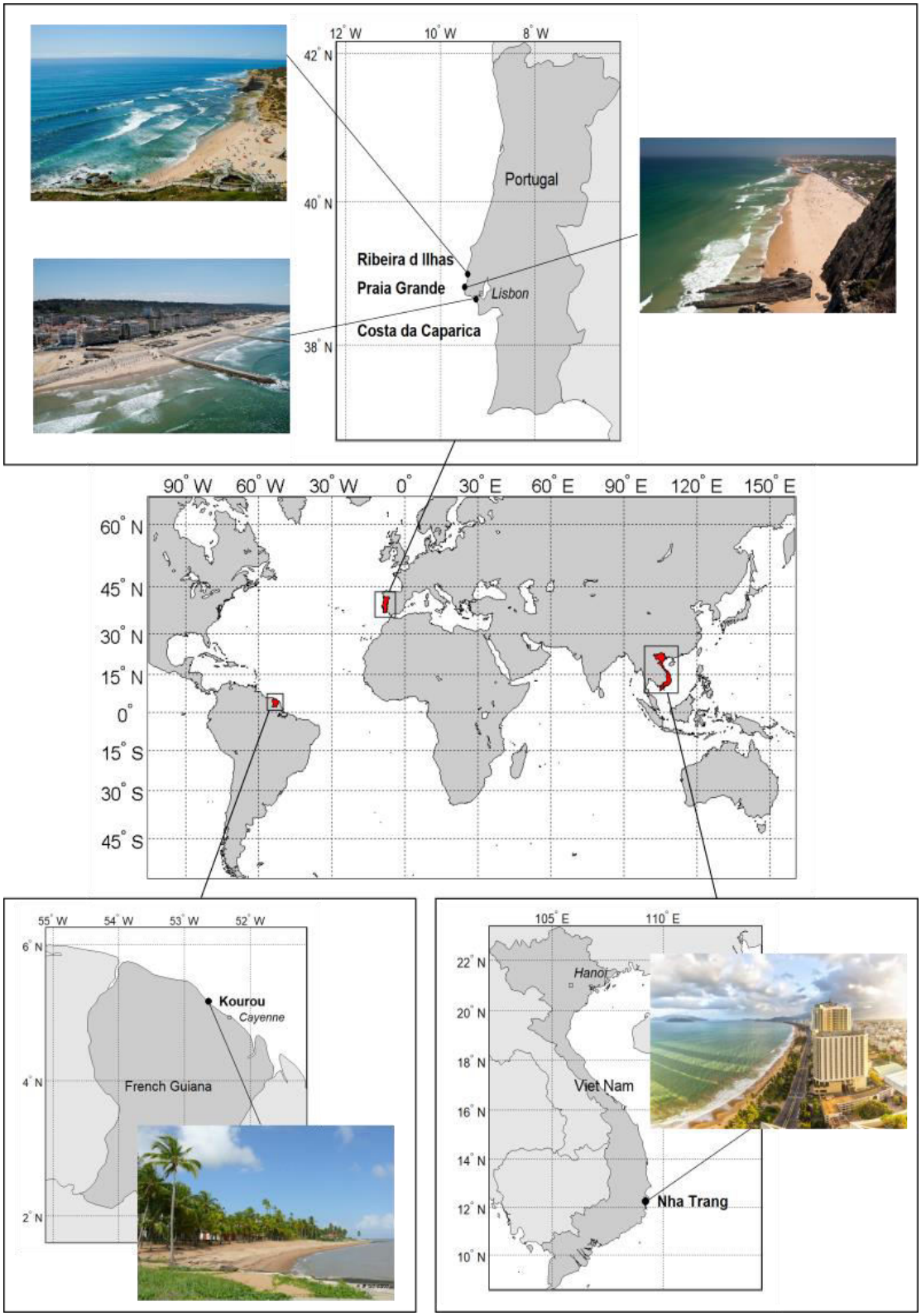

Figure 3.1. World map with study sites location.

3.1.1 Portuguese western coast

This section describes the general oceanographic forcing of the Portuguese western coast. The tidal properties and wave regime are common to the three study sites located on the Portuguese central westcoast, namely Praia Grande (Section 3.2), Costa da Caparica (Section 3.3), and Ribeira d'Ilhas (Section 3.4).

3.1.1.1 Tide and storm surge

The astronomical tide is semidiurnal, with an average period of 12 hours and 25 minutes, resulting in two high tides and two low tides per day (Silveira, 2017). The tidal regime is mesotidal, with average amplitude of the astronomical tide on the order of 2.10 m, reaching a maximum elevation of 4 m (Antunes, 2007). The surge phenomenon associated with storms measured at Cascais tide gauge had a maximum of 0.6 m (Taborda and Dias, 1992; Gama et al, 1994).

3.1.1.2 Wave climate

The dominant wave regime of the Portuguese western coast is characterized by waves coming from NW with average significant heights of 2 m and periods from 7 s to 15 s, according to hindcast wave time series obtained by Dodet et al. (2010) for the period 1953-2008.

Ribeiro (2017) used buoy data to characterize the seasonal wave climate for the period 2009-2015, establishing that the NW direction as dominant, with *Hs* of 2.5 m and 1.9 m during winter/autumn and spring/summer, respectively, and annual median peak period between 11 s and 12 s.

3.2 Praia Grande

Praia Grande (38°48'50.3" N, 9°28'40.9" W) is a headland-bay beach located on a rocky coastal stretch of the Portuguese west coast, in Sintra municipality. The beach extends for about 1 km with a NE-SW orientation, limited southwards by a 50 m high cliff above Mean Sea Level (MSL), in the north by a small headland, and landward by a seawall. It is mainly composed by coarse sands (Oliveira, 2009; Ribeiro, 2017).

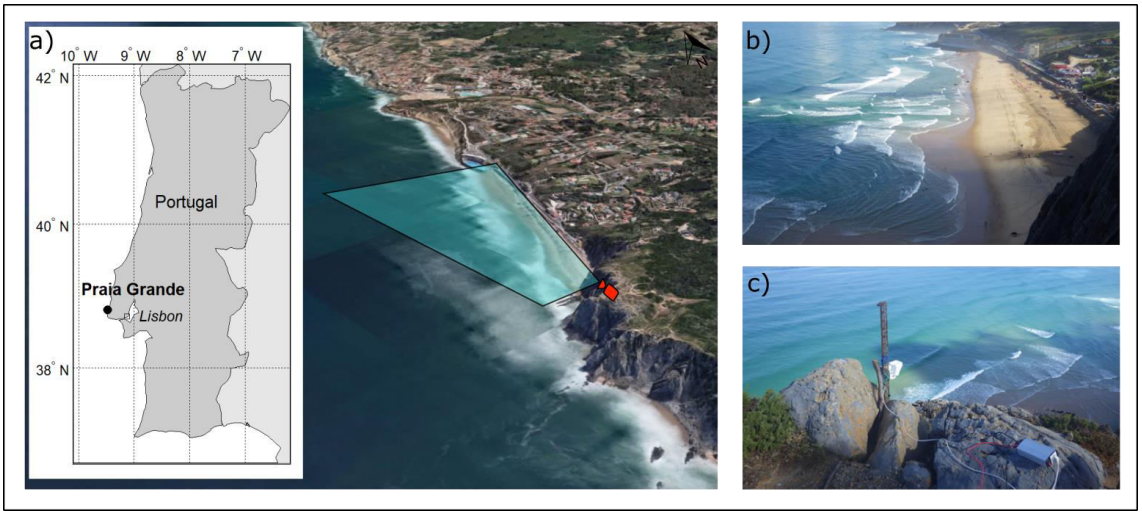

Figure 3.2. a) Praia Grande location, with monitored area and camera position (Google Earth image). b) picture taken at the start of the fieldwork; c) detail of temporary video system installation.

A field experiment was conducted at Praia Grande on 8th of September 2015. The main aim of the experience was to study the longshore drift using fluorescent sand tracers (Ribeiro, 2017).

3.2.1 Topographic data

Topographic data was acquired with RTK-GPS instrumentation. The measured beach profile (Figure 3.3) had a steep beach face ($tan\beta$=0.12) with a low-gradient tide terrace ($tan\beta$=0.09). No significant morphological changes were registered from the comparison between the surveys acquired at the start and at the end of the experience that corresponds to two consecutive low tides (Ribeiro, 2017).

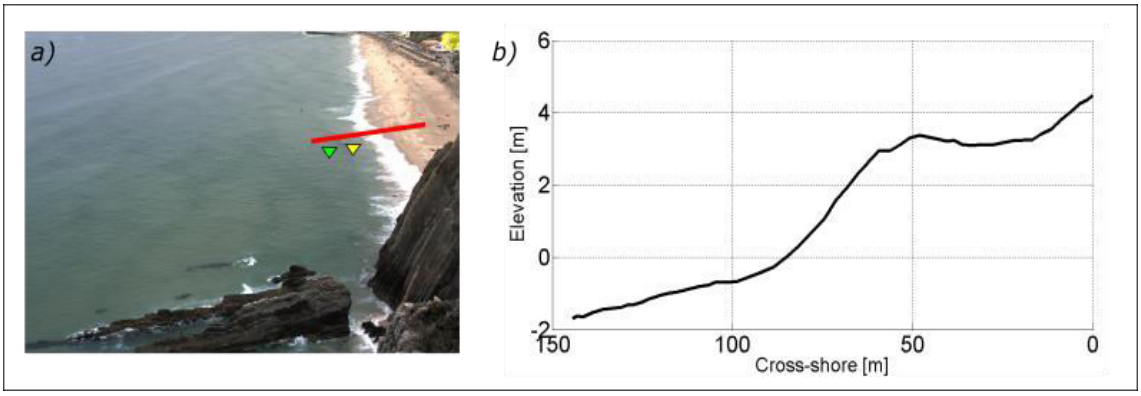

Figure 3.3. a) Praia Grande surveyed profile location (red line) and positions of pressure transducers PT 1 (green triangle) and PT 2 (yellow triangle). b) surveyed beach profile topography.

3.2.2 Tide and wave data

Hydrodynamic conditions in the shoaling and surf zone were obtained by two Pressure Transducers (PTs) deployed during low tide (Figure 3.3). According to both instruments, recorded tidal level ranged between -0.1 m and a maximum of 1.8 m (MSL). Significant wave height *Hs* and mean wave period *Tz* (mean zero crossing period) were almost constant, with average *Hs*=0.65 and average *Tz*=6.5 s (Figure 3.4).

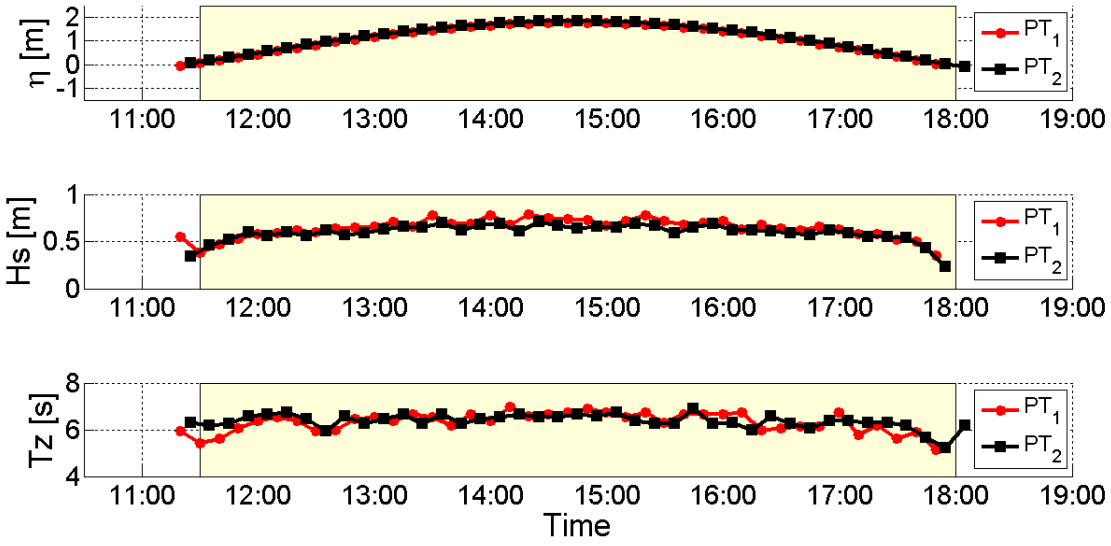

Figure 3.4. Wave data obtained by the two PTs. Water level in respect to MSL (top), significant wave height (middle), mean period (bottom). Yellow rectangle indicates the time window in which video data were available.

3.2.3 Video data

A video monitoring system was temporary installed on the top a cliff around 50 high (MSL), looking sideways at Praia Grande extent (Figure 3.2). The video camera was an IP Mobotix M12, which acquired during 7 hours 2018 x 1536 pixel resolution images, with a frequency of 1 image per second (1 Hz).

Timex and Variance images (Figure 3.5) were produced considering a 10-min acquisition time interval. Images were distortion-corrected using the results obtained by the camera calibration process performed in the laboratory.

Figure 3.5. Camera images at Praia Grande. a) undistorted snapshot; b) Timex; c) Variance.

GPS-RTK equipment was used to collect 12 GCPs on the subaerial beach during the image acquisitions. Automated version of COSMOS software (Taborda and Silva, 2012) was used to rectify 42 Timex and 42 Variance produced over the video sequence (Figure 3.6). Images were projected on the horizontal plane with an elevation equal to the mean water level measured by the PT at the corresponded time interval.

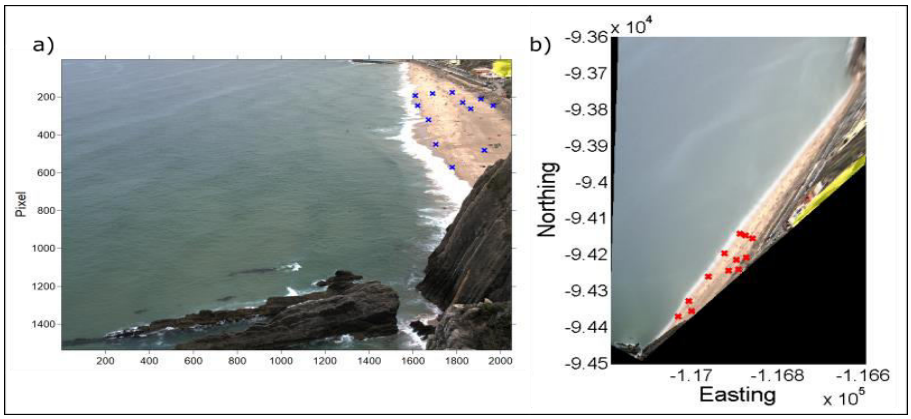

Figure 3.6. a) surveyed GCPs (blue crosses) superimposed to an undistorted frame acquired by the camera; b) example of rectified Timex, with GCPs in World coordinates (red crosses). Image is rectified using ETRS 1989 PTM 06 coordinate system.

Figure 3.7 shows the pixel footprint resolution (Eq. 2.4 and Eq. 2.5) of the rectified image of Praia Grande. The height of the camera installation (70 m) allowed to obtain good spatial resolution. In particular, the profile considered for this study was within a sector of the images in which pixel square footprint was less than 0.1 m^2. As can be noted, alongshore resolution decreased more rapidly than cross-shore resolution since pixel footprint increased.

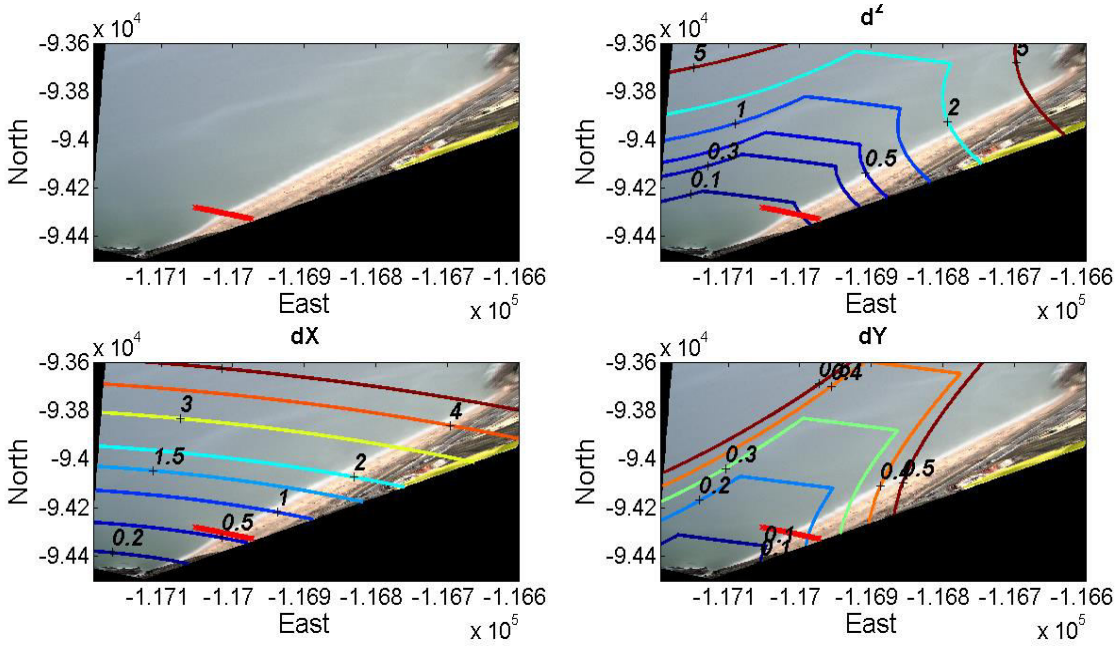

Figure 3.7. Upper row: rectified image and pixel square resolution (d^2). Below: alongshore (dX) and cross-shore (dY) pixel resolution maps. Red line represents the beach profile considered in this study.

3.3 Costa da Caparica

Costa da Caparica coast is a sandy stretch located on the southern margin of the Tagus river inlet. The area represents one of the main sites for coastal recreational activities of Lisbon and Setubal regions.

The study site is Praia do Tarquinio-Paraiso (38°38'30.3"N, 9°14'20.5"W), one of the urban beaches included in Costa da Caparica. It extends for about 400 m, limited sideways by groins and landward by a seawall (Figure 3.8).

Figure 3.8. a) Costa da Caparica location, camera position and monitored area of Tarquinio – Paraiso beach; b) front image of Tarquinio – Paraiso beach and detail of camera installation site; c) original frame extracted from online-streaming surfcam.

3.3.1 Video data

At the Costa da Caparica, video data was acquired by a Surfline (http://www.surfline.com) camera on the 8th floor of a hotel (Figure 3.8). Usually, the camera is set for mechanically rotating and zooming to show different areas of the beach and surf zone. However, the camera was set steady looking at the south part of Praia do Tarquinio – Paraiso beach for twelve days (between 30th of October 2015 and 12th of November 2015).

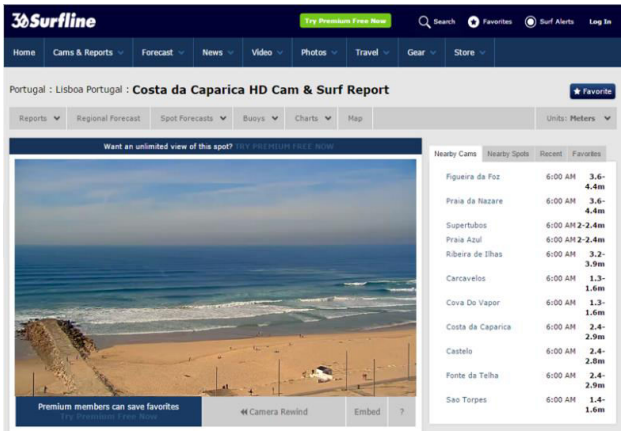

Figure 3.9. Screenshot of Surfline webpage streaming Costa da Caparica images (accessed December 2015).

Video was streamed online (Figure 3.9) at 25 frames per seconds (25 Hz). Video burst were automatically retrieved using a Matlab-based algorithm specifically developed for the aim. Daily dataset was composed by 66 videos, each one representing 10-minutes acquisition. Total dataset consisted in about 800 video bursts.

3.3.2 Topographic data

A field survey was conducted at Praia do Tarquinio-Paraiso on 11th of November 2015. The main aims of the field experience were the topographic characterization of the subaerial beach and the collection of GCPs for camera image rectification.

Beach topographic survey (Figure 3.10) showed that the beach had considerable longshore variability with a variable slope depending on the cross-shore transect considered.

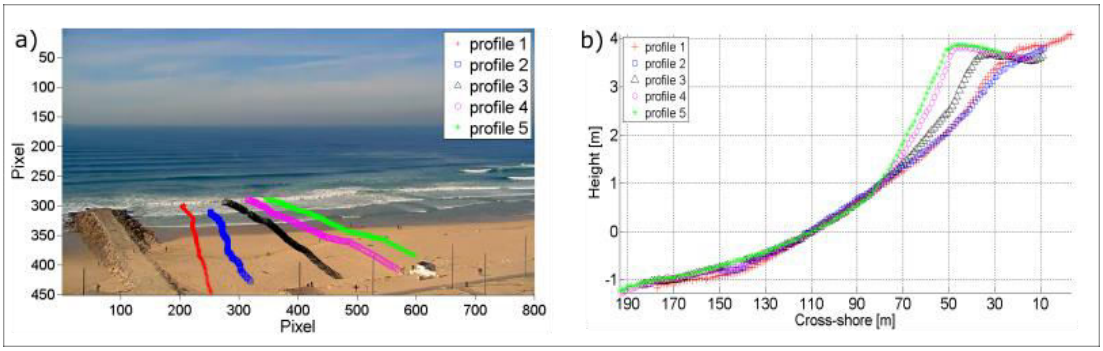

Figure 3.10. a) five surveyed profiles location on camera frame; b) topography of the beach cross-shore profiles.

Among five profiles, beach face slope above 1 m (MSL) varied between 0.05 and 0.1 from south (profile 1) to north (profile 5). The lower part of the beach face (comprised between -1 m and 1 m MSL) show a relatively uniform slope ($tan\beta = 0.05$).

GCPs were collected by RTK-GPS in the field of view of the video camera (Figure 3.101). In total, 38 GCPs were surveyed on the subaerial beach, on the groin and on the seawall, covering an elevation range of 1 to 8 m.

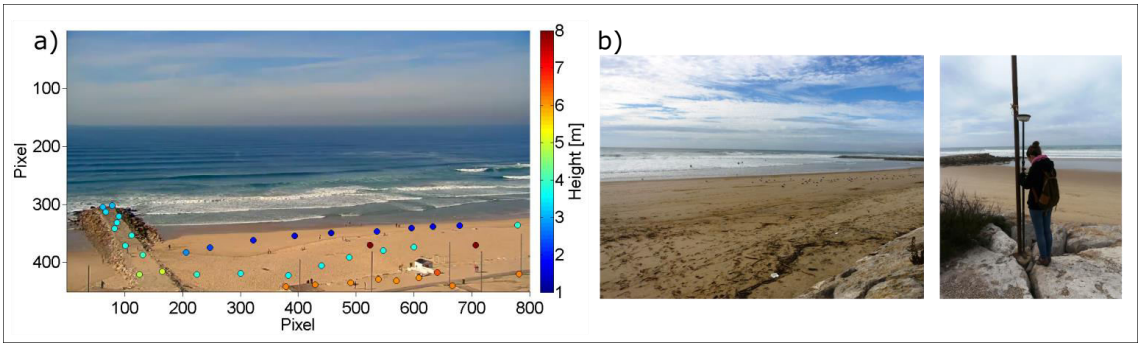

Figure 3.11. GCPs collection. a) GCPs superimposed to camera frame; b) pictures taken during in-situ survey.

3.3.3 Tide and wave data

Time series of water level was retrieved by the tide gauge of Cascais (38.70º N, 9.43ºW), available at the web site of the Portuguese General Direction of the Territory (DGT, ftp://ftp.dgterritorio.pt/Maregrafos/Cascais).

Three different wave data sources were chosen to represent the oceanographic forcing offshore the study site (Figure 3.12). 1) a buoy deployed by the Portuguese Hydrographic Institute offshore Sines at a depth of 95 m (37.92ºN, 8.93ºW); 2) the Water Information Forecast Framework (WIFF - ariel.lnec.pt/; Rogeiro et al., 2014) developed by the Portuguese National Laboratory of Engineering (LNEC), which incorporates a nested application of wave propagation in Portuguese shelf using a third-generation spectral wave model WAVEWATCH III (Tolman, 2009) forced with wind forecasts from the Global Forecast System (GFS) of NOAA; in this case wave data were extracted at a frequency of 3 hours at a point located in front of Costa da Caparica (38.62ºN, 9.39º W at 50 m depth); and 3) Puertos del Estado, which freely provides online hindcasts modeled data for the Iberian Peninsula (SIMAR - www.puertos.es), obtained by coupling WAM and WaveWatch models, forced with the wind data provided by HIRLAM model; in this

case wave data were extracted hourly considering the most representative point for Costa da Caparica over the available grid (38.50º N - 9.50º W).

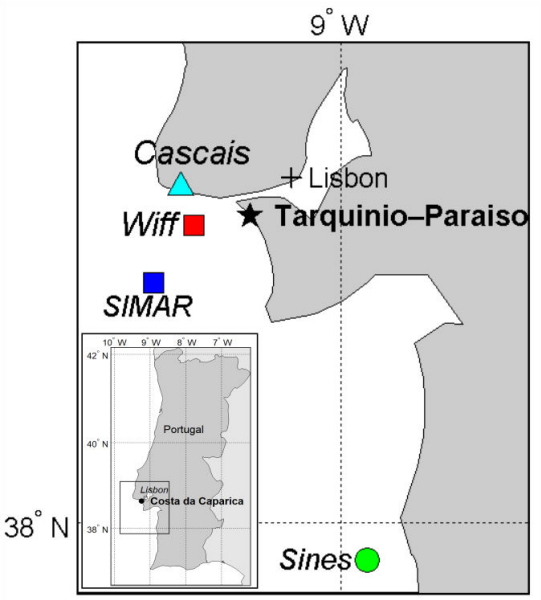

Figure 3.12. Map of wave data sources. Tide gauge of Cascais (cyan triangle), SIMAR and Wiff models grid points (red and blue squares), Sines buoy (green circle).

As expected, significant wave height data varied between the three sources. SIMAR model presented highest wave height and longest wave period. The WIFF model and buoy measurements were in good agreement when wave height was lower than 2 m, however WIFF results were about 20% lower when wave height was higher. Overall, the analysis took in consideration the three sources because of the differences in measures and in spatial position. In fact, while WIFF and SIMAR model grid points are closer from Costa da Caparica, Sines buoy represents direct measurements.

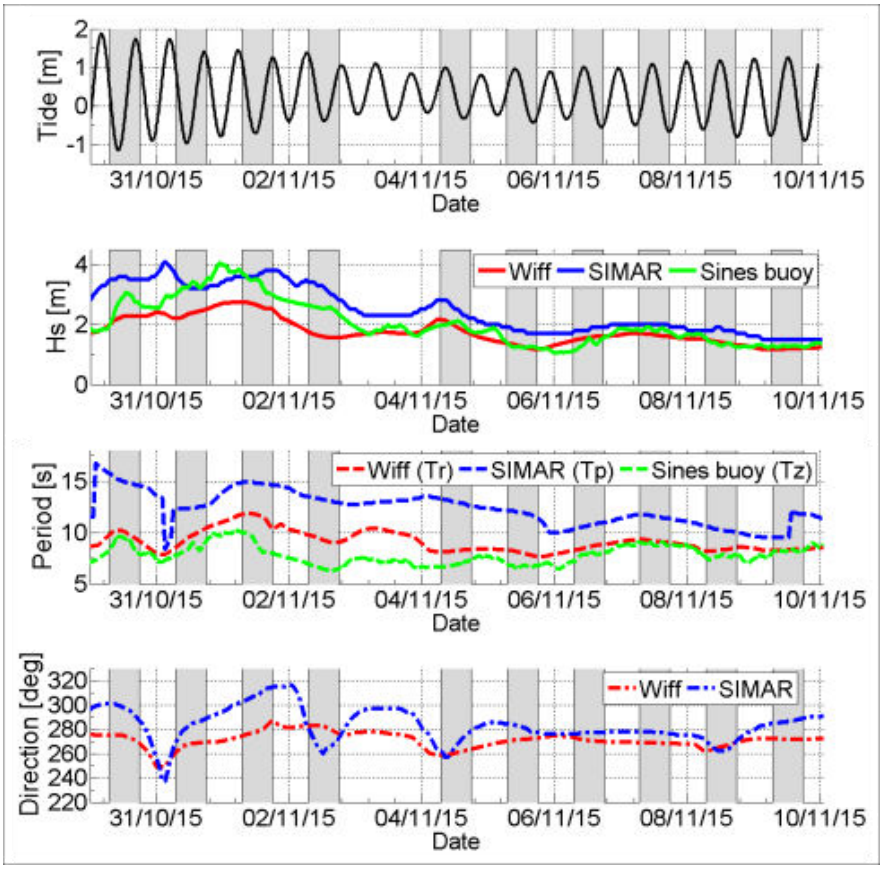

Figure 3.13. Tidal elevation and offshore wave forcing conditions during 10 days at Costa da Caparica. Tide level (MSL) from Cascais gauge, significant wave height (middle top), period (middle bottom) and wave direction from buoy measurements (bottom). Gray rectangles indicate the time windows in which video data were available.

3.3.4 Image post-processing

Over the whole dataset, image frames (Figure 3.14) were extracted at 1 Hz and successively converted in a sequence of 800 Timex and Variance (800 x 450 pixels resolution), 66 Timex and 66 Variance for each day (Figure 3.14).

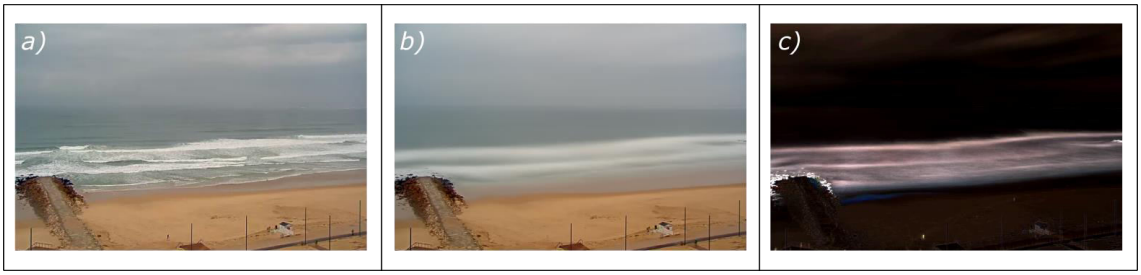

Figure 3.14. Camera images a Costa da Caparica. a) original frame; b) Timex; c) Variance.

The access to the installation site and the technical properties of the camera were denied by the surfcam network company. Thus, camera position in Real-World coordinates, camera internal and external parameters were derived applying *C-Pro* (Sánchez-García et al., 2017) and using surveyed GCPs. Images were considered already undistorted. Data obtained by C-Pro software were used to rectify the image with COSMOS (Figure 3.15). Timex and Variance were rectified projecting the images on the referenced plane identified by the 10-minutes-averaged sea level extracted from Cascais tide gauge (Figure 3.13).

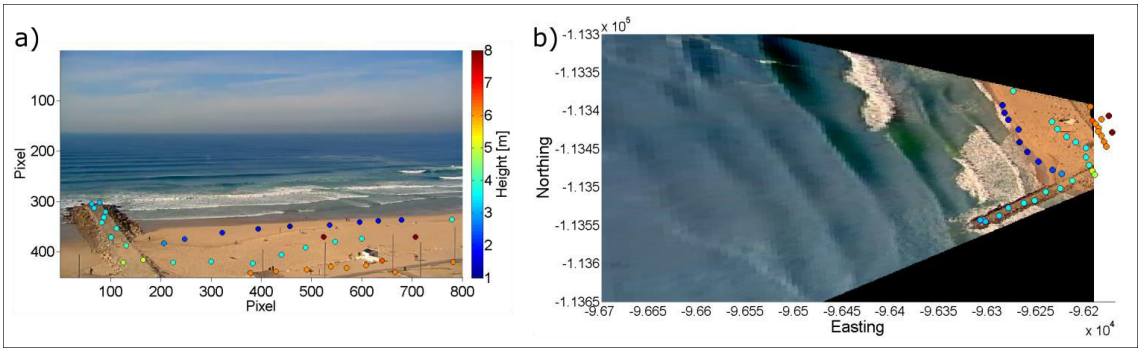

Figure 3.15. a) oblique image and GCPs (circles) in image coordinates. b) rectified image with GCPs in World coordinate (circles). Colorbar indicates GCPs elevation, common to both figures.

The accuracy achieved by *C-Pro* rectification process was checked comparing the positions of the 38 GCPs computed by the software against their surveyed coordinates.

Table 3.1. The reprojection results for the surfcam image rectification and the corresponding mean error, median error, mean absolute error (MAE), mean square error (MSE), root mean square error (RMSE), maximum error (in m).

	mean	***median***	***MAE***	***MSE***	***RMSE***	***max***
(x)	*-0.07*	*-0.10*	*0.65*	*0.68*	*0.82*	*1.74*
(y)	*-0.02*	*0.01*	*0.18*	*0.05*	*0.23*	*0.54*
total	*0.70*	*0.56*	*0.70*	*0.73*	*0.86*	*1.76*

Most projected points errors were within 1 m, with the higher errors found to coincide with the most distant points from the camera. Table 3.1 reports the statistical error analysis of re-projection. The errors over the cross-shore were much larger than longshore

errors. Hence, cross-shore errors weighted more in the computation of the total error, which is expressed as Euclidean distance between the surveyed and re-projected GCP at its corresponding height.

Figure 3.16 shows an example of rectified image Tarquinio-Paraiso and the pixel footprint resolution.

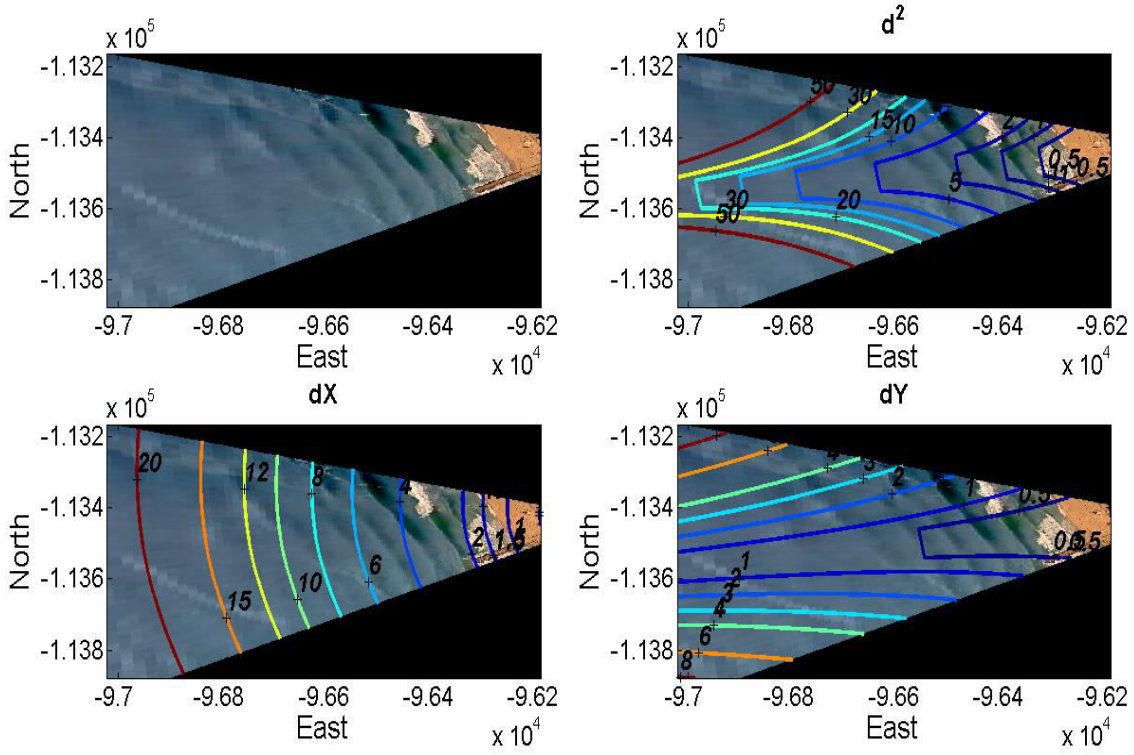

Figure 3.16. Upper row: rectified image and pixel square resolution (d^2). Below: crossshore (dX) and alongshore (dY) pixel resolution maps.

The subaerial beach was within an area where pixel square resolution was lower than 0.5 m^2. The cross-shore resolution rapidly decreased seaward, since the pixel footprint increased.

3.4 Ribeira d'Ilhas

The beach of Ribeira d'Ilhas (38° 59'17.0"N, 9°25'10.4"W) develops on top of a rocky-shore planform located around 50 km north-west to Lisbon (Figure 3.17). The beach extends for about 300 m cross-shore, with a NO-SE orientation, and is limited southwards by 55 m high cliff and in the north by a small headland. This beach is a famous stage for many national and international surfing events.

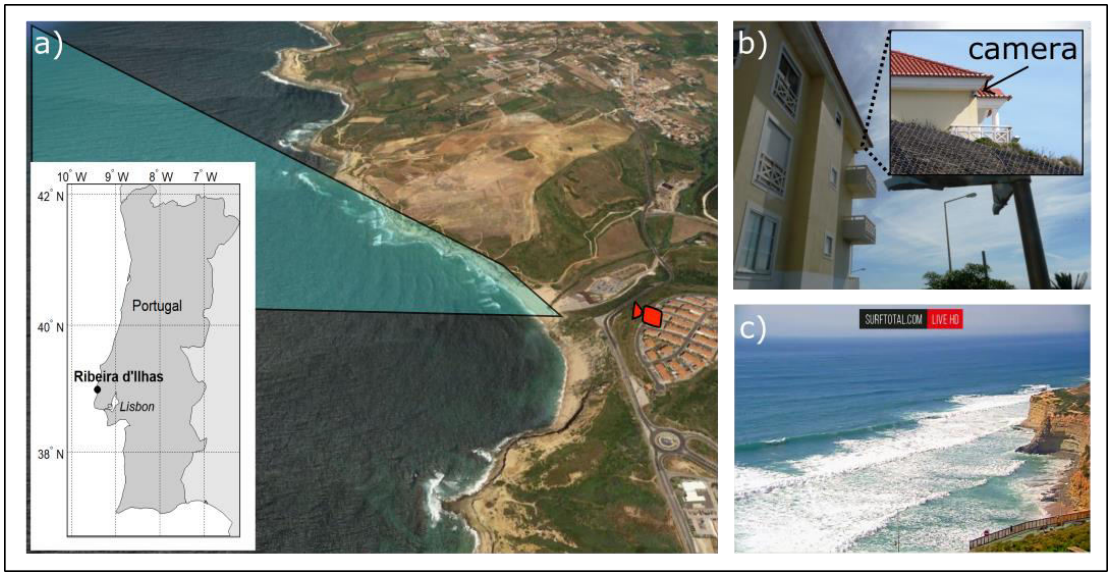

Figure 3.17. a) Ribeira d'Ilhas beach location, camera position and monitored area; b) detail of surfcam installation site; c) original frame extracted from online-streaming video.

3.4.1 Video data

The collaboration with the company Surftotal (www.surftotal.com) allowed the use of the surfcam installed at Ribeira d'Ilhas (Figure 3.17-b).

The video station consisted in a Sony video camera mounted on a house roof at an elevation of about 80 m (MSL) and about 400 m from the Ribeira d'Ilhas beach. The camera was fixed and looking at the shore and nearshore of Ribeira d'Ilhas (Figure 3.17-c) for two days (28th and 29th of March 2017). Images were streamed online at a frequency of 15 frames per second. About 18 hours video bursts were retrieved using a password-protected Uniform Resource Locator (URL) web address supplied by Surftotal company.

Image frames were extracted at a frequency of 5 Hz to limit data storage space and processing time. Such rate sample was considered appropriate to overcome the low frame resolution (800 x 450). The entire dataset consisted of about 380000 frames.

3.4.2 Topographic data

A field experiment was conducted at Ribeira d'Ilhas on 28th and 29th of March 2017. The main aims of fieldwork were the deployment of oceanographic instrumentation, the topographic characterization of the subaerial beach and the acquisition of GCPs for image rectification.

Beach topographic survey was performed using RTK-GPS technology. RTK-GPS mapping covered an area covering 200 m cross-shore and 400 m long-shore, with ground elevation ranging between -1.5 m and 3 m (MSL). Considering a cross-shore distance of 150 m, the rocky-shore platform had a low gradient slope ($tan\beta = 0.01$) in the range of 0÷1.5 m depth. LIDAR survey data (Silva et al., 2012) were coupled with RTK-GPS measurements to characterize the nearshore bathymetry up to a depth of about 10 m (Figure 3.18).

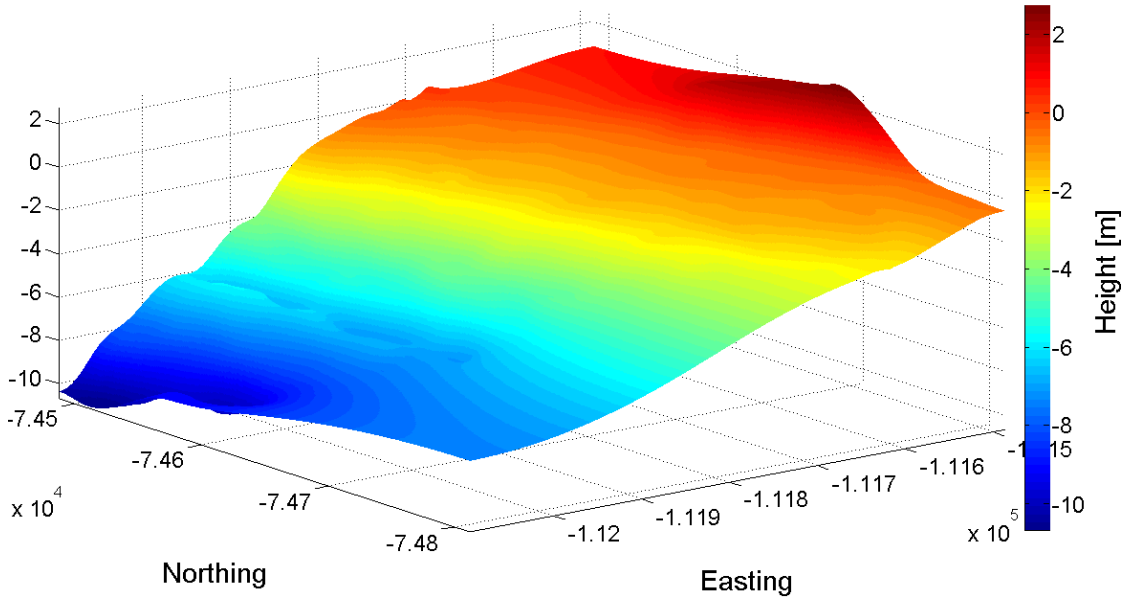

Figure 3.18. Topo-bathymetry at Ribeira d'Ilhas.

A large number of GCPs (about 200) were surveyed with RTK-GPS instrumentation both on the rocky-shore platform, during low tide, and on the top of the cliff.

3.4.3 Tide and wave data

Four Leveltroll pressure transducers (PTs) were placed along a cross-shore transect (Figure 3.19) to measure water level and wave properties during the experience. to measure water level and wave properties during the experience. Sensors covered a cross-shore length of about 35 m with an offset of around 18 m. Data were acquired at 2 Hz.

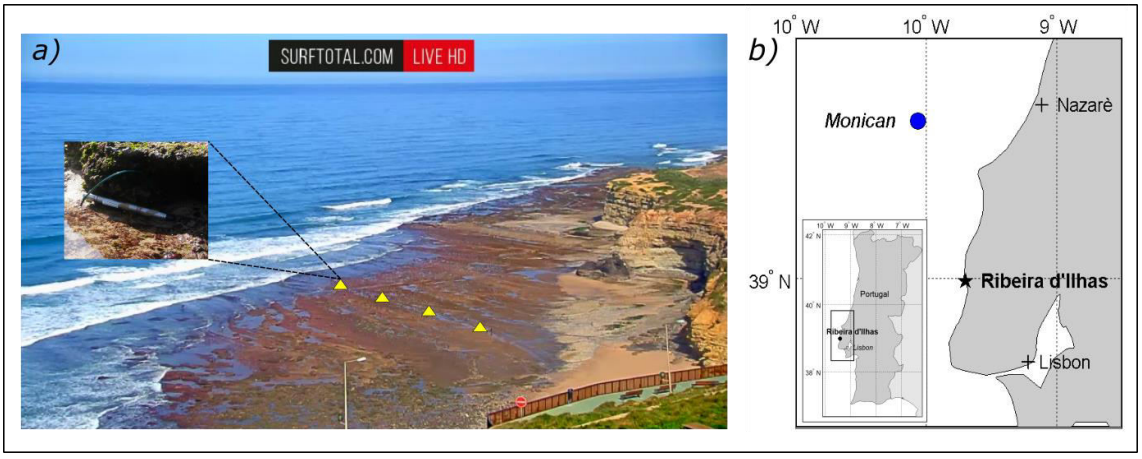

Figure 3.19. a) original frame with detail of PTs installation points (yellow triangles); b) Monican wave buoy location (blue circle).

Pressure data of the most seaward PT were used to measure water level η. Offshore wave data were provided by the WaveScan buoy Monican (Figure 3.19-b) deployed at 80 m depth (39.56ºN, 9.21ºW) by the Portuguese Hydrographic Institute (www.hidrografico.pt).

Figure 3.20 summarizes the hydrodynamics at Ribeira d'Ilhas and Monican buoy. Water level varied between a minimum of -0.94 m and a maximum of 1.8 m for both the two days, when the two flood tide phases were monitored. Significant wave height and peak period were approximately constant on day 28th (1.7 m and around 11.5 s respectively) while on the 29th Hs increased from about 2 m to 3.5 m, whereas peak period decreased from 18 s to 16.5 s.

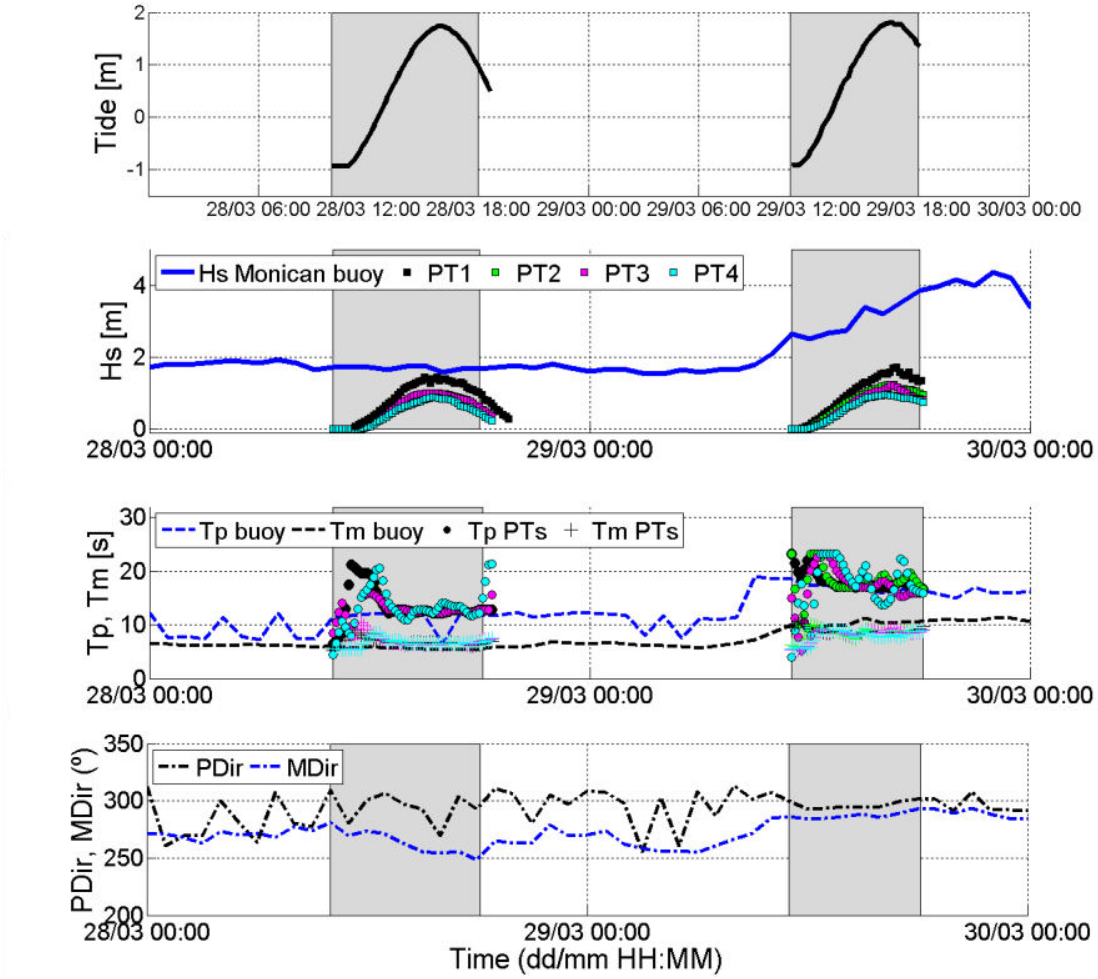

Figure 3.20. Wave and tide time series obtained from Monican buoy and in situ PTs. Tide level (MSL) from PT 1(top), significant wave height. (middle top), peak (Tp) and average (Tm) wave period (middle bottom). Mean (MDir) and power (PDir) wave direction from buoy measurements (bottom). Gray rectangles indicate the time windows in which video data were available.

3.4.4 Image post-processing

The whole dataset of 380000 frames was converted in a sequence of 94 Timex and 94 Variance (800 x 450 pixels resolution, Figure 3.21), 52 Timex-Variance for the first day, 42 for the second day.

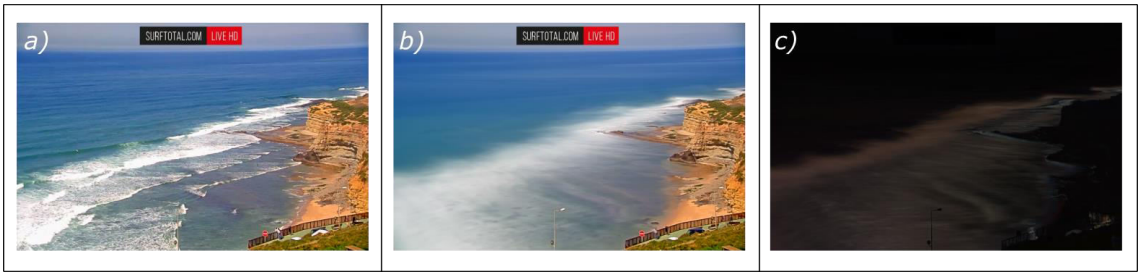

Figure 3.21. Camera images at Ribeira d'Ilhas. a) original frame; b) Timex; c) Variance.

The difficult access to the video camera installation site did not allow to perform the typical camera calibration procedure. Therefore, camera position in Real-World coordinates, camera internal and external parameters were derived using GCPs dataset as input in *C-Pro* software (Sánchez-García et al., 2017). 90 GCPs visible within the image were chosen among the 200 surveyed points, obtaining a GCPs repositioning RMSE of 0.5 m. Camera data obtained by C-Pro software were used to rectify the images (Figure 3.22) using COSMOS tool (Taborda and Silva, 2012).

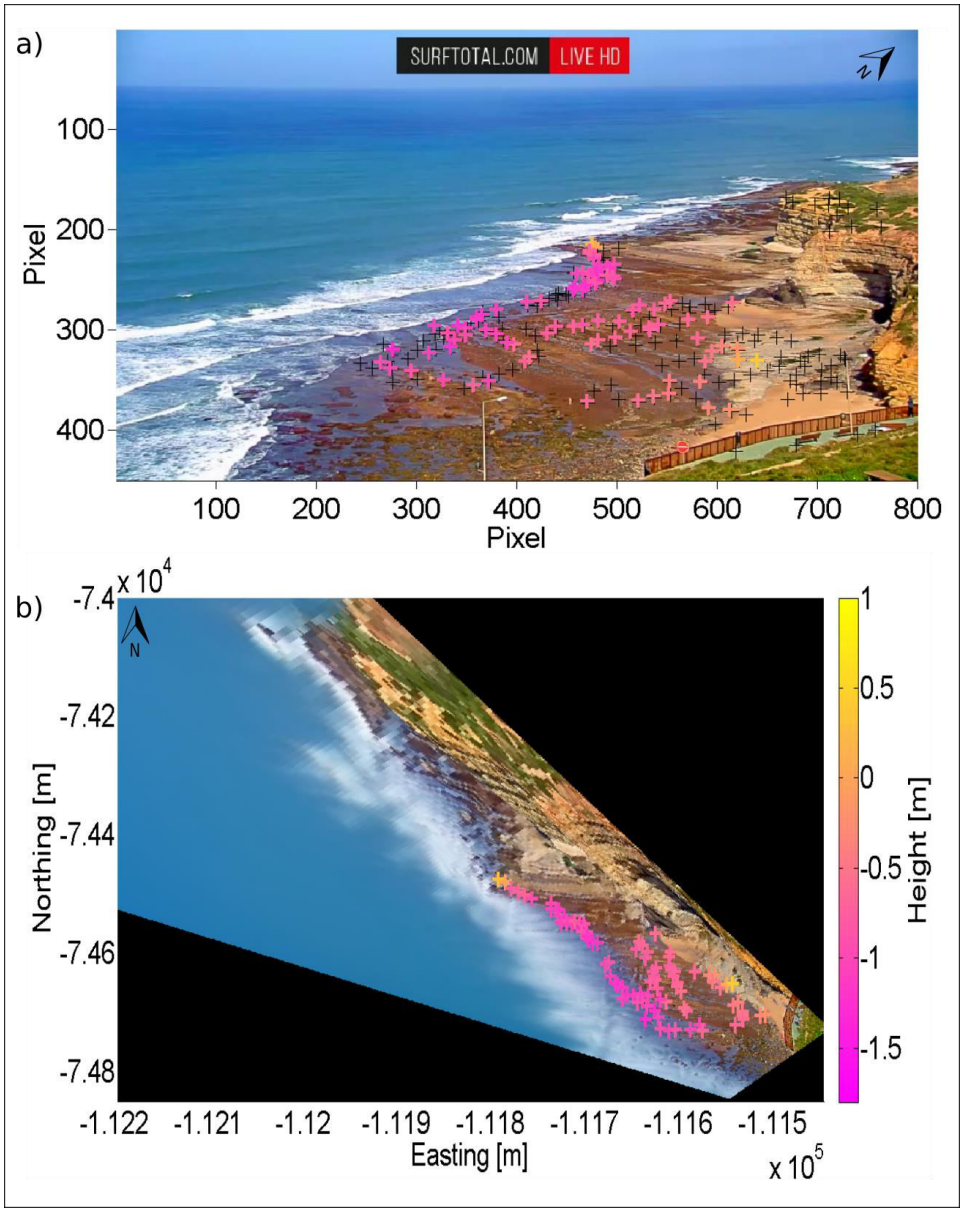

Figure 3.22. a) raw oblique frame with GCPs selected for image rectification; b) rectified image and GCPs used as reference. Black crosses show GCPs surveyed but not used for rectification. Colorbar shows GCPs elevation, common to both images.

3.4.5 Timestack production

10-min Timestacks were generated over the sequence of images acquired during both monitored days. The time series of pixel intensity were sampled along 14 different cross-shore transects (Figure 3.23-a) over the image rectified sequence. Transect orientation was chosen to be perpendicular to wave propagation direction. For selecting the direction, a visual inspection of wave angle was previously made on images.

Timestacks with x-axes and y-axes representing cross-shore distance in meters and time in seconds, respectively, were produced (Figure 3.23-b). Timestacks for a single transect were 52 for the first days and 42 for the second day. Considering the 14 transects, whole dataset comprised 1316 Timestacks.

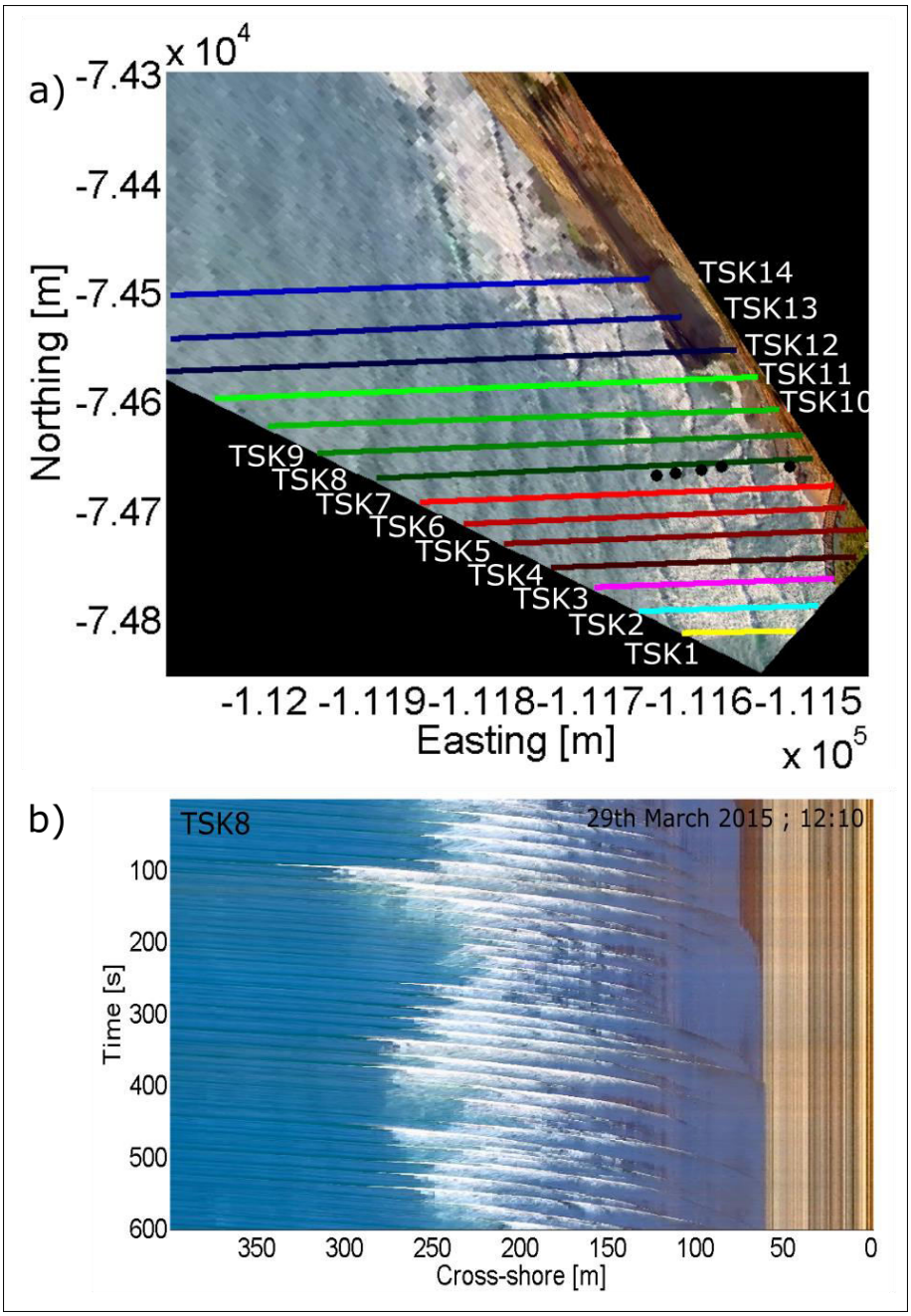

Figure 3.23. a) Transects to produce Timestacks and relative acronym (whyte text); b) example of Timestack produce over transect 8 (TSK8).

Timestacks were numbered from 1 to 14, starting from the most southward transect, and identified with the TSK prefix (Figure 3.23). Altogether, Timestack arrays covered an area of 350 m longshore and 500 m cross-shore. Transect lengths depended on the position and on the rectified image dimension, varying between the minimum of 100 m for TSK 1 and the maximum of 525 m for TSK 12.

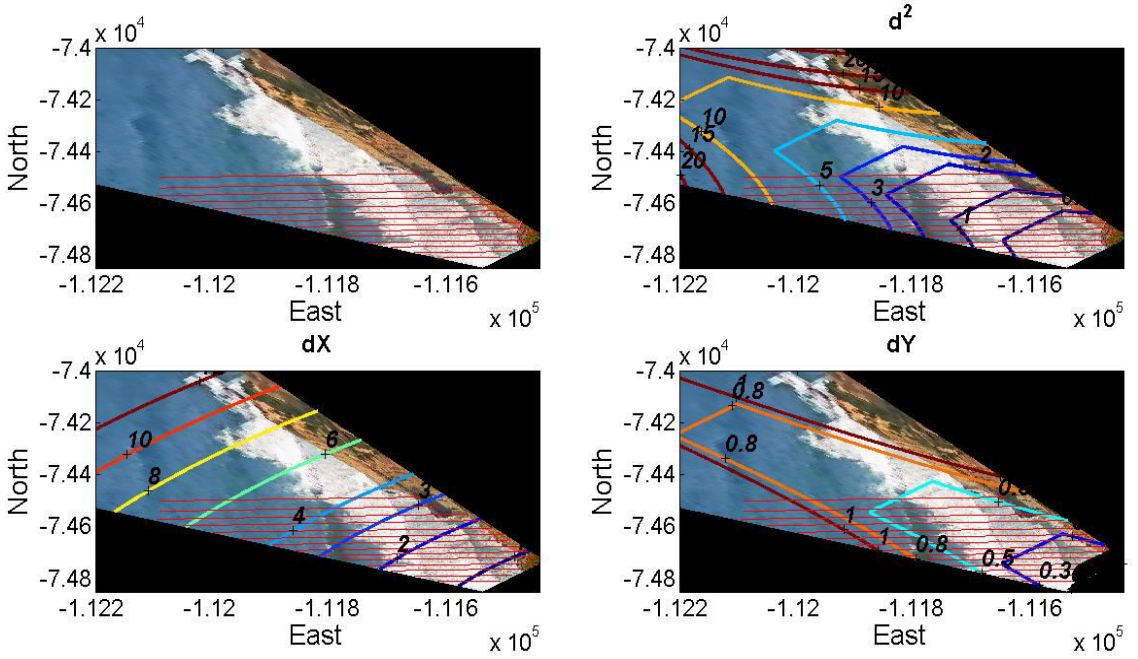

Figure 3.24. Upper row: rectified image and pixel square resolution (d^2). Below: crossshore (dX) and alongshore (dY) pixel resolution maps. Straight red lines represent Timestack transects.

Figure 3.24 shows the pixel footprint resolution of the rectified image of Ribeira d'Ilhas. Despite the low camera image resolution (800 x 450 pixels) and the distance of the camera from the shore (≈ 400 m), all pixel transects that were used to produce Timestacks were within a pixel square resolution of 5 m^2, with minimum cross-shore resolution dX= 7 m and minimum alongshore resolution around dY=1 m.

3.5 Kourou

3.5.1 French Guiana coast

French Guiana is located in northern South America, about 500 km north of the Amazon River mouth, facing the Atlantic Ocean between Suriname and Brazil. This region has a coastline of about 380 km, which is made up of a succession of low sandy stretches, rocky cliffs and estuaries edged by mangroves (Frouin et al., 1997).

The coastline is affected by exceptional regional processes occurring offshore, where alongshore migration of Amazonian mud banks influence wave action and sediment transport towards the coast (Anthony et al., 2015). Tidal range indicates upper mesotidal conditions, with spring tide low- and high-water levels being 1 m and 3.1 m, respectively (Baghdadi et al., 2004). Average significant wave height ranges from 0.75 m in September to 1.6 m during the period of high winds (February to May). Wave height nevertheless varies locally towards the coastline depending on the nature of the seabed and progressively decreases with the interaction of water laden heavily with mud (Baghdadi et al., 2004).

3.5.2 Kourou beach

The study site is one of the most vulnerable site of Kourou beach (5°10'38.4"N, 52°38'49.6"W), a sandy open beach located about 60 km northwest of the French Guyanese capital Cayenne. Here, the morphodynamic influences of mud banks drift to the intertidal beach area are still incompletely understood, as continuous series of field measurements on the shore are missing.

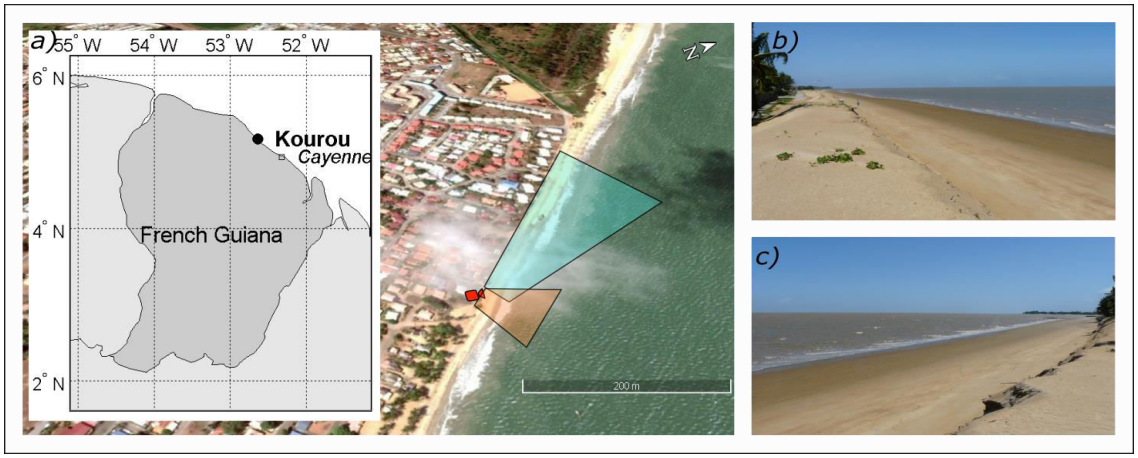

Figure 3.25. a) Kourou beach location, camera position and monitored area.; b) and c) show the views of the study site northward and eastward, respectively.

3.5.3 Video station

A shore-based video monitoring station was implemented for the first time in French Guyana in late November 2017 (Figure 3.26). The optical system was composed by two Axis IP cameras installed on an aluminium tower that was deployed within a private house garden in proximity of the beach. The 10-m high aluminium tower was based on a cement plinth (Figure 3.26-b) that was built for the purpose.

The IP cameras were connected to a Network Attached Storage (NAS) into which acquisition data were stored. To avoid loss of data, the station also included a Power Supply Unity (PSU). The hardware components were hosted inside a weatherproof box (Figure 3.26-c) located under the roof of the private building.

Figure 3.26. Installation of the video monitoring system. a) camera fixing on tower; b) detail of tower base with cement plinth; c) weatherproof box hosting NAS and PSU.

The ongoing monitoring project is expected to deepen the understanding of the correlation between offshore mud banks dynamics and beach behaviour. The video dataset will allow the possibility to evaluate the efficiency of the artificial dune "sand bags" protection system recently built by local authorities (Figure 3.27).

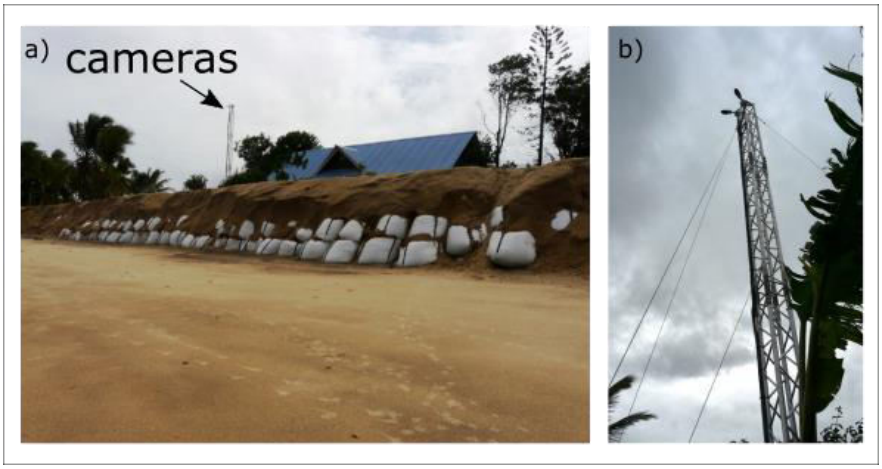

Figure 3.27. Overview of camera installation site. a) camera positions and artificial "sand bags" dune built by local authorities; b) detail of camera tower.

Korou video station is the first system of a shore-based monitoring network that is implemented in French Guyana as a result from the cooperation between coastal scientists and decision makers (French Guyana Coastal Observatory).

3.5.4 Topographic data

A field experiment was conducted at Kourou on 1th of December 2017. Topographic profiles were surveyed with GPS instrumentation. The beach profile (Figure 3.28) had a low gradient beach face ($tan\beta = 0.08$) and did not show significant alongshore variation.

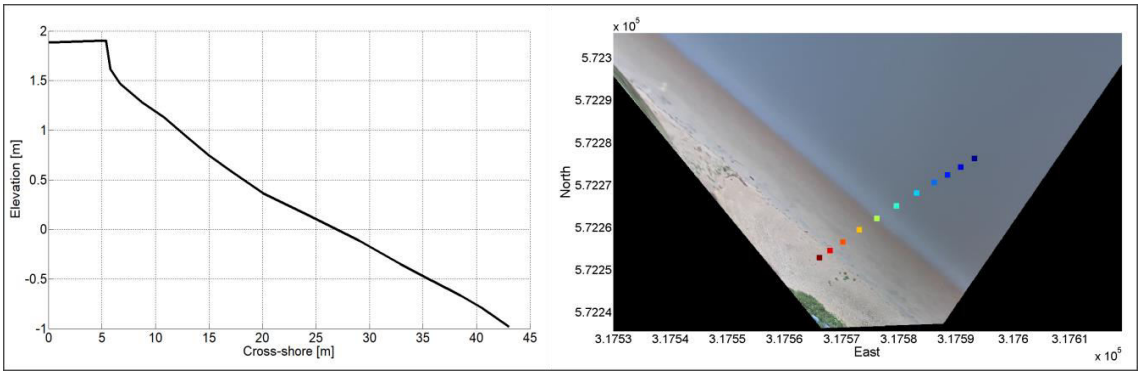

Figure 3.28. Beach profile (left) and relative position on rectified image (circles represents surveyed points).

3.5.5 Tide and wave data

Two PTs were deployed at a depth of 1 m on MSL for measuring water level and wave height during two hours. Besides, daily tidal elevation was retrieved from the tide gauge installed by the "Service hydrographique et océanographique de la marine" at Ile Royal, 15 km NE offshore Kourou. (Figure 3.29).

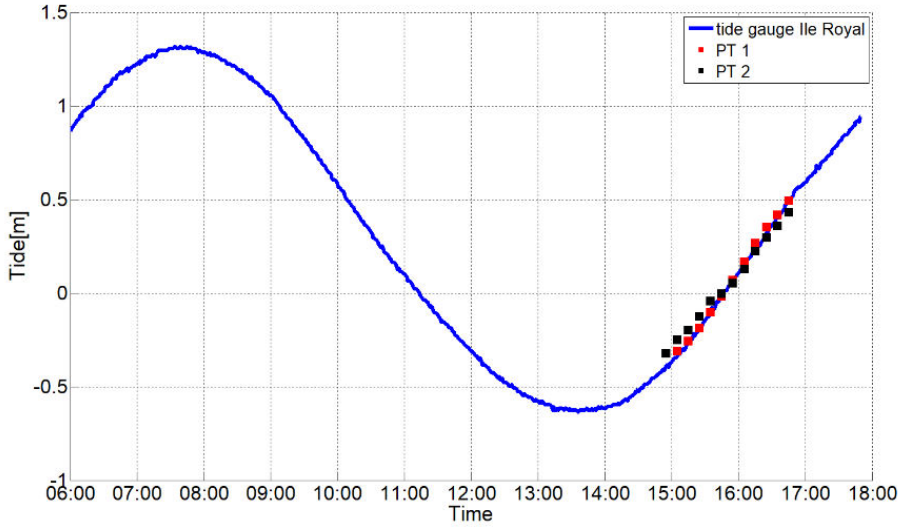

Figure 3.29. Tidal data (blue line) from tide gauge for day 7th of December 2018.Black and red squares shows water elevation measured by the PTs.

3.5.6 Video data

The cameras acquired images continuously during daylight, at 1 Hz. A fully automated set of Matlab algorithms were used for image processing including frame extraction, 10-min Timex and Variance generation (Figure 3.30), image undistortion and image rectification.

Figure 3.30. Camera images at Kourou. a) original snapshot; b) Timex; c) Variance.

Images were distortion-corrected using the results obtained by the camera calibration performed in laboratory before the installation of the video system. GPS-RTK method was used to collect 33 GCPs on the subaerial beach during the image acquisition (Figure 3.31). Images were projected on the horizontal plane with an elevation equal to water level measured by the PT at the corresponded time interval.

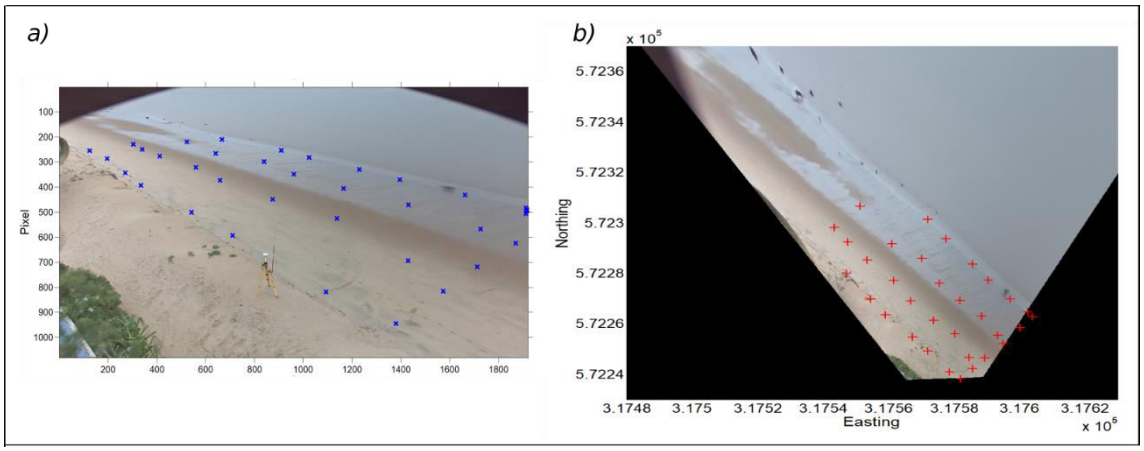

Figure 3.31. a) example of undistorted frame acquired by the camera with surveyed GCPs (blue crosses); b) example of rectified Timex, with GCPs in World coordinates (red crosses).

Figure 3.32 shows the pixel footprint resolution of the rectified image of Kourou. The proximity of the camera allowed to obtain good spatial resolution for the longshore extent of about 150 m covered by the camera. Maximum value of pixel square footprint was less than 0.5 m^2. As expected, alongshore resolution decreased more rapidly than cross-shore resolution.

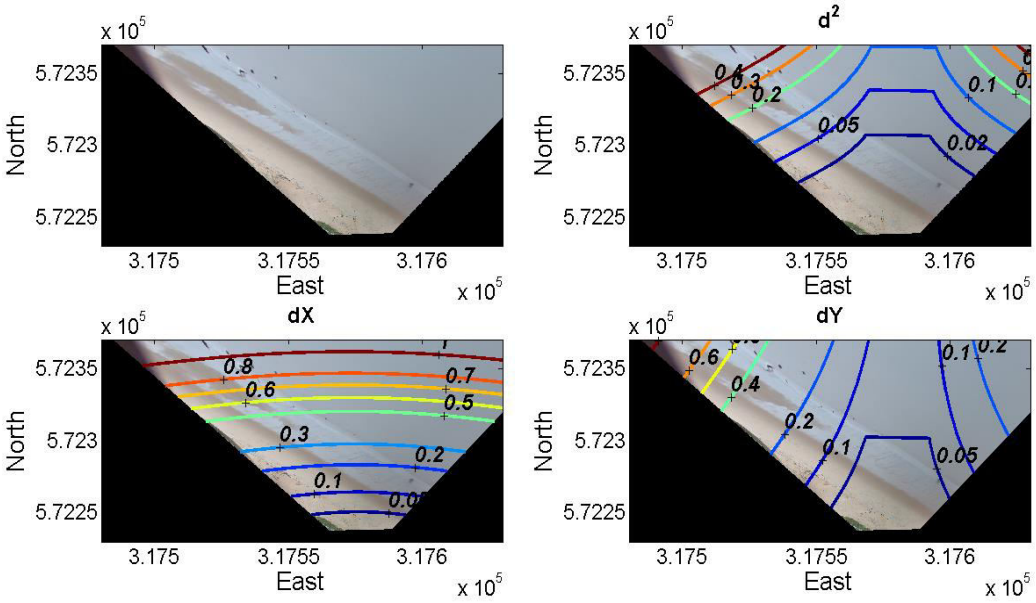

Figure 3.32. Upper row: rectified image and pixel square resolution (d^2). Below: alongshore (dX) and cross-shore (dY) pixel resolution maps.

3.6 Nha Trang

Nha Trang (12°14'38.8"N, 109°11'49.5"W) is a sandy beach located on the South East of Vietnam (Figure 3.33) with a fairly steep beach face slope ($tan\beta = 0.1$) and a narrow (~ 40 m) alongshore uniform and flat ($tan\beta = 0.01$) low tide terrace (Lefebvre et al., 2014). The beach is a mixed wave-dominated micro-tidal environment (max tide range of 1.5 m), with a mix of diurnal and semi-diurnal tide. Apart from extreme events such as Typhoons (Thuan et al., 2016), wave forcing on the beach is mostly generated by SE wind-waves with moderate energy, and Monsoon swells from NE direction (Almar et al., 2017b).

A field experiment was conducted during the end of November and the start of December 2015 at Nha Trang beach (Almeida et al., 2017). For the present work, two days of data were selected for this work, 28th and 29th of November 2015.

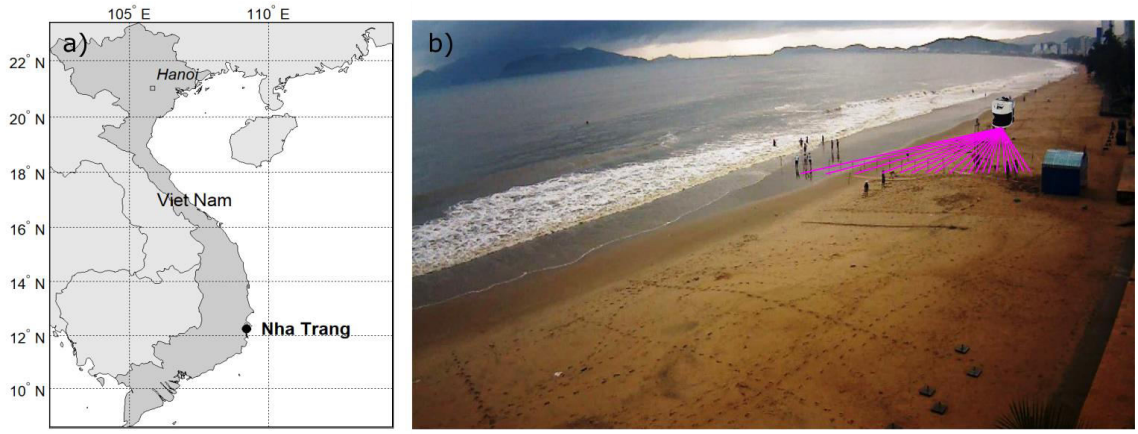

Figure 3.33. a) location of Nha Trang beach. b): installation site of the 2D LiDAR and monitored profile (magenta lines) superimposed to frame acquired by the video system.

3.6.1 Tide and wave data

Wave offshore properties, namely significant wave height (Hs) and peak period (Tp), and water level (η) were obtained by an Acoustic Doppler Current Profiler (ADCP) moored offshore at 15 m depth. The selected 48 hours covered two tidal cycles ranging between – 0.7 and 0.7 m, with tidal amplitude of about 1.4 m. (Figure 3.34). The tide had a mixed character and asymmetrical phases, with rising tidal phases characterized by double high-tide peaks, and ebb phases by a single descending curve. Over the two days, offshore

significant wave height decreased from 1.1 m to 0.8 m, likewise wave peak period dropped from 11 s to 8 s.

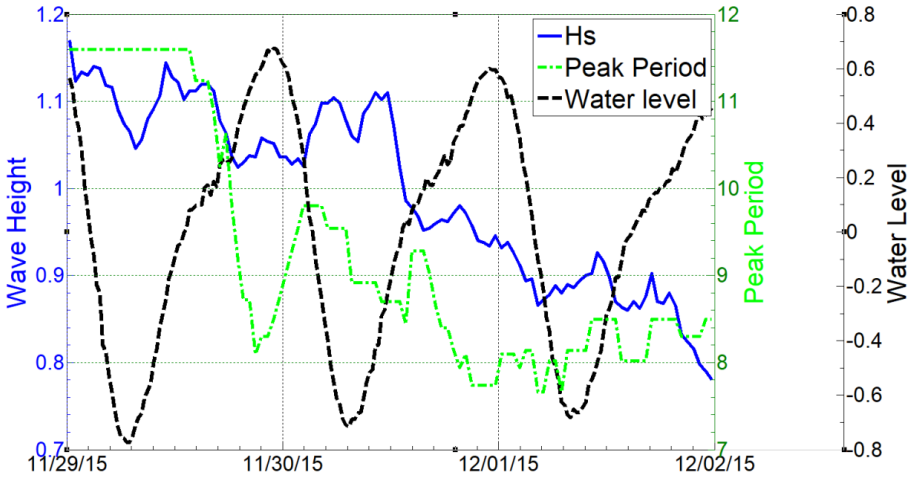

Figure 3.34. Wave significant height (blue line), wave peak period (green line) and water level (black dashed line) measured by ADCP during the experience.

Beach topography was surveyed daily by DGPS to characterize beach intertidal morphodynamics. Surveys were performed in a continuous mode (recording every 0.5 m) along cross-shore transects spaced by 10 m at every low tide.

3.6.2 Remote sensing data

The data collected at Nha Trang were used to investigate the possibility of combining two shore-based remote sensing techniques, namely 2D LiDAR and video imagery, to measure intertidal beach topography.

3.7 Overview

The study sites used in this thesis included sandy and rocky shores, urban and natural environments, dissipative to reflective morphological behaviour beaches. Tidal regimes and wave characteristics are also highly variable depending on the location and on the periods in which the studies were conducted.

Sources of video imagery data were also heterogeneous, comprising temporary deployment of IP cameras, fixed video monitoring station installations and online-streaming surfcams (Table 3.2).

Table 3.2. Video system, beach characteristics and wave conditions observed during the experiments for each study site.

site	Video source	Shore	Intertidal slope (tanβ)	Beach type	Wave height range [m]	Country	sea
Praia Grande	video station	sandy	0.09÷0.12	intermediate	1 ÷ 3.5	PT	NE-Atlantic
Costa da Caparica	surfcam	sandy	0.05 ÷ 0.1	intermediate	0.45 ÷ 0.85	PT	NE-Atlantic
Ribeira d'Ilhas	surfcam	rocky	0.01	dissipative	1.2 ÷ 2.8	PT	NE-Atlantic
Kourou	video station	sandy	0.07 ÷ 0.09	dissipative + tidal mud flat	0.08 ÷ 0.13	GF	NSW-Atlantic
Nha Trang	video station	sandy	0.01÷0.1	Intermediate + low tide terrace	0.8÷1.2	VN	South China Sea

Table 3.3 resumes the type of images used for the application and validation of the techniques developed in this thesis.

At Ribeira d'Ilhas, Timex, Variance and Timestacks dataset produced from surfcam were used to develop new approaches to identify wave transformation domains in the nearshore (Chapter 4), to measure wave breaking height (Chapter 5) and to retrieve nearshore bathymetry (Chapter 7). The considerable developments on the image analysis procedures made with data acquired at this site benefited from the rocky nature of the shore that assured a constant bottom configuration.

The method for measuring wave breaking height (Chapter 5) was also applied to Timex dataset obtained by the temporary video station at Praia Grande, by the Costa da Caparica surfcam and by the video station installed at Kourou.

Video data collected at Nha Trang were coupled with terrestrial LiDAR data to propose a new remote sensing method to measure intertidal beach topography (Chapter 6).

Table 3.3. Type of images used to develop and validate the techniques presented in this thesis.

	Image type			***Techniques***			
Study site	***Timex***	***Variance***	***Timestack***	***Wave Domains***	***Wave Breaking Height***	***Intertidal Topography***	***Subtidal Bathymetry***
Praia Grande	*x*				*x*		
Costa da Caparica	*x*				*x*		
Ribeira d'Ilhas	*x*	*x*	*x*	*x*	*x*		*x*
Kourou	*x*				*x*		
Nha Trang	*x*					*x*	

4. IDENTIFICATION OF WAVE TRANSFORMATION DOMAINS

The present chapter is partially based on the work:

Andriolo, U., Taborda, R., Sanchez-Garcia, E. (2016). Measuring wave runup and intertidal beach topography from online streaming surfcam. X Jornadas do Mar, Naval School of Lisbon, Lisbon, Portugal

4.1 Introduction

The nearshore zone extends between the low tide line and the offshore limit of wave action on the bed (see also Section 1.2). There is a continuous exchange of sediment within these two boundaries, driven by alternations between storm and fairweather conditions (Davidson-Arnott, 2009). The incident wave climate is the dominant process controlling changes in coastal form and evolution. At the same time, nearshore bottom configuration influences the effect of waves and the way in which coastal evolution occurs through the erosion, transport and deposition of sediment material, either eroded by waves and currents or brought to the coast by rivers (Davidson-Arnott, 2009). As waves arrive from deep water into the nearshore, they transform from skewed shoaling waves to asymmetric breaking waves (e.g., Elgar and Guza, 1985) and end up as swash on the beachface.

The shoaling, the surf and the swash zones are often also referred to as morphodynamic zones (Masselink, 1993; Kroon and Masselink, 2002), since each zone is associated not only to a singular type of wave, but also to a particular sediment transport process.

The characterisation of the whole nearshore zone over which sediment transport by waves occurs is important for understanding coastal dynamic. For example, Masselink (1993) related the residence times of shoaling waves, breaking waves and swash/backwash motions over a cross-shore profile to sediment dynamics in the nearshore (e.g., Masselink, 1993). Shoaling waves, for instance, generally result in a relatively small onshore sediment transport, while large quantities of suspended sediment are transported offshore under breaking waves (Price and Ruessink, 2008).

In most existing applications of the morphodynamic-zone approach to understand beach behavior (e.g., Masselink, 1993; Kroon and Masselink, 2002; Masselink et al., 2006), the boundary between the shoaling and surf zone was assumed to equal a specific wave height H to water depth h ratio, while the swash zone was set to commence where the tidal water level intersects the beach face (Poate and Ruessink, 2008). Nevertheless, several different ratios were used for H/h ratios (e.g., H/h=0.8 in Masselink,1993;

H/h=0.3 in Masselink et al.,2006), therefore such arbitrarily may have caused estimates of the residence times to be imprecise.

Previous efforts to identify the different regions with the use of video imagery were done with visual inspection (Poate and Ruessink, 2008), however manual procedures are not feasible for large dataset analysis. On the other hand, automated procedures were mainly based on image classification technique, with focus on water -wet sand - dry sand interfaces (Hoonhout et al., 2014, Hoonhout and Radermacher, 2015; Hoonhout et al. 2015) and intertidal beach morphological features detection (Quartel et al., 2006) with recognition of breaker zone (Revollo et al., 2016). However, the above-cited methodologies require sophisticated and computationally demanding image processing algorithms. More importantly, their application does not encompass the distinct wave transformation domains across the nearshore area.

4.2 Motivation and objectives

This chapter present a simple automated methodology able to identify each single wave transformation domain from video imagery. The method aims to support hydro- and morphodynamic studies evaluating the spatial distribution of wave transformation domains in the nearshore area. This is achieved correlating Timestack image pixel intensity variation to wave features and thus to wave transformation domains in the nearshore.

The technique is fully automated, computationally easy, and can be applied directly to Variance images, which have been produced from all video monitoring stations worldwide, allowing to extend the characterization of the nearshore area alto in the alongshore dimension.

4.3 Methods

4.3.1 Concepts

The concepts developed in this chapter are illustrated with the use of surfcam image acquisition at Ribeira d'Ilhas beach. Timestacks images from this study sites provided a good example for developing this study, as wave transformation processes were particularly well represented.

On Timestack images, pixel intensity values can be related to water elevation due to the incident light reflection on the water surface (Lippmann and Holman, 1989). When waves enter shallower waters, they shoal due to the change in water depth. The shadow created by the reduction of sunlight reflection on the water surface is visible on Timestacks as an abrupt drop of pixel intensity (e.g., Catalan and Haller, 2008). On these images, the time is represented on the vertical y axis (which increases from up to down according to Matlab image axis convention), therefore wave trajectories have always a negative slope (Figure 4.1).

When the wave amplitude reaches a critical level, the wave breaks creating turbulent whitewater spilling down its face. The typical white foam of breaking waves is visible on Timestacks as high-intensity white pixels (e.g., Yoo, 2007; Almar et al., 2012a). Therefore, the incipient breaking point coincides with the change between dark and white pixels (Figure 4.1) of each single wave feature visible on the image (e.g., Haller and Catalan, 2009). When broken waves reaches the shore, they dissipate their energy in form of wave swash on the emerged beach slope. Wave swash excursion patterns, or wave runup, are generally represented as cuspades rhythmical in time, generated by the uprush and backwash movements on the foreshore slope (Figure 4.1)

According to these conceptual descriptions, single wave transformation processes can be recognized on Timestack, consequentely the monitored nearshore zone can be segmented based on image characteristics

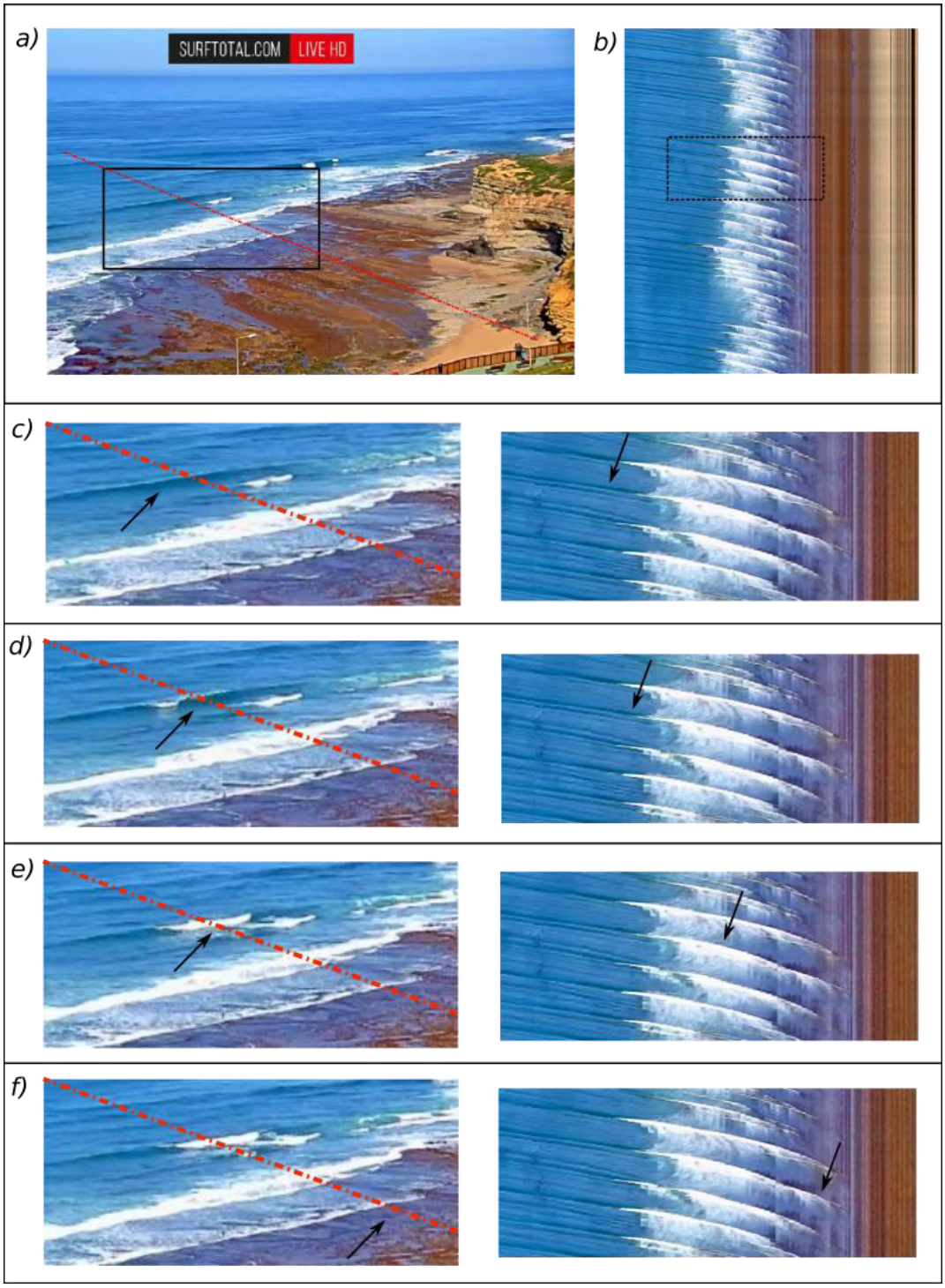

Figure 4.1. Waves characteristics on Timestack. Original image (a) and 10-min Timestack (b). Black boxes indicate the image area reproduced in detail below. Dashed red line represent the transect chosen to produce Timestack. c) Shoaling non-breaking waves troughs are represented as darker straight features on oblique (left) and Timestack image (right). Breakpoints (d) coincide with the change in pixel intensity, from dark pixel (shoaling) to white pixel (breaking foam). Broken waves (e) are represented by white pixel stripes on Timestakcs, whereas light white pixels represent ocean foam. Wave swash movements (f) are identified by the rhythmic cuspades in the swash zone

4.3.2 Wave transformation domains

A preliminary stage consisted in manually marking each singular breaking point and discrete wave swash excursion on a 10-min Timestack (Figure 4.2-a). Likewise, wave swash limit reached by a singular wave was detected at the end of the typical white stripe drawn at the shoreward end of the broken wave.

As real sea state is composed by irregular waves, the position of the breakpoint changed within the surf zone as function of breaker height and water depth. In the nearshore, the beach profile typically decreases toward the shoreline. For simplicity, it is further assumed that the highest waves break farther from the shoreline, whereas smaller waves break nearer the shore. Following this assumption, given the 10-minutes time interval used for Timestack production, the farthest breakpoint from the shore can be indicated as X_{Hmax}, since it represents the location where the highest wave broke. Likewise, the closest breakpoint to the shoreline coincides with the smallest breaking wave and can be indicated as the location where the smallest wave broke (X_{Hmin}).

The minima and the maxima seaward discrete swash positions among all marked swash limits were defined as Sw_{min} and Sw_{max}, respectively.

Following the definitions of wave processes domains adopted and reported in Chapter 1, the boundary between shoaling and surf zone is identified by the first-occurring breaking point, coinciding therefore with X_{Hmax}. The shoreward breakpoint X_{Hmin} locates the boundary between outer and inner surf zones. Finally, the swash zone is comprised between the Sw_{min} and Sw_{max} minimum and maximum swash excursions.

From this initial visual analysis, the identification of the different wave domains was done manually using breakpoints and swash locations on Timestacks. Shoaling, inner-outer surf, swash zones were clearly identified (Figure 4.2-b).

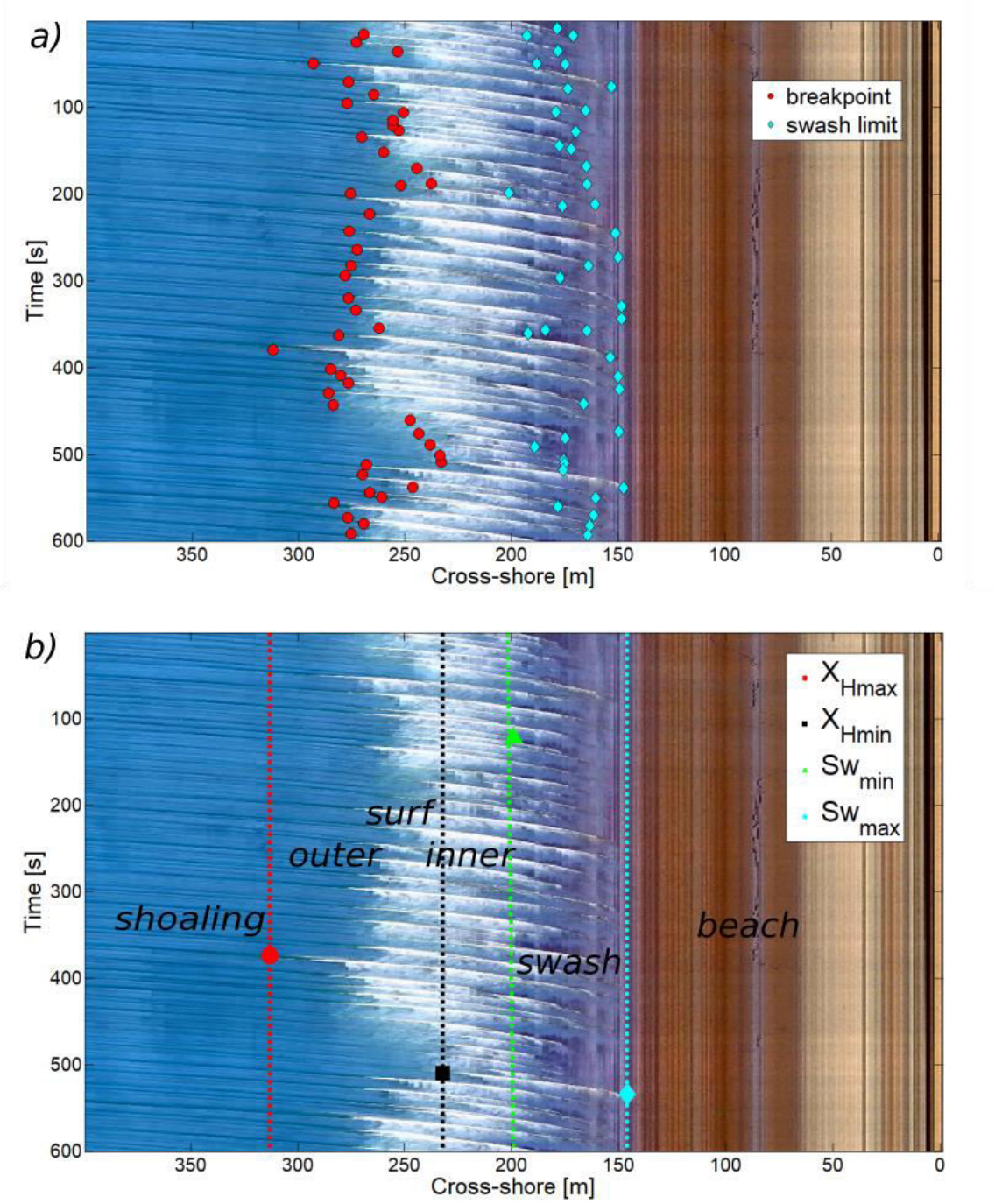

Figure 4.2. a) single breakpoints (red circles) and swash edges (cyan diamonds) manually marked on Timestack. b) wave transformation domains defined by the points marked on Timestack.

4.3.3 Timestack pixel intensity

As seen from Timestack visual inspection, pixel intensity brightness characterizes the representation of different wave types. In the following, pixel brightness variation was analysed to find a likely relation to wave transformations domains.

The variation of Timestack pixel intensity can be described by the average pixel intensity profile ($\bar{I}_{px}$) and the standard deviation of the pixel intensity ($\sigma_{I_{px}}$), computed along the time-axis as follow:

$$\bar{I}_{px} = \frac{1}{n}\sum_{i=1}^{n} I_{x,i} \qquad \textit{Eq. 4-1}$$

and

$$\sigma_{I_{px}} = \sqrt{\frac{1}{n-1}\sum_{i=1}^{n}(I_{x,i} - \bar{I}_{px})^2} \qquad \textit{Eq. 4-2}$$

where $I_{x,i}$ is the pixel intensity value and n the number of pixels.

Figure 4.3 illustrates the shapes of the average pixel intensity $\bar{I}_{px}$ (Figure 4.3-a) and standard deviation $\sigma_{I_{px}}$ (Figure 4.3-b) over the profile.

Timestack is an RGB image, therefore $\bar{I}_{px}$ and $\sigma_{I_{px}}$ profiles were computed for each colour band separately to be thorough. Signals were simply superimposed to the Timestack image to show their shape, as the absolute magnitude of intensity values are not in focus here. Note that on Timestack, $\bar{I}_{px}$ and $\sigma_{I_{px}}$ plots have inverse y-axis due to Matlab convention for image axis.

The $\sigma_{I_{px}}$ profiles had similar shape, differing only in intensity values. On the contrary, $\bar{I}_{px}$ profiles were similar over the nearshore zone, whilst their shapes diverged considerably over the swash zone.

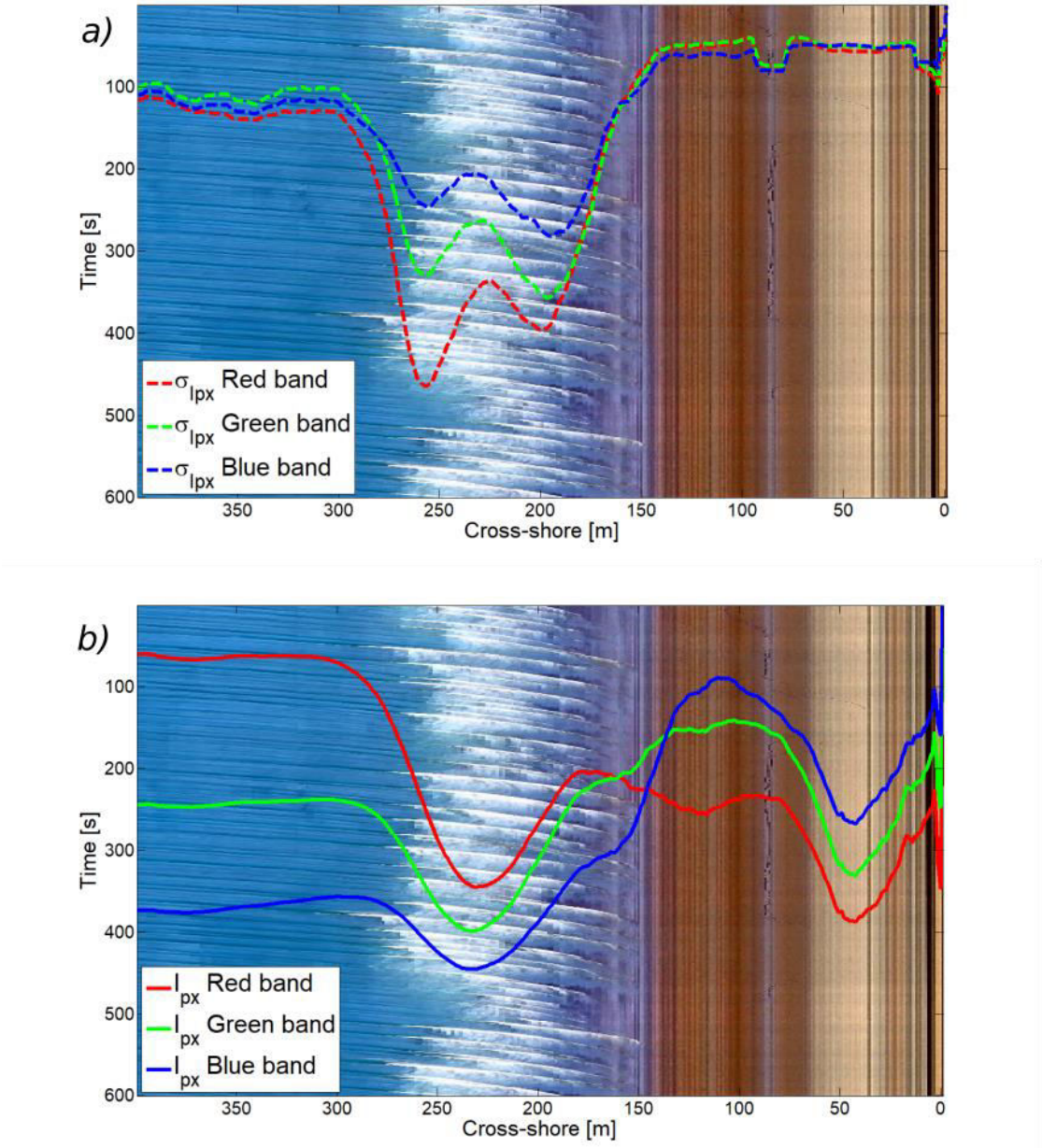

Figure 4.3. a) Standard deviation of pixel intensity $\sigma_{I_{px}}$ for Red (red line), Blue (blue line) and Green (green line) band of Timestack; b) averaged pixel intensity $\bar{I}_{px}$ for Red (red line), Blue (blue line) and Green (green line) band of the Timestack. Note that $\bar{I}_{px}$ and $\sigma_{I_{px}}$ are superimposed to Timestack for description purpose and have inverted y-axis unit.

The single Blue band was chosen for further analysis and applications. As the objective was to detect wave transformations processes, the Blue color band represented better both dark blue pixel of shoaling waves and white pixel of breaking waves.

4.3.4 Pixel intensity statistics and visual analysis

Single Blue band of $\bar{I}_{px}$ and $\sigma_{I_{px}}$ are shown in Figure 4.4-a on Timestack, while the unity-based Min-Max normalizations of $\bar{I}_{px}$ and $\sigma_{I_{px}}$ that were used to set up the algorithm are illustrated in Figure 4.4-b. Both pixel intensity statistics ($\bar{I}_{px}$ and $\sigma_{I_{px}}$) were coupled to the visual breakpoints locations previously marked on Timestack, representing the transitions points between different wave domains, namely X_{Hmax}, X_{Hmin}, Sw_{min} and Sw_{max} (Figure 4.4).

The average of pixel intensity $\bar{I}_{px}$ was characterized by an almost constant value in the shoaling zone and by a Gaussian-like shape in the breaking zone, where the white foam of breaking waves increased the brightness value. In the analysed Timestack, the peak of the Gaussian-like shape coincided with the limit between the outer and inner surf zones, X_{Hmin}. Finally, $\bar{I}_{px}$ dropped at the location of the dry beach and was not related to swash zone boundaries.

The $\sigma_{I_{px}}$ was almost constant in the shoaling zone, where the pixel intensity variability did not change as consequence of a regular shoaling waves patterns over time. The signal started to increase at the first incipient breaking wave, whose location delimitated the boundary between shoaling and the outer surf zone (X_{Hmax} on Figure 4.4-a, and point A in Figure 4.4-b). In the outer surf zone, some waves were breaking and some are still shoaling towards the shore. Successively, $\sigma_{I_{px}}$ reached a first local maximum (point B), after which it decreased to a local minimum value (point C) whose position coincided to the last incipient wave breaking point X_{Hmin}, and therefore delimited the boundary between outer and inner surf zone (see also maximum of $\bar{I}_{px}$ profile). Yet, $\sigma_{I_{px}}$ increased till reaching a second peak (point D), which identified the minimum wave swash position Sw_{min} and the start of the area in which swash processes occurred. After such position, $\sigma_{I_{px}}$ drastically dropped till a minimum value (point E) which approximated the boundary between wet sand and dry beach area Sw_{max}.

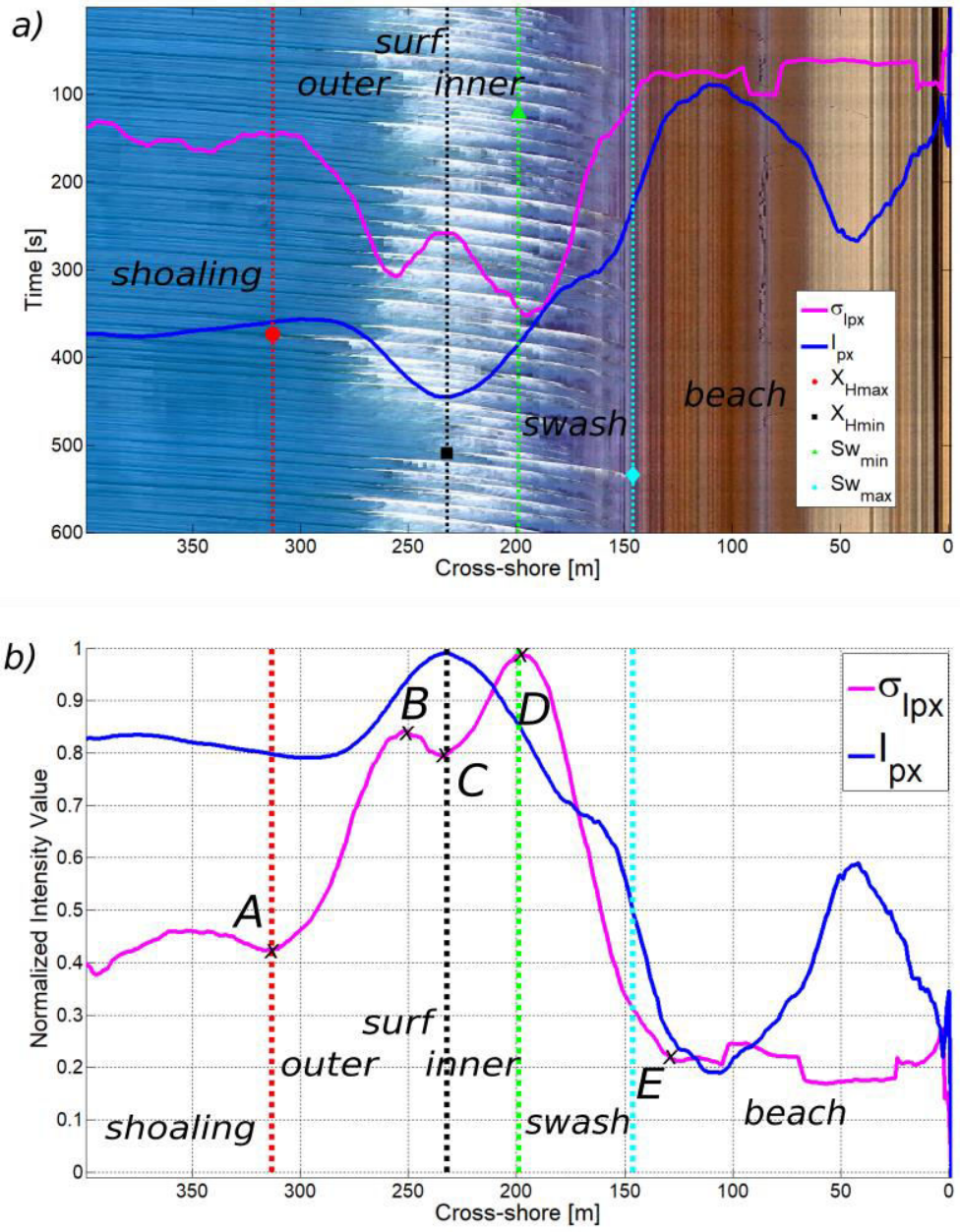

Figure 4.4. a) Wave transformation domains superimposed to Timestack combined with $\bar{I}_{px}$ and $\sigma_{I_{px}}$. b) Min-Max $\bar{I}_{px}$ (blue line) and $\sigma_{I_{px}}$ (magenta) plotted together with wave transformation regions boundaries. Specific points on signals can be identified. A = start of seaward modal shape of $\sigma_{I_{px}}$; B= seaward peak of bimodal distribution of $\sigma_{I_{px}}$; C = local minimum of $\sigma_{I_{px}}$ between bimodal peaks; D = seaward peak of bimodal distribution of $\sigma_{I_{px}}$; E = shoreward foot of shoreward bimodal distribution of $\sigma_{I_{px}}$. C is also the main peak of Gaussian-shape of $\bar{I}_{px}$.

Overall, $\sigma_{I_{px}}$ was characterized by a bimodal distribution, under whose limits surf and swash zones were comprised (points A-E). The valley between the two maxima of the distribution (point C) coincided with the boundary between outer and inner surf zones, whereas the most shoreward maximum of the distribution located the edge between inner surf and swash zones (point D).

Considering $\bar{I}_{px}$ and $\sigma_{I_{px}}$ patterns across the surf zone, the latter was selected to support the methodology as all the wave transformations domains could be identified by its shape.

4.3.5 Validation on Timestacks dataset

In the previous section, findings from a single Timestack investigation suggested that specific local minima and maxima of $\sigma_{I_{px}}$ profile could be directly related to wave transformation domains boundaries. In order to confirm the previous findings, a set of 94 rectified Timestacks generated by the "surfcam" acquisition at Ribeira d'Ilhas during two days were analysed, namely 52 Timestacks from video acquisition of day 28th and 42 during day 29th.

Visual procedure consisted in outlining from visual inspection the boundaries between shoaling surf and swash zones on Timestacks (first and last breaking point, X_{Hmax} and X_{Hmin}, minimum and maximum swash Sw_{min} and Sw_{max}). Yet, the specific points were manually marked (A, B, C, D, E in Figure 4.4) on each $\sigma_{I_{px}}$ plot computed from images. Table 4.1 reports the matching points that were verified by this first manual analysis.

Table 4.1. Relation between wave transformation domain boundaries, breakpoints marked on Timestacks (see also Figure 4.44-a) and specific points marked on $\sigma_{I_{px}}$ plot (see also Figure 4.4-b).

Wave domain boundary	***Breakpoints***	$\boldsymbol{\sigma_{I_{px}}}$
shoaling- surf zone	X_{Hmax}	A
outer-inner surf zone	X_{Hmin}	C
surf – swash zone	Sw_{min}	D
swash zone-dry beach	Sw_{max}	E

Besides the visual and the manual procedures, a dedicated algorithm was implemented to automatically recognize the particular points (A, B, C D and E) in the Min-Max normalized $\sigma_{I_{px}}$. The two peaks of the bimodal distribution (points B and D in Figure 4.4-b) were found using a peak finder algorithm. Point B corresponded to the global maxima, whereas the point D was found as the second highest peak over the signal. Points B and D positions were defined as the left-most and right-most peak, respectively. The bell-shaped valley (point C) was successively identified as local minima between the two peaks. Finally, points A and E were recognized computing the first derivative of the $\sigma_{I_{px}}$ profile, which returned the value of the slope of the signal. A threshold value of 0.002 was set to identify A and E as the locations in which the distribution shape changed slope before B and after D, respectively.

To validate the approach for nearshore zonification using pixel brightness variation, the correlation between $\sigma_{I_{px}}$ points and wave transformations boundaries was tested using the results of the visual and manual procedures (refer to Table 4.1) for 94 Timestacks, which were produced during different tide elevation and wave conditions. Finally, the performance of the automatic detection algorithm was verified against both datasets.

4.3.6 Application on Variance images

Since pixel variation $\sigma_{I_{px}}$ of a Timestack can be directly obtained by sampling the pixel intensity on Variance image (Figure 4.5) over the same transect used to generate the Timestack (Simarro et al., 2015), the method presented for Timestacks was directly applied to Variance to extend the identification of the wave transformation domains alongshore.

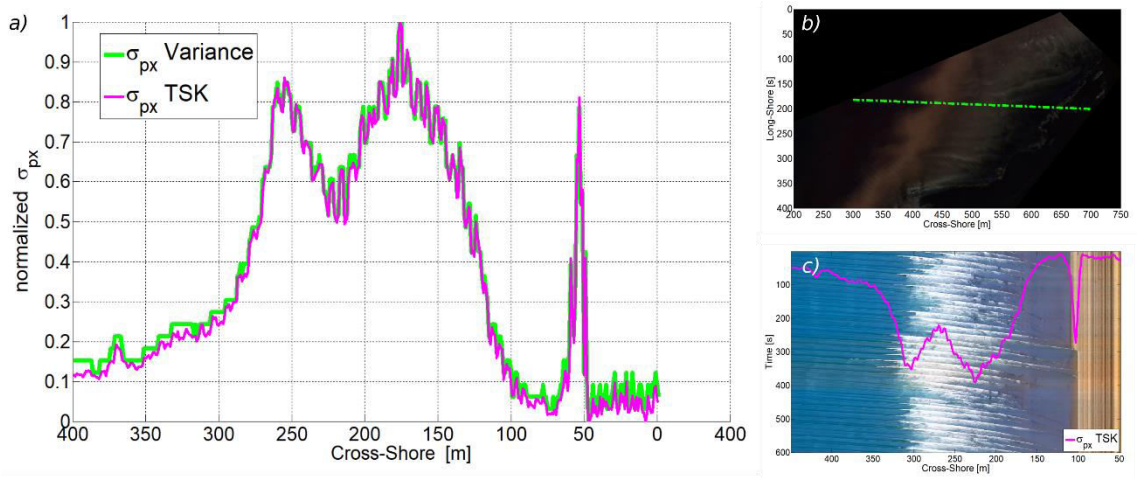

Figure 4.5. Identity of profiles $\sigma_{I_{px}}$ (a) extracted from Timestack (b) and from Variance (c) using the transect chosen to generate Timestack (dashed green line in b).

4.4 Results

4.4.1 Pixel intensity statistics and visual analysis

Figure 4.6 presents the comparison between the locations derived from visual analysis on Timestacks and the specific points manually demarked on $\sigma_{I_{px}}$ profile plot.

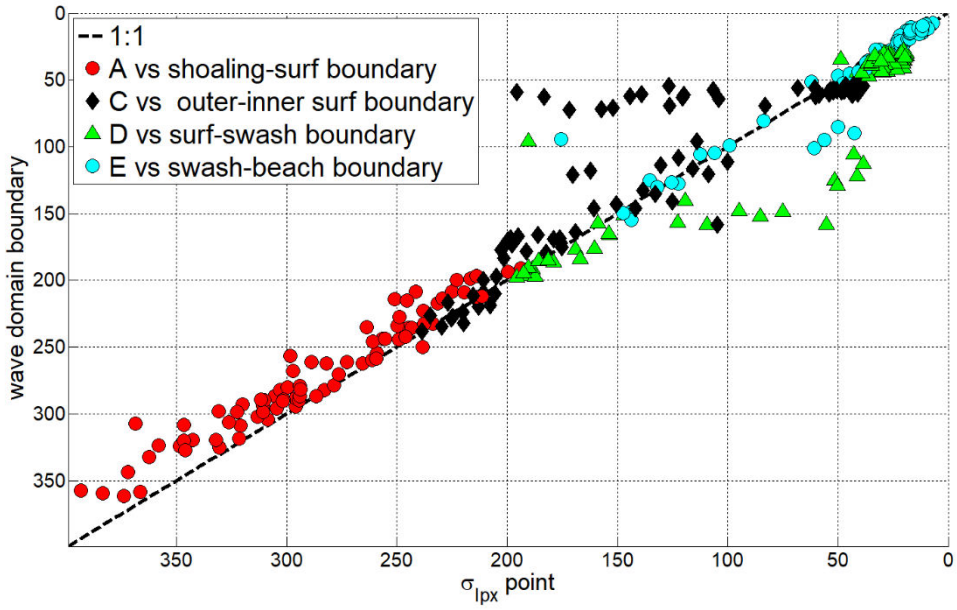

Figure 4.6. Breakpoints and swash limits manually identified on $\sigma_{I_{px}}$ profile against wave transformation domain boundaries manually picked on Timestacks. Red dots = most seaward breakpoints; black diamonds = most shoreward breaking; magenta triangles = minimum swash positions; cyan dots = maximum swash.

Over the considered 94 Timestack, the first wave breaking location on $\sigma_{I_{px}}$ (point A) was found slightly seaward than the shoaling-surf zone boundary visually located on Timestacks. Maximum differences were about 50 m over a covered cross-shore length of 450 m. Disparities might be caused by the subjectivity in marking the first wave breakpoint and the change in slope of $\sigma_{I_{px}}$ profile.

The points C, D, E coincided with the relative domains limits of wave processes inner-outer surf, surf -swash and max swash limits, respectively. However, some data were scattered far from the identity line and showed disparities of about 150 m with the points marked on Timestacks. These were the cases in which $\sigma_{I_{px}}$ profile did not show

the typical bimodal distribution shape seen in Figure 4.4, due to high irregularity of wave breaking and by the site-specific wave dissipation on the (almost) horizontal slope at Ribeira d'Ilhas beach.

4.4.2 Pixel intensity statistics and automatic procedure

The automatic detection was affected by irregularity of wave breaking and Timestack quality, especially regarding the surf and swash zone limits. In some cases, the detection algorithm did not perform properly due to the anomalous pixel intensity variation on Timestacks generated by the high swash dissipation rate on the rocky platform of Ribeira d'Ilhas.

Despite the inaccuracies in the automatic detection, RMSE was about the 10% the length of the observed 450 m transect length for the specific wave transformation domain boundaries encountered.

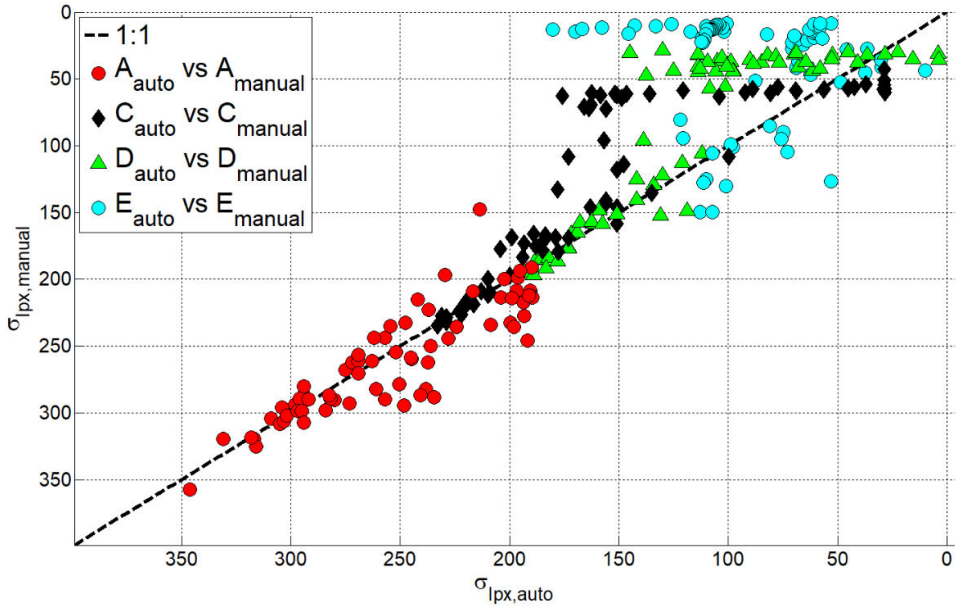

Figure 4.7. Automatic detection of specific breakpoints against the manually picked on $\sigma_{I_{px}}$ profile. Red dots refer to the most seaward breakpoints, black diamonds are the last (most shoreward) breaking points, magenta triangles the minimum swash positions and cyan dots the maximum swash.

4.4.3 Manual and automatic performances

Figure 4.8 presents the overall relationship between manual and automated procedures from the 94 Timestack analysed. Comparison between the visual procedure on Timestacks and the manual identification on $\sigma_{I_{px}}$ confirmed that $\sigma_{I_{px}}$ profile can be used to identify the different wave transformation zones.

Regarding the automatic identification of the specific points by the developed algorithm, shoaling -surf zone boundary was well identified, as well as the limit between outer and inner surf zone. The detection of the boundaries between inner surf and swash zone was the most inaccurate when automatic algorithm was applied. This was due to the noisy $\sigma_{I_{px}}$ in those images in which wave breaking positions were highly irregular over the cross-shore profile. The pixel intensity anomalies depended on the high dissipation characteristic of Ribeira d'Ilhas low gradient slope which induced errors and imprecision in the automatic algorithm detection.

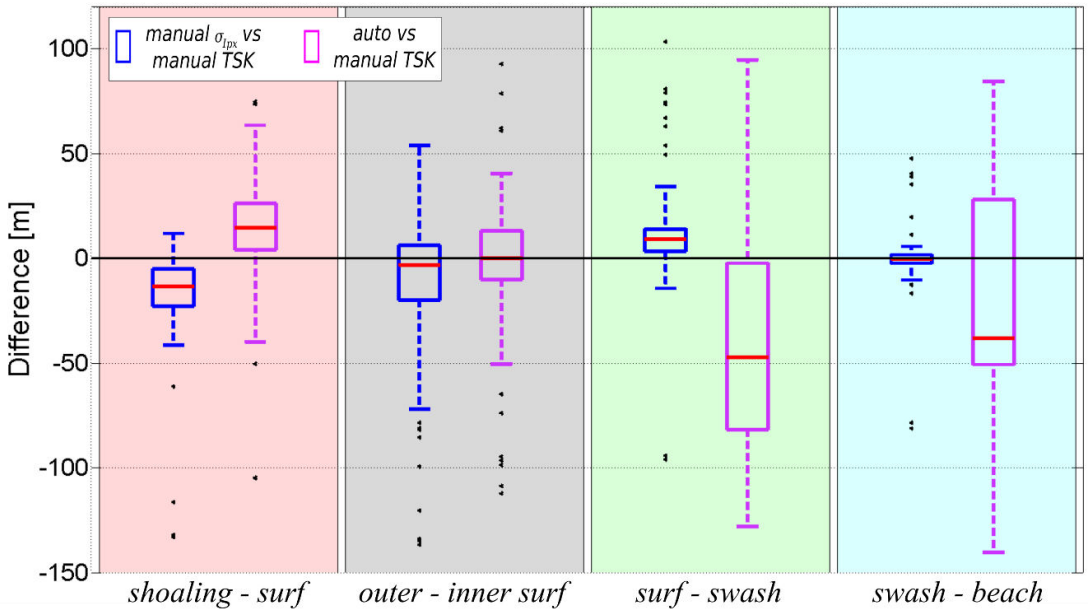

Figure 4.8. Boxplot of the relationship between the specific points identified on $\sigma_{I_{px}}$ profile and the wave transformation domain boundaries visually found on Timestacks, from manual (blue boxes) and automatic (magenta boxes) procedures.

Finally, the edge between swash zone and subaerial dry beach showed to be not precise, however this boundary can also be considered as shoreline (Boak and Turner,

2005). Therefore, the integration of a shoreline detection algorithm (e.g., Aarninkhof et al., 2003; Almar et al., 2012b, Osorio et al., 2012; Sobral et al., 2013; Valentini et al., 2017b) to the proposed method would be advantageous for a precise delimitation of the swash zone.

4.4.4 Wave transformation domains on Timestack

Figure 4.9 shows an example of the temporal variation of wave transformation domains identified automatically over half a tidal cycle at Ribeira d'Ilhas on day 29th. As the sea elevation increased, the seaward breaking point moved shoreward, shifting the start of the surf zone towards the shore. At the same time, the last breaking point occurred closely to the coast and shifted the start of the swash zone over milder beach slope.

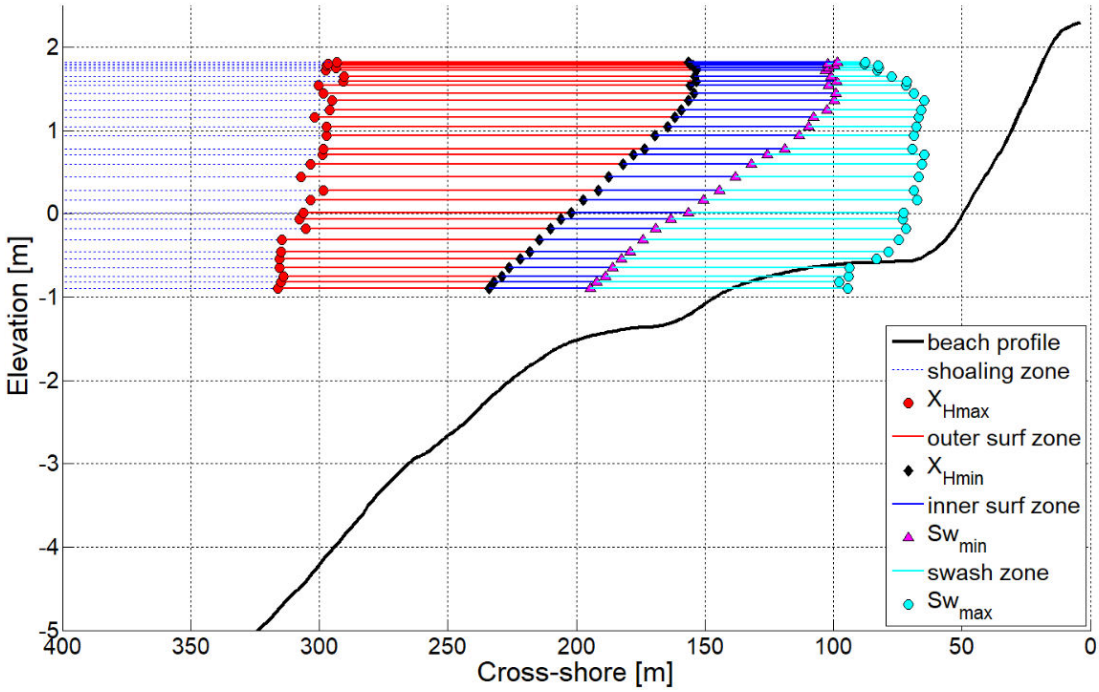

Figure 4.9. Example of wave transformation domains variation. Region are plotted over the beach profile, at the correlated tidal elevation during a half a tidal cycle. Shoaling zone is represented by dotted blue line, outer surfzone by red line, inner surf zone by blue line and swash zone by cyan line. Magenta circles indicate the transition between shoaling and surf zones, blue diamonds the boundary between outer and inner surf zones, magenta triangles the limit between surf and swash zones.

Analysing the change in length of the different sectors (Figure 4.10), it can be noticed that the outer surf zone increased from around 60 m to about 120 m over the half a tidal cycle (tidal-range of 2 m), while the inner surf zone length remained almost constant around 50 m.

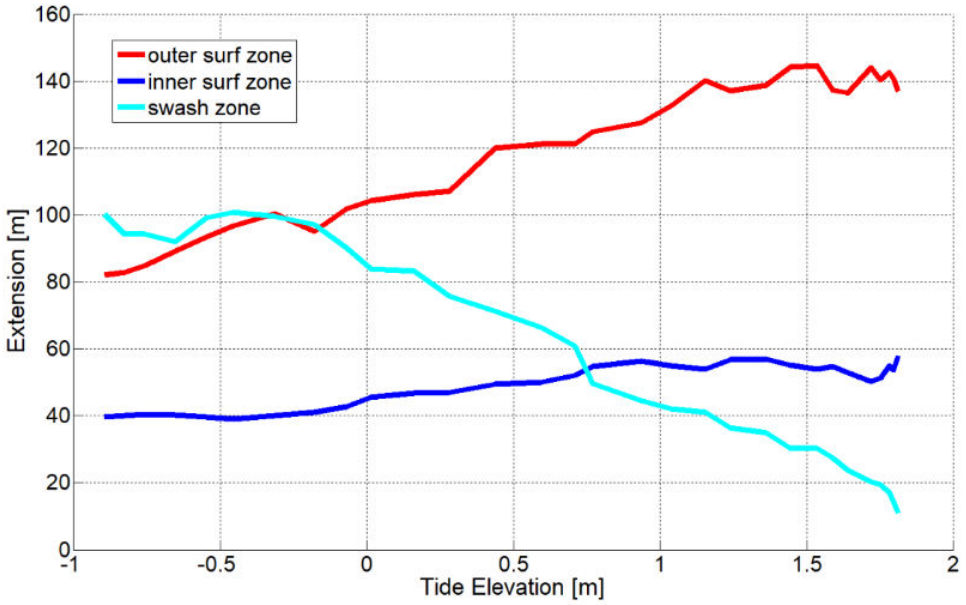

Figure 4.10. Quantification of wave transformation domains variation during half a tidal cycle. Red line represents the change of outer surf zone, blue line of the inner surf zone, cyan line the swash zone extent change during the increasing water level between -1 and 1.8 m.

4.4.5 Wave transformation domains on Variance

To apply the technique to Variance, a total of 120 cross-shore transects were sampled on Variance. The series of transects covered an alongshore distance of about 300 m. Wave transformation domains for the entire monitored area were derived applying the automatic detection at each Variance transect, both on oblique (Figure 4.11-a,b) and rectified image (Figure 4.11-c,d).

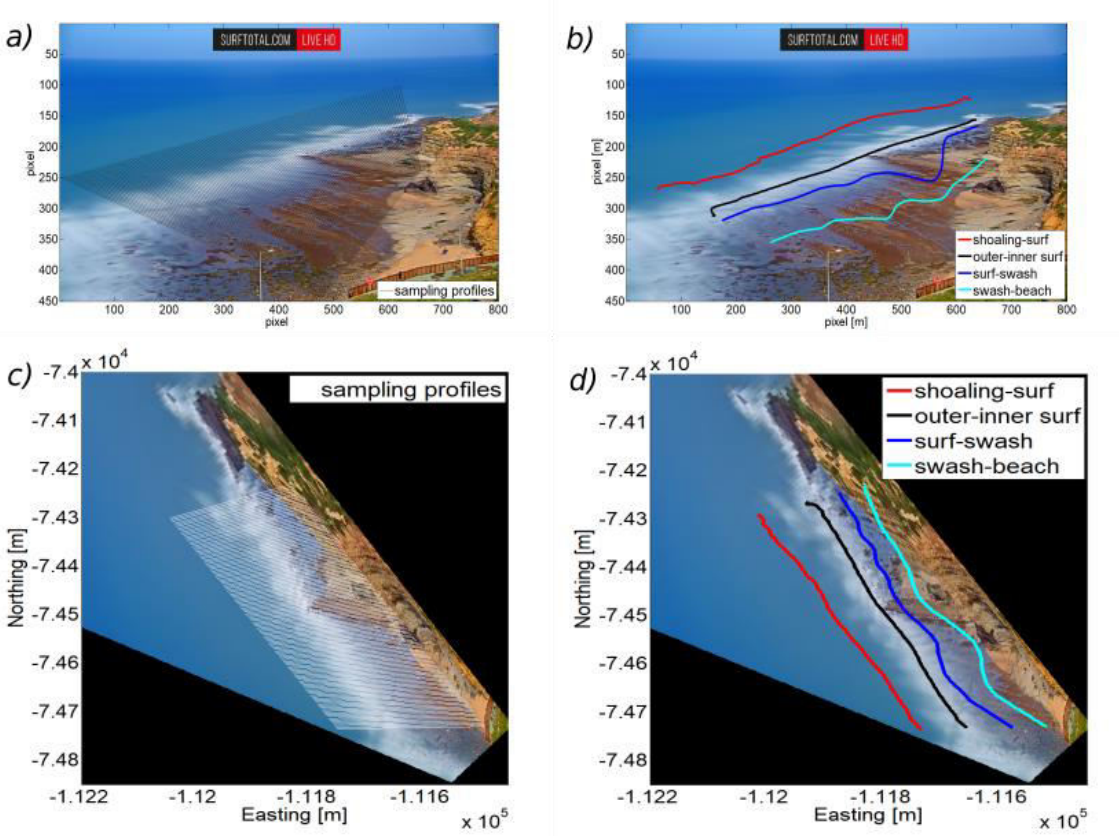

Figure 4.11. Example of wave transformation domains identified on oblique (b) and rectified image (d). Thin black (a) and white (c) lines plotted on oblique Timex represent the 120 profiles sampled on Variance images for the application of the methodology. Profiles are plotted on Timex for better representation.

The areas were well identified also by using Variance, even though Timex images were used in Figure 4.11 for a clearer representation. Note that line representing the boundary between outer and inner surf zone coincided with the breakpoint visible on Timex, as verified in Figure 4.4 and reported in Table 4.1.

4.5 Discussion

The investigation presented in this chapter found a strong relation between wave hydrodynamics and Timestack pixel intensity statistics. The proposed methodology allowed the clear identification of shoaling, surf and swash zones directly from the standard deviation of pixel brightness $\sigma_{I_{px}}$.

The method provides a new tool to study the mophodynamic and associated sediment transport within the nearshore. In fact, the approach offers an appropriate alternative to identify the wave transformation domain boundaries based on spatial variation of breakpoints, overcoming the subjectivity of visual determination on Timex used by Price and Ruessink (2008), and the different hydrodynamic parameters used in previous works (Masselink, 1993; Kroon and Masselink, 2002; Masselink et al., 2006). The possibility of applying the method to Variance offers the advantage of extending such studies to alongshore dimension.

The method is easily reproducible and fast computing, as it depends on simple image processing algorithms. The full processing of 120 $\sigma_{I_{px}}$ profiles over 94 Variance, produced over 15 hours of video acquisition, required about 100 seconds, which is a relative efficient time for the considered dataset.

Along with the possibility of describing the accurate spatio-temporal wave transformation domains variability over different hydrodynamic conditions, the technique can support the application of stand-alone automatic procedures for image analysis. Specific areas of the image can be previously extracted to fasten, for instance, shoreline detection (e.g., Valentini et al., 2017b) and wave breaking height (e.g., Almar et al., 2012a) among all. From the analysis of $\sigma_{I_{px}}$ profile, the bimodal distribution was associated to two unimodal overlapping distribution: the left-most part distribution was related to incipient breaking point location, while the right-most part was linked to wave breaking and dissipation processes.

In case of barred beaches, waves firstly break over the bar and successively break on the shore. Here, it can be observed a multimodal $\sigma_{I_{px}}$ profile (Figure 4.12) as shown in Holland et al. (2009) and in Guedes et al. (2011b).

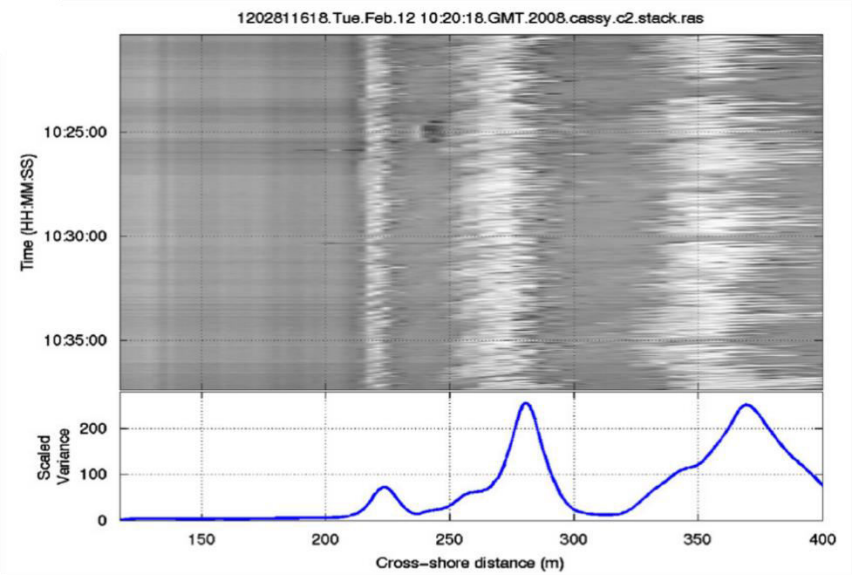

Figure 4.12. Timestack image shows changes in surf zone due to wave breaking patterns. Inset gives $\sigma_{I_{px}}$ profile of a barred beach (from Holland et al., 2009).

The likely limitations of the technique are related to the sea state conditions. For example, the clear identification of the boundaries between the different zones can be difficult if wave features (both shoaling and breaking) are not well visible. Swell conditions are ideal for the application, since shoaling and regular breaking wave patterns are well observable and distinct on images. On the contrary, during unorganized sea or low wave energy, the typical shoaling wave shadow may not be evident on the sea surface and on Timestacks.

Image quality is also important, being weather conditions and sun reflection on sea surface crucial for the correct application of the proposed methodology. For instance, pixel intensity variation of images acquired during foggy days, darkness or rainy conditions might result unusable. In addition, sun glitter and clouds might induce anomalous $\sigma_{I_{px}}$ profile shape. Taken in account that all these weather-related factors are common to occur in a natural environment, the technique robustness might be improved using relative large dataset to profit from time windows during favourable conditions.

5. ESTIMATION OF WAVE BREAKING HEIGHT

5.1 Introduction

Wave height at the breaking point is an essential component of any study of coastal processes, and a key parameter for a wide variety of coastal engineering applications including the estimation of sediment transport (e.g. Bird, 2000), the design of coastal structure (e.g. EUROTOP, 2007; Van der Meer, 2011), and coastal risk assessment (e.g., Horsburgh et al., 2017).

Direct measurements of wave breaking height in the surf zone are complex due to the difficulties related to the installation of oceanographic instrumentation at high energetic locations. This is especially true at sandy coasts, where bottom dynamics generally does not allow safe mooring of the instruments such as pressure gauges and Acoustic Doppler Current Profilers (ADCP). Moreover, the placement of oceanographic devices might endanger people using the littoral for recreational activities, such as bathing, surfing and fishing.

Wave models are widely used to estimate wave breaking height at the coast. Camenen and Larson (2007) and Robertson (2013) provide a review on empirical models to estimate wave breaking height. Numerous methods and relationships have been presented and published, which, in general, found the wave breaking height as function of the water depth at the breaking point (h_b) and the sea bottom slope under the breakpoint (m_b). Therefore, the models require bathymetric data and/or offshore wave conditions, which are not always available. In addition, most of wave empirical breaking models were derived using data from laboratory experiments, in which hydro- and morphological conditions were strictly under control. Applied on a random sea state in the field, results are subjected to uncertainties in reproducing the several processes occurring in the surf zone.

Video monitoring has been proven a cost-effective technique for estimating wave breaking height (H_b) in the coastal zone. Most of the studies were based on the use of Timestack images, since this kind of images allowed to retrieve breakpoint position in the surf zone. Several works used oblique Timestacks produced from images collected in the field and applied photogrammetric corrections to estimate wave height at the breaking point (De Vries et al., 2010; Gal et al., 2011; Shand et al., 2012; Robertson, 2013). Besides, Almar et al. (2012a) used rectified planar Timestacks to derive estimation of H_b

based on the photogrammetric relation between breaking point location, wave roller length and camera position. The method was validated with data collected in a wave tank experiment, with high-frequency video-data sampling (25 Hz) and indoor light conditions. Although the methodology showed good results when applied on video data acquired in the field (Angnuureng et al., 2016), the fundamental image processing procedures dedicated to wave roller length estimation (Almar et al., 2012a) require intensity threshold calibration and depend on image pixel quality, along with being merely applicable on Timestacks.

5.2 Motivation and objectives

Existing methods to measure wave breaking height from video imagery are based on the use of Timestacks. The production of these images is a relatively computing-demanding task, which is not often set routinely by the coastal video systems installed worldwide (e.g., Valentini et al, 2017a, personal communication).

To author knowledge, Huntley et al. (2009) is the only published work that attempted the use of Timex to estimate wave breaking height. The technique was based on the detection of the surf zone position seaward edge, which was linked to the maximum wave breaking height through empirical formulas available in literature. Despite the lowest RMSE of 0.28 m achieved by the methodology using a variety of available models for wave breaking (Battjes and Janssen, 1978; Thornton and Guza, 1983; Baldock et al., 1998; and Lippmann et al., 1996), further work were suggested to investigate more accurately the link between video imaging data and fraction of breaking waves.

The main objective of this section is to find a relation between breakpoint location statistics and wave breaking height, in order to set a simple technique for estimating wave breaking height using Timex. Timex images have been stored for decades by several coastal video-monitoring stations worldwide and have been used for many coastal engineering and scientific studies (see Section 2.4.1). A new methodology would respond to the need of simple remote sensing techniques to measure wave breaking height in the nearshore zone, with the use of commonly produced and utilized Timex.

5.3 Methods – I

This section describes an implemented conceptual model to measure wave breaking based on video imagery and bathymetric data. The model was developed and validated using the pixel brightness properties of Timestacks, namely averaged pixel intensity, being applicable on Timex.

Successively, a second complementary methodology is proposed, which estimates wave breaking height directly and exclusively from breaking patterns visible on Timex.

5.3.1 Breakpoint location statistics

One Timestack generated by images acquired at Ribeira d'Ilhas (Section 3.4) was chosen to study the breaking wave process in the nearshore.

Re-calling that, on Timestacks, the incipient breaking point coincides with the change between dark and white pixels (Section 4.3.1), the breakpoints of each wave were manually marked on the image (Figure 5.1), with the purpose of analyzing their spatial variability in the surf zone. From visual analysis, breakpoints were distributed within a cross-shore extent of about 150 m, from a maximum distance of 300 m and a minimum distance of 150 m from the shoreline.

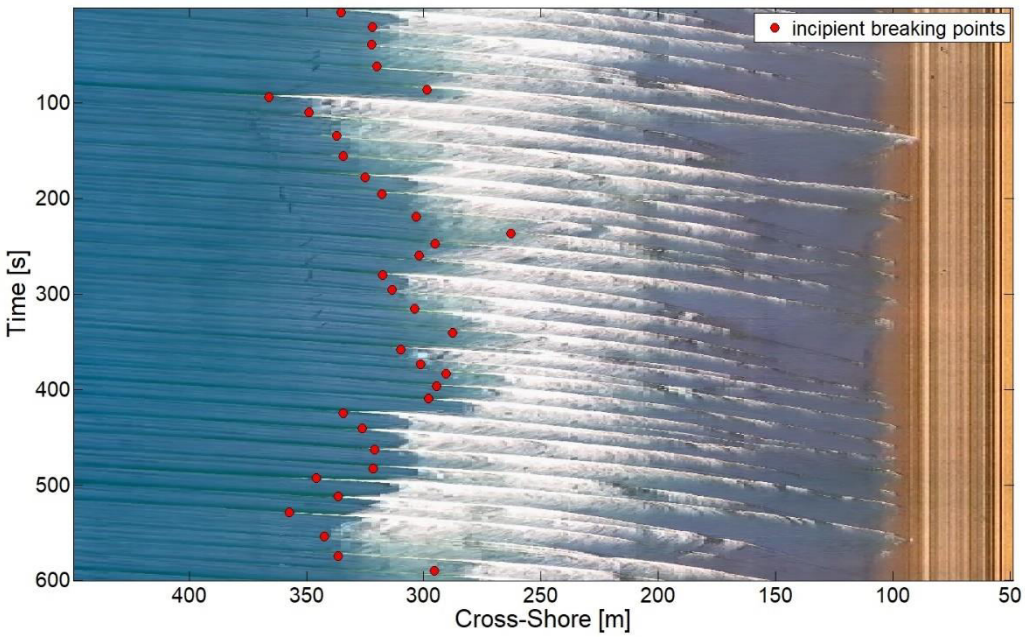

Figure 5.1. Incipient wave breaking points (red circles) manually detected on Timestack.

Considering that at most beach profiles water depth decreases from offshore to inshore, it is assumed from hereafter that the higher waves break farther from the shoreline, whereas smaller waves break closer to the shore. Following this assumption, wave breaking position statistics (Figure 5.2) were computed from the number of incipient points manually picked on Timestacks to find:

- X_{Hmax} as the first breaking point (farthest from the shore);
- X_{Hs} as the significant wave height position, averaging the 33% of the farthest-from-shoreline;
- $X_{H1/3}$ as the location of the 33^{d} percentile of all breaking positions;
- X_{Hm}as the mean position among all breaking positions;
- $X_{H2/3}$ as the location of the 67^{d} percentile of all breaking positions;
- X_{Hmin} as the location where 100% of the waves have broken, coinciding with the smallest breaking wave and the closest breakpoint to the shore.

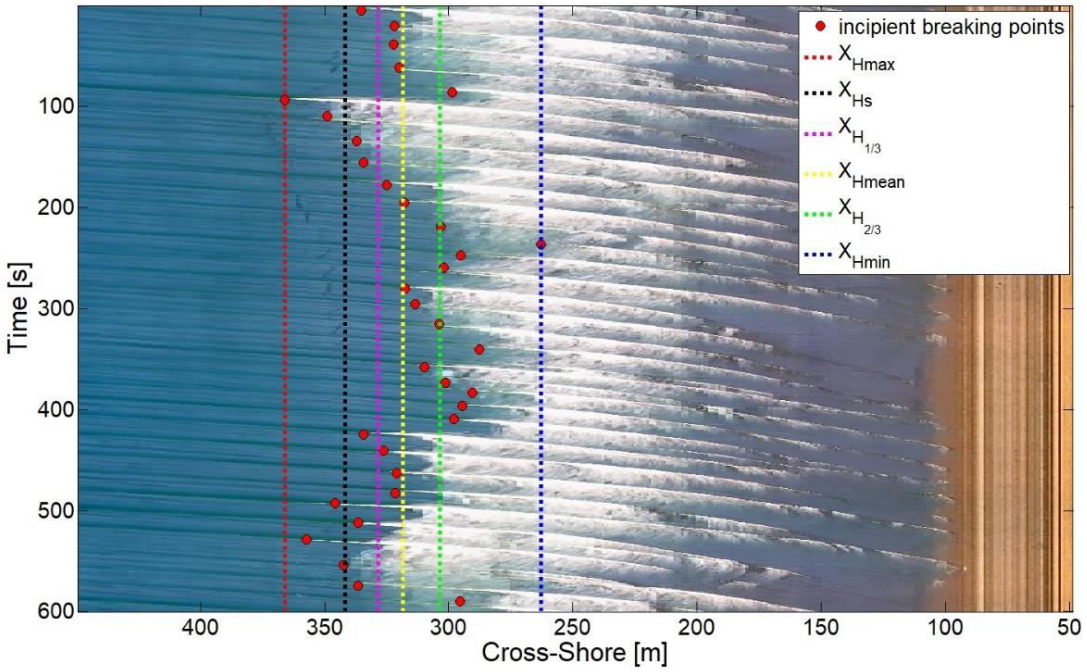

Figure 5.2. Breakpoints location (red circles) and computed breakpoints position statistics (dashed lines) superimposed on Timestack.

5.3.2 Pixel intensity variation

With the main purpose of verifying if statistics of pixel intensity variation can be used to spot breakpoint locations, similarly to the technique previously described for wave transformation domains (Section 4.3.4), standard deviation of the pixel intensity ($\sigma_{I_{px}}$) and the average pixel intensity profile ($\bar{I}_{px}$) were extracted along the time-axis of Timestack following equations 4.1 and 4.2, respectively.

Pixel intensity variation was already used to identify incipient breaking point (Almar et al. 2012a) or associated to wave breaking over a bar (e.g, Aarninkhof and Ruessink, 2004; Guedes et al., 2011b). Nevertheless, $\sigma_{I_{px}}$ and $\bar{I}_{px}$ profiles have not been related to wave breaking statistics yet, therefore an extensive analysis between video imaging data and breakpoint statistics was performed. Figure 5.3 shows a Timestack example in which $\sigma_{I_{px}}$ and $\bar{I}_{px}$ profiles are superimposed on image and coupled to breakpoint statistical positions.

Regarding $\sigma_{I_{px}}$ profile, it was previously shown (Figure 4.4) that the point in which $\sigma_{I_{px}}$ started to increase after an almost-constant linear (point A in Figure 5.3-b) matched the most seaward breakpoint X_{Hmax}, while the local minima point C between the two peaks of bimodal distribution (Figure 5.3-b) corresponded to the location in which the last smallest wave broke (X_{Hmin}). From the analysis of incipient breakpoints statistic, it can be added that the seaward peak of the bimodal distribution (point B in Figure 5.3-b) coincided with the 67th percentile of incipient breaking location ($X_{H2/3}$).

From the analysis of $\bar{I}_{px}$ profile, the peak of the Gaussian-like shape (point P in Figure 5.3-b) coincided with the position of the most onshore breaking point X_{Hmin}. The point in which the Gaussian-like shape of $\bar{I}_{px}$ profile started (point F in Figure 5.3-b) was found spotting the significant wave height breaking position X_{Hs}.

Finally, neither $\sigma_{I_{px}}$ and $\bar{I}_{px}$ profiles had any significative matching points with X_{Hm} and $X_{H1/3}$ locations statistics.

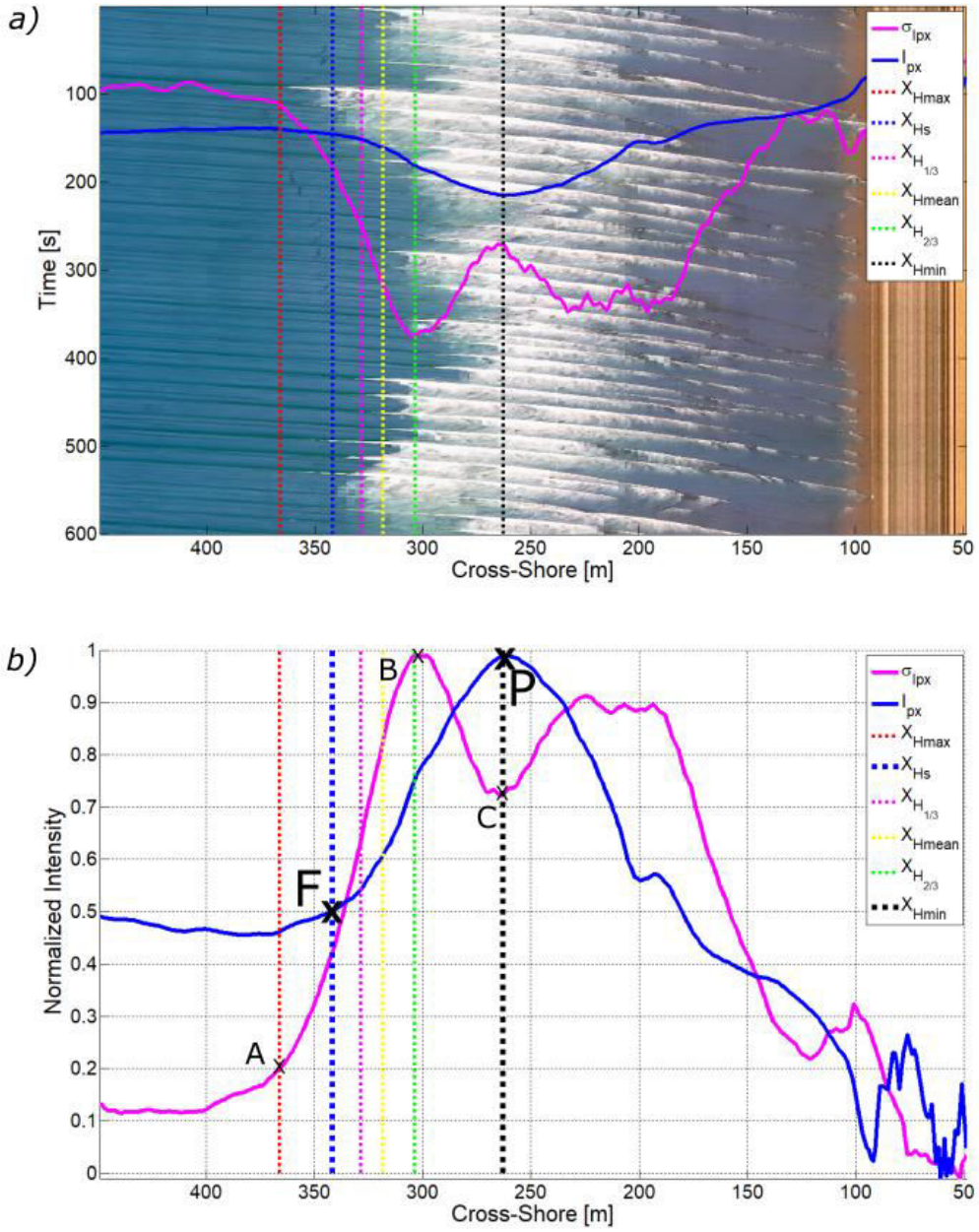

Figure 5.3. a) Plot of $\sigma_{I_{px}}$ (magenta solid line) and $\bar{I}_{px}$ (blue solid line) on Timestack. b) MinMax normalized $\sigma_{I_{px}}$ and $\bar{I}_{px}$ plot. Dashed vertical lines refer to breakpoint statistics: X_{Hmax} (red), X_{Hs} (black), $X_{H1/3}$(magenta), X_{Hm} (yellow), $X_{H2/3}$(green) and X_{Hmin}(blue).

Table 5.1 resumes the relations found from the analysis of a single Timestack between wave breakpoints and the specific points of pixel intensity variation. Note that the specific

points P and C, from $\sigma_{I_{px}}$ and $\bar{I}_{px}$ respectively, corresponded both on the last breakpoint position.

Table 5.1. Relationships between incipient breakpoint and pixel intensity variation. Denomination of the points refers to Figure 5.3-b.

Breakpoints location statistics	$\bar{I}_{px}$	$\sigma_{I_{px}}$
X_{Hmax}	-	A
X_{Hs}	F	-
$X_{H2/3}$	-	B
X_{Hmin}	P	C

5.3.3 Breakpoints from pixel intensity

Further analysis focused on the relations of point F against X_{Hs} and point P against X_{Hmin}, both found on $\bar{I}_{px}$ profile, as the significant wave height is the most common wave height statistic parameter used for representing wave forcing.

The matching between breakpoint locations and the specific points of $\bar{I}_{px}$ was tested using 94 Timestacks produced over the same profile from Riberia d'Ilhas dataset (Section 3.4). Breakpoint statistics X_{Hs} and X_{Hmin} were calculated for each Timestack, after that all incipient points were marked on images, while points F and P were manually detected on the correspondent $\bar{I}_{px}$ profiles.

Figure 5.4 presents the relation between the specific points, showing the high correlation between X_{Hs} and point F (R^2=0.93) and between X_{Hmin} and point P (R^2=0.99).

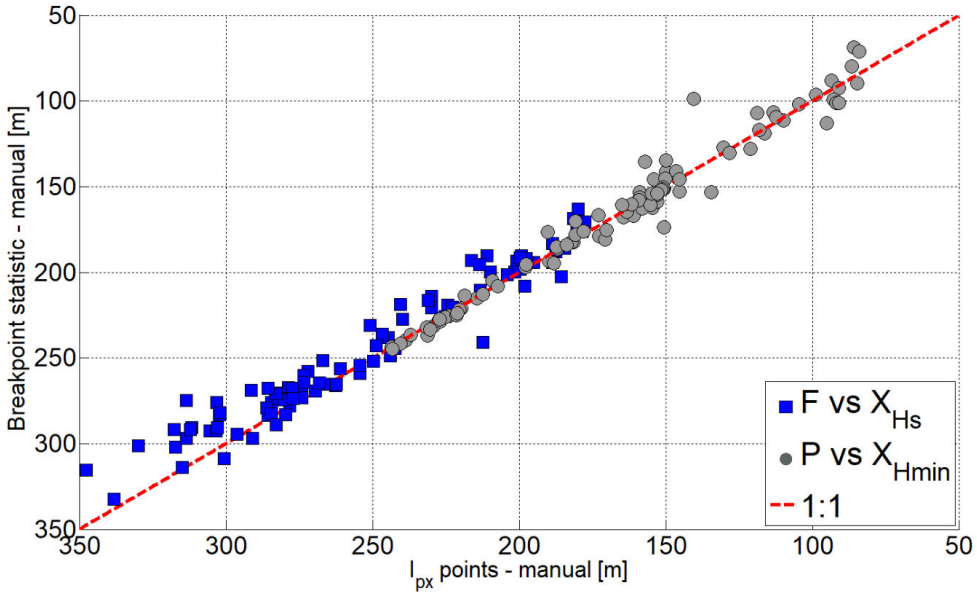

Figure 5.4. Specific point of $\bar{I}_{px}$, namely F and P (refer to Figure 5.3-b) versus breakpoint statistical locations.

As the manual procedure confirmed that X_{Hs} and X_{Hmin} can be also found using $\bar{I}_{px}$ profile, an automated detection algorithm was set to extract F and P points on the 94 $\bar{I}_{px}$ profiles computed over the Timestack dataset. The peak of the Gaussian-like shape (point P) was found using a peak finder algorithm, which searched for the global maximum of the Min-Max normalized $\bar{I}_{px}$.

The first derivative of Min-Max normalized $\bar{I}_{px}$ represented the slope of $\bar{I}_{px}$ at each point. Hence, starting from the seaward limit of Timestacks, the point F was identified as the first point of the derivative exceeding a threshold value of 0.002. This value was found as the median value among interpolation records between X_{Hs} dataset and all the 94 derivatives of $\bar{I}_{px}$ identifying F point.

5.3.4 Conceptual model for breaker height estimation

With the aim of relating the previously noteworthy points found on $\bar{I}_{px}$ profile to wave breaking height, a conceptual model was built from the simple expression that represents the change in elevation and related horizontal space as:

$$m = \frac{\Delta y}{\Delta x} \qquad \textit{Eq. 5.1}$$

where *m* is the slope, Δy and Δx the ratio between the elevation and the horizontal length, respectively. Applying this concept to two wave breaking positions, the expression becomes:

$$m = \frac{h_{b1} - h_{b2}}{L} \qquad \textit{Eq. 5.2}$$

where h_{b1} and h_{b2} are the water depths at the two breaking points, and L the distance between the two breaker locations. Yet, re-writing such simple relation to the case of the positions found through the statistical analysis of the incipient breaking points (Figure 5.5), Eq. 5.2 becomes:

$$m_{Hs} = \frac{h_{b,Hs} - h_{b,Hmin}}{L_{Hs}} \qquad \textit{Eq. 5.3}$$

where m_{Hs} is the average bottom slope under breaking conditions ($m_{Hs} = tan\beta$), $h_{b,Hs}$ is the water depth at breaking under X_{Hs}, $h_{b,Hmin}$ at X_{Hmin}, and L_{Hs} is the distance between the two positions, namely X_{Hs} and X_{Hmin}, which can be expressed as:

$$L_{Hs} = X_{Hs} - X_{Hmin} \qquad \textit{Eq. 5.4}$$

Finally, according to the analysis in the previous section, L_{Hs} can also be found using the specific points F and P identified on $\bar{I}_{px}$ profile, as:

$$L_{Hs} = P - F \qquad \textit{Eq. 5.5}$$

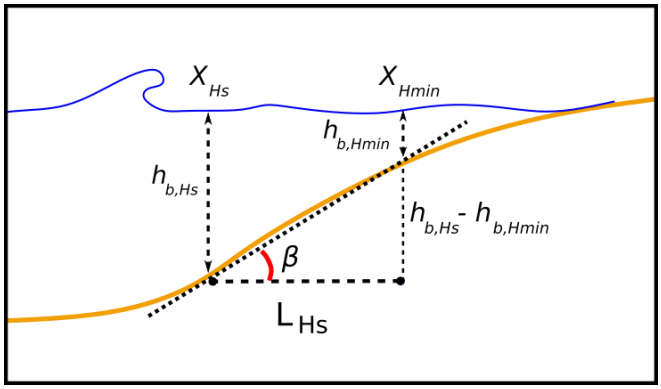

Figure 5.5. Conceptual model sketch. Yellow line represents the sea bottom and blue line the water level.

At this point, we can also re-formulate Eq. 5.3 as:

$$h_{b,Hs} - h_{b,Hmin} = m_{Hs} * L_{Hs} \qquad \textit{Eq. 5.6}$$

and yet, introducing a correction factor δ, $h_{b,Hs}$ can be singularly expressed as:

$$h_{b,Hs} \cong \frac{1}{\delta} * m_{Hs} * L_{Hs} \qquad \textit{Eq. 5.7}$$

where the correction factor δ is:

$$\delta = 1 - \left(\frac{h_{b,Hmin}}{h_{b,Hs}}\right) \qquad \textit{Eq. 5.8}$$

At breaking point, the simplest historical relation between wave height and water depth (McCowan, 1894) is:

$$\frac{H_b}{h_b} = \gamma \qquad \textit{Eq. 5.9}$$

where H_b is the wave breaking height, h_b is the water depth at the breaking, γ is the breaker index. If it is assumed that γ has the same value for both breaker points, Eq. 5.7 becomes:

$$Hs_b \cong \frac{1}{\delta} * m_{Hs} * L_{Hs} * \gamma \qquad \textit{Eq. 5.10}$$

that expresses the wave breaking height as proportional to the ratio between water depths at breaking locations$\left(\frac{1}{\delta} = \frac{h_{b,Hs}}{h_{b,Hs} - h_{b,Hmin}}\right)$, to the distance between the two breakpoints L_{Hs}, to the beach slope m_{Hs} under L_{Hs}, and to the dimensionless γ breaker index.

5.3.5 Video-derived breaking parameters

Hydro- and morpho-dynamic parameters needed for resolving Eq. 5.10 were retrieved from the image analysis.

The distance L_{Hs} was found as the distance between the points P and F (Eq. 5.1), which were retrieved from $\bar{I}_{px}$ profile of Timestacks with the automatic detection algorithm developed for the aim.

Water depths at breaking $h_{b,Hs}$ and $h_{b,Hmin}$ were found interpolating the respective breakpoints statistics positions with the bathymetric profile. Although Eq. 5.10 only contained $h_{b,Hs}$ and $h_{b,Hmin}$, two more water depths, namely $h_{b,Hmax}$ and $h_{b,Hm}$, were additionally found for a comprehensive analysis. Subscript *b* stays for "breaking", while *H* subscript indicates the relative location to breakpoints distribution where the depth was extracted.

The beach slope m_{Hs} under breaking conditions was determined interpolating the limits of length L_{Hs} to the sea bottom profile.

The Iribarren number is the non-dimensional surf similarity, also known as "breaker parameter", that describes the type of breaking wave on beaches (Iribarren and Nogales, 1949; Battjes, 1974). The Iribarren number combines the beach slope (or engineering structure inclination) to wave steepness, and it is given by:

$$\xi \cong \frac{tan\beta}{\sqrt{Ho/Lo}} \qquad \textit{Eq. 5.11}$$

where β is the beach slope, and the ratio H_o/L_o represents wave steepness calculated with offshore wave height H_o and wavelength L_o. Iribarren number (Table 5.2) was calculated in this work using the video-derived m_{Hs} and the offshore wave measured by the buoy (H_o and L_o).

Table 5.2. Breaker type dependence on Iribarren number

Breaker type	***Range***
Surging or collapsing	ξ *>3.3*
Plunging	*0.5<* ξ *<3.3*
Spilling	ξ *<0.5*

5.3.6 Breaker index

The breaker index γ expresses the wave height-to-water depth ratio where the wave breaks, commonly calculated through the simple relation expressed in Eq. 5.9 (e.g., McCowan, 1894; Horikawa, 1988).

Choosing the adequate value for the breaker index to solve Eq. 5.10 is not an easy task. Along with many different single values proposed in literature, also more sophisticated formulas for γ have been suggested introducing as coefficients the bottom slope *m* and the deep-water wave steepness H_o/L_o (e.g., see Camenen and Larson (2007) and Robertson (2013) for a comprehensive resume of formulations). Salmon et al. (2015) discerned among three different breaker indexes, namely γ_{BJ} γ_{TJ} and γ_b, which were respectively found considering H_{max}, H_{rms} and H_{min} by different authors. However, Eq. 5.10 referred to the significant wave breaking height Hs_b, which was not taken in consideration by the previously cited works.

A simplistic solution for encountering breaker index associated to Hs_b was adopted scaling the γ_{BJ} to $\gamma_{b,Hs}$. For the aim, the ratio between wave height statistics found by Kamphuis (2000) was used:

$$H_{0.1} = 1.52 * H_S \qquad \textit{Eq. 5.12}$$

where $H_{0.1}$ is the height exceeded by 1% of the waves, thus close to H_{max}, and H_S the wave significant height.

The simplest $\gamma_{BJ} = 0.73$ proposed by Battjes and Janssen (1978) and adopted by wave breaking model SWAN (Booij et al., 1999) was considered. Consequently, it can be assumed that:

$$\gamma_{BJ} = 1.52 * \gamma_{b,Hs} \qquad \textit{Eq. 5.13}$$

where the subscript *BJ* is referred to Battjes model (Battjes and Janssen, 1978), which used H_{max} (see also Salmon et al., 2015). Thus, it was found $\gamma_{b,Hs} = 0.48$, that was considered as breaker index input in Eq. 5.10.

5.3.7 Wave breaking height model

The SWASH hydrodynamic model was used to simulate wave breaking height over the profile corresponding to the Timestack transect previously used (Section 5.3.1). SWASH (an acronym of Simulating WAves till SHore) is a non-hydrostatic wave-flow model capable to predict transformation wave propagation from offshore to the beach for studying the surf zone and swash zone dynamics (Zijlema et al., 2011).

The model grid was set with a cross-shore grid size of 1 m over the beach profile to reproduce Timestack spatial properties. Initial time step of 0.001 s and time duration of the numerical simulation was 600 seconds were set for run the model. A weak boundary was applied at the wave boundary, and the Sommerfeld radiation condition was set at the end of the numerical domain to minimize the effect of wave reflection.

Numerical simulations on SWASH model were calibrated with the wave significant height measured by the four pressure transducers installed in the surf zone (see Ribeira d'Ilhas experimental set up in Section 3.4). The main efforts were directed to estimate the best Manning coefficient n, which expresses the roughness (or friction) applied to the water flow by the sea bottom surface. The best Manning's value representing the rocky platform was found as n=0.07. The best performing geometric breaking parameters input for the model were found as α_{SWASH}= 0.6 and β_{SWASH}=0.3.

Wave hydrodynamic input were taken from offshore wave buoy measurements (significant wave height H_o and peak period T_p), while water level η was taken from measurements of the most seaward pressure transducer installed in the surf zone.

Significant wave breaking height over the profile was computed as

$$Hs_{b,SWASH} = 4 * std(ws) \qquad \textit{Eq. 5.14}$$

where std(ws) was the standard deviation of the water surface elevation time series resulted from each of the numerical model run.

5.4 Results - I

This section describes the wave breaking height results obtained from the implemented conceptual model.

5.4.1 Automated procedure

Figure 5.6 shows the automatic detection performance in finding the points P and F on $\bar{I}_{px}$, against X_{Hs} and X_{Hmin} locations manually marked on Timestacks. Both P and F positions were accurately extracted ($y \simeq 0.99x$ and $R^2 \simeq 0.97$) by the automated algorithm on $\bar{I}_{px}$ profiles. From these measures, the distance L_{Hs} was calculated using Eq. 5.5.

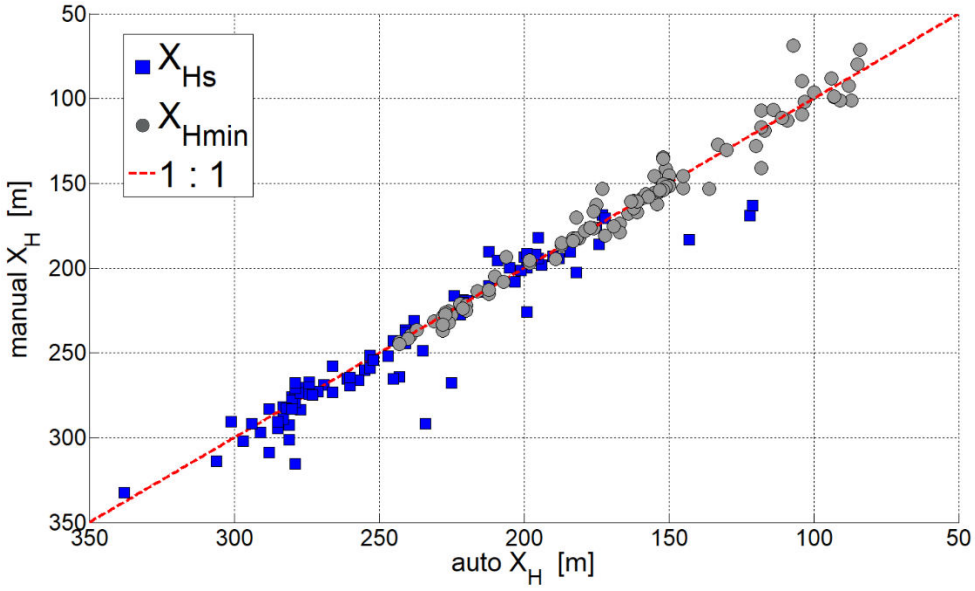

Figure 5.6. Breakpoint locations found by automatic algorithm against breakpoint statistic positions computed from manual procedure.

On day 28th, L_{Hs} varied between 36 m and 100 m, with a mean value of 65 m (Figure 5.7). On day 29th, L_{Hs} length was between 42 m and 170 m, with mean value of 95 m. Note that the leftmost point of L_{Hs} line, corresponding to X_{Hs}, was most of the time seaward the most seaward pressure transducer installed in the nearshore on day 29th. For this reason, wave height values measured by the pressure transducers on day 29th could not be completely associated to wave breaking height.

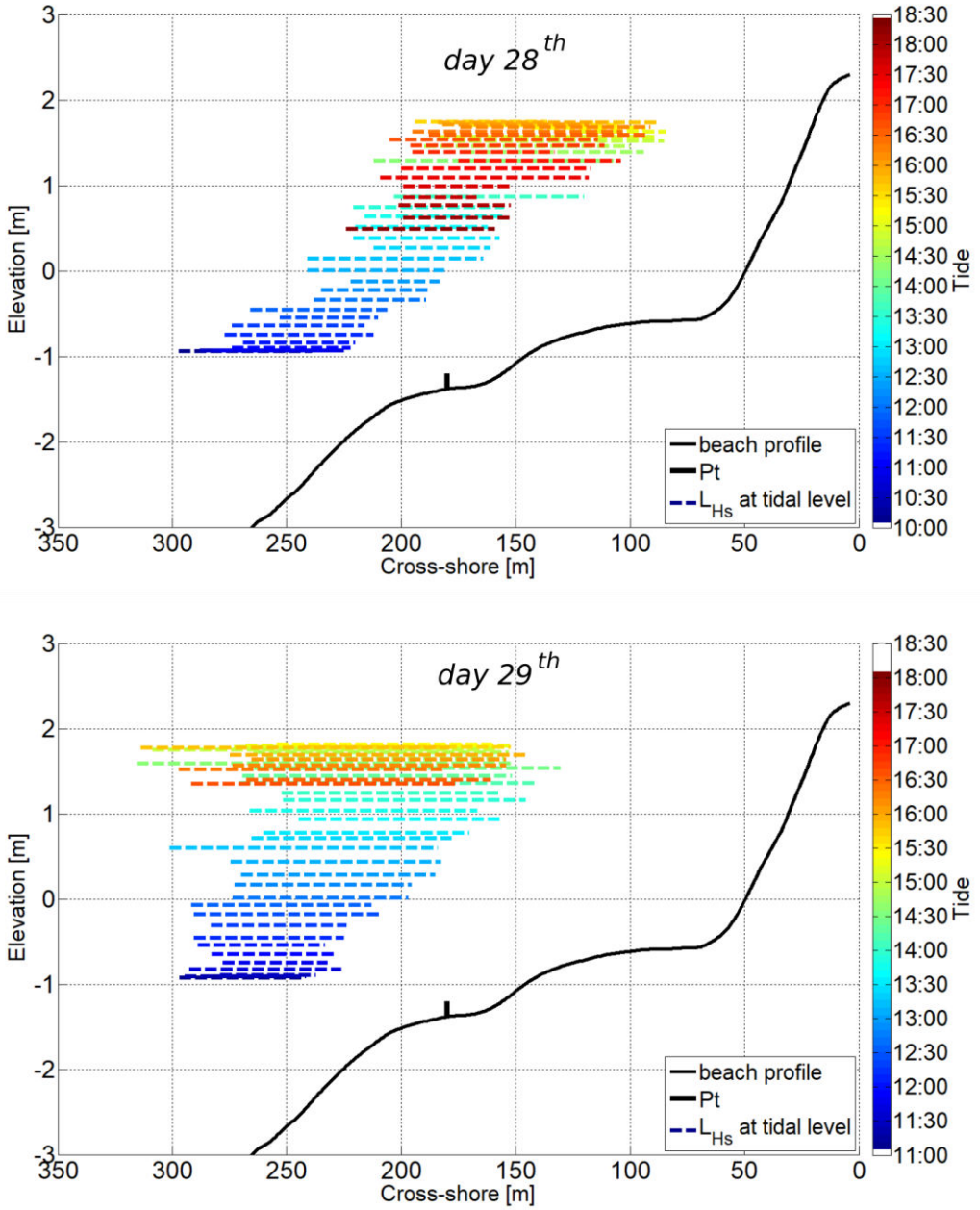

Figure 5.7. Video-derived L_{Hs} (dashed horizontal lines) for each 10-min Timestack plotted over beach profile at the related tidal level. The left border of each line represents the incipient breaking statistical location X_{Hs} , while the rightmost point is X_{Hsmin}. On beach profile (thin black line), black bold line indicates the position of the most seaward pressure transducer installed.

5.4.2 Slope under breaking conditions

The beach gradient under breaking conditions m_{Hs}, found extracting beach profile interval under L_{Hs}, varied between a minimum slope of $m_{Hs} = 0.005$ and a maximum of $m_{Hs} = 0.035$ (Figure 5.8).

Iribarren number (Eq. 5.11) resulted to be low, comprised between values of 0.04 and 0.48, indicating spilling wave breakers ($\xi < 0.55$, Table 5.2). On spilling breakers, the crest spills down the wave face creating foam and turbulent water, as wave fronts travel across the gently-sloped beach. Spilling breakers slowly dissipate their energy since the breaking process last for a longer time than other waves (e.g., Gaughan and Komar, 1975).

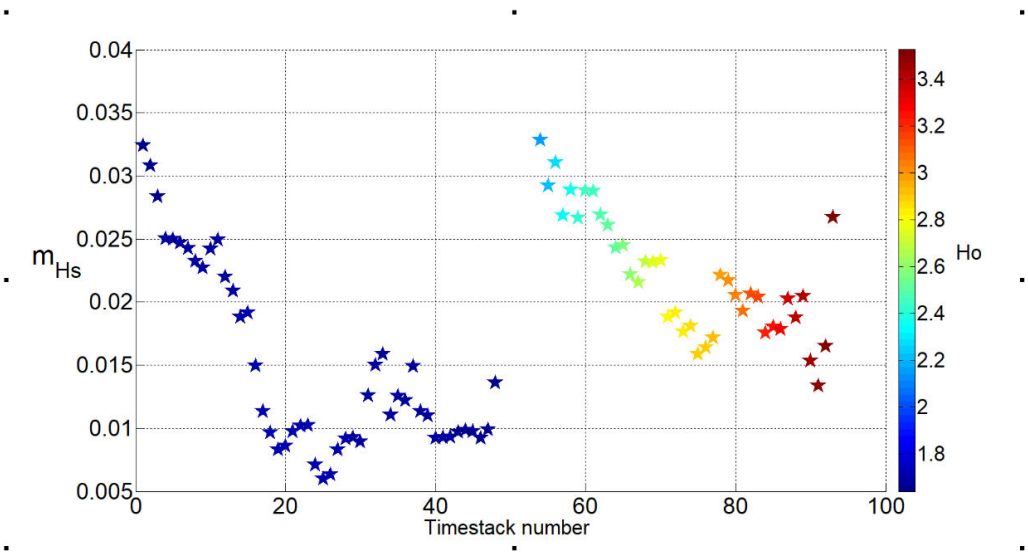

Figure 5.8. Slope under breaking condition varying with 10-min Timestack number (from 1 to 52 for day 28th, from 53 to 94 for day 29th). Colors refer to offshore significant wave height H_o.

5.4.3 Water depth at breakpoints

Figure 5.9 shows the water depths related to the breaking points statistical positions extracted over the two days. Both $h_{b,Hs}$ and $h_{b,Hmin}$ were found with the automatic procedure (Section 5.3.1), while $h_{b,Hmax}$ and $h_{b,Hmean}$ were derived from the first manual analysis (Section 5.3.1) and are shown for a comprehensive analysis. Comparing the results obtained during the two days (Figure 5.9), water depth at breaking increased on second day as much increased offshore wave height, which was almost double higher than on first day.

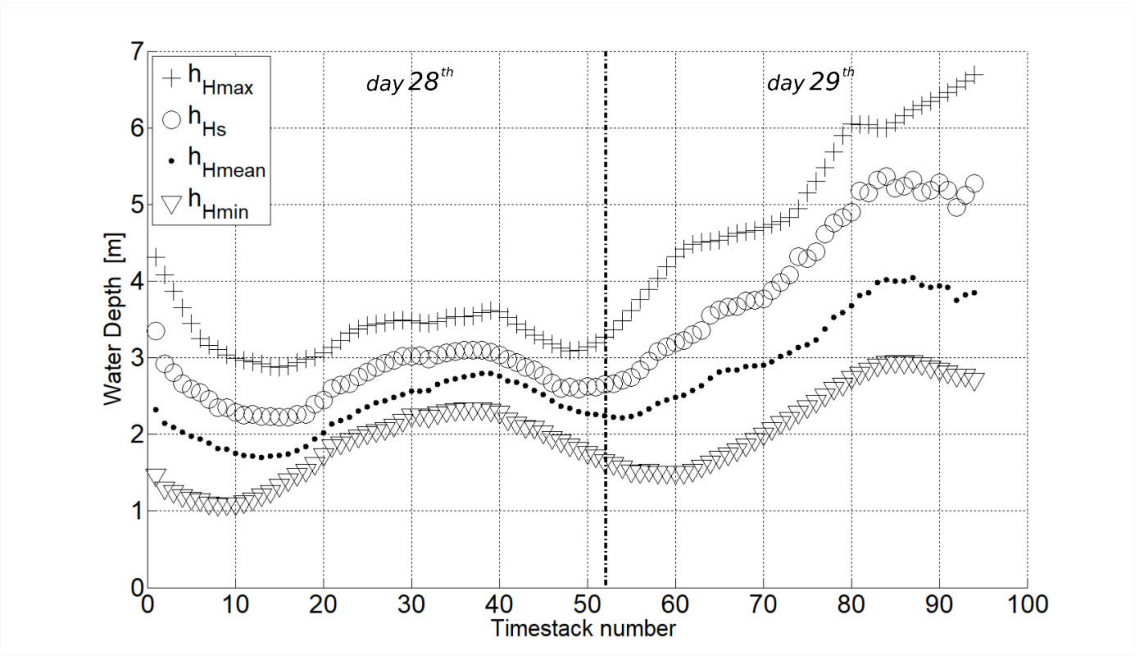

Figure 5.9. Water depth at the different wave breaking statistical positions. Crosses indicate water depth $h_{b,Hmax}$ at H_{max}, circles indicate $h_{b,Hs}$ at H_s, dots are $h_{b,Hmean}$ at H_m , triangles are $h_{b,Hmin}$ at H_{min}. x-axis indicate Timestack number (1 to 52 for day 28th, 53 to 94 for day 29th).

Table 5.3 reports the median values of the ratio between the water depths calculated at the breakpoints statistical positions. The relation $\frac{h_{b,Hmin}}{h_{b,Hs}}$ was found = 0.57, and was used to calculate the correction factor δ $(= 1 - \left(\frac{h_{b,Hmin}}{h_{b,Hs}}\right)$; Eq. 5.8) and thus to resolve Eq. 5.10.

Interestingly, the ratio between one position and the following one towards the shoreline was found almost constant for the slope range considered, as:

$$\frac{h_{b,Hmax}}{h_{b,Hs}} \cong \frac{h_{b,Hs}}{h_{b,Hmean}} \cong \frac{h_{b,Hmean}}{h_{b,Hmin}} \qquad \textit{Eq. 5.15}$$

Finally, $h_{b,Hmax}$ was found being double higher than $h_{b,Hmin}$, while $h_{b,Hs}$ was around the 80% $h_{b,Hmax}$.

Table 5.3. Matrix of ratios between water depths. The ratio is intented as value in the first column divided for the water depth at first row for values upper the matrix diagonal, vice-versa for the values under the matrix diagonal.

0 < mHs < 0.03	$h_{b,Hmax}$	$h_{b,Hs}$	$h_{b,Hmean}$	$h_{b,Hmin}$
$h_{b,Hmax}$		*1.27*	*1.56*	*2.04*
$h_{b,Hs}$	*0.78*		*1.24*	*1.67*
$h_{b,Hmean}$	*0.64*	*0.8*		*1.33*
$h_{b,Hmin}$	*0.46*	*0.57*	*0.74*	

A third analysis regarded the relationships between offshore significant height H_o and water depth at breaking. Table 5.4 reports the indexes found by a regression fitting y = ax, showing how the ratio increased as the breakpoints moved towards the shoreline.

Table 5.4. Ratio between offshore significant wave height H_O and water depth h at different statistical locations. Data are divided based on beach slope m_{Hs}. R^2 is the goodness of fit of linear regression y=ax.

	$H_o/h_{b,Hmax}$		$H_o/h_{b,Hs}$		$H_o/h_{b,Hmean}$		$H_o/h_{b,Hmin}$	
		R^2		R^2		R^2		R^2
$0 < m_{Hs} < 0.03$	*0.53*	*0.66*	*0.66*	*0.67*	*0.82*	*0.55*	*1.09*	*0.05*
$0.015 < m_{Hs} < 0.03$	*0.54*	*0.54*	*0.70*	*0.76*	*0.90*	*0.76*	*1.26*	*0.46*

It is of interest to note that excluding the data for lower slope than 0.015, the ratio H_o/h_b increased as much as considering water depths closer to the shore, where beach gradient was lower. This confirmed the sensitivity of ratio H_o/h_b to the beach slope, therefore higher values of H_o/h_b are expected for steeper beach gradients.

Regarding the ratio $H_o/h_{b,Hmax}$, value found was consistent with criteria derived from experimental wave flume experiment by Yao et al. (2013), that described spilling breaker occurring when $0.55 < H_o/h_{b,Hmax} < 0.35$.

5.4.4 Wave breaking height assessment from conceptual model

Wave significant breaking height $Hs_b$was computed for the 94 Timestacks produced over 2 days, resolving Eq. 5.10 with automatically video-derived parameters, namely the length L_{Hs}, the ratio $h_{b,Hs}/h_{b,Hmin}$, the beach slope m_{Hs} and the considered breaker index $\gamma_{b,Hs}$.

The consistency of the conceptual model to measure Hs_b is shown in Figure 5.10, where results from video imagery are shown against SWASH model output at X_{Hs} location.

Figure 5.10 shows also that SWASH model output well matched the wave significant height measured from the pressure transducer, therefore the model results represented a proper comparison to validate video-derived estimation of Hs_b.

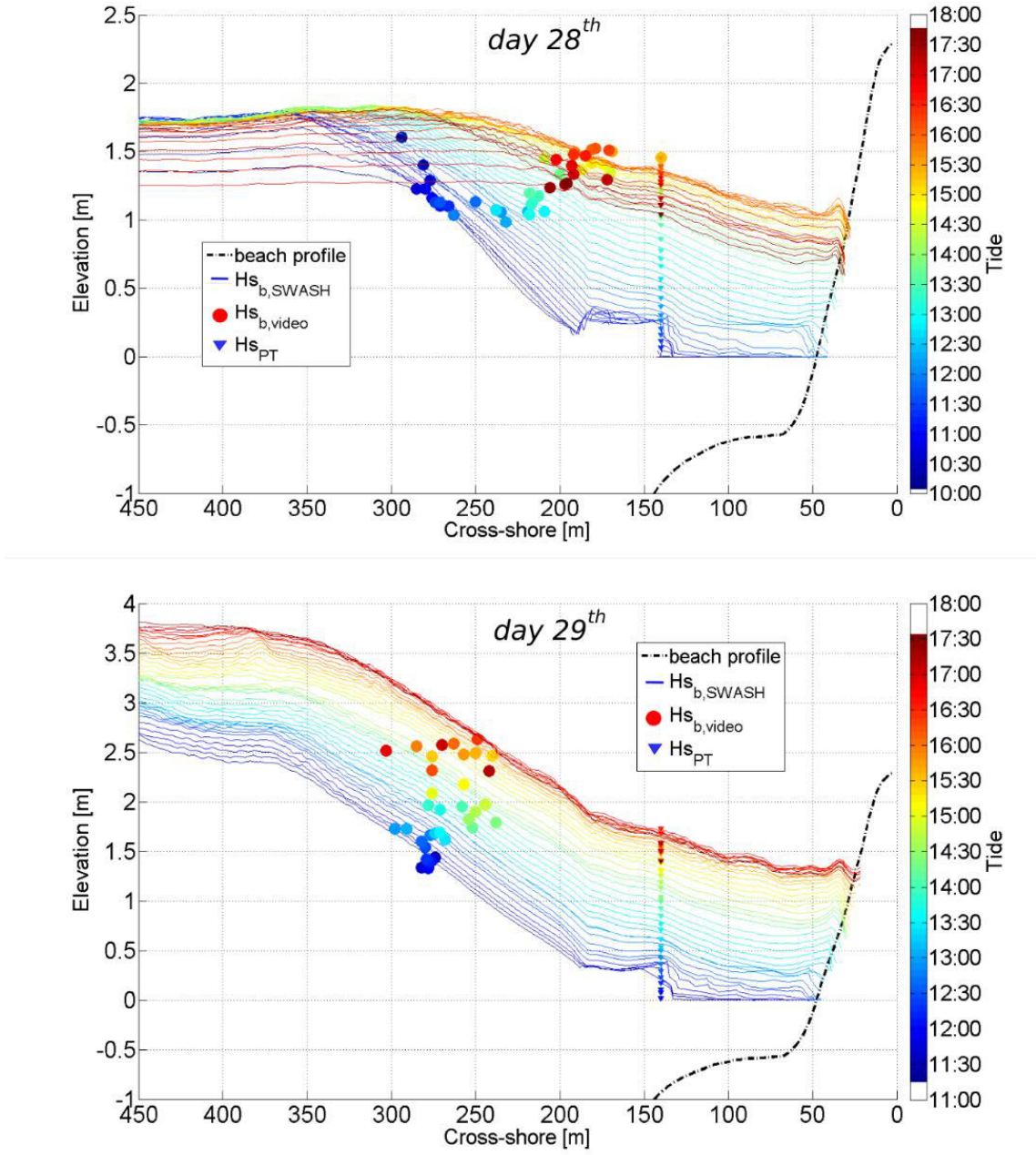

Figure 5.10. $Hs_{b,video}$(filled circles), plotted at the related X_{Hs}, against $Hs_{b,SWASH}$ (colored lines). Triangles column around x=148 m shows the wave significant height measured by the most seaward pressure transducer. Colors refer to tidal level.

In order to quantify the accuracy of the video-derived results, $Hs_{b,video}$ was compared to $Hs_{b,SWASH}$ extracted at X_{Hs}. The overall RMSE was 0.29 m, higher on day 29th and smaller on day 28th. (Table 5.5). Modeled $Hs_{b,SWASH}$ varied between 1 m and a maximum

of 3.3 m, hence Normalized Root Mean Square Error (NRMSE) of video-derived Hs_b was between 10% and 16% of the measures, respectively.

Table 5.5. Disparities between $Hs_{b,video}$ and $Hs_{b,SWASH}$.

	Median	***MSE***	***RMSE***	***NRMSE***
28th (52 values)	*0.04 m*	*0.02 m*	*0.16 m*	*10%*
29th (42 values)	*0.2 m*	*0.14 m*	*0.38 m*	*16%*
dataset (94 values)	*0.14 m*	*0.08 m*	*0.29 m*	*14%*

Achievements of the proposed method were quite satisfactory, considering the many variables involved in the process of breaking.

Figure 5.11 shows the best fitting line between results and modelled wave height (y=1.09 x, R^2 = 0.8). The slight disparities between video-derived and target values obtained by SWASH model might depend likely exclusively on the sensitivity of the formulation (Eq. 5.10) to the breaker index.

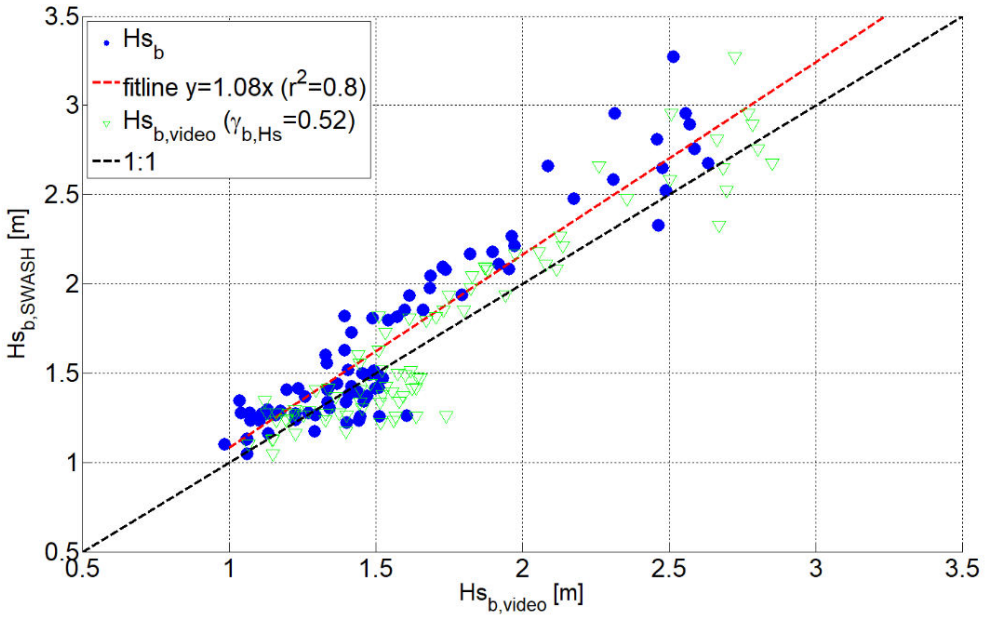

Figure 5.11. Results of $Hs_{b,video}$ against $Hs_{b,SWASH}$ (blue circles) and best fitting line (dashed red). Black dashed line is the identity line. Green triangles represent data obtained imposing best fitting, which was obtained with breaker index $\gamma_{b,Hs}$=0.52

The best fitting line between the two different Hs_b data was searched making varying $\gamma_{b,Hs}$ in Eq. 5.10. The best matching was found for $\gamma_{b,Hs}$= 0.52, close to $\gamma_{b,Hs}$=0.48 previously computed from the scaling approach. The RMSE generated using $\gamma_{b,Hs}$=0.52 (green triangles in Figure 5.11) was of 0.26 m, slightly smaller than the error obtained by the method (RMSE=0.29 m, see Table 5.5). However, this analysis intended to show the high sensitivity of $Hs_{b,video}$ to the breaker index value.

It is worth to note that the same value of $\gamma_{b,Hs}$=0.52 would also be obtained resolving the small amplitude wave theory (Eq. 7 in Kamphuis, 1991) using γ_{BJ} = 0.73.

The satisfactory results confirmed the necessity of scaling and adapting the breaker index γ_{BJ} to significant wave height parameter, and the goodness of the approach (Section 5.3.6) considered for such purpose.

5.4.5 Breaker index

In order to further investigate the ideal breaker index values and providing new insights of wave breaker index for Hs_b, Figure 5.12 shows the γ_b values that were computed interpolating SWASH model wave height with video-derived water depths.

The ratio $H_{max\,b,SWASH}/h_{b,Hmax}$ was used to find $\gamma_{b,max}$, which exactly matched γ_{BJ} = 0.73. The ratio $H_{mean\,b,SWASH}/h_{b,Hmean}$ was computed to be through and led to $\gamma_{b,Hmean}$=0.37.

Finally, the median value for $\gamma_{b,Hs}$ was found equal to 0.55, higher than the adopted $\gamma_{b,Hs}$=0.48. Therefore, further investigation should focus on the determination of the correct breaker index value to obtain more precise wave breaking height measurements.

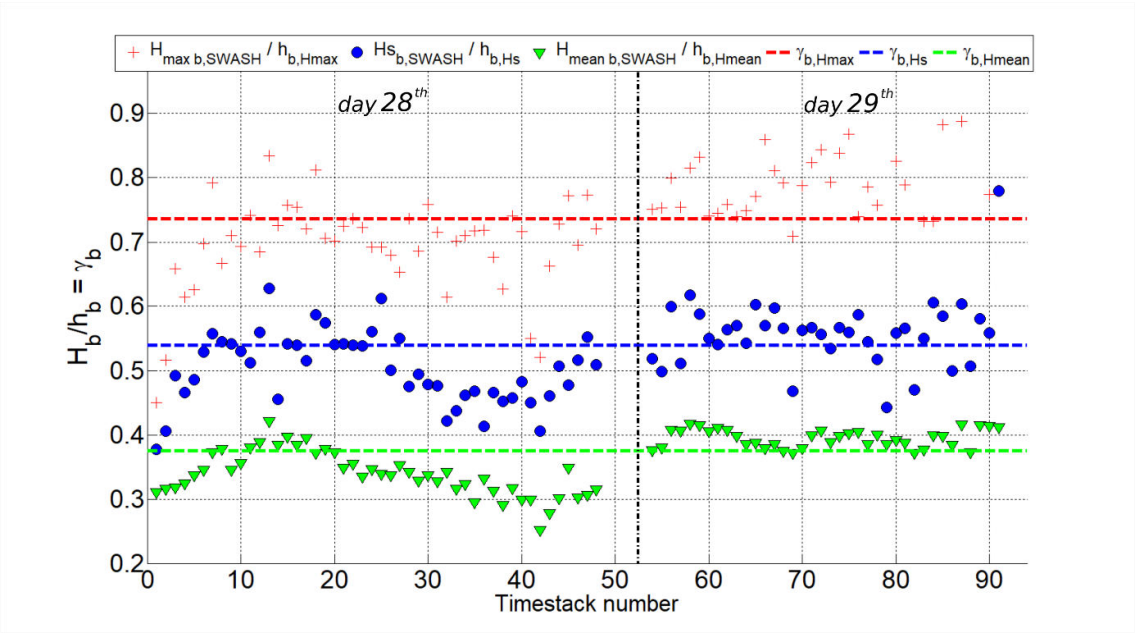

Figure 5.12. Breaker index found using SWASH results and video-derived water depths. Dashed lines represent respective median values. X-axis refers to 10-min Timestack number (1 to 52 for day 28th, 53 to 94 for day 29th).

5.5 Methods - II

The solution of the conceptual model (Eq. 5.10) presented in Section 5.3.4 implied the knowledge of beach bathymetry for deriving beach slope and water depth at breaking. Bathymetric profile is not always available, especially in the breaker zone where waves, low water column and high sediment dynamics make difficult the sea bottom survey of the area.

An empirical relation between wave breaking height and breaking pattern visible on video imagery would be an interesting solution to overcome such a need of bathymetric profile.

5.5.1 L_{Hs} versus hydrodynamic parameters

With the purpose of investigating if video-derived L_{Hs} can be singularly used to estimate wave breaking height, Figure 5.13 compares the trend of L_{Hs} to hydrodynamic and morphological parameters during tidal modulation.

A first observation suggested a likely relationship between offshore significant wave height H_o and L_{Hs} (Figure 5.13). On day 28th, when wave height remained constant over the time, L_{Hs} length increased and decreased following tidal elevation. Nevertheless, on day 29th, L_{Hs} had double length than on the first day, in response to higher H_o. Overall, L_{Hs} appeared to be positively correlated to offshore wave significant height, since L_{Hs} were almost double on day 29th than on day 28th, when waves were smaller.

The water depth at breaking $h_{b,Hs}$ and wave breaking pattern L_{Hs} had the same tendency over the dataset. As seen before (Eq. 5.9 in Section 5.3.4), water depth was historically one of the hydraulic parameter to be directly related to wave breaking height (McCowan, 1894).

The slope m_{Hs} under L_{Hs} significantly changed over the time, as water level increased and breaking location moved towards the shore (as seen in Figure 5.7). The slope m_{Hs} had an opposite trend of L_{Hs}, with steeper slope corresponding to shorter L_{Hs}. Slope decreased when the breakpoints were closer to the shoreline, since the slope gets milder. Therefore, more dissipative conditions conformed with longer L_{Hs}.

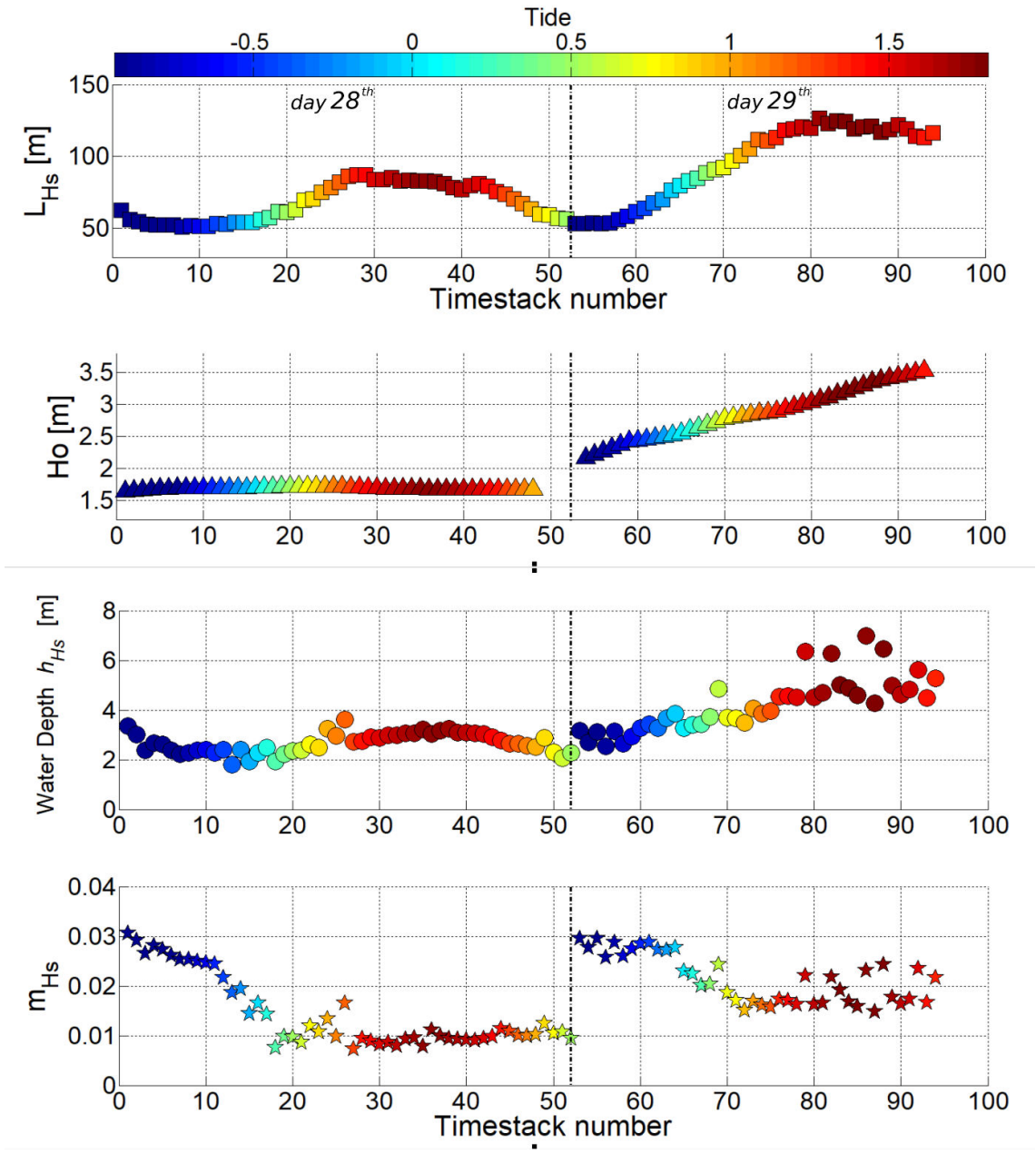

Figure 5.13. L_{Hs} records (squares) versus offshore significant wave height H_o (triangles), water depth $h_{b,Hs}$ (circles) and beach slope m_{Hs} (pentagrams). Vertical black dashed line divides data from day 28th (left) and day 29th (right).

All above observations were supported by the computation of Pearson correlation (Figure 5.14), which expresses the linear correlation between L_{Hs} and the several variables tested.

As noted before in this section, L_{Hs} was found positively correlated to H_o and water depth $h_{b,Hs}$, whereas negatively correlated to beach slope and consequently to Iribarren number.

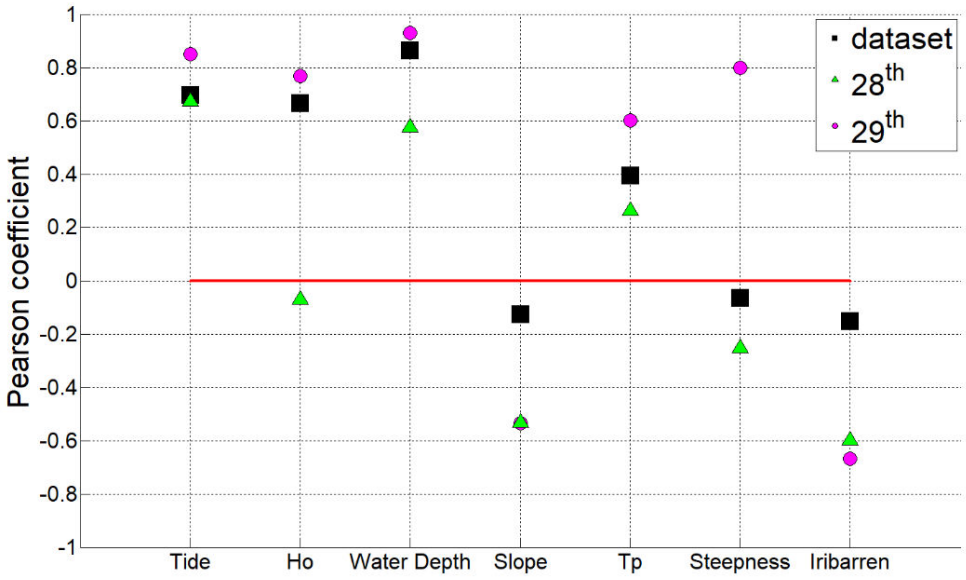

Figure 5.14. Pearson correlation of L_{Hs}. Magenta circles indicate values from day 28th, green triangles values from day 29th, black squares the results obtained considering the whole dataset.

As the highest positive correlation was registered between L_{Hs} and $h_{b,Hs}$, the direct relation between video-derived wave breaking pattern L_{Hs} and hydrodynamic parameter $h_{b,Hs}$ will be analysed in the following section.

5.5.2 L_{Hs} and water depth

Figure 5.15 shows a direct comparison between L_{Hs} and water depth $h_{b,Hs}$ extracted at the X_{Hs} over the two days.

The best fitting value for the ratio $L_{Hs}/h_{b,Hs}$ was found as:

$$\frac{L_{Hs}}{h_{b,Hs}} \cong 24 \qquad \textit{Eq. 5.16}$$

with a $R^2 = 0.75$ and slope coefficient of 95% confidence bounds between values 23 and 25. Results suggest that the video-derived breaking pattern length L_{Hs} can be strongly related to water depth at breaking statistic location X_{Hs}.

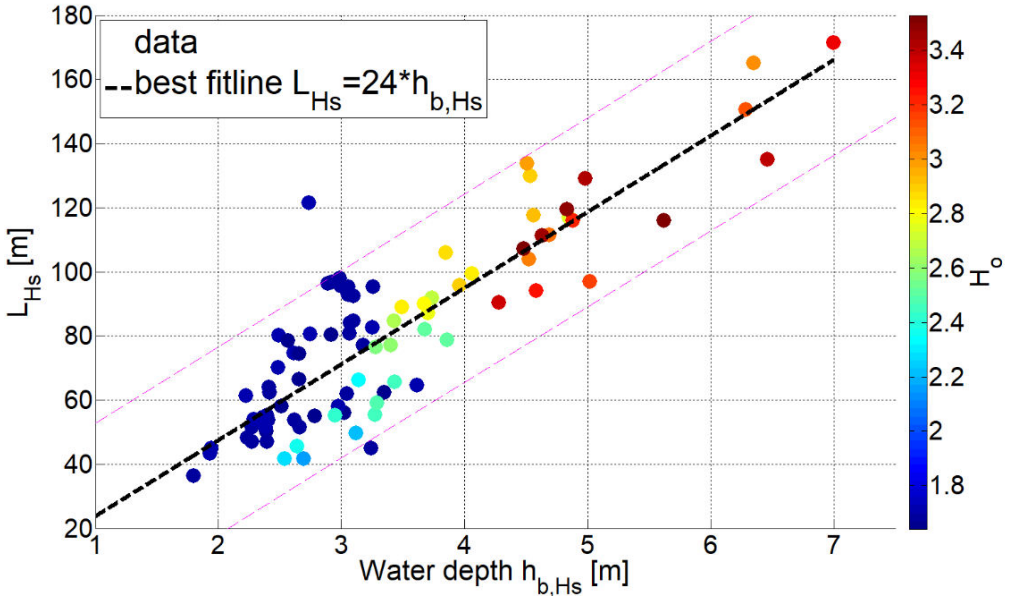

Figure 5.15. L_{Hs} versus water depth $h_{b,Hs}$. Black dashed line indicates the best fitting y=ax. Dashed magenta lines represent upper and lower 95% prediction bounds.

The parameterization in Eq. 5.16 is interesting in the perspective that water depth at breaking is also considered in most of wave breaking height empirical formulations (e.g., Camenen and Larson, 2007; Robertson, 2013). As the analysis shows that video-derived L_{Hs} might overcome the requirement of bathymetry for empirical wave breaking height estimation, following Eq. 5.16, the simplest formulas for wave breaking height:

$$\frac{Hs_b}{h_{b,Hs}} = \gamma_{b,Hs} \qquad \textit{Eq. 5.17}$$

can be re-written as

$$\frac{Hs_b}{L_{Hs}\,/\,24} = \gamma_{b,Hs} \qquad \textit{Eq. 5.18}$$

where Hs_b is calculated from video-derived parameter L_{Hs} and the breaker index $\gamma_{b,Hs}$.

Following the new findings, Hs_b was re-computed using L_{Hs} automatically derived from video imagery dataset (see Section 5.4.1) and choosing the best value of $\gamma_{b,Hs}$ found on Section 5.4.5 ($\gamma_{b,Hs} = 0.55$), as:

$$Hs_b = \frac{L_{Hs}}{24} * 0.55 \qquad \textit{Eq. 5.19}$$

5.6 Results - II

5.6.1 L_{Hs} for wave breaking height

The new results of Hs_b are plotted in Figure 5.16 against the SWASH model output, which were already presented in Figure 5.10 and in Figure 5.11.

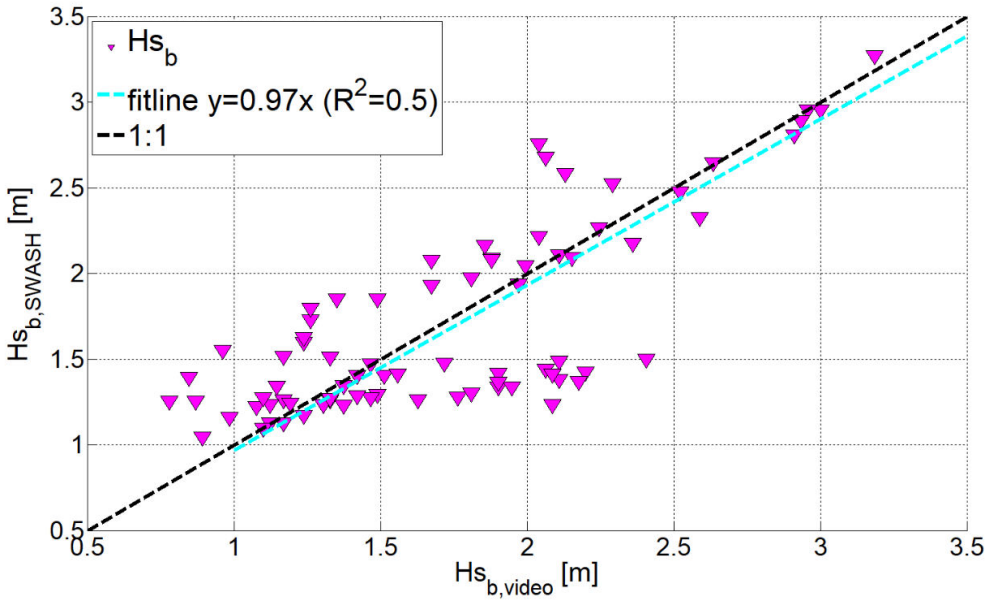

Figure 5.16. Video-derived significant wave breaking height $Hs_{b,video}$ computed as $\frac{L_{Hs}}{24} * 0.55$, versus modelled $Hs_{b,SWASH}$. Black dashed line is the identity line. Cyan dashed line is best fitting line for y=ax.

For wave breaking heights lower than 1.5 m, the results were spurious in relation to the identity line. These disparities were likely due to the fact that smallest waves broke over an almost planar beach slope, suggesting that Eq. 5.19 was too simplistic and should include beach gradient parameter as Eq. 5.10 did.

A second source of error might be associated to the stationary offshore wave conditions. As in the new formulation L_{Hs} is directly related to wave height, the relation $L_{Hs}/24$ varied exclusively with the tidal elevation when wave height was constant. This generated uncertainties and spurious data, which nevertheless might be reduced and corrected with a moving average window.

Table 5.6. Disparities between $Hs_{b,video}$ and $Hs_{b,SWASH}$.

	Median	***MSE***	***RMSE***	***NRMSE***
28th (52 values)	*-0.07 m*	*0.16 m*	*0.4 m*	*23%*
29th (42 values)	*0.19 m*	*0.17 m*	*0.41 m*	*19%*
dataset (94 values)	*-0.01 m*	*0.16 m*	*0.4 m*	*23%*

Considering the whole dataset, a total RMSE=0.40 m was obtained by the new $Hs_{b,video}$ computation (Table 5.6), a higher value than the RMSE obtained by the first proposed methodology presented in Section 5.4.4 (RMSE=0.29 m, Table 5.5). Despite the lower accuracy of this second method, the new $Hs_{b,video}$ was found exclusively from the video-derived wave breaking pattern L_{Hs}, without any additional information about bathymetry.

5.6.2 Surf zone bathymetry estimation from L_{Hs}

Since it was found that L_{Hs} can be related to the water column at the breaking point, an attempt was made to estimate the sea bottom bathymetry under the wave breakpoints.

Figure 5.17 shows the points inferred under X_{Hs} location, using the water column elevation assumed to be equal to $L_{Hs}/24$ and corrected with tidal elevation corresponding in time.

Even though bathymetry uncertainties were high over low slope profile < 0.05, steeper sectors and deeper bottom height of the beach profile were adequately described, indicating that the relation $L_{Hs}/24$ might be also used as a rough estimation of surf zone bathymetry.

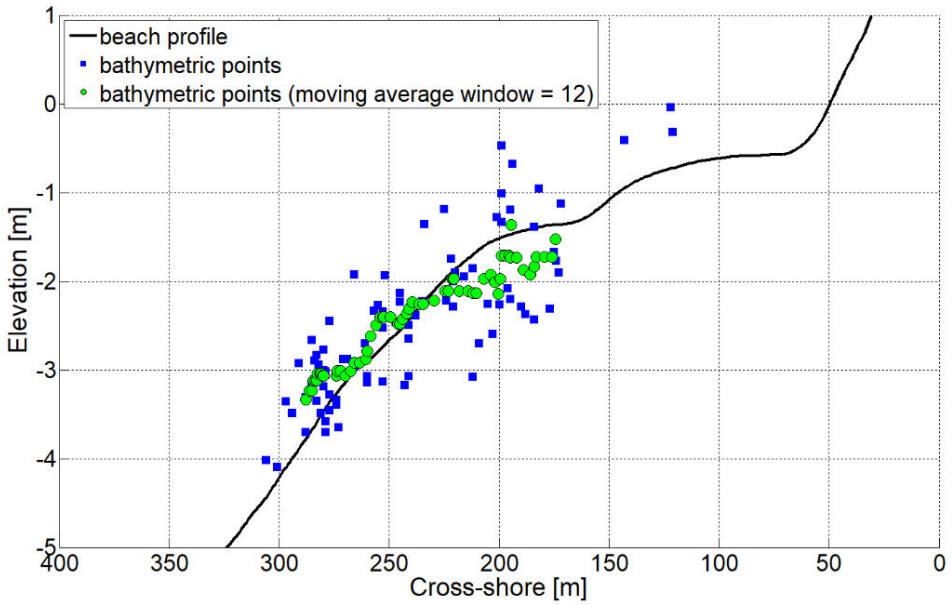

Figure 5.17. Attempt of deriving surf-zone bathymetry using $L_{Hs}/24$. Blue squares are obtained after tidal correction. Green circles are averaged data. Black line represents the beach profile.

5.6.3 L_{Hs} from Timex – Application to study sites

At this point, it was proved that the wave breaking pattern L_{Hs} , automatically found from profile $\bar{I}_{px}$ (Section 5.3.2), could be used to measure wave breaking height Hs_b and, additionally, for a rough estimation of beach profile under breaking conditions.

The $\bar{I}_{px}$ profile was previously computed on Timestack, as average of pixel intensity brightness over image. As Timex images are produced averaging the pixel intensity of the whole image (Section 2.4.1), extracting on this image the pixels along the same transect used to generate Timestack gives the same $\bar{I}_{px}$ profile obtained from time-space image (Figure 5.18). Therefore, L_{Hs} can be directly found from Timex.

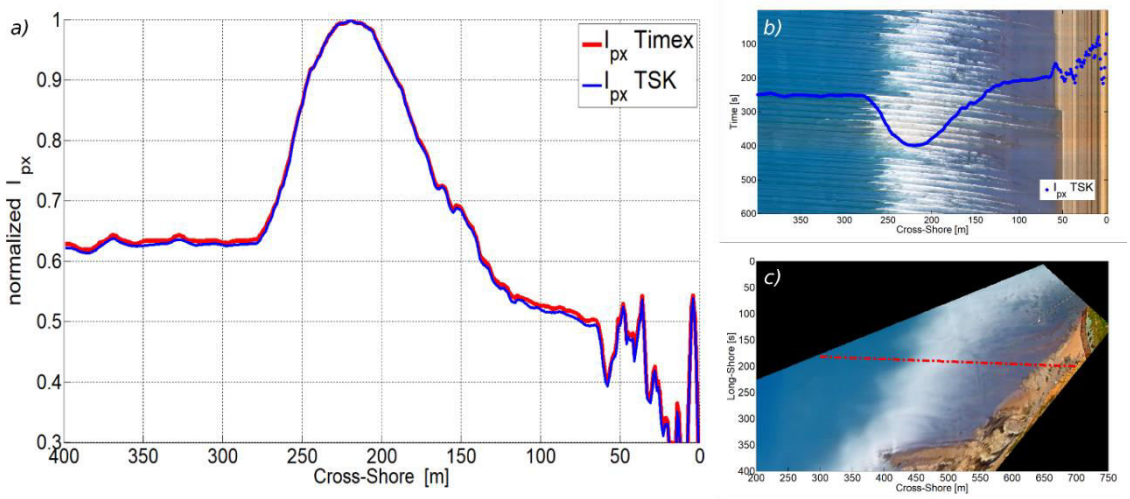

Figure 5.18. Identity between profiles $\bar{I}_{px}$ (a) extracted from the Timestack (b) and from the Timex (c) using the transect chosen to produce Timestack (dashed red line)

With the aim of testing and validating the method for different beach slopes and various wave characteristics, cross-shore $\bar{I}_{px}$ profile was extracted from Timex produced from video imagery collected at three additional study sites, namely Praia Grande (Section 3.2), Costa da Caparica (Section 3.3) and Kourou (Section 3.5) beaches.

The wave breaking height was computed using the relation:

$$Hs_b = \frac{L_{Hs}}{24} * \gamma_{b,Hs} \qquad \text{Eq. 5.20}$$

where L_{Hs} was computed by the algorithm for a fully automatic procedure (Section 5.3.3), and breaker index $\gamma_{b,Hs}$= 0.55 was used.

5.6.4 Wave breaking height at Praia Grande

Timex produced at Praia Grande beach (Section 3.2) from 7 hours video acquisition were used to measure wave breaking height at the shore.

Automatic detection was applied to one transect sampled from rectified Timex and coinciding with one surveyed beach profile to find L_{Hs} and m_{Hs} under breaking conditions (Figure 5.19).

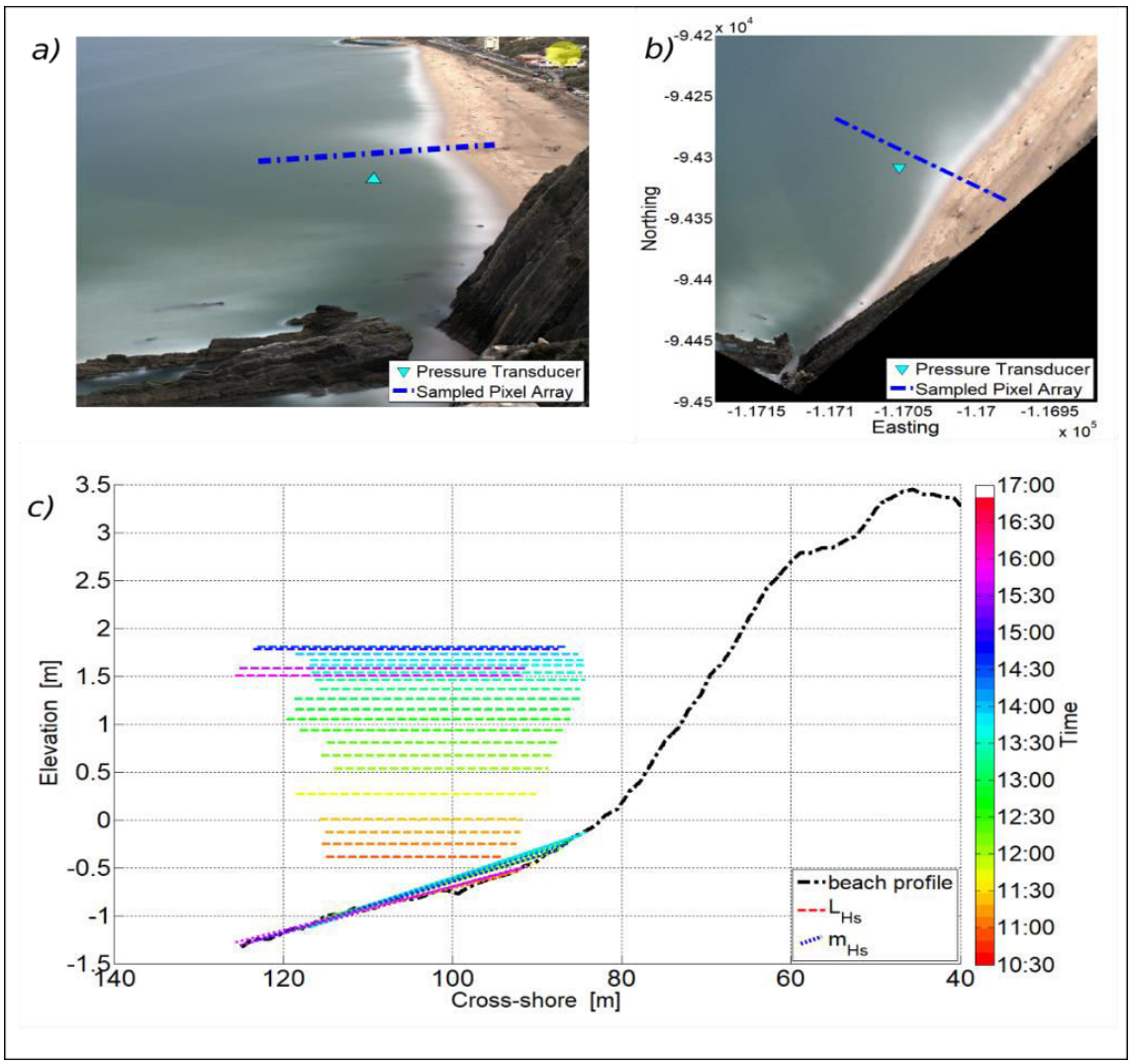

Figure 5.19. Cross-shore profile used for sampling $\bar{I}_{px}$ indicated on oblique (a) and rectified (b) Timex. c) Results of L_{Hs} (dashed horizontal colored lines) plotted at the corresponding tidal elevation, and m_{Hs} obtained from interpolation with beach profile (dashed colored oblique lines).

Along with $\gamma_{b,Hs}$= 0.55, a second value for the breaker index was iteratively found using the relation proposed by Madsen et al. (1976):

$$\gamma_{BJ} = 0.72 * (1 + 6.4 * tan\beta) \qquad \textit{Eq. 5.21}$$

where tanβ is the beach slope m_{Hs} computed for each Timex using the breakpoints positions under L_{Hs} and the beach profile surveyed (Figure 5.19-c). The breaker index γ_{BJ} was scaled following Eq. 5.13 to compute $\gamma_{b,Hs}$ as:

$$\gamma_{b,Hs} = 0.658 * \gamma_{BJ} \qquad \textit{Eq. 5.22}$$

where γ_{BJ}=0.73.

Figure 5.20 resumes the wave breaking height obtained from Timex analysis compared to the pressure transducer placed in the surf zone (Section 3.2.2). Wave breaking height was in general well estimated, except for few intervals in which values were overestimated.

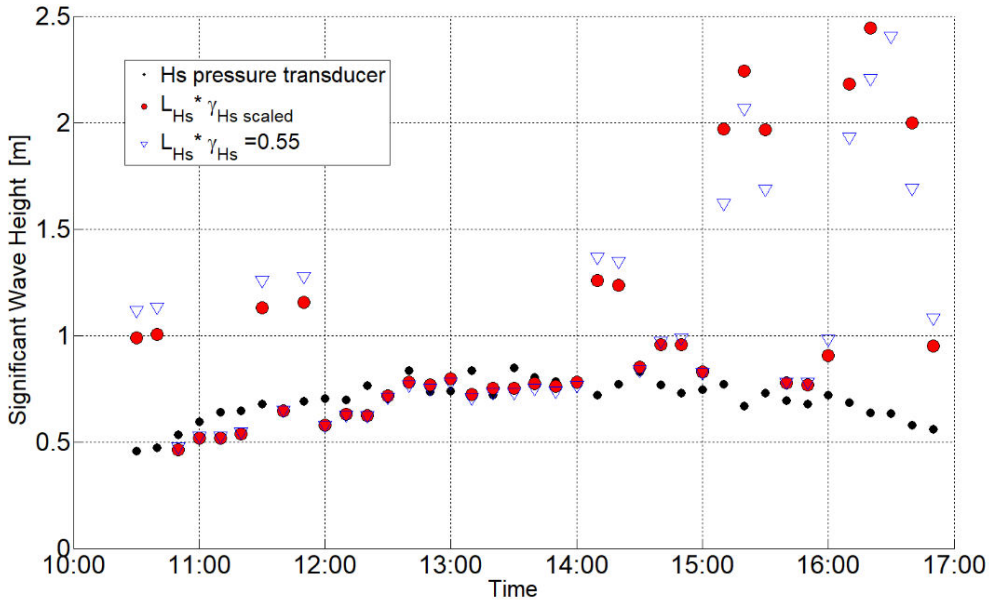

Figure 5.20. Significant wave breaking height $Hs_{b,video}$ obtained at Praia Grande (red circles and blue empty triangles) versus significant wave height measured by the pressure transducer placed in the surf zone (black dots). Hs_b was computing using Eq. 5.20 and different γ_{Hs}

One source of errors was related to images quality. Some of the images resulted superimposed during the hours in which sun brightness was more intense. Pixel intensity

variation was anomalous due to a wrong camera brightness set-up. This occurred in the case in which wave height was estimated higher than 1.5 m (Figure 5.20).

A second source of error might be associated with the pixel array sampling methodology, together with the specific wave hydrodynamic conditions on the shore at Praia Grande beach. The developed technique sampled the pixels array on a perpendicular transect to shoreline and breaker pattern line, while wave breaking was sometimes influenced by the presence of a rip current on the shore and visible on Timex (Figure 5.19) at Praia Grande beach. Consequently, L_{Hs} became longer and wave breaking height higher (in Figure 5.20, wave height estimation between 1 m and 1.5 m).

The breaker index determination was also satisfactory, considering the sensitivity of the equation to this parameter. Beach slope m_{Hs} varied between 0.02 and 0.03, and $\gamma_{b,Hs}$ values calculated from Eq. 5.22 were close to the value of 0.55 previously used for Ribeira d'Ilhas (Section 5.4.5).

5.6.5 Wave breaking height at Costa da Caparica

The Timex dataset collected at Costa da Caparica (Section 3.3) was used to test the methodology on a barred sandy beach over relative extended period and large variability of sea state conditions. From ten days of video observations, a total amount of 654 Timex images was considered, 66 images for each day.

A single cross-shore profile, spanning between the emerged beach and a position located about 650 m offshore, was sampled over rectified Timex dataset (Figure 5.21-c) to retrieve $\bar{I}_{px}$ profile. Wave breaking height Hs_b was computed solving Eq. 5.20, with L_{Hs} extracted from $\bar{I}_{px}$ by the fully automatic algorithm and the breaker index $\gamma_{b,Hs} = 0.55$.

Video-derived Hs_b was compared to three different wave data (Figure 5.21-a):

- measurements from a buoy deployed by the Portuguese Hydrographic Institute offshore Sines at a depth of 95 m;
- the Water Information Forecast Framework (WIFF) hindcast model developed by the Portuguese National Laboratory of Engineering (LNEC);
- hindcast model for the Iberian Peninsula (SIMAR - www.puertos.es).

For detailed descriptions of the wave data sources, refer to Section 3.3.3.

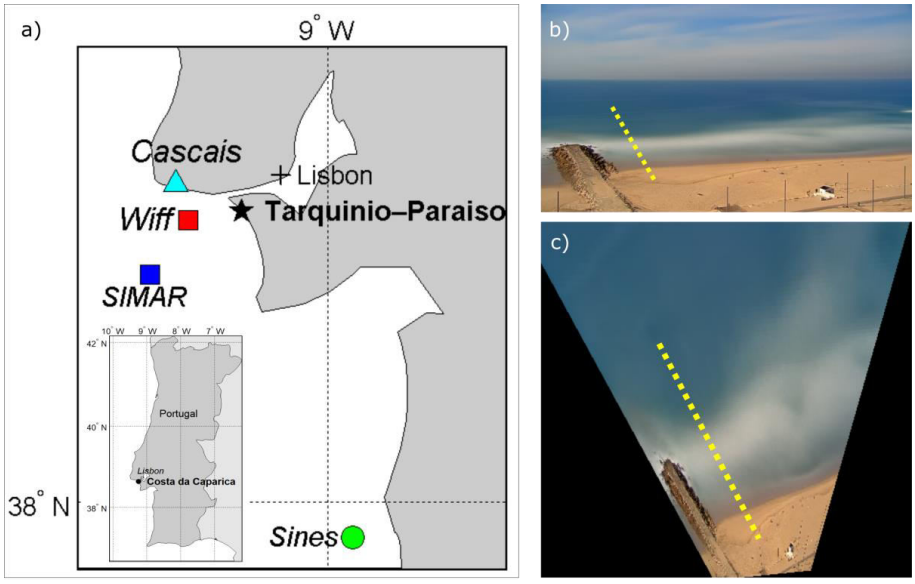

Figure 5.21. a) map of wave data sources. Hindcast models point grid (squares) and buoy (circle).Cyan triangle shows wave gauge for tide data, black star the study site location. b) oblique Timex; c) rectified Timex. Yellow dashed line represents the cross-shore transect used to sample $\bar{I}_{px}$ profile.

Figure 5.22 shows the assessed wave breaking height Hs_b against the three sources wave height timeseries. The trend of Hs_b followed the trend of buoy and hindcast models data.

The values of Hs_b were closer to the WIFF models output, since the grid point was nearer the shore than the other two wave datasets points. Nevertheless, wave model data described unbroken nearshore waves, whereas video-derived results represented wave at the break point and within the surf zone. As wave height at breaking is influenced by currents, sea bottom variation, local wind and tide (e.g., Dean and Dalrymple, 1984), a direct comparison between offshore wave height and breaking height values was not possible.

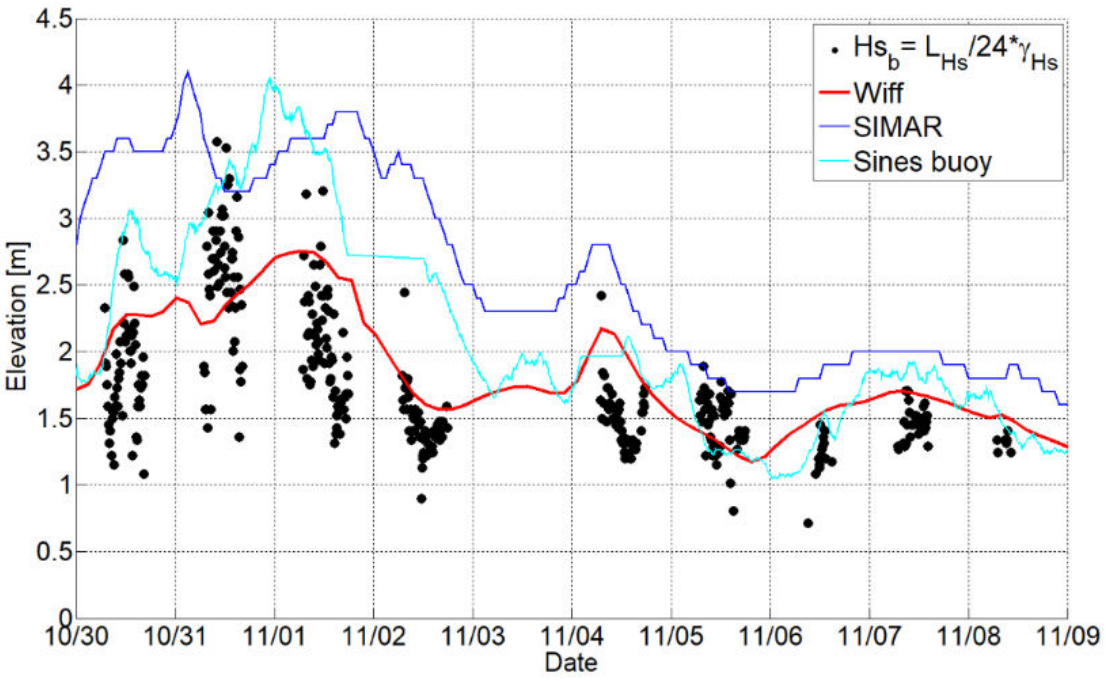

Figure 5.22. Significant wave breaking height $Hs_{b,video}$ obtained at Caparica (black circles) through 9 days dataset, versus significant wave height from hindcast models WIFF (red line), SIMAR (blue line) and measured by Sines buoy (cyan). Note that there was a gap of video data on day 3^d of November.

For a clear representation, the results were filtered with a moving average window of 1 hour and 30 minutes (Figure 5.23-a) and daily-averaged (Figure 5.23-b). Yet, a significant relationship between Hs_b from Timex and wave data sources indicated the goodness of the video-derived data, although it was missing a direct comparison with measurements in the surf zone.

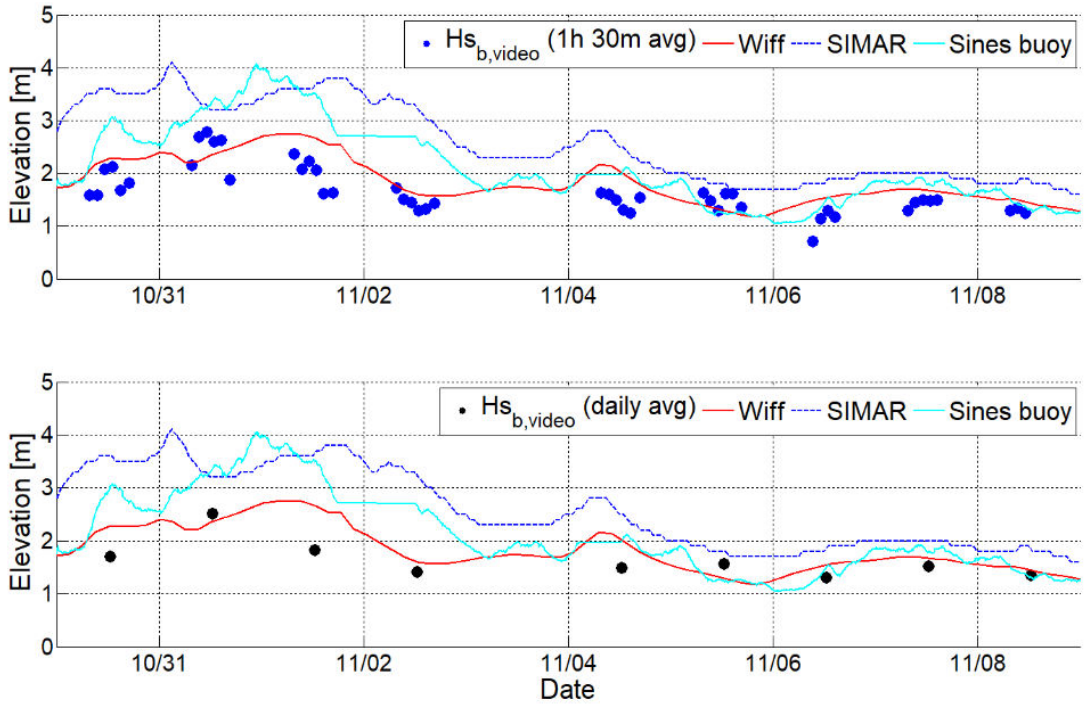

Figure 5.23. a) Significant wave breaking height $Hs_{b,video}$ with a median filter of 1 hour and 30 minutes (blue circles); b) significant wave breaking height $Hs_{b,video}$ with a daily median filter (black circles). Significant wave height from hindcast models WIFF (red line), SIMAR (blue line) and measured by Sines buoy (cyan) are common to both figures.

The daily-averaged values of $L_{Hs}/24$ were used to verify the possibility of estimating bathymetry and beach slope in the surf zone (Figure 5.24). Beach slope found by the fitting procedure varied between 0.015 and 0.04, with higher values when breakpoints were closer to the shore and over a likely present inner bar. These results were used to compute $\gamma_{b,Hs}$ with Eq. 5.21 (Madsen et al. 1976) and Eq. 5.22. Breaker index $\gamma_{b,Hs}$. ranged between 0.52 and 0.6, with a median value of 0.55, same value previously obtained from Ribeira d'Ilhas data (Section 5.4.5). Although bathymetric data were not available for the period in which video were acquired, a comparison with a previous complete survey of the nearshore zone suggested that the estimated beach slope might be realistic.

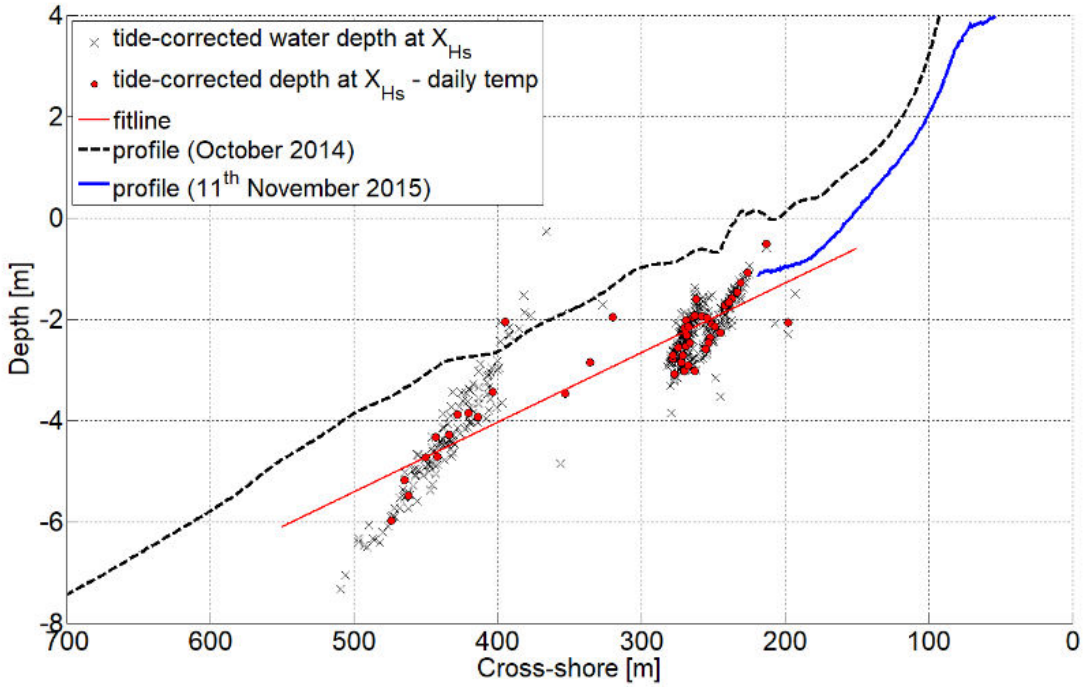

Figure 5.24. Attempt of deriving surf-zone bathymetry through tidal correction of $L_{Hs}/24$. Black dashed line represents the beach profile surveyed on October 2014 (about one year prior the video acquisitions). Blue line shows the beach profile surveyed on the following day the experience.

5.6.6 Wave breaking height at Kourou

Timex images produced from the first day of video acquisition by the video monitoring station at Kourou (Section 3.5) were used to test the wave breaking height estimation at a low energy coast. A cross-shore array of 200 m was sampled on 71 Timex images (Figure 5.25) during a full tidal cycle.

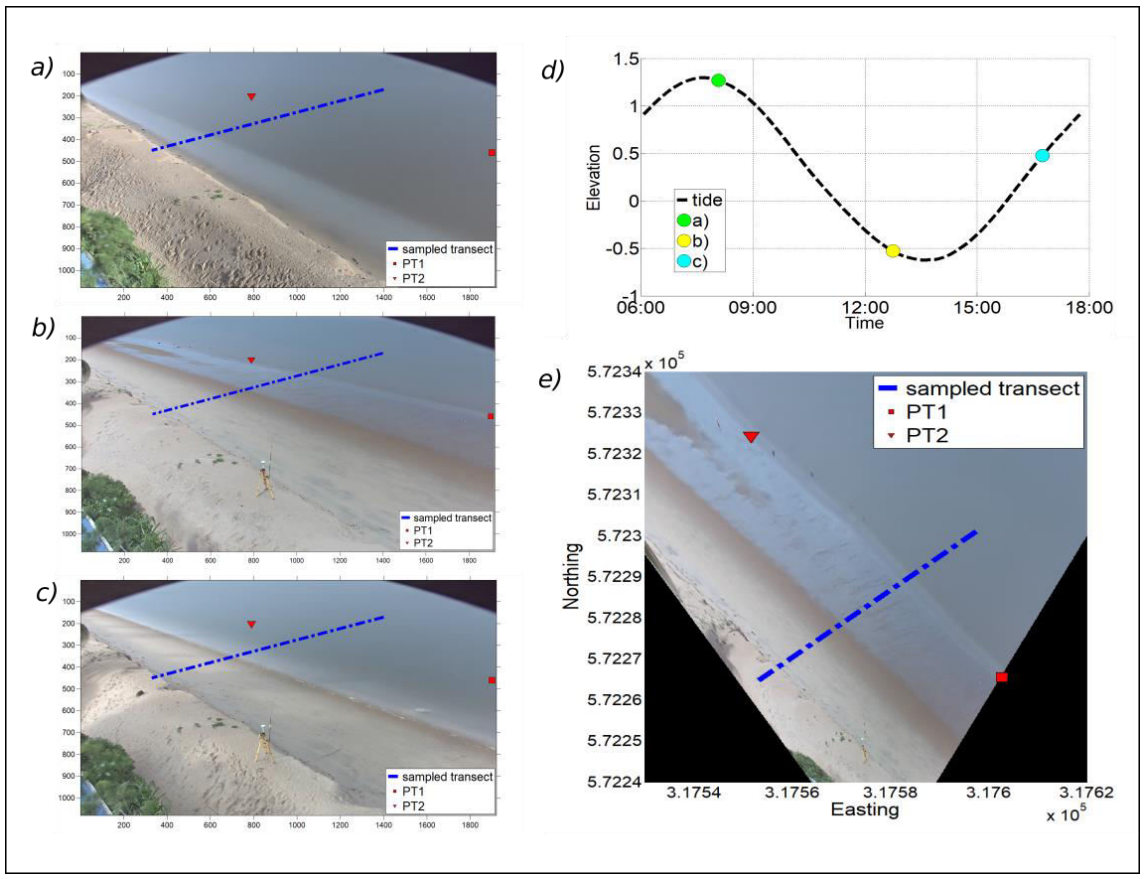

Figure 5.25. Timex images at different tidal elevation (a,b,c). d) Tidal modulation and related time (circles) at which example of Timex are shown in a), b), and c) windows. e) Example of rectified Timex. Blue dashed line represents the cross-shore transect used to sample $\bar{I}_{px}$ profile. Red triangle and square show PTs locations.

Wave breaking height Hs_b was computed solving Eq. 5.20, with L_{Hs} extracted from $\bar{I}_{px}$ by the fully automatic algorithm and the breaker index $\gamma_{b,Hs} = 0.55$. Video-derived Hs_b was compared to wave data measured by two pressure transducers installed at the surf zone. Results (Figure 5.26) showed that the proposed methodology was also feasible to correctly estimate low Hs_b (~0.1 m), although comparison with oceanographic instrumentations was available for short time (about 2 hours, twelve measurements).

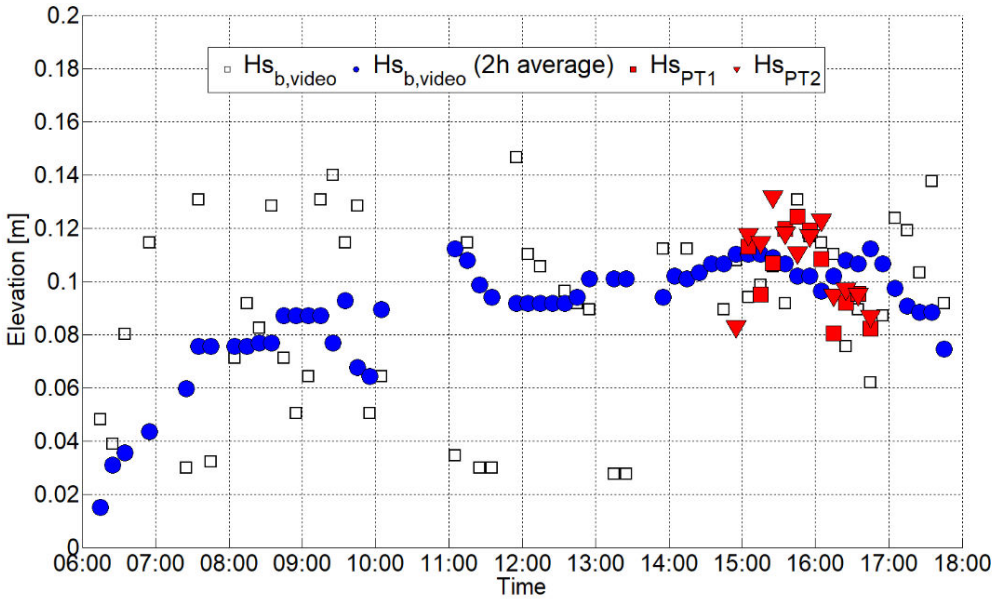

Figure 5.26. Significant wave breaking height $Hs_{b,video}$ measured at Kourou (empty squares) from 71 Timex. Blue circles represent data obtained with a two-hours moving average window. Red squares and triangles show significant wave height Hs_{PT} measured by the two PTs.

5.7 Discussion

5.7.1 Wave breaking height

The possibility of using video imagery for estimating wave breaking height is of great interest, since it is a crucial parameter for coastal studies and in-situ direct measurements are difficult tasks.

The two approaches proposed in this work to measure wave breaking height from video imagery were successful and showed satisfactory results. While the first approach (Eq. 5.10) couples the video-derived parameter L_{Hs} to the available bathymetric data, the second approach proposes the relationship $L_{Hs}/24$ for replacing the water depth parameter on the simplest wave height calculation formula (Eq. 5.19). The latest has much potential for remotely measuring wave height exclusively from video imagery, without the need of additional data. The good assessments obtained at three different study sites (Table 5.7) confirmed the technique as a valid alternative to the first methodology if bathymetry is not known.

Table 5.7.. RMSE values obtained from $Hs_b = \frac{L_{Hs}}{24} * 0.55$. NRMSE is found normalizing RMSE for the mean value of wave height reference in each site

site	***Camera type***	***N files (10min intervals)***	***Wave height range [m]***	***RMSE [m]***	***NRMSE***
Ribeira d'Ilhas	*Surfcam*	*94*	*1 – 3.5*	*0.4*	*23%*
Praia Grande	*Camera station*	*39*	*0.45 – 0.85*	*0.5*	*42%*
Caparica	*Surfcam*	*654*	*1.17 – 2.76*	*0.33*	*22%*
Kourou	*Camera station*	*12*	*0.08 – 0.13*	*0.02*	*20%*

Overall, the NRMSE for three of the four considered sites was around 20%, even though image sources and resolutions, along with sea state characteristics and number of data, varied consistently among the sites. Errors at Praia Grande were higher due to a combination of poor image quality and specific site characteristics.

In contrast with previous H_b predictors from video, which merely used Timestacks, the proposed techniques have the main advantage of being directly applicable on Timex, which are standard products generated by coastal video-monitoring stations worldwide. Yet, the direct use of Timex allows the observation of wave height along-shore variability in those sites in which, for example, coastal structures or bathymetry determine dissimilarity of wave characteristics along the coast.

5.7.2 Surf zone bathymetry

A second interesting result to emerge is the estimation of bathymetric profile from the video-derived feature L_{Hs}. Indeed, the surf zone is one of the most difficult area to survey due to the high wave energy and dynamicity of the sea bottom, along with the low water column that make problematic the bathymetry mapping.

Even though results were quite scattered and lack in precisions, the video-derived sea bottom profile had enough accuracy to evaluate the beach gradient. For instance, the beach slope is a fundamental parameter to calculate the Iribarren number (Iribarren and Nogales, 1949; Battjes, 1974), which characterizes beach behaviour (dissipative, reflective or intermediate) and wave breaking characteristics (spilling, surging, plunging).

5.7.3 Breaker index

Both methodologies (Eq. 5.10 and Eq. 5.20) used for wave height estimation were sensitive to the breaker index parameter. The approach solution of scaling γ_{BJ}, which was refereed to H_{max}, and adapting the breaker index to Hs_b was crucial to the results assessment.

Although longer video dataset coupled with detailed beach topography might provide better insights of breaker index of $\gamma_{b,Hs}$, the value $\gamma_{b,Hs} = 0.55$ was found feasible for different wave breaking height and beach slope. It was also shown that the rough estimation of beach gradient from the empirical relation $L_{Hs}/24$ might support the

calculation of $\gamma_{b,Hs}$. Nevertheless, further investigation should better investigate the value of $\gamma_{b,Hs}$ with different type of wave breaking (plunging, spilling, collapsing and surging) and bottom slopes.

5.7.4 Computational performance

Coastal video-monitoring dataset are usually large in number of images, therefore automatic techniques must be computationally fast. The developed Matlab-based series of algorithm for extracting the interested $\bar{I}_{px}$ and for delivering wave breaking height was very fast performing. For instance, delivering Hs_b from 40 Timex of Praia Grande (596x901 pixels, 1 Mb) lasted about 2 seconds, while about 2 minutes was the time necessary to process 654 Timex images (830x711, 1 Mb) and estimate Hs_b at Costa da Caparica with 10 days dataset. The speed of the process depended principally on the image size and sampled transects length. Data processing were done on an Intel Quad 2 Q2400 2.67 Gb with 4Gb Ram.

5.7.5 Limitations

The limitation of the first method presented in this chapter is the need of the bathymetric profile, as bottom data are not always available due to logistic constraints. Although the second methodology does not require beach profile, results accuracy was poor when wave breaking height was constant during a long period.

Common to both methodologies, the main limitation is related to the likely inaccuracy in sampling Timestack transect or $\bar{I}_{px}$ profile on the rectified Timex not perpendicular to the breaking line. The non-perpendicularity between wave breaking pattern and the cross-shore transect used to sample $\bar{I}_{px}$ profile might lead to inaccuracy. As seen for instance at Praia Grande (Section 5.6.4), breaking line was not parallel to the shore, therefore the length of L_{Hs} resulted longer and wave breaking height estimation was almost double than the measured Hs_b. A solution to overcome this issue might be to build a procedure to detect the breaker line previously the sampling of $\bar{I}_{px}$ profile, in order to choose the right inclination for sampling the pixel array. However, while regular incipient and breaking dissipation lines could be easy to detect, a wide inner surf area with highly irregular

breaking patterns might cause difficulties in automatic peaks detections and generate errors in wave breaking height estimation.

The method was calibrated and validated using Timestacks and Timex generated over an image sequence of 10 minutes, which is the most common interval used by coastal video-monitoring stations for secondary images production. Since the special points on pixel intensity variation $\bar{I}_{px}$ were found related with breakpoint positions, the methodology should also be validated on Timex and Timestack produced over different time intervals.

6. INTERTIDAL BEACH TOPOGRAPHY ASSESSMENT

The present chapter is based on the communication:

Andriolo, U., Almeida, L.P., Almar, R. (2018). Coupling terrestrial LiDAR and video imagery to perform 3D intertidal beach topography. (in review)

6.1 Introduction

Efficient and accurate measurements of beach topography are fundamental to understand the processes that drive coastline evolution. At the foreshore, hydrodynamic forcing by waves, tide and currents determine sediment transport and beachface dynamics that need to be evaluated with sufficient resolution in both time and space (Komar, 1976; Short, 2004; Masselink et al., 2011). Conventionally, in-situ survey methods involve the use of differential GPS instrumentation (RTK-GPS) which require intensive human effort (e.g., Mason et al., 2000). Hence, the sampling frequency may not resolve the beach variability at the required time-space scales due to the logistical commitments. Remote sensing methods emerge in this context as an interesting alternative solution for this type of field measurements (e.g., Harley et al., 2011).

Video monitoring technique has been widely used for the continuous monitoring of the coastal zone (Holman and Stanley, 2007) to overcome the restrictions of field surveys. Typical video-monitoring system is composed by one (or more) Internet Protocol (IP) camera mounted at an elevated position looking at the nearshore. The Time-exposure (Timex) images are produced from a sequence of images to average out the high-frequency waterline oscillation (swash motions) and identify the average shoreline position, as the border between dry and wet sand (Boak and Turner, 2005). On the Timex, shoreline can be extracted manually (Harley et al., 2013) or using automated detection methods based on pixel intensity characterization (e.g., Aarninkhof et al., 2003; Almar et al., 2012b), edge detection (e.g., Osorio et al., 2012) or color segmentation (e.g., Sobral et al. 2013; Valentini et al., 2017b). Due to the limitations of the monoscopic-view, a fixed single-camera only resolves the horizontal dimensions of the shoreline position (x and y), and hence, additional information is required to estimate the shoreline elevation. To overcome this limitation, Aarninkhof et al. (2003) proposed a methodology, considered "standard" nowadays, that formulated shoreline elevation as:

$$z_{sl} = z_o + \eta_{sl} + z_{swash} \qquad \textit{Eq. 6.1}$$

where z_o is the combined astronomical and meteorological tide level, η_{sl} is the wave set-up and z_{swash} is the swash-induced water height on the foreshore slope.

Wave set-up η_{sl} is estimated using standard empirical equations (e.g. Holman and Sallenger, 1985; Holland et al., 1995) or applying wave propagation numerical models (e.g. Aarninkhof et al., 2003). Swash-related parameter z_{swash} can be determined using measured wave parameters (e.g., Aarninkhof et al., 2003; Vousdoukas et al., 2011) or wave runup parameterization (e.g. Sobral et al., 2013). Following Aarninkhof et al. (2003) method, the intertidal 3D beach topography can be obtained from a single-camera by combining consecutive shoreline elevation contour lines along the time (recorded at different tidal levels). While such approach reduces significantly the logistics involved in the acquisition of topographic data, the dependence on correct estimations of the hydrodynamic forcing (meteorological tide, wave and swash processes) can represent an additional source of error.

A recent innovative remote sensing solution for intertidal beach mapping is the use of terrestrial Light Detection And Ranging (LiDAR) technology. Like the video cameras, the 2D LiDAR can be deployed locally, on a stable structure (e.g., tower), and set to record high frequency (e.g., 20 Hz) measurements of the beach topography, inner-surf wave processes and swash motions (Almeida et al., 2013). The 2D LiDAR sensors have proven to be able to acquire high quality measurements of waterline elevation (Vousdoukas et al., 2014; Brodie et al., 2015; Blenkinsopp et al., 2016; Almeida et al., 2017) and simultaneously beach topographic changes (Blenkinsopp et al., 2010; Almeida et al., 2015). While this tool can be seen has one of the most accurate to measure shoreline elevation, the limited spatial coverage (only measures 2D), restricts its application to a specific cross-shore section of the beach.

Considering that the main limitation of the video technique is the fact that it cannot measure the shoreline elevation (vertical component), LiDAR emerge in this context as an ideal candidate to overcome this observational problem.

The aim of this work is to investigate the possibility of coupling LiDAR and video imagery to perform detailed beach intertidal topography at Nha Trang (Section 3.6). As LiDAR provides precise shoreline elevation and punctual video shoreline position, both methods can be combined and complemented to perform accurate 3D beach intertidal topography mapping.

6.2 Field site and experimental setup

A field experiment was conducted during the end of November and the start of December 2015 at Nha Trang beach (Almeida et al., 2017), a sandy beach located on the South East of Vietnam (Figure 6.1). Two days of data were selected for this work (28th and 29th of November 2015).

The study area is located at the North region of Nha Trang, a medium-to-coarse sandy beach (D_{50} = 0.3 mm) with a fairly steep beach face slope ($tan\beta$=0.1) and a narrow (~ 40 m) alongshore uniform and flat (~ 0.01) low tide terrace (Lefebvre et al., 2014). The beach is a mixed wave-dominated micro-tidal environment (max tide range of 1.5 m), with a mix of diurnal and semi-diurnal tide. Apart from extreme events such as Typhoons (Thuan et al., 2016), wave forcing on the beach is mostly generated by SE wind-waves with moderate energy, and Monsoon swells from NE direction (Almar et al., 2017b).

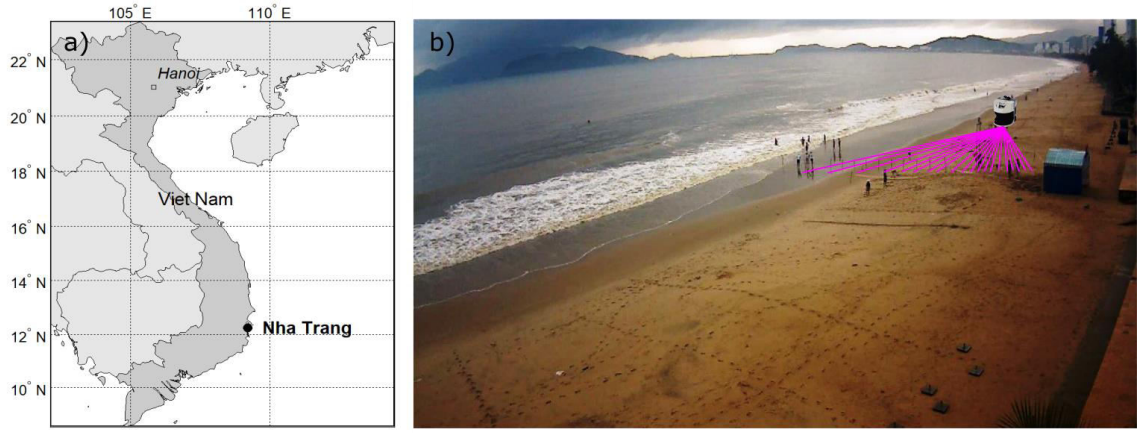

Figure 6.1. a) location of Nha Trang beach. b): 2D LiDAR deployment position and monitored profile (magenta lines) superimposed to frame acquired by video system.

Wave offshore properties, namely significant wave height and peak period, and water level were obtained by an Acoustic Doppler Current Profiler (ADCP) moored offshore at 15 m depth. The selected 48 hours covered two tidal cycles ranging between about 0.7 and 1.15 m (Figure 6.2). The tide had a mixed character and asymmetrical phases, with rising tide phases characterized by double high-tide peaks, and ebb phases by a single descending curve. Over the two days, offshore wave significant height

decreased from 1.1 m to 0.8 m, likewise wave peak period dropped from 11 s to 8 s (Figure 6.2).

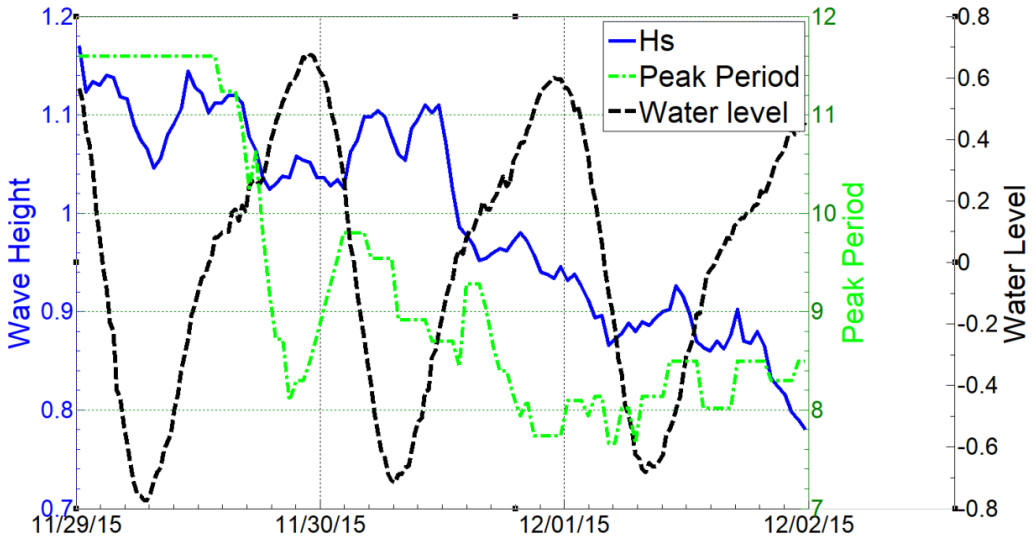

Figure 6.2. Wave significant height (blue line), wave peak period (green line) and water level (black dashed line) measured by ADCP during the experience.

Topographic survey was carried out by RTK-GPS daily to accurately characterize beach intertidal morphodynamics. Surveys were performed in a continuous mode (recording every 0.5 m) along cross-shore transects spaced by 10 m at every low tide.

6.3 Methods

6.3.1 Terrestrial LiDAR

A 2D LiDAR (SICK LMS500) mounted on the top of a metallic tower was installed on the beach to measure high frequency swash zone morpho- and hydrodynamics (Figure 6.1-b). The LiDAR sensor is a two-dimensional mid-range laser-scanner (maximum range ≈ 50 m) that emits pulsed laser beams (infrared light; λ = 905 nm). Laser beams are deflected on an internal mirror placed inside the scanner head, which rotates at regular angular steps at 25 Hz and scans the surroundings (180°) with an angular resolution of 0.166°. The distance to the target (water surface or dry and wet sand surface) is calculated from the propagation time that the light requires from emission to reception of the reflection at the sensor. The LiDAR setup allowed a complete coverage of the whole swash zone with a spatial resolution varying from 0.01 m at the Nadir point (zero grazing angle) to 0.4 m at the most seaward valid observation location (Almeida et al, 2017).

6.3.2 Video System

One Vivotek IP camera was installed on an electricity post at about 11 m above Mean Sea Level (MSL) looking southward the NhaTrang beach (Figure 6.1-b) The 1500 x 700 image acquisition took place at a frequency of 2 Hz. Being Nha Trang an urban beach, the beach was lit by artificial lights allowing video imagery acquisition also during nighttime.

Camera Calibration toolbox (Bouget, 2007) was used to estimate camera's intrinsic parameters and to correct raw frames from distortions inducted by lens curvature. Rectification process (Taborda and Silva, 2012) was performed using 24 Ground Control Points (GCPs), previously surveyed by RTK-GPS within the field of camera view. Images were projected on the horizontal plane with an elevation equal to water level η measured by the ADCP at the corresponded time.

Time-exposure images (Timex) were generated by averaging image pixel intensity over an interval of 15 minutes image sequence (Holman and Stanley, 2007). Figure 6.3-a shows the footprint spatial resolution of the generated plan-view video images.

LiDAR profile was covered with a maximum cross-shore pixel square footprint of about 0.1 m^2, while shoreline alongshore image spatial resolution degraded till 0.5 m^2 at the furthest point from the camera. In addition, Timestack images (e.g., Holland and Holman, 1993; Holman and Stanley, 2007; Almar et al., 2012a; Almar et al., 2017a) were produced along LiDAR profile from rectified image sequence to verify the synchronization, in time and space, between LiDAR and video horizontal runup observations (Figure 6.3-b).

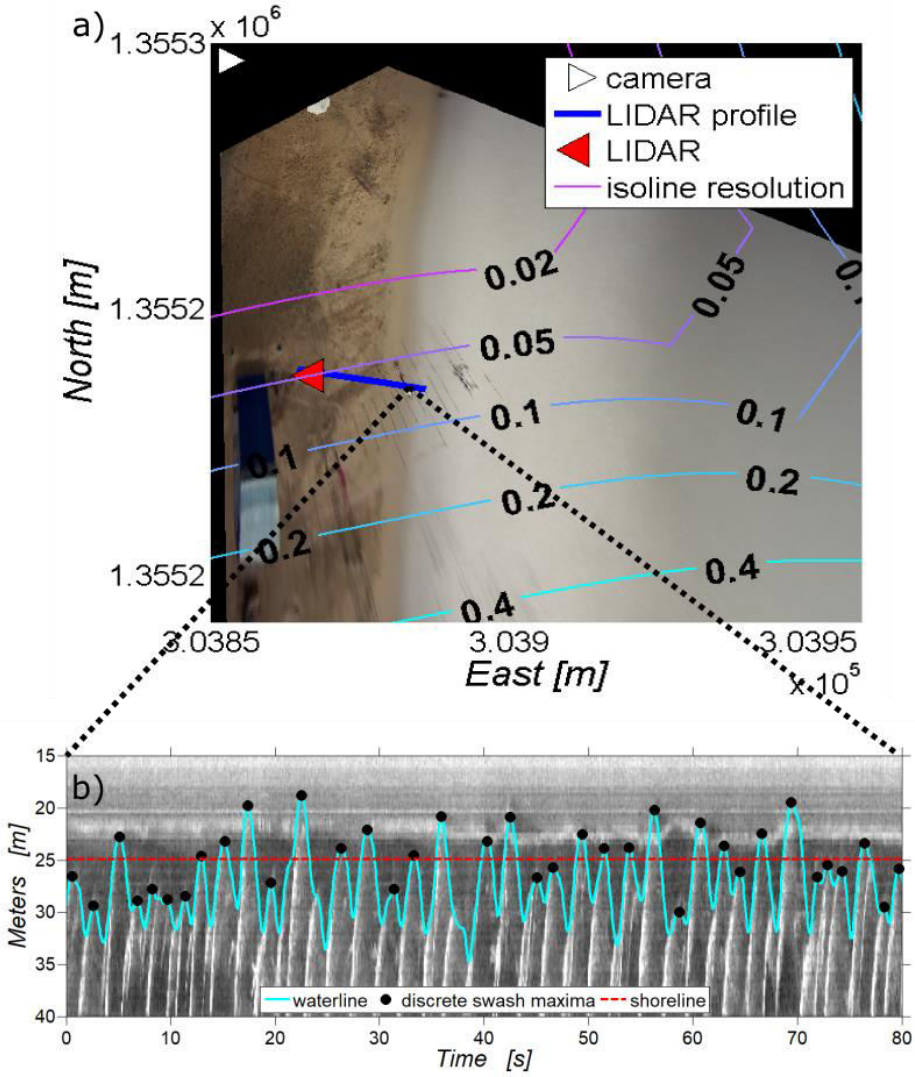

Figure 6.3. LiDAR-video measurements. a) isolines indicate pixel square footprint resolution of rectified image, in m^2; b) example of rectified Timestack produced from image sequence over LiDAR profile. Water oscillation measured by LiDAR is superimposed on Timestack in cyan. The matching with the waterline designed by Timestack confirmed the spatial-temporal synchronization between camera and LiDAR. Black circles show discrete swash positions Sw derived by peak-identifier algorithm. Red dashed line represents the shoreline position shX_{LiDAR}.

A preliminary selection of data based on quality control took place prior the development of the technique, with both automatic procedure and visual inspection. Data were discarded due to the limited range of laser scanning during low tide using an elevation threshold, while discontinuous measurements of the camera were visually found through the dataset.

At last, 22 hours of LiDAR observations and the respective 88 Timex were considered for the present study, all being acquired during night hours (Figure 6.4). LiDAR measurements were discarded during low tide which occurred during morning time, while video data were corrupted (day 29th) or missing (day 30th) during afternoon time. The 22 hours were divided into four sub-intervals, distinguishing falling tide and rising tide phases

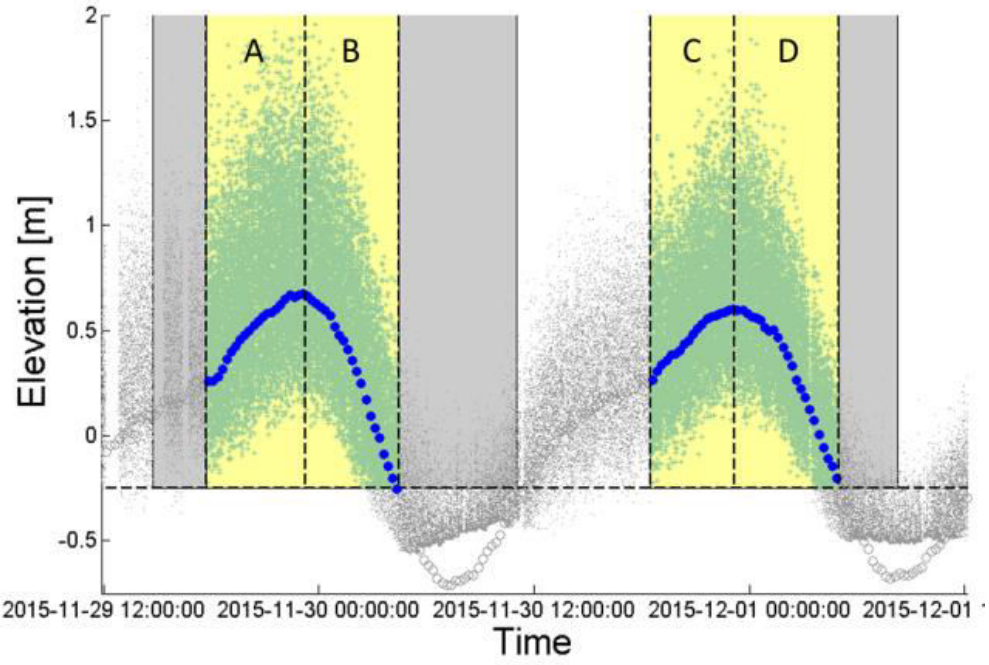

Figure 6.4. Selected data. Wave runup measured by LiDAR (green dots), tide (blue circles) and time windows of video data (yellow rectangles) selected. Discarded data are plotted in gray. Letters A-B-C-D indicate the four tidal phases considered.

6.3.3 Shoreline definition and detection

To correctly combine LiDAR and video data, a definition of shoreline common to both techniques was adopted. In this work, shoreline was defined as the average all the discrete swash maxima identified within each 15-min segments of video and LiDAR data (see example in Figure 6.3-b).

On LiDAR data, a moving-average time window variance filter was applied to all measurements, to separate the topography from the water, following the approach described in Almeida et al. (2015). After data processing, horizontal swash excursions Sw and vertical wave runup Z_{up} were organized into 15-minutes consecutive segments of data. The discrete swash maxima Sw_{max} were automatically detected by a peak-identifier algorithm and both shoreline position (shX_{LiDAR}) and shoreline elevation (shZ_{LiDAR}) were directly extracted from Sw and Z_{up}, respectively (Figure 6.3).

On Timex, shoreline detection was calibrated using LiDAR measurements. Firstly, pixel intensity arrays were sampled on Timex along LiDAR profile. Secondly, pixel intensity arrays were compared with LiDAR horizontal shoreline position shX_{LiDAR} to determine the matching intensity value. Following such comparison, it was found that LiDAR shoreline position coincided with the local minima on the pixel intensity array extracted from Timex (Figure 6.5), therefore shoreline position shX_{VIDEO} on the LiDAR transect was automatically extracted over the 88 Timex. In order to detect the Shoreline contour was detected sampling a total amount of 50 pixel arrays alongshore on Timex. Local minima were automatically encountered on each pixel array to draws shoreline contour for the whole beach extent visible on image (Figure 6.5).

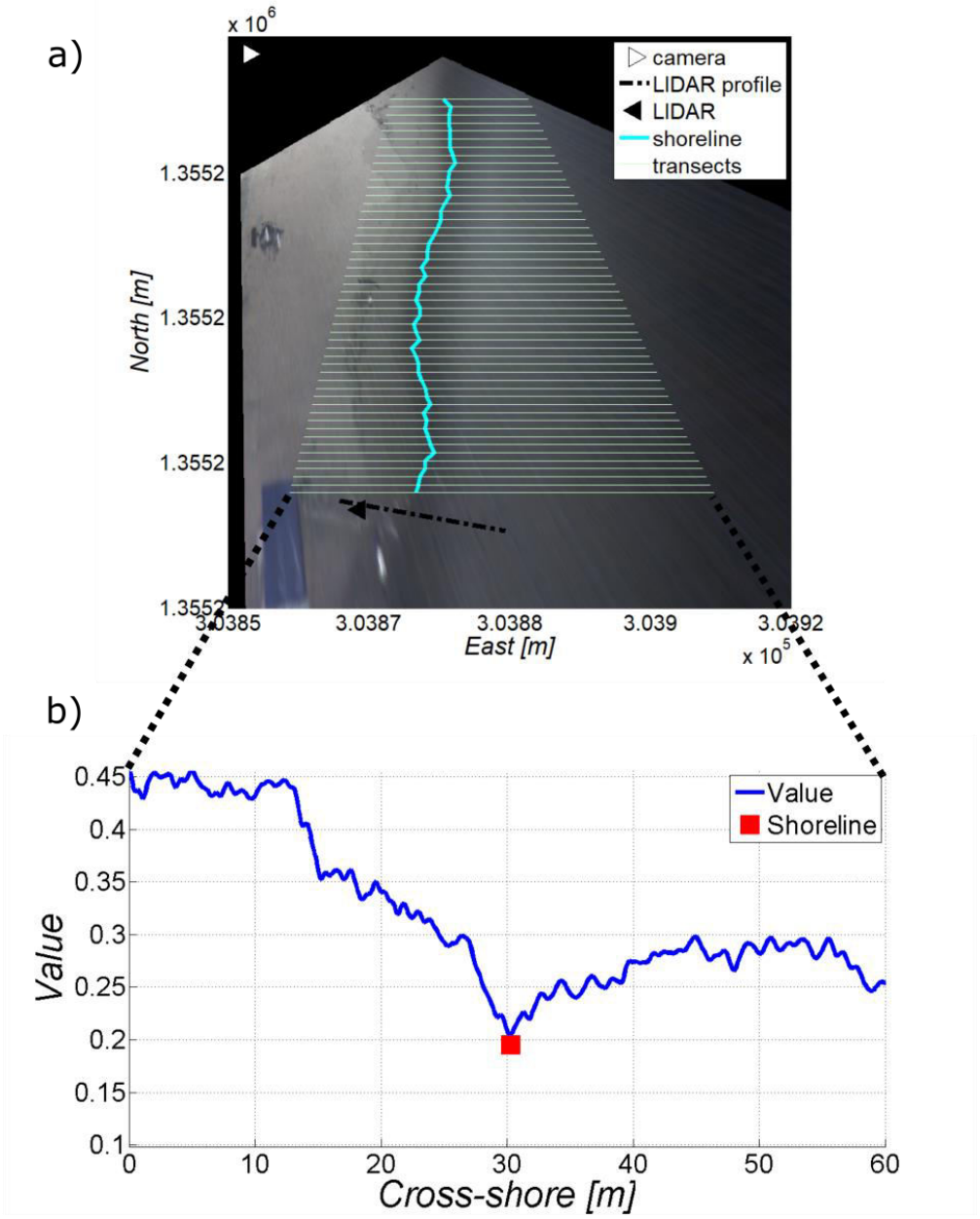

Figure 6.5. Shoreline position calibration. a) Rectified Timex image with 50 sampled profiles (white lines) and video-derived shoreline contour (cyan). b) Pixel intensity values sampled on Timex over LiDAR profile. Shoreline LiDAR position was found coinciding with the signal local minimum (red square).

6.3.4 Intertidal beach topography

Video-derived horizontal shoreline position was transformed into elevation using LiDAR elevation shZ_{LiDAR} at the corresponded time. Beach profiles surveyed by the conventional RTK-GPS method were compared to the results to evaluate the accuracy of the proposed technique.

The deviations between shX_{LiDAR} with shX_{VIDEO} were considered to estimate the performance of horizontal detection as:

$$\delta_d = shX_{LIDAR} - shX_{VIDEO} \quad \text{Eq. 6.2}$$

Although such analysis was limited to LiDAR profile, it was assumed that such error also indicated the accuracy of the shoreline contour detection on Timex.

The elevation offset δ_e representing the vertical accuracy was calculated as:

$$\delta_e = Z_{dGPS} - Z_{VL} \quad \text{Eq. 6.3}$$

where Z_{dGPS} is the elevation of RTK-GPS surveyed profiles and Z_{VL} (subscript VL stays for "Video-Lidar") the profile elevation assessed by the proposed technique. Offset δ_e was expressed in terms of Root Mean Square Error (RMSE) for each compared profile.

Resulting performance of the methodology was achieved following the approach proposed by Aarninkhof et al. (2003), which multiplied the error δ_d by the beach slope to treat the total error δ_z in vertical scales as:

$$\delta_z = (\delta_d * tan\,\beta) + \delta_e \quad \text{Eq. 6.4}$$

where δ_d is the horizontal error, β is the mean beach slope, δ_e the elevation error. Values of δ_d, δ_e and therefore δ_z were all expressed in term of RMSE.

Finally, two DEMs were obtained from LiDAR-video to test the feasibility of the combined system to support the analysis of beach morphological changes.

6.4 Results

6.4.1 Shoreline detection

Figure 6.6 shows the comparison between shX_{VIDEO} and the shX_{LiDAR}. Recalling that errors are reported as RMSE, average horizontal δ_d was found equal to 1.1 m. Discerning the analysis between rising and falling tide, the regular and faster ebb-phase allowed more precise shoreline detection (δ_d=0.65 m) than the mix rising phases (δ_d=1.3 m). Yet, during ebb phases (B and D) tidal range was about double (~1 m) than during the two rising tide phases (A and C).

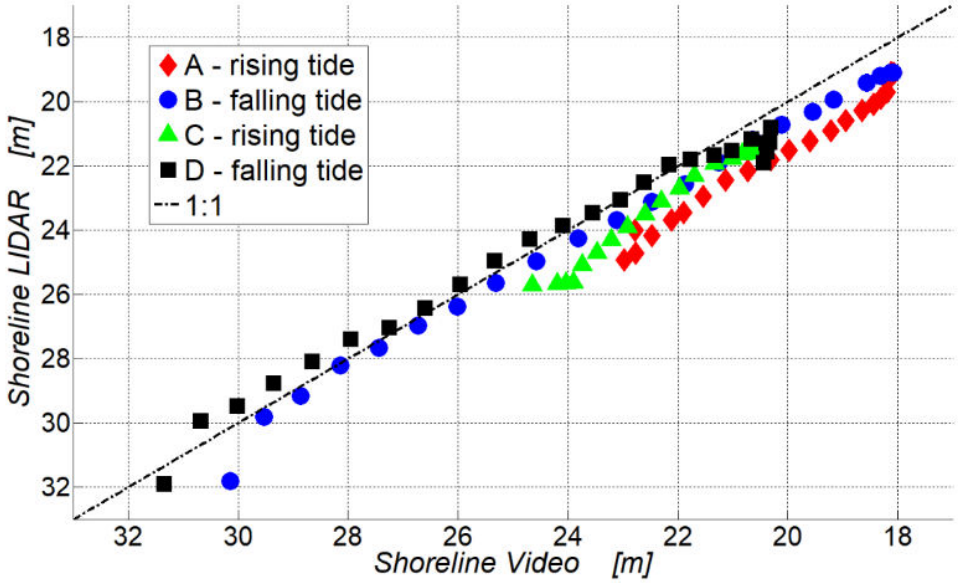

Figure 6.6. Horizontal shoreline positions detected on Timex over LiDAR profile versus horizontal shoreline positions from LiDAR measurements. X-axis represents distance in m from basepoint on upper beach.

Considering the higher accuracy in the match between shX_{VIDEO} and shX_{LiDAR}, the larger cross-shore coverage and the higher tidal range, only the two falling tide phases (B and D) were considered to further test the feasibility of LiDAR- video system to perform the beach intertidal topography.

Figure 6.7 shows the 20 shoreline contours extracted on the 20 Timex during tidal phase B. The alongshore video shoreline elevation contour was built using shoreline elevation measured by 2D LiDAR.

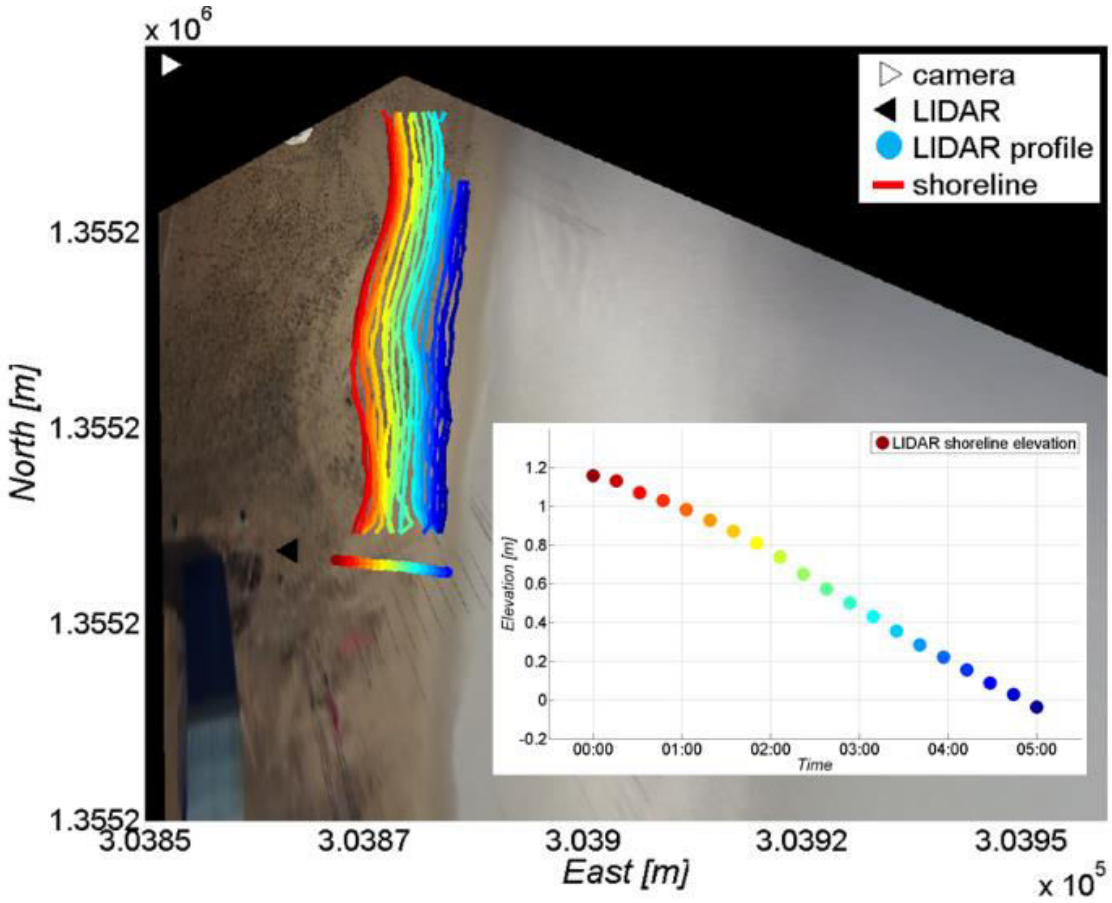

Figure 6.7. Example of shoreline contours detected on video during tidal phase B. White box: shoreline elevation measured over LiDAR profile by 2D LiDAR during the ebb phase B. Colors are related to elevation change.

6.4.2 Intertidal beach topography

Comparison between the surveys obtained by the combined video-LiDAR system and by the conventional RTK-GPS technique is shown in Figure 6.8. The map had a 1 m alongshore and 0.1 m cross-shore elevation resolution, therefore the remote sensing results described with more details the foreshore beach topography than RTK-GPS survey.

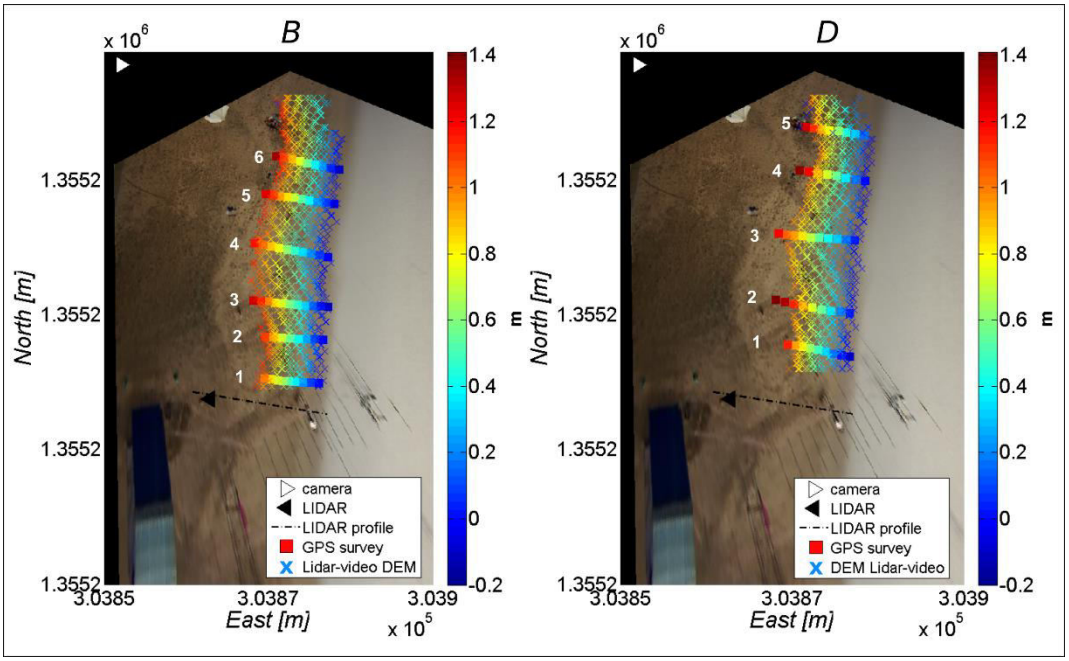

Figure 6.8. Digital Elevation Models obtained with data from tidal phase B (left) and D (right). Data obtained by LiDAR-video combination (crosses) versus RTK-GPS surveyed profiles (COLORED squares). White numbers indicate profile numeration for reference (see also Table 6.1).

All 11 profiles obtained by the conventional RTK-GPS survey were considered for evaluating the accuracy of the results (Table 6.1). The differences of vertical error δ_e were equivalent to about 5% of the tidal range and were of the same order of magnitude as the accuracy of the RTK-GPS instrumentation (approximately ±0.05 m in vertical). Instead, the horizontal error caused by the inaccuracy of shoreline detection projected on the beach slope, $\delta_{d,tan\beta}$, had larger influence than vertical error δ_e on the final performance. Overall, following Eq. 6.4, the average RMSE obtained by video-LiDAR system was equal to 0.128 m, similar for both tidal phases considered in this study, with maximum error at shoreline that did not exceed 0.152 m.

Table 6.1 Horizontal ($\delta_{d,tan\beta}$), vertical (δ_e) and total (δ_z) RMSE. For profile number and location, refer to Figure 6.8

tidal phase	profile	δd	$tan\beta$	$\delta d_{, tan\beta}$	$\delta d_{, tan\beta, MEAN}$	δe	$\delta e_{, MEAN}$	δz	$\delta z_{, MAX}$	$\delta z_{, MEAN}$
B	1	0.71	0.137	0.097	0.084	0.047	0.044	0.144	0.145	0.127
	2		0.119	0.084		0.043		0.127		
	3		0.098	0.069		0.032		0.101		
	4		0.117	0.083		0.062		0.145		
	5		0.126	0.089		0.041		0.130		
	6		0.114	0.081		0.036		0.117		
D	1	0.59	0.124	0.074	0.072	0.049	0.057	0.123	0.152	0.129
	2		0.134	0.079		0.073		0.152		
	3		0.096	0.057		0.05		0.107		
	4		0.128	0.076		0.05		0.126		
	5		0.124	0.074		0.062		0.136		

Two DEMs were produced during the ebb tidal phases (B and D) elevating the shoreline contours to shZ_{LiDAR} computed at corresponded time (Figure 6.9). The grid covered an area of about 400 m^2, with a resolution of 0.15 m. The comparison of the two DEMs allowed the observations of the rapid morphological changes in the swash zone (Almeida et al., 2017), with a precise description of the evolution of beach cusps and horns not easily discernible in data acquired by more traditional field methods with such relatively short temporal and spatial scales.

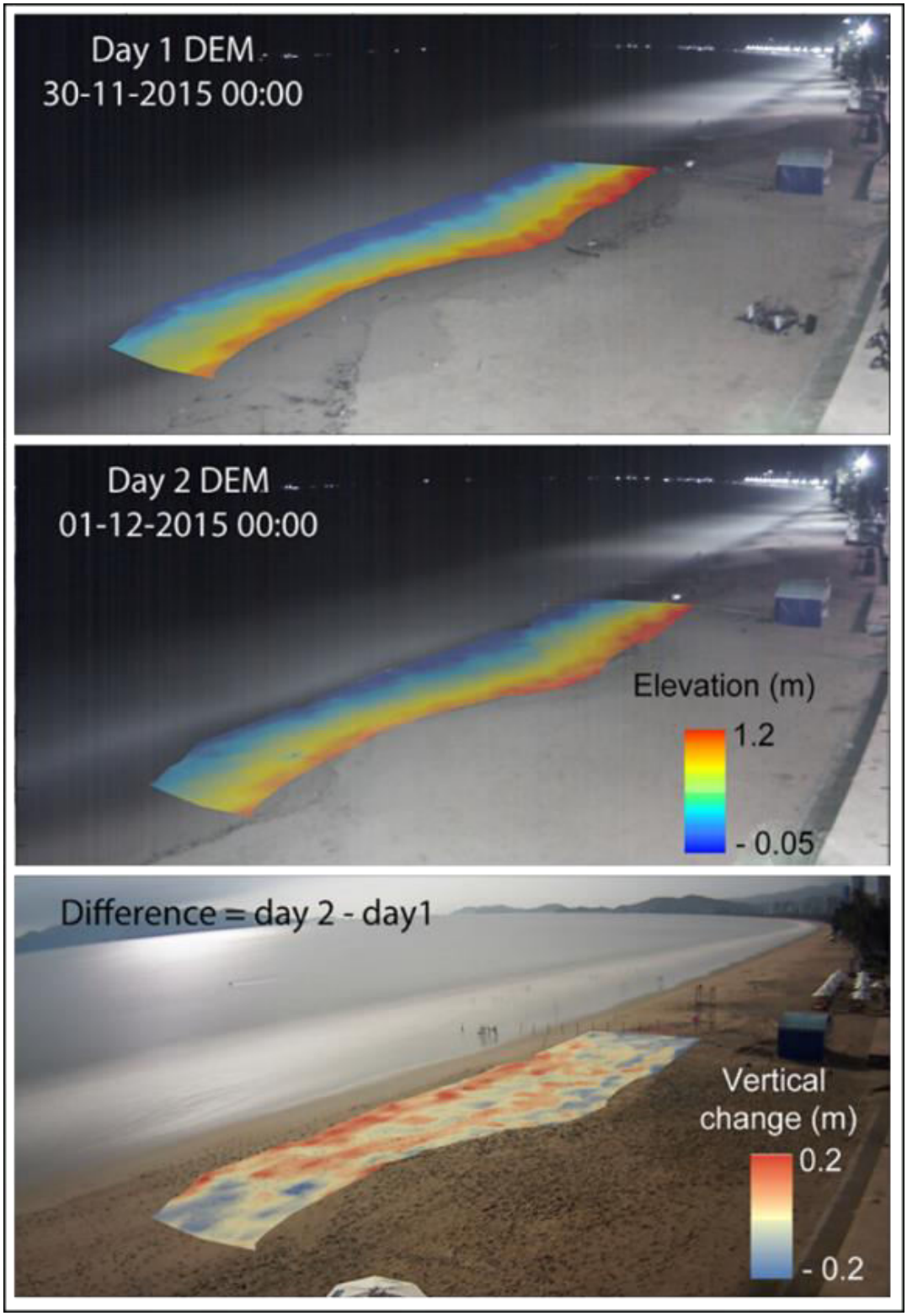

Figure 6.9. Digital Elevation Models (upper and middle plot) and short-term beach morphological change assessment from their difference (lower plot).

6.5 Discussion

The present work provides a demonstration that the combination of LiDAR and video methods can be used to perform 3D beach intertidal topography with an excellent level of precision. The overall performance analysis of the LiDAR-video approach showed that 3D intertidal beach topography mapping was performed with a RMSE of approximately 0.12 m. Despite the uncertainties generated by image rectification process (Uunk et al., 2010), the level of accuracy obtained with this remote sensing approach can be considered has a very satisfactory result.

Terrestrial LiDAR has been successfully used to provide precise measures of runup processes (e.g., Blenkinsopp et al., 2012; Almeida et al., 2013; Brodie et al., 2015) and shoreline elevation, therefore the combined LiDAR-video system approach is very likely to be more accurate than the standard video intertidal mapping, which relied on empirical equations and wave numerical modeling (Aarninkhof et al., 2003). As an example, the 2% of exceedance of the vertical runup measured by the 2D LiDAR during this experiment was compared against runup empirical formulation proposed by Stockdon et al. (2006), which included both wave set-up and swash processes.

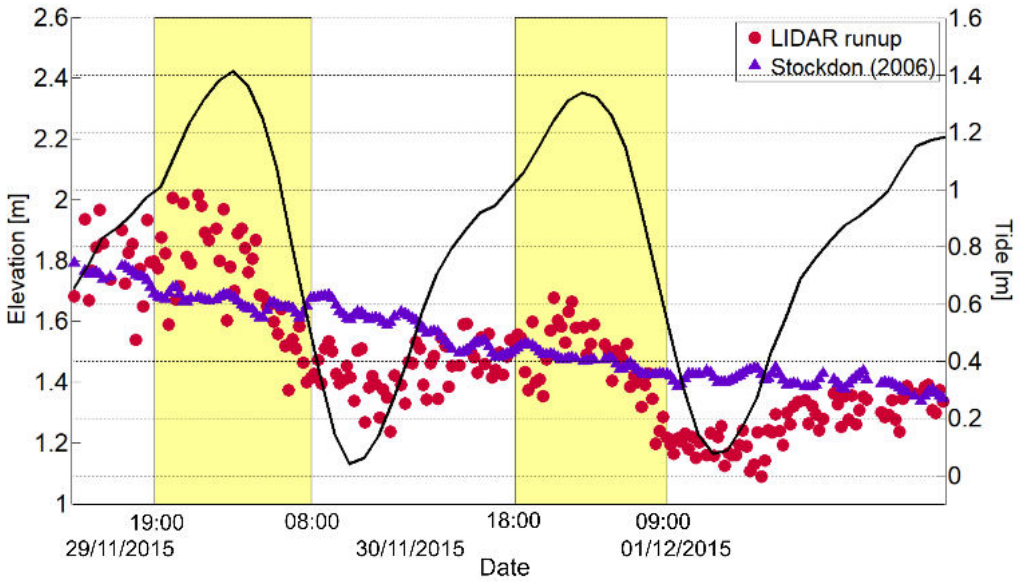

Figure 6.10. Runup $R_{2\%}$ measured by LiDAR (red dots) and predicted using Stockdon et al. (2006) equation (violet triangles). Tide is presented in black line. Background yellow rectangles indicate the time windows of the present work.

The results in Figure 6.10 show that during mild wave conditions (last two tide cycles) the match between observations and predictions is good, however under energetic wave conditions the differences increased till about 0.5 m. Such differences are representative of the magnitude of error associated to the approach that relies on wave set-up and runup estimations (Plant and Holman, 1997; Madsen and Plant, 2001; Aarninkhof et al., 2003; Sobral et al., 2013; Vousdoukas et al., 2011). Moreover, it is clear that at complex beaches such as Nha Trang, characterized by steep upper beach and low tide terrace, empirical run up predicitons did not describe the distinct regimes observed at different tide stages (reflective at high tide and dissipative during low tide). Using LiDAR direct measurement of the shoreline elevation means that errors associated with tide (astronomical and meteorological), wave induced set-up and runup estimations are left out of the video intertidal mapping. Moreover, LiDAR-video system does not require any additional data source to produce intertidal mapping since the shoreline observations are directly related to the local vertical datum and horizontal coordinate system.

Some of the limitations of the LiDAR-video system are the constrained 2D LiDAR range (approximately 60 m). The coverage would increase by elevating the LiDAR tower, although reducing the horizontal resolution and likely endangering tower stability (Almeida et al., 2015). On the other hand, video cameras are light dependent, thus the application of the proposed methodology may be unfeasible over the night, not allowing continuous beach monitoring. At Nha Trang beach, the existence of road lights made possible the use of video imagery also over nighttime, but such conditions are not always available. A technical solution would be the deployment of thermal InfraRed (IR) camera, which have already been used in coastal studies (Carini et al., 2015).

Spatially, the shoreline mapping by video was limited by the low-lying camera and the presence of objects placed in proximity of the shore, such as the LiDAR tower and the poles for studying swash (as in Almar et al., 2016). Their projected height on rectified images disturbed the automated shoreline detection, restricting this study to 70 m alongshore span. The installation of the camera on a higher elevation might overcome such issues.

The crucial point for the successful application of LiDAR-video combination is to verify the geographical matching between LiDAR data and rectified images, along with establishing a common definition of shoreline using swash statistics. Existing algorithms dedicated to shoreline detection on Timex can be calibrated using LiDAR without the need of long-term dataset. In this perspective, the use of Variance images should be investigated as it would offer significant advantages in shoreline detection (Simarro et al., 2015).

7. SUBTIDAL BATHYMETRY ASSESSMENT

The present chapter is partially based on the works:

Andriolo, U., Azevedo, A., Silva, A.N., Taborda, R. (2016). Video imagery technique for wave celerities estimation: results over a rocky-shore platform. 4th Jornadas de Engenharia Hidrográfica, Lisbon, Portugal (ISBN978-989-705-097-8)

Andriolo, U., Mendes, D., Azevedo, A., Taborda, R., Silva, A.N. (2017). Bathymetric inversion from video imagery: investigation in the surf zone. 4th Estuarine and Coastal Morphodynamics Conference (MEC 2017). Porto, Portugal

7.1 Introduction

Nearshore bathymetry is a major coastal feature that influences coastal processes and dynamics. The acquisition of nearshore bathymetry is highly required, as coastal hydrodynamic and wave impact on the coast mostly depends on the configuration of the sea bottom.

One of most widely used technique for acquiring bathymetric data relies on single- or multi-beam echo-sounding sonar systems mounted beneath a vessel's hull. As the methodology requires the use of a boat, the applicability of echo-sounding systems is constrained by the limited water depth and breaking wave process in shallow waters, where vessels cannot operate efficiently and safely. Remote sensing techniques such as airborne Light Detection And Ranging (LiDAR) systems have been applied to survey nearshore bathymetry to overcome vessel use restrictions. Nevertheless, due to the costs and logistical difficulties, the frequency of the surveys performed with conventional techniques do not provide the necessary number of measurements for monitoring the high-dynamic morphological changes occurring in the nearshore zone. In this context, video remote sensing is a valuable alternative technology that can overcome the above limitations.

The estimation of the coastal bathymetry from imaging started with the experiment during the Second World War, when such information was necessary to the Allies to arrive to the coast of Normandy. Nearshore depth information was retrieved from wavelengths and wave celerity determined from airborne photo imagery (Hart and Miskin, 1945; Seiwell, 1946; Williams, 1947; Coleman and Lundahl, 1948).

7.1.1 Linear wave dispersion relation

Wave celerity is the speed at which wave propagate towards the shore. In deep water (when ratio between local water depth h and wavelength L_o is greater than 0.5), wave celerity primarily depends on wavelength as:

$$c = \frac{L_0}{T} = \frac{g}{2\pi}T = \sqrt{\frac{gL_0}{2\pi}} \qquad \textit{Eq. 7.1}$$

where T is the wave period, g is the gravitational acceleration and L_o the offshore wavelength.

Approaching the coast, waves become less dispersive and wave phase depends more strongly on water depth. The wavelength and period of the wave are related to the water depth by the dispersion relationship:

$$\sigma^2 = g * k * \ tanh(kh) \qquad \textit{Eq. 7.2}$$

where $\sigma=2\pi/T$ is the angular frequency (T wave period) and $k=2\pi/L_o$ is the wavenumber. Considering that wave celerity c can be also written as:

$$c = \frac{L}{T} = \frac{\sigma}{k} \qquad \textit{Eq. 7.3}$$

Eq. 7.2 can be re-written as:

$$c = \sqrt{\frac{gL}{2\pi} * tanh(\frac{2\pi}{L}h)} \qquad \textit{Eq. 7.4}$$

which describes celerity in the nearshore.

In shallow waters ($h/L_o < 0.05$), under the assumption of small wave amplitude and locally horizontal bottom, the simplest case of linear wave theory expresses the wave celerity as:

$$c = \sqrt{gh} \qquad \textit{Eq. 7.5}$$

However, a number of previous researches have shown that the linear shallow water dispersion relation underestimates the observed breaking wave speed phase, both in the field (e.g., Thornton and Guza, 1982; Stockdon and Holman, 2000; Holland, 2001) and

in the laboratory (e.g.; Stive, 1980; Stansell and MacFarlane, 2002) because of the finite amplitude effects.

Within the surf zone, where wave break and nonlinear effects of finite wave amplitudes are predominant, empirical alternative was proposed to approximate breaking wave phase with modified shallow water as:

$$c = \alpha\sqrt{gh} \qquad \textit{Eq. 7.6}$$

where α is a constant to be determined. Typical proposed value was α=1.3 (Stive 1980, Schäffer et al., 1993; Madsen et al., 1997), with slight differences found when a wave-by-wave approach was applied (α=1.06÷1.32 Stansby and Feng, 2005; α=1.2, Almar et al., 2011; α=1.14 Tissier et al., 2011, α=1.18 Postacchini and Brocchini, 2014).

7.1.2 Depth inversion technique with Timestacks

The main concept of using video imagery for retrieving nearshore topography is based on the measurements of wave celerity in the nearshore. Depth inversion is the indirect technique that exploits the relations between wave celerity and local water depth to determine the sea bottom.

As previously seen in Section 4.3.1, shoaling and breaking waves patterns can be recognized on Timestack images. The present chapter aims to present video remote sensing data as a way to derive surface wave celerity from wave pattern on image, hence to determine bathymetry through depth inversion technique.

In the last two decades, several methods have been proposed to derive nearshore bathymetry with the use of video Timestack images. Focusing on the methodology used for measuring wave celerity on these images, three main groups of methods can be distinguished based on frequency domain analysis (Stockdon and Holman, 2000; Zikra, 2012; Holman et al., 2013), time domain analysis (Almar et al., 2008; Liu et al., 2012), and wave feature detection using image processing technique (Yoo, 2007; Catalan and Haller, 2008). A second distinction can be made based on the adopted method for depth inversion, dividing between the application of linear wave theory (Stockdon and Holman, 2000; Zikra, 2012; Holman et al., 2013) and non-linear wave theory (Yoo, 2007, Catalan and Haller, 2008; Almar et al., 2011).

Stockdon and Holman (2000) computed wave celerity from the time series of cross-shore pixel brightness intensity using cross-spectral scheme. The results of linear depth inversion showed a mean bias error in shallow water (less than 3 m in depth) three times higher than the mean bias of -0.20 m in deeper water, tending to increase with increasing wave heights. Thus, this method was not successful at depth inversion where waves were breaking.

Yoo (2007) extracted individual wave crest trajectories from Timestacks to calculate wave phase celerity using Radon transform. Non-linear depth inversion was achieved coupling video-derived information to three model components, namely wave breaker model, wave dissipation model and wave shoaling model. Bathymetric results showed a mean bias of about 0.1 m when compared to ground truth data. Nonetheless, this work was restricted to the surf zone till a maximum depth of 3 m, where all the wave properties could be properly derived.

Catalan and Haller (2008) computed wave phase speeds using a feature tracking algorithm and cross-correlation technique applied to Timestacks. The experiment in laboratory facility tested several linear and non-linear wave dispersion relations depth inversion technique. Local depth was retrieved with an accuracy of about 10% with the best solution for non-linear depth inversion.

Almar (2009) measured wave celerity applying a double cross-correlation on Timestack from video acquisition at Biscarrosse beach, achieving a bathymetry map with an RMSE of 0.95 m with four days of video acquisition. Almar et al. (2011) re-proposed the technique for wave celerity assessment coupled to non-linear Boussinesq wave model during laboratory experiment. Video-derived wave measurements included wave height, wave period and wave celerity. For the considered laboratory case, error on bathymetry varied between 8% and 14% depending on the non-linear model applied on depth inversion.

Liu et al. (2012) measured wave celerity applying simple cross-correlation technique to the time series of the pixels brightness intensities sampled directly from rectified images. Water depth was derived from the linear wave theory's dispersion relationship. Estimated bathymetry matched the ground truth data with an approximated bias of 0.3 m, although larger discrepancy was observed within the surf zone.

Zikra (2012) used wave number inversion method, based on cross- spectral correlation technique (Plant et al., 2008) for the bathymetry inversion method. Results were lower in the area between shoreline and breaker zone, however analysis was limited till a depth of 2 m.

Holman et al. (2013) developed a tool to estimate submerged bathymetry based on ocean wave celerity, called cBathy, that has been incorporated in Argus package and was applied on numerous sites worldwide. Its complexity derived from several years of development (e.g., Lippmann and Holman, 1989; Lippmann and Holman, 1990; Lippmann and Holman, 1991; Holman et al., 1993; Holland et al., 1997; Stockdon and Holman, 2000; Holland, 2001; Plant et al., 2002; Alexander and Holman, 2004; Holman and Stanley, 2007; Plant et al., 2008; Plant et al., 2009) and achieved good results by a sophisticated series of algorithm based on cross-spectral analysis. Field tests showed a bias and RMSE of about 0.50 m, with largest bias near the offshore limits of analysis and near the steep shoreline. Performance was excellent for small waves but degraded somewhat with increasing wave height.

Table 7.1 resumes characteristics and errors of the above-revised works. Note that a direct bias comparison among the state-of-art works is difficult due to the different nearshore morphology and hydrodynamics among the studies, along with the variable spatial and temporal coverage of the video imagery.

*Table 7.1. Review of reported depth inversion performances. Errors are expressed in term of RMSE- Values with subscript * are mean bias.*

Author	Year	Study site	Wave dispersion relationship	Error breaking area	Error shoaling area	Method for celerity
Stockdon & Holman	2000	Duck (USA)	linear	0.6 m	0.2 m	cross-spectral analysis - EOF
Yoo	2007	Myrtle Beach (USA)	non-linear	0.1 m	0.4m	wave trajectory
Catalan & Haller	2008	Laboratory	non-linear	10%		cross-correlation
Almar	2009	Biscarosse (France)	linear	0.95 m		double cross-correlation
Almar et al.	2011	Laboratory	non-linear	8%-14%		double cross-correlation
Liu et al.	2012	Miyazaki (Japan)	linear	0.3* m		cross-correlation
Zikra	2012	Hasaki (Japan)		0.44 m		wavenumber
Holman et al.	2013	Duck (USA)	linear	0.51 m	0.19 m	cross-spectral analysis – Kalman temporal filter

7.2 Motivation and objectives

The existing methodologies to derive nearshore bathymetry from Timestacks have both strengths and weaknesses. The works that estimated wave celerity in frequency domain achieved satisfactory bathymetric map in the range of depth 3÷10 m, whereas they lacked in accuracy in the breaker zone. On the other hand, wave celerity computed by time domain analysis used non-linear wave theory for depth inversion, hence the computation of additional wave parameters such as wave breaking height and wavelength were necessary to assess bathymetric measurements.

Overall, the existing techniques were tested in laboratory (Catalan and Haller, 2008; Almar et al., 2011), during low energy wave and low energy environment (Yoo, 2007, Liu et al., 2012), or were validated with ground truth data collected at different time than video acquisition (Zikra, 2012). The tool cBathy (Holman et al., 2013) has been extensively used worldwide (Table 7.2), however it was never applied for waves bigger than 2.0 m (Brodie at al., 2018) and showed inaccuracy increasing proportionally with wave height.

Table 7.2. cBathy application sites and performance statistics (from Brodie at al., 2018).

Date	Hs (m)	Tp (s)	Bias (m)	RMSE (m)	Tide (m)	Location	# Obs.	Reference	Notes
2009–2011	0.25–2.00	–	0.19	0.51	0.98	Duck, NC USA	16	Holman et al., 2013	
Mar-2013 to Mar-2014	<1.65	–	0.59	0.79	–	SandEngine Netherlands	6	Rutten et al., 2017	$-10 < depth < -5$ m
Mar-2013 to Mar-2014	<1.65	–	−0.01	0.34	–		6		$-5 < depth < -1$ m
Mar-2013 to Mar-2014	<1.65	–	−0.92	0.34	–		6		$-1 < depth < 0$ m
13-Jul-13	–	7.1	−0.41	0.56	>3	Agate Beach, OR, USA	1	Holman et al., 2013	
17-May-12	1.19	5–7	0	0.52	–	New River Inlet, NC, USA	1	Holman and Stanley, 2013	
10-Apr-14	1.16	10.5	–	1.06	2.78	Porthtowan, Cornwall, England	1	Bergsma et al., 2016	
20-Feb-13	0.64	5.8	−0.18	1.01	1.4–1.9	Kijkduin, Netherlands	1	Wengrove and Henriquez, 2013	$\hat{h}_k$ results
17-Apr-14	0.52	10.4	–	2.05	6.03	Porthtowan, Cornwall, England	1	Bergsma et al., 2016	
01 to 04 Jul-13	<0.50	–	–	0.48–0.66	–	SandEngine, Netherlands	1	Radermacher et al., 2014	
17-Feb-13	0.22	8.5	−0.5	1.27	1.4 to 1.9	Kijkduin, Netherlands	1	Wengrove and Henriquez, 2013	$\hat{h}_k$ results
	Average:		−0.26	0.91					

In such context, this study proposes a novel methodology to assess wave celerity in the spatial domain, making use of the distinction between shoaling and breaking wave patterns on Timestacks.

The Timestacks produced from surfcam video acquisition at the high-energy coastal environment of Ribeira d'Ilhas beach (Section 3.4), on the western Portuguese coast, were used to develop the methodology. During the two days of video acquisition, wave conditions were stationary (H_s=1.7 m) on the first day, while on the second day significant wave height increased from 1.7 m to 3.7 m.

The rocky nearshore platform at this study site (Section 3.4.2) permitted to test and validates the methodology on a known and non-movable sea bed, setting this work apart from all others field-related video depth inversion works.

This work represents the first attempt of measuring wave celerity and retrieving nearshore bathymetry from video imagery at the Portuguese coast.

7.3 Methods

Video-based depth inversion technique requires image processing procedures and wave celerity measurements to achieve local bathymetry map (Figure 7.1).

In this section, a novel methodology to measure wave celerity and to retrieve nearshore bathymetry from Timestacks is described.

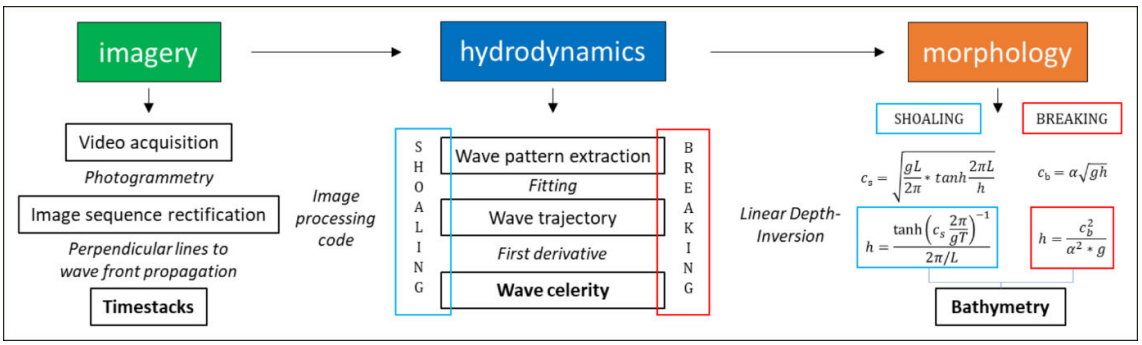

Figure 7.1. Flow chart of video depth inversion technique.

7.3.1 Conceptual model

As seen before in Section 4.3.1, Timestack is a time-space image in which each wave feature represents the trajectory of a wave travelling through cross-shore spatial dimension over time.

Considered the wave trajectory as moving point *s(t)* travelling in time *t* through space *x*, the average velocity is given as:

$$\bar{v} = \frac{\Delta x}{\Delta t} \qquad \textit{Eq. 7.7}$$

where $\bar{v}$ is the average velocity of a point moving through a displacement Δx between two positions during a time interval Δt (Figure 7.2-a).

In Physics, a second kind of velocity, the instantaneous velocity, describes the punctual speed *v* at any instant *t* as:

$$v = \lim_{\Delta t \to 0} \frac{\Delta x}{\Delta t} = \frac{dx}{dt} \qquad \textit{Eq. 7.8}$$

where the limiting value *v* is the first derivative of *x* with respect to time *t*, which is also the slope of the tangent line to the function *s(t)* at any particular point (Figure 7.2-b).

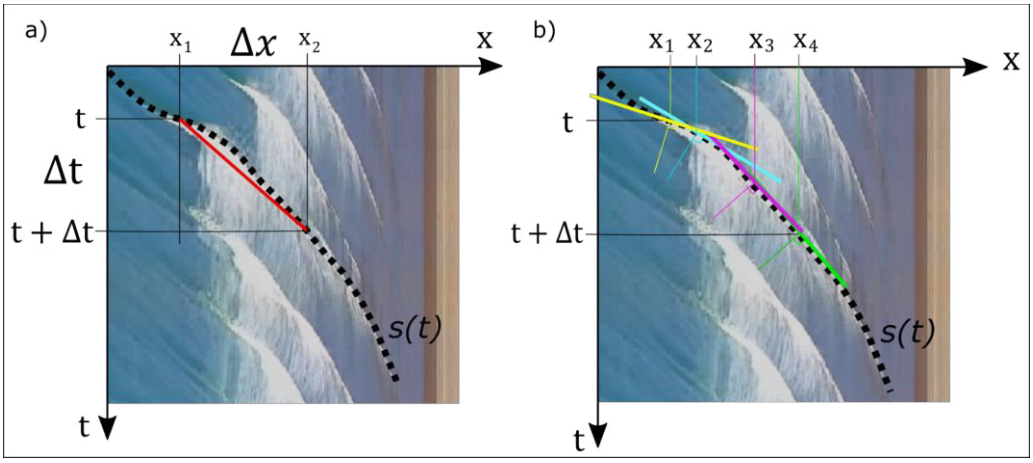

Figure 7.2. Wave trajectory on Timestack (black dotted line). a) concept of average wave speed between two positions x_1 and x_2; Red line represents $\frac{\Delta x}{\Delta t}$; b) proposed methodology, which measures celerity as derivative value of wave trajectory at a point. Colored lines shows tangent line at x_j points.

Previous works (e.g., Almar et al., 2008; Catalan and Haller, 2008; Liu et al., 2012) computed wave phase speed as the mean propagation velocity in time.

In this work, the measurement of wave celerity as instantaneous velocity is proposed. Firstly, wave patterns were extracted by an image processing algorithm from Timestacks. Successively, wave instantaneous celerity was computed as the first derivative of the extracted wave trajectories.

The methodology distinguished between shoaling and breaking wave patterns, allowing a different approach for the depth inversion technique based on the type of wave. Simple wave dispersion linear theory formula (Eq. 7.4) was applied to shoaling domain, whereas inverted Eq. 7.6 was used to infer sea bottom depth at wave breaking domain.

7.3.2 Study sites and video data

The surfcam video-acquisition at Ribeira d'Ilhas beach was chosen to develop and validate the depth inversion procedure. The site was particularly suitable for this study, as the nearshore area was constituted by non-movable rocky bottom, and detailed bathymetry was available from LiDAR (chosen from 2 m to 11 m depth; Silva et al., 2012) and RTK-GPS surveys (from shoreline to 2 m depth). The two surveys were joined to produce a single bathymetry map that covered about 117000 m^2 in the range of depth 0 to11 m (Figure 7.3-c).

Video dataset collected at Ribeira d'Ilhas was used to produce 10-min Timestacks. Shoreline orientation is typically taken as reference for Timestack production (e.g., Yoo, 2007; Almar, 2009), because in general waves tend to reorganize their direction perpendicular to the shore when entering in the shallow water (Komar, 1976; Dean and Dalrymple, 1984). However, in the study case, the coastline was delimited by irregularly shaped rocky cliff toe, where large boulders are scattered over the rocky shore platform, therefore finding a perpendicular line to the shore was a difficult task. Therefore, as the aim was to measure wave propagation speed, pixel arrays were sampled selecting the main perpendicular profile to wave propagation direction.

Several rectified frames were visually analysed to manually mark wave front lines propagating towards the shore, with the aim of selecting 14 cross-shore transects perpendicular to wave front. Transects were used to sample cross-shore pixels array and produce Timestacks over the rectified image sequence. Timestacks were numbered from 1 to 14, starting from the most southward transect, and called with the acronym TSK (Figure 7.3).

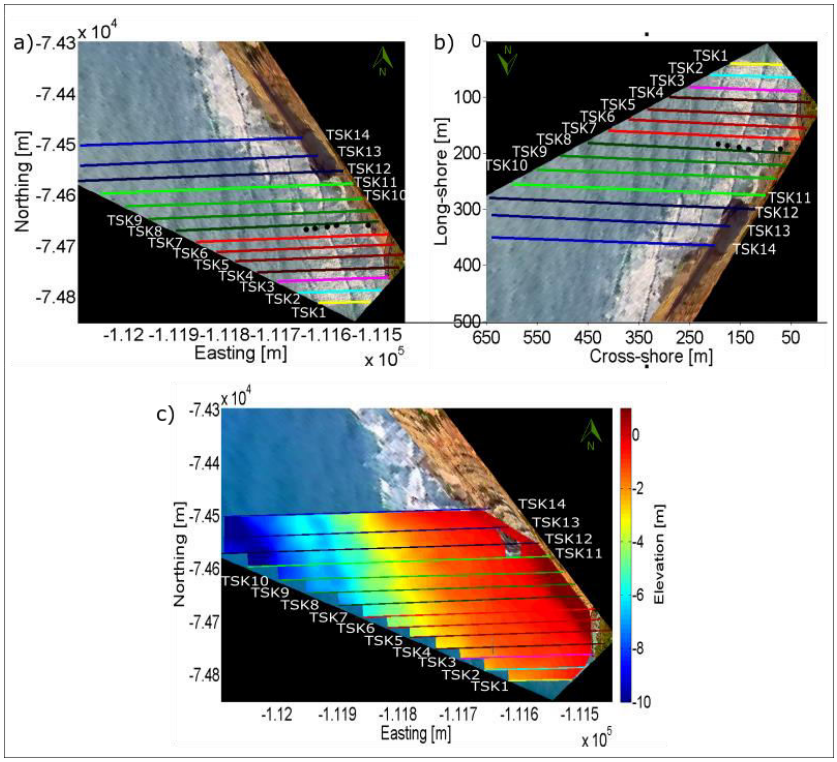

Figure 7.3. Map of Timestack profiles plotted on rectified image in world coordinates (a), distance in meters (b) and superimposed on the ground truth bathymetry (c).

Transect cross-shore lengths varied between the minimum of 100 m for TSK 1 and the maximum of 525 m for TSK 12 (Figure 7.3-b). Timestacks transects were spaced with and alongshore offset of 25 m, covering the whole area where surveyed bathymetry was available (Figure 7.3-c), which extended about 350 m longshore and around 600 m cross-shore.

From video acquisitions, 10-minutes Timestacks for a single transect were 52 for the first days and 42 for the second day. Considering the 14 transects, whole dataset comprised 1316 Timestacks.

7.3.3 Wave trajectory extraction from Timestack

An image processing code was built to extract the wave trajectories corresponding to shoaling and breaking waves (Figure 7.4). The algorithm entailed four steps: i) pixel intensity correction was applied to the Red Band of Timestacks to enhance the contrast between wave patterns and image background; ii) different intensity thresholds were set to separate shoaling waves (dark pixel lines) and breaking waves (bright pixel lines) in two distinctive datasets; iii) a Sobel edge detection filter was applied to each set, and finally; iv) lines were extracted in pixel form. The relatively simple algorithm run completely automatically and was developed with open-source software (Python and OpenCV). Time coordinate and cross-shore position of each pixel was labelled into an ASCII file format to automate the following processing steps.

The ASCII file was read in Matlab environment and processed by a set of codes to clean raw wave trajectories detection. Firstly, acceptance thresholds were set to consider only waves patterns composed by a certain minimum number of pixels. This step removed erroneous detection determined by breaking waves foam, sun glitter, cloud shadow, and in general small wave patterns that did not represent correctly wave trajectory. A minimum acceptance threshold of 60 pixels was found feasible for both breaking and shoaling waves. Secondly, accepted wave patterns were fitted by a second order polynomial to correct and filter out scattered noise. The final product was a dataset of lines in time-space domain (Figure 7.4-right) representing single wave trajectories through the nearshore area. The dataset comprised both shoaling and breaking waves, separately.

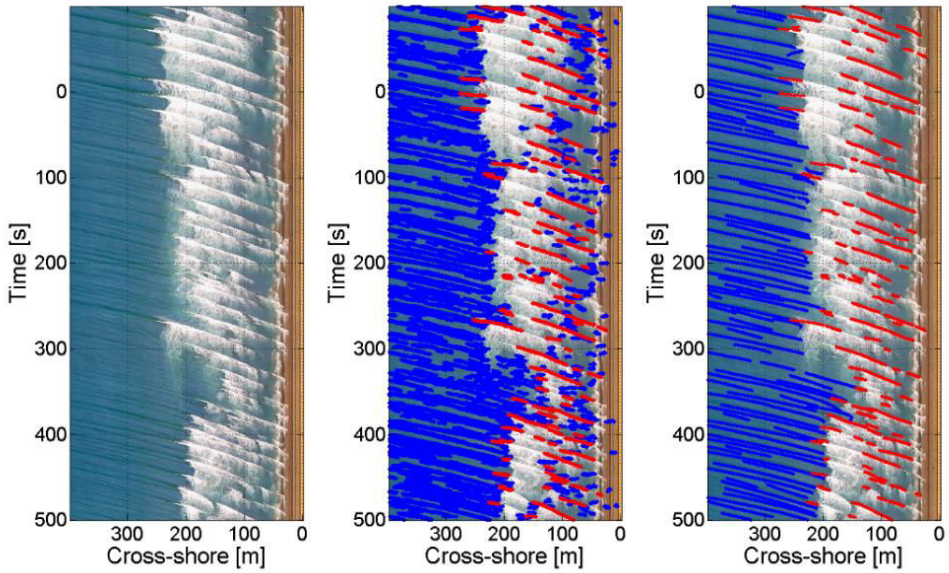

Figure 7.4. Example of original Timestack (left), detection algorithm output (middle) and fitting process results (right). Blue lines represent shoaling waves and red lines breaking waves.

The performance of wave features detection was evaluated by visual inspection of the outputs. Taken in consideration the complexity of the task, algorithm outcomes were satisfactory despite the simplicity of the code steps. Detection inaccuracy occurred mostly on those images in which pixel intensity changed due to moving clouds in the sky. The changing in pixel brightness made difficult to perform a correct detection of the wave trajectory during such atmospheric event, because pixel intensity thresholds were previously set using images acquired during optimal conditions. A second type of erroneous detection was related to the hydrodynamics properties of the real sea state. Sea surface elevation varied in time due to different wave height and period, wind conditions, and water level. In addition, waves interacted with the current and the sea bottom, hence it was common to observe irregular wave patterns, with wave trajectories interacting with other wave trajectories. Although these issues occurred occasionally, filtering and fitting process was set to remove wrong or not accurate detections, such as short or unclear wave features and spurious data (Figure 7.4-right).

7.3.4 Wave celerity assessment

Following the simple physical concept that the first derivative of a line in time-space domain represents the instantaneous velocity of a point travelling through space (Section 7.3.1), the first derivative was computed for each wave trajectory the dataset in order to retrieve wave celerity of each detected wave.

To obtain a representative wave celerity profile, a cross-shore 2 m grid (corresponding to 2 pixels interval on Timestack) was considered to compute the median values among all wave celerities measured within each 10 minutes Timestacks (Figure 7.5).

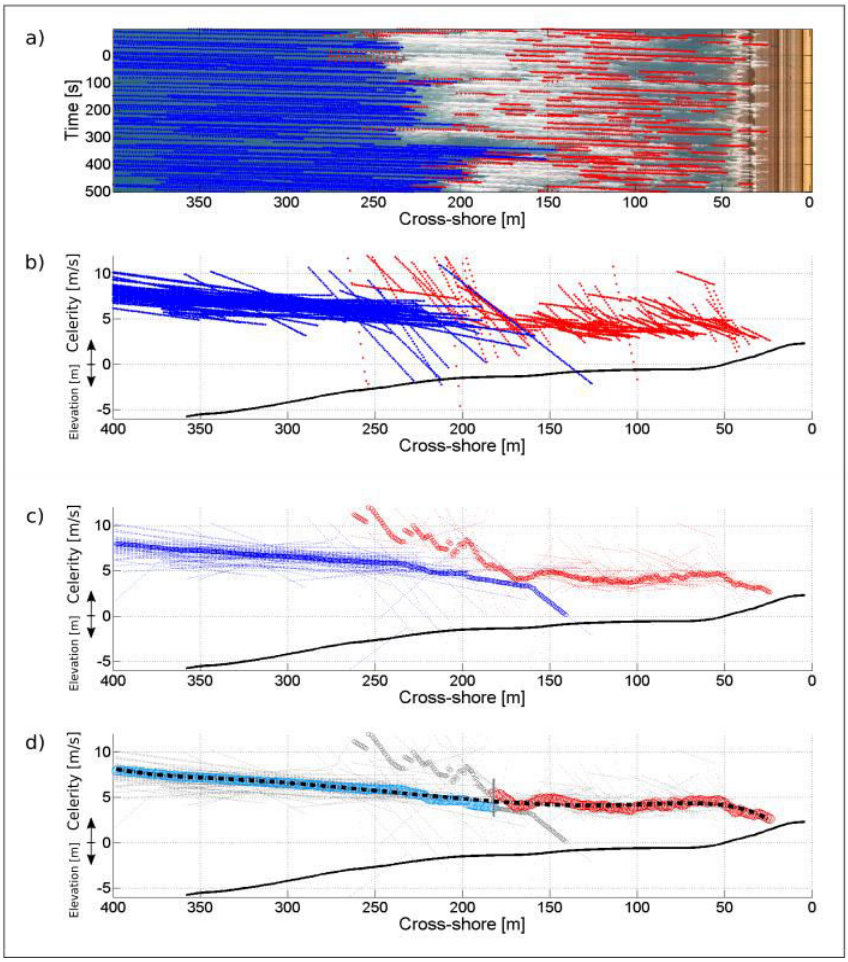

Figure 7.5. Sequence of steps to measure wave celerity. Blue color refers to shoaling celerity, red color to breaking celerity. a) filtered data from image processing results on Timestack; b) first derivative output plotted over the correspondent beach profile (solid black line); c) median value of shoaling and breaking celerity among all data; d) celerity profile (dashed black line), obtained joining shoaling and breaking celerity. Data plotted in grey were discarded based on the outer/inner surf boundary (horizontal dark grey line at x=180 m).

7.3.5 Depth inversion

Bathymetry map was assessed using depth inversion technique from the measured celerity profiles. Shoaling wave celerity c_s was used to resolve the inverted Eq. 7.4 to obtain sea bottom depth as:

$$h = \frac{tanh\left(c_s^2 * \frac{2\pi}{gL}\right)^{-1}}{2\pi/_L} \qquad Eq.\ 7.9$$

where c_s is shoaling celerity and g is the gravity acceleration.

Breaking/broken wave celerity c_b was used to retrieve depth in the surf zone using modified linear wave theory (Eq. 7.6) as:

$$h = \frac{c_b^2}{\alpha^2 * g} \qquad Eq.\ 7.10$$

where the value α was chosen after the analysis of wave celerity measured by the proposed technique.

7.3.6 Validation

Beach profiles derived from depth inversion technique were compared to the corresponding nearshore profiles extracted from the surveyed bathymetry. In addition, two bathymetry maps were produced, one for each day. Results were compared to ground truth data as:

$$error = h_{video} - h_{ground\ truth} \qquad Eq.\ 7.11$$

in term of Bias (mean error), Median Error, Mean Squared Error (MSE), and Root Mean Square Errors (RMSE). Positive bias values indicated depth underestimation, while negative values meant overestimation of local depth from video technique.

7.4 Results

The results presented in this section are based on the images acquired over two rising tide phases, one for each day of observations, from low tide to high tide. Breaking wave celerity refers to values computed from wave patterns detected inside the inner surf zone. Shoaling celerity, instead, is considered from those values computed from the most seaward point visible on Timestacks till the last breaking point of 10-minute interval, which was found as the main peak of pixel average intensity following the technique previously described in Section 5.3.3.

7.4.1 Wave celerity

Figure 7.6 shows celerities obtained over all the profile in respect to depth for both days. Shoaling and breaking waves are plotted separately. Measured shoaling celerities were plotted against wave linear wave approximation, namely Eq. 7.4 and Eq. 7.5.

As waves propagate into shallower water, their wavelength decrease, however video technique was not set to measure wavelength L needed to resolve Eq. 7.4. Therefore, the changing length of L over the nearshore was calculated using the direct method proposed by Hunt (1979), as L_H.

Regarding shoaling celerity, it is possible to observe how speeds for higher depth were slower during high tide (clearer green dots) and faster during low tide (see depth range 6÷10 m). On the contrary, shoaling values before breaking were faster during high tide than during low tide for the same depth (3÷5 m). It is also worth to note that shoaling celerity values were more homogeneous during higher wave and period on day 29th, while on day 28th spurious data were registered during low tide. In general, measured shoaling celerity was found in agreement with the linear wave dispersion computed using L_H, in particular during day 28th. As expected, simple linear relation (Eq. 7.5) did not describe properly the wave phase speed for depth higher than 4 m.

Breaking wave celerity had similar values during both days. As already observed by other authors (Catalan and Haller, 2008; Tissier et al., 2011), extreme breaking speed values were found about two time faster than the wave speed model. These anomalies

were the result of the apparent wave acceleration due to the sudden decrease in height when wave crest collapsed at the incipient breaking point.

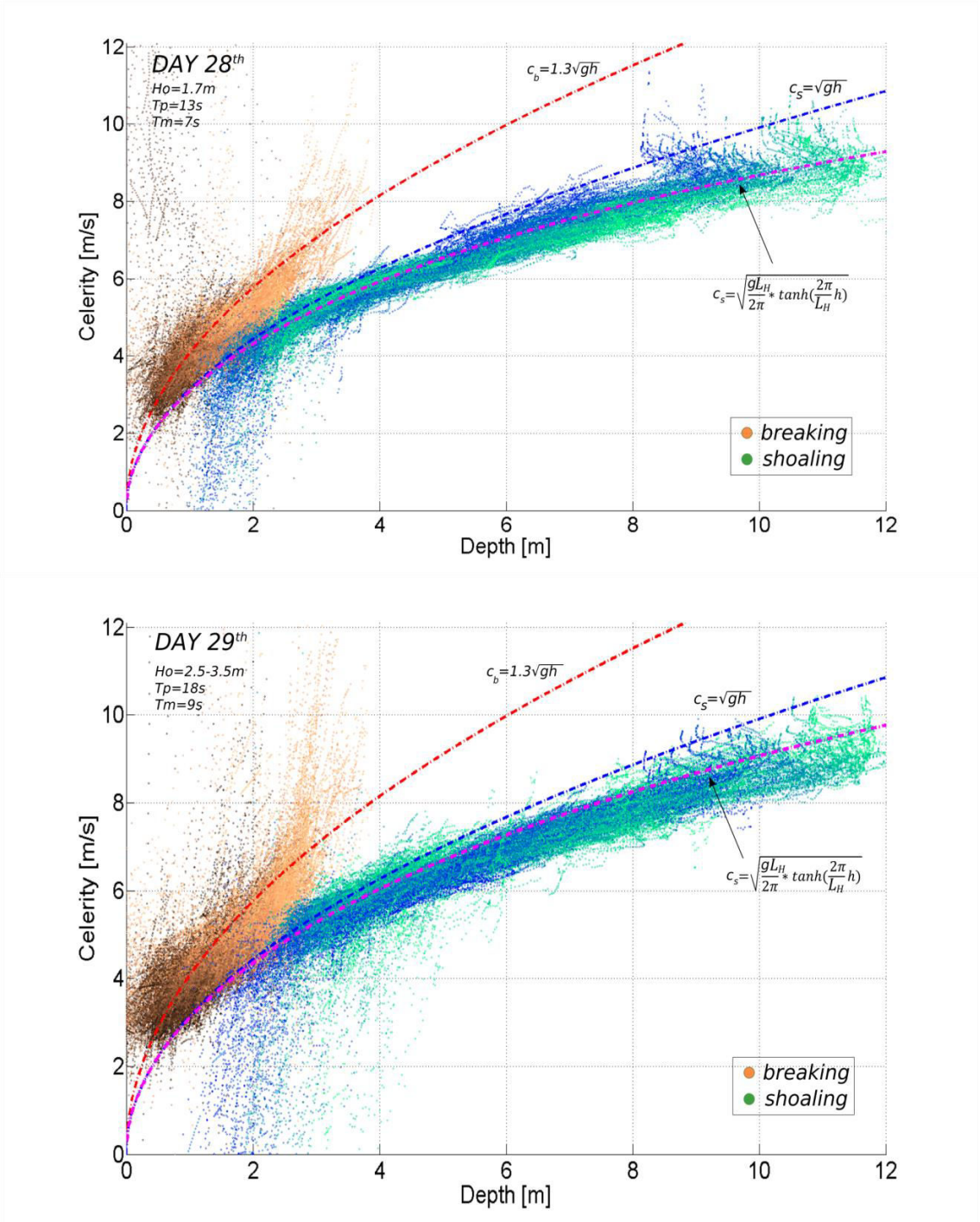

Figure 7.6. Shoaling (blue/green dots) and breaking (black/orange dots) celerity measures versus depth. Light to dark color tones refer to low and high tide, respectively. Dashed lines indicate modelled celerity with different linear wave approximations.

Table 7.3 resumes the number of celerity data obtained in relation with estimation of number of waves observed. The proposed methodology allowed to accurately describe the wave celerity with a high amount of records. Assuming that each wave pattern was correctly detected by the image processing algorithm, in average, the celerity profile of each wave was represented by around 120 values. In practice, some waves were not marked by the detection algorithm, therefore the number of measures was higher for less waves than the total amount that reached the shoreline.

Table 7.3. Wave celerity data resume. T_m is wave mean period measured by pressure transducers.

	28th		29th	
	C_b	C_s	C_b	C_s
Number of records	128000	151400	133500	147000
Tm (mean period)	7 s		9 s	
Duration of observations	4h 30min		5h	
Number of waves	2700		1800	

7.4.1.1 Shoaling celerity analysis

Figure 7.7 shows the normalized relative probability density function and the cumulative distribution function obtained with the measured shoaling celerity over the two days, computed till a depth of 12 m. Shoaling celerity was characterized by an average c_s=6.25 m/s and a standard deviation σ_s = 1.7 m/s.

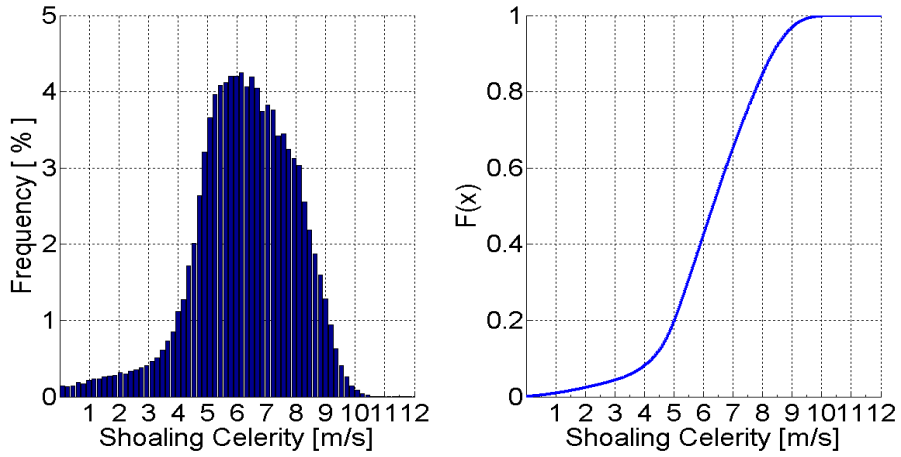

Figure 7.7. Shoaling wave celerity probability density function (left) and cumulative distribution function (right).

The plot of the measured shoaling celerity, made dimensionless using the gravitational acceleration g, period T, and deep water phase speed over the Airy wave theory (Figure 7.8), indicated that waves were shoaling under a regime of shallow and intermediate deep water regimes. On day 28th (green squares) the small wave period determined higher ratio h/L_o, while longer L_o during day 29th resulted in most waves shoaling over shallow water regime.

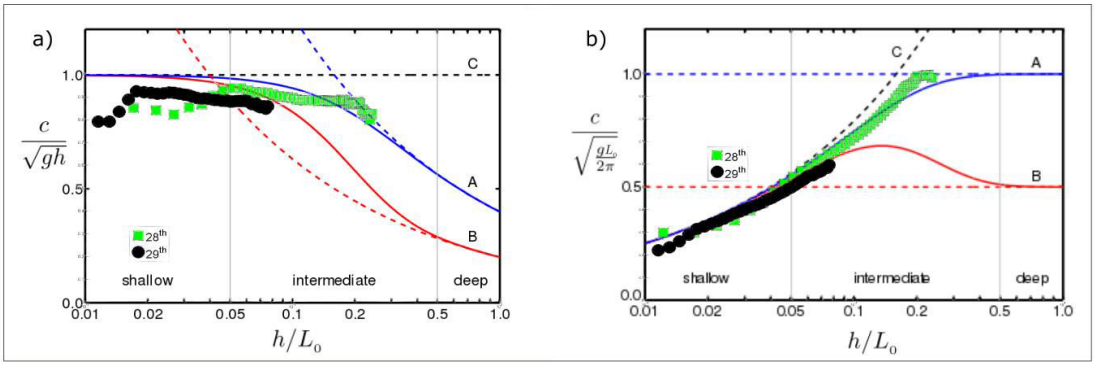

Figure 7.8. Wave dispersion and shoaling celerity from day 28th (green squares) and 29th (black circles). Phase velocity divided by shallow-water phase velocity (a) and deep-water celerity (b) as a function of relative depth h/L$_o$. Blue lines (A): phase velocity. Red lines (B): group velocity. Black dashed line (C): phase and group velocity valid in shallow water. Blue and red solid lines: dispersion relation valid in arbitrary depth. Dashed lines (blue and red): deep water limits.

The last analysis concerned the comparison (Figure 7.9) between measured and predicted wave shoaling celerity using linear wave dispersion solved with L_H calculated from Hunt (1979) formulation. Measurements were in good agreement with modelled values, indicating that Hunt (1979) solution was suitable for depth inversion technique. Shoaling celerity values lower than about 4.5 m/s were plotted for comprehension and were not considered for depth inversion, as they were measured within the inner surf zone where waves were breaking (Figure 7.6).

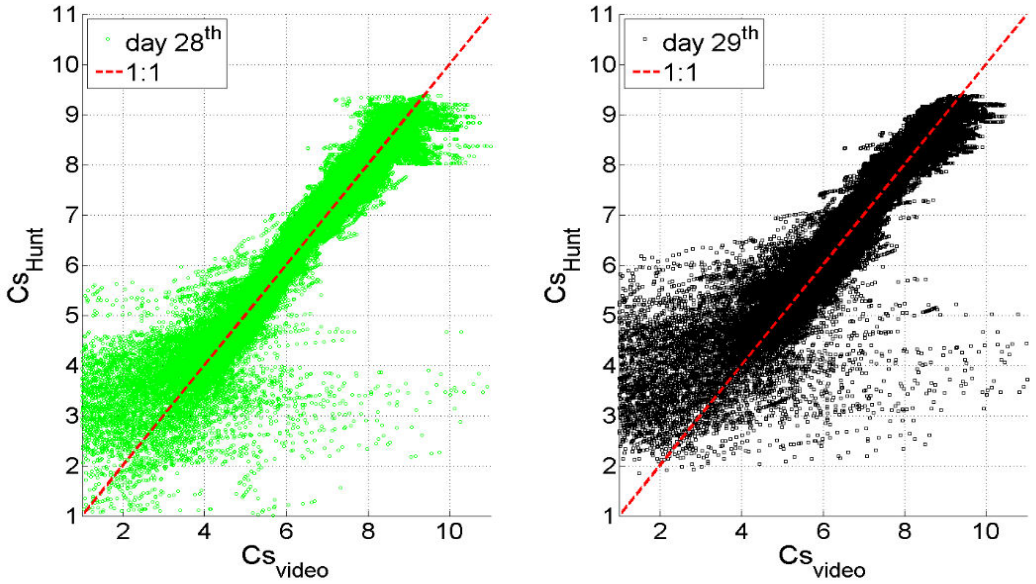

Figure 7.9. Measured shoaling celerity versus predicted shoaling celerity computed using Hunt (1979) formulation to approximate wavelength.

7.4.1.2 Breaking celerity analysis

Figure 7.10 illustrates normalized relative probability density function and cumulative distribution function obtained with measured breaking celerity over the two days. Breaking celerity was characterized by an average c_b=4.76 m/s and a standard deviation σ_c = 1.51 m/s, results that were comparable to the values obtained by Postacchini and Brocchini (2014) using cross-correlation technique from Truc Vert field data (c_b = 4.47 m/s, σ_c = 1.09 m/s).

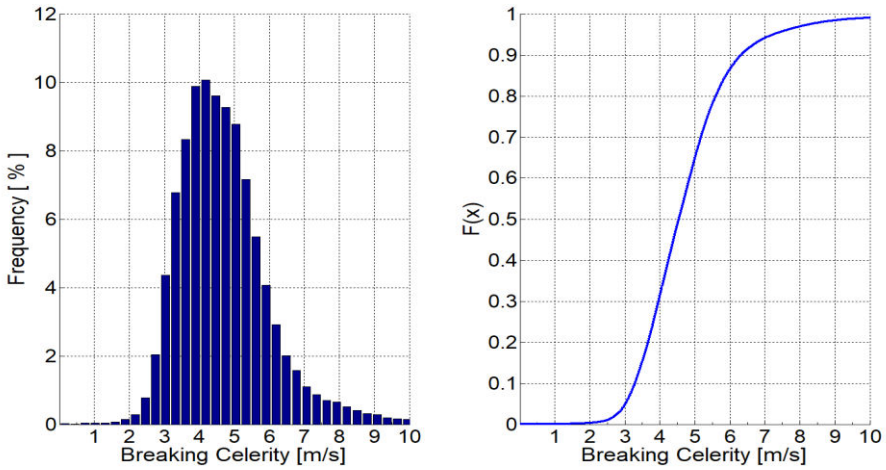

Figure 7.10. Breaking wave celerity probability density function (left) and cumulative distribution function (right).

Breaking celerity dataset was previously (Figure 7.6) compared exclusively to the linear theory equation modified with α=1.3 (Stive 1980; Schäffer et al., 1993; Madsen et al., 1997), nonetheless a better approximation of the term α would lead to a better depth inversion. Best performing α for breaking celerity dataset was found α=1.21 (Figure 7.11), with R^2=0.8. Considering daily values separately, analysis led to about the same values, with α=1.21 and α=1.2 for the first and second day, respectively. Value of best fitting α=1.21 was similar to α=1.14 arisen from field measurements (Tissier et al., 2011) and α=1.18 found by Postacchini and Brocchini (2014) using wave-by-wave analysis.

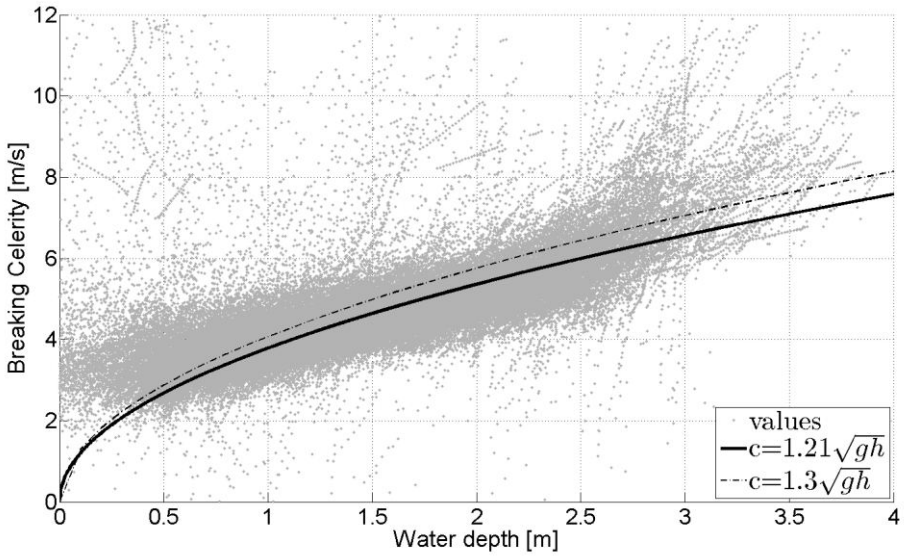

Figure 7.11. Best fitting α parameter for wave breaking celerity.

Figure 7.12 shows the measured celerities normalized by the linear approximation in shallow water as a function of the non-linearity parameter $\epsilon = H/h$, which quantifies the non-linear effect in the surf zone. Non-linearity parameter ϵ was computed using the local water depth h and the wave height H measured by the most seaward pressure transducer (Section 3.4.3).

Results were consistent with observations of previous works that used cross-correlation technique to measure wave breaking celerity (Tissier et al, 2011; Postacchini and Brocchini, 2014).

Median and average breaking celerity (blue and green filled dots), computed for heights interval of 0.25 m, were similar in values, and followed the exponential trend

found by Tissier et al. (2011, equation c_1 in Figure 7.12) in the range $0.3 < \epsilon < 0.6$. Between $\epsilon = 0.6$ and $\epsilon = 1.1$, data agreed with the formulation c_2, while from $\epsilon = 1.5$ data followed equation c_3. Formulations c_2 and c_3 were proposed by Postacchini and Brocchini (2014), using breaking celerity values computed using cross-correlation method.

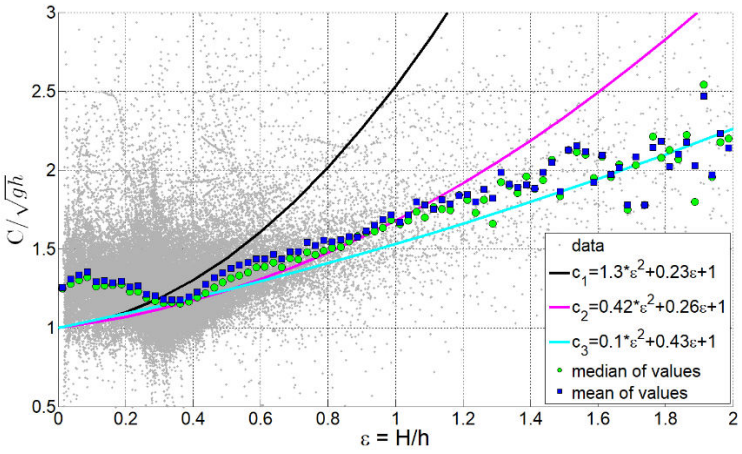

Figure 7.12. Normalized wave breaking celerity against non-linearity parameter ϵ. Expression c_1 is from Tissier et al. (2011), c_2 and c_3 from Postacchini and Brocchini (2014).

7.4.2 Depth inversion technique

After the accurate analysis of shoaling and breaking celerity, depth inversion technique was applied to retrieve nearshore bathymetry. For shoaling waves, linear wave dispersion relation was written for local depth as:

$$h = \frac{tanh\left(c_s \frac{2\pi}{gT}\right)^{-1}}{2\pi/L_H} \qquad \textit{Eq. 7.12}$$

As there was not analytical solution for h, iterative method between h and L_H was necessary to solve the equation.

Local depth within the surf zone was found inverting Eq. 7.6, and using best fitting value of α=1.21 as:

$$h = \frac{c_b^2}{1.21^2 * g} \qquad \textit{Eq. 7.13}$$

7.4.2.1 Subtidal profiles

The underwater profiles along the target area obtained from depth inversion technique are shown in Figure 7.13. Estimates closely approximated ground truth data both in shoaling and surf zone, with not complex shape well reproduced with cross-shore grid of 2 m.

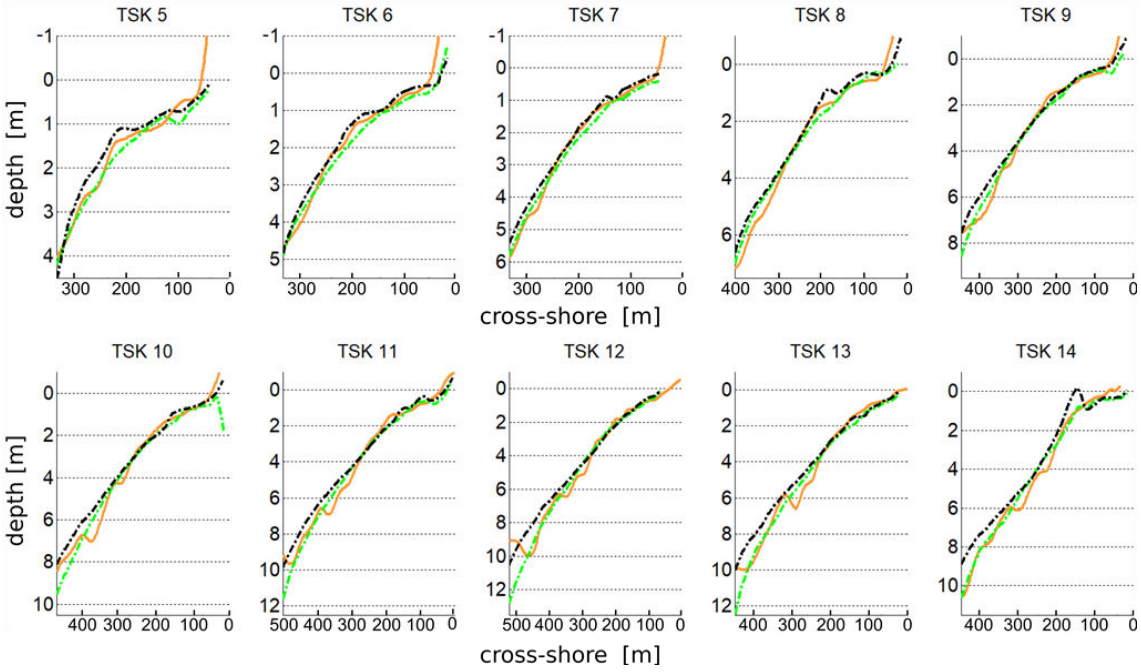

Figure 7.13. Comparison between ground truth data (orange thick lines) and video-measured profiles from day 28th (green dashed line) and day 29th (black dashed line).

Mean bias for the profiles measured on day 28th was between 0 and -0.2 m, negative values indicating that depth was in average overestimated (Figure 7.14). RMSE varied between 0.1 m and 0.8 m, with an average RMSE=0.4 m among all profiles. Estimates during more energetic sea state from day 29th registered instead positive mean bias between 0.2 m and 0.5 m, therefore depth was in average underestimated with higher waves. RMSE spanned between 0.25 m and 0.7 m, with a mean RMSE = 0.5 m, comparable to values obtained with data from day 28th.

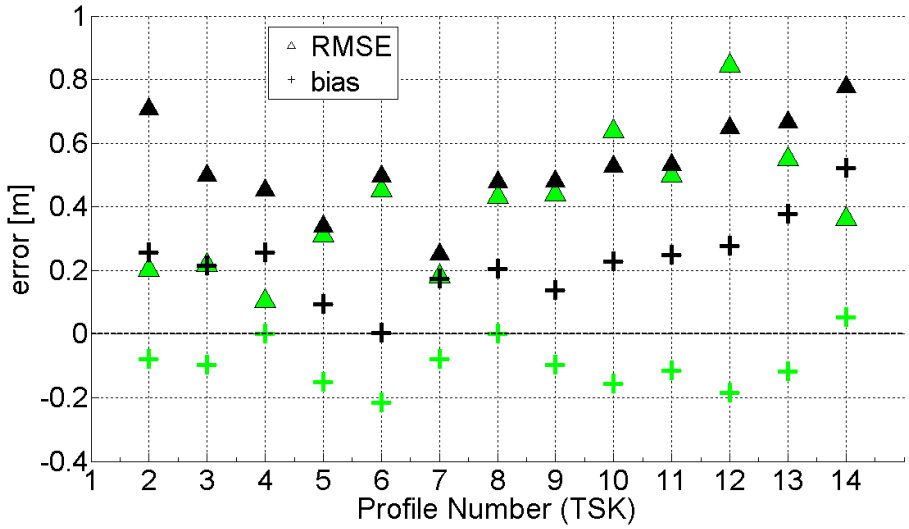

Figure 7.14. Mean bias (crosses) and RMSE errors (triangle) in profile estimation. Green color refers to data from day 28th, black to the day 29th.

The distribution of bias (Figure 7.15-a) for the dataset from day 28th shows that mean bias was about -0.1 m, with 50% of values (difference between 75th and 25th percentiles). Regarding dataset from day 29th (Figure 7.15-b), average bias was 0.08 m, with interquartile comprised between 0.04 m and 0.38 m, therefore the magnitude of depth underestimation with higher waves during the second day was larger than the overestimation on first day. Such analysis is confirmed by Figure 7.16, in which 2450 bias records between video-derived and surveyed profiles are plotted in dependence to depth. Highest disparities were registered at deepest points on day 28th, and at around 7 m depth on day 29th.

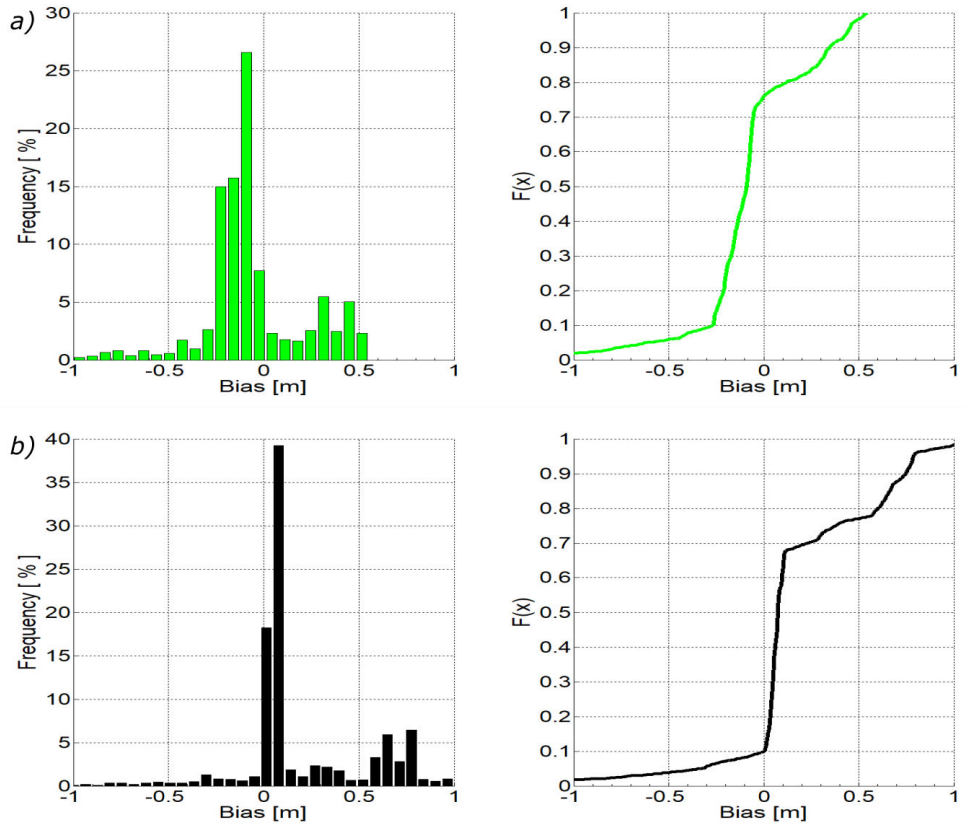

Figure 7.15.Probability (left) and cumulative (right) error distributions in bathymetric estimations from day 28th (a) and day 29th (b).

Common to both days was the underestimation of local depth between 3.5 and 7 m depth. This is in contrast with previous works (Holman et al., 2013; Bergsma et al., 2016), that overestimated true depth in shallow water. However, in this study case, underestimation bias was determined by the presence of local depressions which were difficult to retrieve from depth inversion technique. Overall, normalized bias by depth (Figure 7.16, lower plot) was always lower than 20 % for day 28th and than 15 % for day 29th. These percentages were smaller than the one obtained by Catalan and Haller (2008) when wave linear theory was used to invert celerity measured with cross-correlation, and comparable with accuracy obtained by Almar et al. (2011) using non-linear dispersion relation.

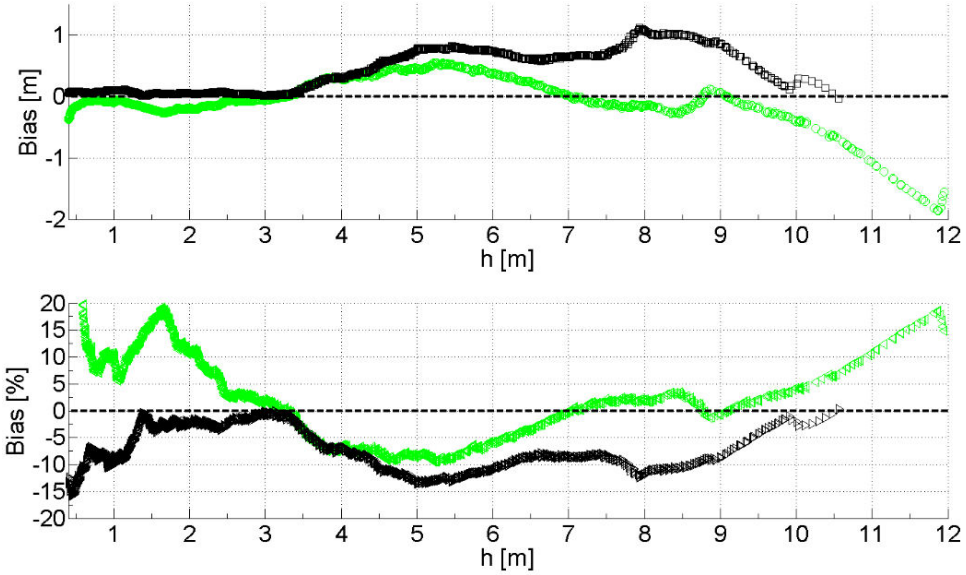

Figure 7.16. Depth dependence of bias (upper plot) and normalized bias with local depth in percentage (lower plot) for day 28th (green) and day 29th (black).

7.4.2.2 Bathymetry map

Bathymetry maps achieved with depth inversion technique from both days are shown in Figure 7.17 and Figure 7.18, separately. The results from 14 cross-shore transects were interpolated to a 1x1 m grid using Matlab built-in natural neighbour interpolation technique. Comparison with best available ground truth is also displayed to visualize performance of the results.

The averaged wave breaking line found with the methodology described in Section 5.3.3 was used to merge local depth map produced from shoaling and breaking celerity, which were obtained distinctively.

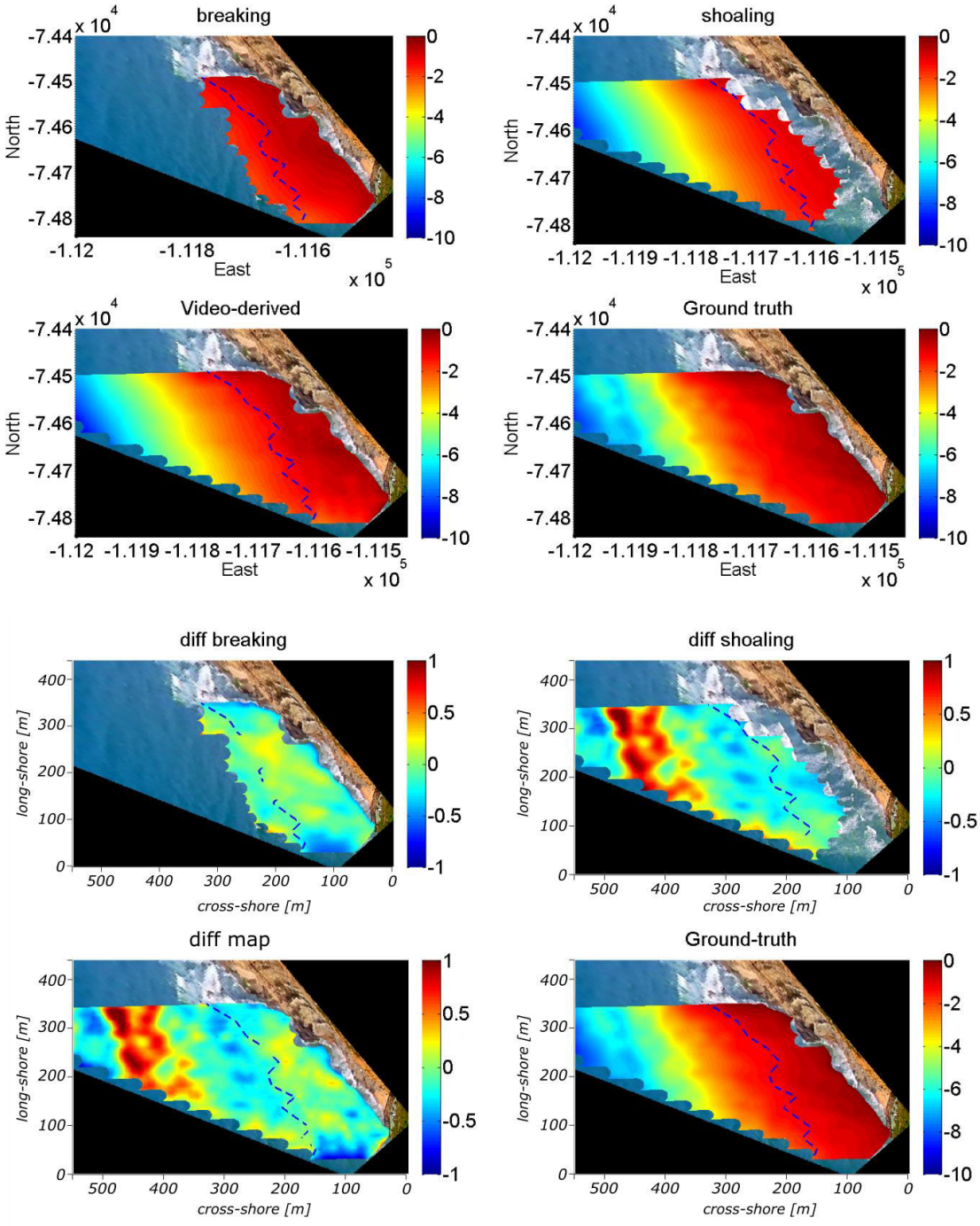

Figure 7.17. Bathymetry map obtained with data from day 28th. Dashed blue line indicates the mean breaking line, used as boundary between breaking and shoaling celerity.

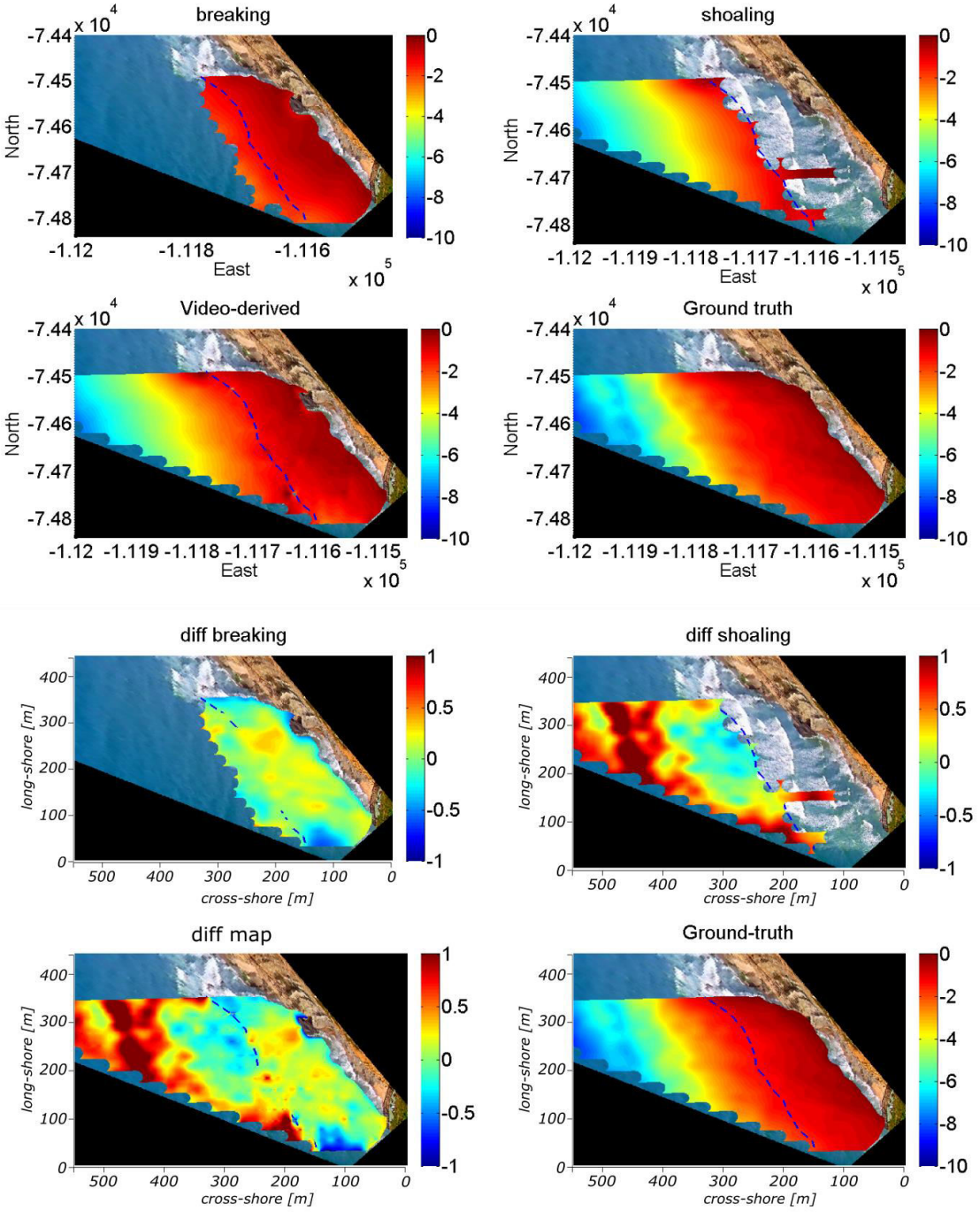

Figure 7.18. Bathymetry map obtain with data from day 29th. Dashed blue line indicates the mean breaking line, used as boundary between breaking and shoaling celerity.

Table 7.4 resumes data characteristics and errors found for both days. On day 28th, bathymetry map was achieved using 4 hours and 30 minutes video acquisition, with 27 Timestacks for each profile, processing a total amount of 378 Timestacks. Video acquisition was slightly longer on second day, therefore total number of Timestacks processed was 420. Breaking zone bathymetry was estimated with the same RMSE performance during both days, while errors for shoaling zone map were higher during the second day.

Table 7.4. Results statistics of video depth inversion technique.

						SHOALING					BREAKING					TOTAL				
date	Time Interval	#TSK per profile	Hs [m]	Tp [s]	tidal range	# point	Bias	Median error	MSE	RMSE	# point	Bias	Median error	MSE	RMSE	# point	Bias	Median error	MSE	RMSE
28th	4h 30m	27	1.64 ÷ 1.77	9.50 ÷ 12	-0.94 ÷ 1.74	82974	0.00	-0.10	0.12	0.35	49530	-0.96	-0.07	0.04	0.19	103506	-0.03	-0.08	0.12	0.34
29th	5h	30	2.50 ÷ 3.40	16 ÷ 18	-0.89 ÷ 1.81	66747	0.44	0.40	0.41	0.64	54025	0.02	0.05	0.04	0.20	105458	0.27	0.16	0.27	0.52

Figure 7.19 describes the error statistics in relation to depth computed from the interpolated bathymetry grid. Previous works (Holman et al., 2013) found the depth inversion bathymetry much dependent on depth. Assessed bathymetry from day 28th did not show such strong dependence on depth, while errors for day 29th increased as depth increased. Estimations in the breaking zone were lower than RMSE=0.3 m for both days.

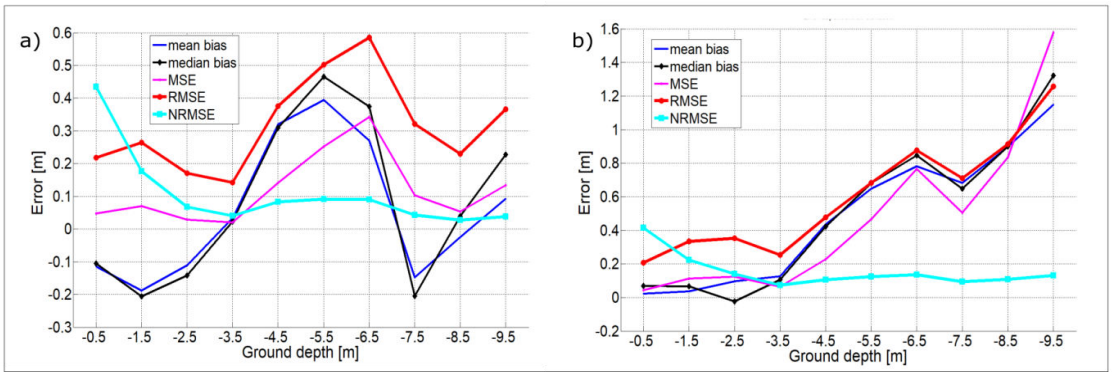

Figure 7.19. Depth dependence for error of bathymetry map from day 28th (a) and day 29th (b). Normalised RMSE (NRMSE) was calculated dividing the RMSE for the local depth.

Overall, higher errors in bathymetry assessment were just registered in the shoaling zone during higher waves, while breaking zone bathymetry was retrieved with the same accuracy during both days. This suggests that one source of error may be related to the wave dispersion relation adopted, as linear dispersion relation did not properly described more significant wave dispersion during the second day. However, this analysis deserves deeper investigations.

7.5 Discussion

The main objective was to develop a methodology to video-derive bathymetry at high-energy coastal environment, where direct conventional surveys are difficult and sporadic due to logistical and economic constraints. Video data acquired by a surfcam installed at Ribeira d'Ilhas beach, on the western Portuguese coast, were used to test the methodology during high energy wave forcing, with measured offshore significant wave height between 1.7 m and 3.7 m.

The immobile rocky sea bed allowed a proper evaluation of the method, despite the fact that field conditions did not permit to fully control hydrodynamic and photogrammetric parameters as could be done in laboratory experiments (Catalan and Haller, 2008; Almar et al., 2011).

The method was capable of achieving a bathymetric map with short time interval data (half a tidal excursion) because of the large number of celerity values computed by the proposed methodology. In this perspective, longer acquisitions may provide higher precision in retrieving sea bottom depth (Almar, 2009).

Results showed the feasibility of the methodology in retrieving bathymetry within the range of camera view till a depth of 11 m. The accuracy was comparable to more sophisticated video-based depth inversion algorithms (Table 7.1) which showed inaccuracy increasing proportionally to wave height (e.g., Holman et al., 2013; Brodie et al., 2018) and lacked in testing performance during high wave height as occurred in the presented work (Yoo, 2007; Liu et al., 2012; Brodie et al., 2018).

One of the main advantages of the proposed method is the separate measurements of shoaling and breaking wave celerity. The wave pattern recognition code run to retrieve shoaling and breaking wave patterns simultaneously, nevertheless, it allowed the distinction between the two domains, thus easing the use of two different formulations for assessing depth inversion bathymetry.

In the perspective of applying depth inversion on barred beaches, shoaling and breaking wave distinctions should permit a proper estimation of sand bar depth over tidal modulation, also considering that the likely existence of sand bar might be detected on Timex (e.g., Lippmann and Holman, 1989; Lippmann and Holman, 1990; Coco et al.,

2005; Aarninkhof and Ruessink, 2004; Armaroli and Ciavola, 2011; Guedes et al., 2011b; Angnuureng et al., 2017) or by the wave transformation domain technique developed in this work (Chapter 4) prior the application of depth inversion method. At the same time.

7.5.1 Wave celerity computation

The image processing code for extracting shoaling and breaking waves was intentionally simple, easy to reproduce and applicable to video data collected during different sea states, light conditions and camera properties. However, the code was tested when wave signatures were clearly visible on Timestacks, since swell and high wave height designed stronger features on the sea surface. Small adjustments to the image processing algorithm, such as pixel intensity enhancement and threshold set up, might be needed to assess proper wave pattern detection during low wave height. For this reason, future work will test the code on images collected during low wave height at low-energy environments.

The concept of instantaneous velocity computed from wave trajectories detection allowed to exhaustively describe wave celerity map on the nearshore area, both for shoaling and breaking waves. Wave trajectory detection and first derivative concept allowed to consider a large number of celerity measurements for the application of depth inversion technique. Despite the fact that it is missing in this work a comparison with other techniques (Stockdon and Holman, 2000; Yoo, 2007; Almar et al., 2008; Catalan and Haller, 2008; Liu et al., 2012; Zikra, 2012; Holman et al., 2013), measured breaking celerity was in agreement with values obtained with field data by cross-correlation technique (Tissier et al., 2011, Postacchini and Brocchini, 2014). Computed wave speed at the incipient breaking point was often overestimated, a result in line with previously works (Catalan and Haller, 2008; Tissier et al., 2011).

7.5.2 Sources of error and limitations

One source of error for bathymetry map was related to wave dispersion relationship. Investigation in finding the best solution for depth inversion was previously done in the laboratory (e.g., Catalan and Haller, 2008), however further research should be addressed with field data. In this perspective, an approximation of wavelength measures from Timestack (Almar, 2009) might help the accuracy of the wave dispersion solution.

The main limitations of the technique are common to previous video-based works, which are related to photogrammetry and video data quality (Uunk et al., 2010, Bergsma et al., 2016). In addition, low wave energy or vague sea state may affect accuracy and performance, as shoaling and breaking waves patterns are difficult to detect on Timestacks in such hydrodynamic conditions.

A likely source of error in celerity computation might be related to the non-perperdicularity of Timestacks transect to wave direction. As previously described, wave direction was taken as reference to produce Timestack in this work. Nevertheless, it should be considered that the effective perpendicular line to wave direction might depend on the specific nearshore location, since waves can be subjected to diffraction/refraction caused by obstacles such as breakwaters, headlands, and alongshore irregularity of the bathymetry. Moreover, wave propagation angle itself can vary during the observations. It can be assumed that some waves approached the coast with different angle from the one used as reference to sample pixel arrays, and also that some waves might have been subjected to refraction/diffraction in shallow water. However, such anomalies constituted spurious data that were filtered out by the fitting procedure, especially considering that in average about 1400 waves were observed per day. Visual inspection procedure to choose transect inclination considered at least six images per hour over the two days. In addition, over Ribeira d'Ilhas nearshore rocky platform, offshore waves usually align to the coast quite regularly. For this characteristic, the site is also known as one of the main recreational spot for surf in Portugal.

Overall, the uncertainties generated by non-collinearity between Timestack profile and wave direction would require deeper investigation. An automated detection of wave front would allow to fully automate the procedure of Timestack production.

8. CONCLUSIONS

The central aim of this thesis was to achieve *synoptic hydrodynamic and morphology measurements in the nearshore through the exploitation of video monitoring technique*.

To achieve the main objective, this dissertation has presented four techniques capable to describe the essential nearshore hydrodynamic factors, such as wave breaking height and wave celerity, and the key morphological features, namely subtidal bathymetry and intertidal beach topography. The combination of the methodologies presented in this thesis provides a comprehensive coverage of nearshore processes (Figure 8.1).

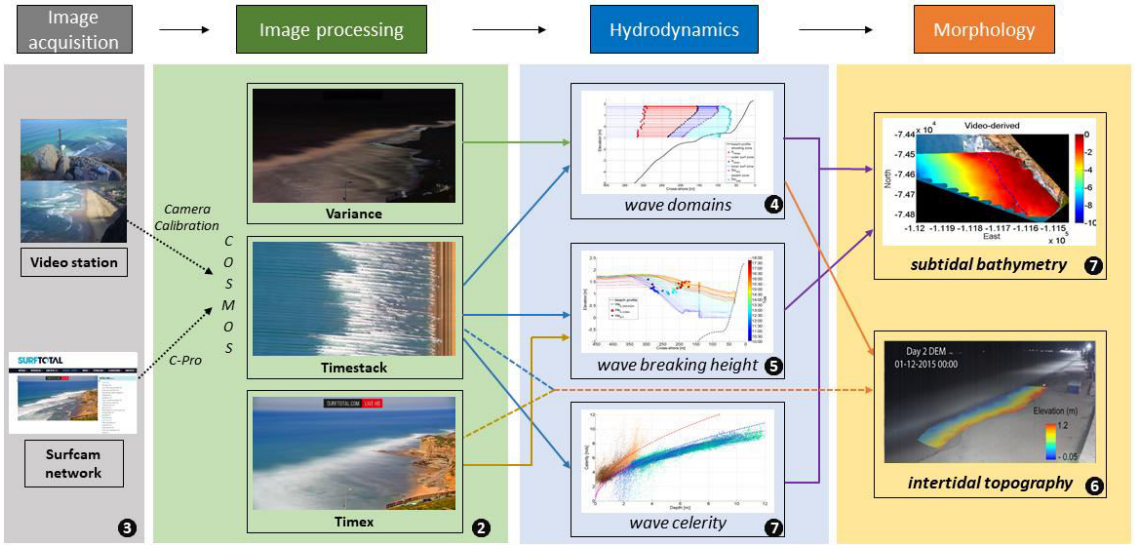

Figure 8.1. Flow chart of the techniques developed in this thesis. White numbers inside black circles indicate the relative chapter.

The techniques are easy replicable and do not require sophisticated image processing coding, in line with the second aim of this thesis, which required to build *simple and efficient methodologies to overcome the complexity of image processing procedures and speed up digital signal operation.*

Video image acquisition was performed either by dedicated video stations (temporary or fixed) and by taking advantage of the available surfcam infrastructure. The author installed one temporary video station at a beach located on the West Portuguese coast (Section 3.2), and a fixed video monitoring station at one beach in French Guinea (Section 3.5). Moreover, the author had also access to video data collected at a Vietnamese beach from a video station (Section 3.6).

An interesting development performed in the scope of the present work consisted in the exploitation of coastal images provided by online streaming surfcams. The procedure set to acquire and rectify the online-streamed images allowed the use of images from two sites on the Portuguese coast (Sections 3.3 and 3.4), achieving the third aim of this thesis, which was to set a methodology to *exploit existing data acquisition infrastructures (like "surfcams") for coastal process studies*.

In this chapter, the conclusion remarks for each of the presented techniques are reported.

8.1 Identification of wave transformation domains

The knowledge of shoaling, surf and swash zone extents over a cross-shore profile can lead to a qualitative estimation of sediment transport and morphodynamic processes in the nearshore (Price and Ruessink, 2008). In addition, the technique might also help in classifying beach morphology behaviour (Wright and Short, 1984).

Extraction of wave characteristics from video images benefits from the prior knowledge of the nearshore domains, as wave transformation from the deep water up to the swash, can have a significant impact on the characteristics of the image. For example, the foam generated by the breaking process or the alternation of wet/dry episodes that occur at the swash have profound influence on the cross-shore variation of the images signature. In fact, existing stand-alone algorithms for coastal image analysis (e.g. shoreline detection, wave measurements, sand bar position) can benefit from a clear separation of the nearshore domains to ease the automation of the processing of image datasets.

It was found that the standard deviation of pixel intensity along the cross-shore dimension of Timestack images allows to discriminate shoaling, surf and swash zones (Section 4.4.3). Wave breakpoint location statistics was proved to be related to pixel intensity variation on the Timestack images. The boundaries between the wave transformation domains are identified by specific local minima and maxima points. The possibility of applying the method directly to Variance eases the study of alongshore wave hydrodynamics (Section 4.4.5).

Further effort should improve pixel intensity statistical analysis, adding different study cases such as single or multi-barred beaches.

8.2 Measuring wave breaking height from video imagery

Estimates of wave height at the breaking point using video images were supported by the development of two methods.

The first method (Section 5.3) is based on a conceptual model that couples the statistical breakpoint position on Timestacks with the bathymetry under breaking conditions. The comparison of measured/modelled and video-derived wave heights at the breakpoint shows a good consistency, with a clear dependence on breaker index value.

A second methodology (Section 5.5) empirically relates the length of image-derived breaking pattern to water depth at breaking and thus to wave breaking height through the consideration of a breaker index. Wave breaking height measured by the proposed empirical relation shows about 80% of accuracy when applied to four sites, characterized by different image sources and wave forcing.

It is worthwhile to note that both methodologies can be successfully applied to Timex, a standard image product that have been produced by all video-monitoring systems worldwide. The capability to estimate wave breaking height from Timex represents an interesting opportunity to couple hydrodynamic measurements to the diffuse applications of Timex (Section 2.4.1), such as sand bar identification and shoreline monitoring.

Although the developed methodologies were successfully tested at different sites (Sections 5.6.4, 5.6.5 and 5.6.6), long-term Timex dataset available worldwide might verify and demonstrate the empirical relation between wave breaking pattern length and wave height at breaking.

8.3 Intertidal beach topography assessment

The feasibility of coupling LiDAR measurements and video imagery to assess 3D intertidal beach topography was successfully investigated. The use of a coupled LiDAR-video system has shown to have great potentiality for beach intertidal topography assessment.

Shoreline elevation, measured locally on LiDAR profile, was applied to the entire shoreline contour detected on rectified Timex (Section 6.3.3). Coupling the information derived from the two systems allowed to overcome the spatial limitations of the both the technologies, and beach features such as beach cusps and horns were detailed described. The results shows the RMSE of the LiDAR-video topographic measurements are within the range of errors of conventional survey methods such as RTK-GPS thus giving good perspective about the method accuracy (Section 6.4.2). Findings suggest that shoreline elevation, even and if only precisely measured at a single profile, can successfully be applied to the shoreline contour coverage.

Future works should test the technique during more energetic hydrodynamic conditions and different beach morphologies, with beach surveys conducted regularly during video monitoring acquisition.

8.4 Subtidal bathymetry assessment

Linear depth-inversion technique was applied to retrieve nearshore subtidal bathymetry from video-derived wave celerity during energetic sea state. The presented methodology measures wave phase speed in the space domain (Section 7.3.4), while previous techniques were based on spectral and time-domain analysis of Timestacks.

The approach allowed a depth-inversion solution with short-term video acquisition (5 hours) and lead to results that are comparable to more sophisticated algorithms (Section 7.4.2).

The technique opens a new possibility to better understanding the interaction between shoaling and surf zone, as shoaling and breaking wave celerities are measured distinctly.

Further work will compare wave celerity measures against different methodologies and will test depth-inversion technique on complex movable sandy bottom with the presence of a sand bar.

8.5 Perspectives

Coastal video monitoring technique offer excellent spatio-temporal resolutions, in combination with cost-efficient long-term data sampling. The use of surfcam networks for coastal monitoring has a huge potential as it benefits from an existing infrastructure with obvious economic and logistic advantages. Considering the wide number of freely available streaming surfcams worldwide, this conception is of great interest to foster coastal video monitoring use in the understanding of coastal processes and hazard mitigation.

With coastal risk assessment and coastal management becoming more important nowadays due to climate change, the importance of synoptic measurements of hydrodynamic parameter and morphologic characteristics in the nearshore is expected to increase. The combination of the methodologies presented in this thesis provides a comprehensive coverage of nearshore processes, enabling a synoptic representation of hydrodynamics and morphology. These methodologies may foster the implementation of new video-based operational systems and support the quasi-real time determination of coastal indicators and early warning systems for coastal hazards.

References

Aagaard, T. and Holm, D. (1989). Digitization of wave runup using video records. Journal of Coastal Research, 5:547–551

Aarninkhof, S.G.J. (2003). Nearshore bathymetry derived from video imagery, PhD thesis, Civil Engineeirng, Delft University of Technology, Delft, Netherlands, pp. 175

Aarninkhof, S.G.J., Turner, I.L., Dronkers, T.D.T., Caljouw, M., Nipius, L., (2003). A video-based technique for mapping intertidal beach bathymetry. Coastal Engineering 49, 275–289

Aarninkhof, S. and Ruessink, B. G. (2004). Video observations and model predictions of depth-induced dissipation. IEEE Transactions on Geoscience and Remote Sensing, 42(11), 832–844. https://doi.org/10.1109/TGRS.2004.835349

Alexander, P.S. and Holman, R.A. (2004). Quantification of nearshore morphology based on video imaging. Marine Geology. 208, 101–111. https://doi.org/10.1016/ j.margeo.2004.04.017.

Almar, R., Bonneton, P., Senechal, N., Roelvink, D. (2008). Wave celerity from video imag- ing: A new method, in 'Proceedings of the 31st International Conference Coastal Engineering', pp. 1–14.

Almar, R. (2009). Morphodynamique littorale haute fréquence par imagerie vidéo. PhD thesis. University of Bordeaux. 228 p.

Almar, R., Cienfuegos, R., Catalán, P. A., Birrien, F., Castelle, B., Michallet, H. (2011). Nearshore bathymetric inversion from video using a fully non-linear Boussinesq wave model. Journal of Coastal Research, 64, 3–7.

Almar, R., Cienfuegos, R., Catalán, P.A., Michallet, H., Castelle, B., Bonneton, P., Marieu, V. (2012a). A new breaking wave height direct estimator from video imagery. Coastal Engineering, 61, 42-48.

Almar, R., Ranasinghe, R., Sénéchal, N., Bonneton, P., Roelvink, D., Bryan, K. R., Parisot, J. (2012b). Video-Based Detection of Shorelines at Complex Meso–Macro Tidal Beaches. Journal of Coastal Research, 284, 1040-1048.

Almar, R., Michallet, H., Cienfuegos, R., Bonneton, P., Tissier, M., Ruessink, G. (2014). On the use of the Radon Transform in studying nearshore wave dynamics. Coastal Engineering. http://doi.org/10.1016/j.coastaleng.2014.06.008

Almar, R., Almeida, P., Blenkinsopp, C., Catalan, P. (2016). Surf-Swash Interactions on a Low-Tide Terraced Beach. Journal of Coastal Research, 75(sp1), 348-352.

Almar, R., Blenkinsopp, C., Almeida, L. P., Cienfuegos, R., Catalán, P. A. (2017a). Wave runup video motion detection using the Radon Transform. Coastal Engineering, 130(August), 46–51. http://doi.org/10.1016/j.coastaleng.2017.09.015

Almar, R., Marchesiello, P., Almeida, L., Thuan, D., Tanaka, H., Viet, N. (2017b). Shoreline Response to a Sequence of Typhoon and Monsoon Events. Water, 9(6), 364.

Almeida, L. P., Masselink, G., Russell, P., Davidson, M., Poate, T., McCall, R., Turner, I. (2013). Observations of the swash zone on a gravel beach during a storm using a laser-scanner (LiDAR). Journal of Coastal Research, 65, 636-641

Almeida, L.P., Masselink, G., Russell, P.E., Davidson, M.A. (2015). Observations of gravel beach dynamics during high energy wave conditions using a laser scanner. Geomorphology, 228, pp. 15-27.

Almeida, L. P., Almar, R., Marchesiello, P., Benshila, R., Blenkinsoff, C., Martins, K., Daly, C. (2017). Swash dynamics of a sandy beach with low tide terrace. Proceedings Coastal Dynamics, ASCE, Helsingor, Denmark

Alvarez-Ellacuria, A., Orfila, A., Gómez-Pujol, L., Simarro, G., Obregon, N. (2011). Decoupling spatial and temporal patterns in short-term beach shoreline response to wave climate. Geomorphology, 128 (3-4) , 199-208. doi:10.1016/j.geomorph.2011.01.008

Angnuureng, D.B. (2016). Shoreline response to multi-scale oceanic forcing from video imagery. PhD thesis. Earth Sciences. Université de Bordeaux. 183 pp.

Angnuureng, D. B., Almar, R., Addo, K. A., Castelle, B., Senechal, N., Laryea, S. W., Wiafe, G. (2016). Video oberservation of waves and shoreline change on the microtidal james town beach in Ghana. Journal of Coastal Research, 1(75), 1022–1026. https://doi.org/10.2112/SI75-205.1

Angnuureng, D. B., Almar, R., Senechal, N., Castelle, B., Addo, K. A., Marieu, V., Ranasinghe, R. (2017). Shoreline resilience to individual storms and storm clusters on a meso-macrotidal barred beach. Geomorphology, 290, 265-276. doi:10.1016/j.geomorph.2017.04.007

Anthony E.J., Gardel A., Dolique F., Brunier G., Péron C. (2015). Mud Banks, Sand Flux and Beach Morphodynamics: Montjoly Lagoon Beach, French Guiana. In: Maanan M., Robin M. (eds) Sediment Fluxes in Coastal Areas. Coastal Research Library, vol 10. Springer, Dordrecht

Antunes, C. (2007). Previsão de Marés dos Portos Principais de Portugal. FCUL Webpage, http://webpages.fc.ul.pt/~cmantunes/hidrografia/hidro_mares.html

Armaroli, C. and Ciavola, P. (2011). Dynamics of a nearshore bar system in the northern Adriatic: a video-based morphological classification. Geomorphology, vol. 126, p. 201-216, ISSN: 0169-555X, doi: 10.1016/j.geomorph.2010.11.004

Atkinson, A. L., Power, H. E., Moura, T., Hammond, T., Callaghan, D. P., Baldock, T. E. (2017). Assessment of runup predictions by empirical models on non-truncated beaches on the south-east Australian coast. Coastal Engineering, 119, 15-31. doi:10.1016/j.coastaleng.2016.10.001

Baldock, T., Holmes, P., Bunker, S., Van Weert, P. (1998). Cross-shore hydrodynamics within an unsaturated surf zone. Coastal Engineering, 34(3-4), 173-196. doi:10.1016/s0378-3839(98)00017-9

Baghdadi, N., Gratiot, N., Lefebvre, J., Oliveros, C., Bourguignon, A. (2004). Coastline and mudbank monitoring in French Guiana: contributions of radar and optical satellite imagery. Canadian Journal of Remote Sensing, 30(2), 109-122. doi:10.5589/m03-059

Bailey, D. G. and Shand, R. D. (1994). Determining Wave Run-up using Automated Video Analysis. Proceedings 2nd NZ Conference on Image and Vision Computing, 2111–21110.

Battjes, J.A. (1974). Surf similarity. Proceedings of the International Conference on Coastal Engineering: 466 - 479.

Battjes, J. A. and Janssen, J.P.F. (1978). Energy loss and set-up due to breaking of random waves, in Proceedings of Sixteenth Coastal Engineering Conference, pp. 569–587, Am. Soc. of Civ. Eng., New York.

Bechle, A. J., Wu, C. H., Liu, W., Kimura, N. (2012). Development and Application of an Automated River-Estuary Discharge Imaging System. Journal of Hydraulic Engineering, 138(4), 327-339. doi:10.1061/(asce)hy.1943-7900.0000521

Bergsma, E.W.J., Conley, D.C., Davidson, M.A., O'Hare, T.J. (2016). Video-based nearshore bathymetry estimation in macro-tidal environments. Marine Geology 374, 31–41. https:// doi.org/10.1016/j.margeo.2016.02.001

Bird, E.C. (2000). Coastal geomorphology: An introduction. Chichester: Wiley.

Birkemeier, W. A., Long, C. E., & Hathaway, K. K. (1997). DELILAH, DUCK94 & SandyDuck: Three Nearshore Field Experiments. Coastal Engineering 1996. doi:10.1061/9780784402429.313

Blenkinsopp, C.E., Mole, M.A., Turner, I.L., Peirson, W.L. (2010). Measurements of the time-varying free-surface profile across the swash zone obtained using an industrial LiDAR. Coastal Engineering, 57, 1059-1065.

Blenkinsopp, C. E., Turner, I. L., Allis, M. J., Peirson, W. L., Garden, L. E. (2012). Application of LiDAR technology for measurement of time-varying free-surface profiles in a laboratory wave flume. Coastal Engineering, 68, 1-5.

Blenkinsopp, C. E., Matias, A., Howe, D., Castelle, B., Marieu, V., Turner, I. L. (2016). Wave runup and overwash on a prototype-scale sand barrier. Coastal Engineering, 113(September 2015), 88–103. http://doi.org/10.1016/j.coastaleng.2015.08.006

Boak, E.H. and Turner, I.L. (2005). Shoreline Definition and Detection: A Review. Journal of Coastal Research, 214, 688-703.

Booij, N., Ris, R.C., Holthuijsen, L.H. (1999). A third-generation wave model for coastal regions, Part I, Model description and validation, Journal of Geophysical Research. C4, 104, 7649-7666.

Bouguet, J.Y. (2007). Camera Calibration Toolbox for Matlab. Available at: http://www.vision.caltech.edu/bouguetj/calib_doc/. (accessed November 2017)

Bracs, M. A., Turner, I. L., Splinter, K. D., Short, A. D., Lane, C., Davidson, M. A., Cameron, D. (2016). Evaluation of Opportunistic Shoreline Monitoring Capability Utilizing Existing "Surfcam" Infrastructure. Journal of Coastal Research, 319(March), 542–554. http://doi.org/10.2112/JCOASTRES-D-14-00090.1

Brignone, M., Schiaffino, C. F., Isla, F. I., Ferrari, M. (2012). A system for beach video-monitoring: Beachkeeper plus. Computers and Geosciences, 49, 53–61. http://doi.org/10.1016/j.cageo.2012.06.008

Brinkkemper, J. A., Lanckriet, T., Grasso, F., Puleo, J. A., Ruessink, B. G. (2014). Observations of turbulence within the surf and swash zone of a field-scale sandy laboratory beach. Coastal Engineering, 113, 62–72. http://doi.org/10.1016/j.coastaleng.2015.07.006

Brodie, K.L., Raubenheimer, B., Elgar, S. (2015). LiDAR and Pressure Measurements of Inner-Surfzone Waves and Setup. Journal of Atmospheric and Oceanic Technology, 32, pp. 1945 - 1959.

Brodie, K. L., Palmsten, M. L., Hesser, T. J., Dickhudt, P. J., Raubenheimer, B., Ladner, H., Elgar, S. (2018). Evaluation of video-based linear depth inversion performance and applications using altimeters and hydrographic surveys in a wide range of environmental conditions. Coastal Engineering, 136, 147-160. doi:10.1016/j.coastaleng.2018.01.003

Camenen, B. and Larson, M. (2007). Predictive Formulas for Breaker Depth Index and Breaker Type. Journal of Coastal Research, 23, 1028–1041. https://doi.org/10.2112/05-0566.1

Carini, R. J., Chickadel, C. C., Jessup, A. T., Thomson, J. (2015). Estimating wave energy dissipation in the surf zone using thermal infrared imagery. Journal of Geophysical Research: Oceans, 120(6), 3937-3957.

Catálan, P. A. and Haller, M. C. (2008). Remote sensing of breaking wave phase speeds with application to non-linear depth inversions. Coastal Engineering. http://doi.org/10.1016/j.coastaleng.2007.09.010

Chickadel, C.C. (2007). Remote Measurements of Waves and Currents over Complex Bathymetry. PhD thesis. College of Oceanic and Atmospheric Sciences. Oregon State University.

Ciavola, P., Ferreira, O., Haerens, P., Van Koningsveld, M., Armaroli, C., Lequeux, Q. (2011a). Storm impacts along European coastlines. Part 1: The joint effort of the MICORE and ConHaz Projects. Environmental Science & Policy, 14(7), 912-923. doi:10.1016/j.envsci.2011.05.011

Ciavola, P., Ferreira, O., Haerens, P., Van Koningsveld, M., Armaroli, C. (2011b). Storm impacts along European coastlines. Part 2: lessons learned from the MICORE project. Environmental Science & Policy, 14(7), 924-933. doi:10.1016/j.envsci.2011.05.009

Coco, G., Bryan, and G. Payne, The next era for cam-era, Coastal news., 2004.

Coco, G., Bryan, K.R., Green, M.O., Ruessink, B.G., Turner, I.L., Van Enckevort, I.M.J. (2005). Video observations of shoreline and sandbar coupled dynamics, Proceedings of Coasts and Ports 2005, Adelaide, pp. 471–476, 2005.

Coco, G., Payne, G., Bryan, K.R., Ramsay, D., Dolphin, T. (2006). The use of video-based sys- tems to monitor shoreline dynamics, Proceedings of the 1st Arabian Coast Conference, Dubai.

Coleman, C. and Lundahl, A. (1948). Symposium of military photographic interpretation, under water depth determination by aerial photography. Photogrammetric Engineering .

Contardo, S. and Symonds, G. (2015). Sandbar straightening under wind-sea and swell forcing. Marine Geology, 368, 25-41. doi:10.1016/j.margeo.2015.06.010

Costanza, R., De Groot, R., Sutton, P., Van der Ploeg, S., Anderson, S. J., Kubiszewski, I., Turner, R.K. (2014). Changes in the global value of ecosystem services. Global Environmental Change, 26, 152-158. doi:10.1016/j.gloenvcha.2014.04.002

Davidson-Arnott, R.G.D. (2009). Introduction to Coastal Processes and Geomorphology. Cambridge University Press, Cambridge, England. 442pp

Davies, J.L. (1973). Geographical Variation in Coastal Development. Hafner Publishing Co., New York, 204p.

Dean, R. G. and Dalrymple, R. A. (1984). Water Wave Mechanics For Engineers And Scientists. Singapore: World Scientific Publishing Company.

De Vries, S., Hill, D., De Schipper, M., Stive, M. (2011). Remote sensing of surf zone waves using stereo imaging. Coastal Engineering, 58(3), 239-250. doi:10.1016/j.coastaleng.2010.10.004

Dodet, G., Bertin, X., Taborda, R. (2010). Wave climate variability in the North-East Atlantic Ocean over the last six decades. Ocean Modelling, 31(3-4): 120-131.

Elgar, S. and Guza, R.T. (1985). Shoaling gravity waves: comparisons between field observations, linear theory, and a nonlinear model. Journal of Fluid Mechanics, 158(-1), 47. doi:10.1017/s0022112085002543

Elko, N., Feddersen, F., Foster, D., Hapke, C., Mcninch, J., Mulligan, R., Ozkan-haller, H. T., Plant, N., Raubenheimer, B. (2014). The future of nearshore processes. American Geophysical Union, Ocean Sciences Meeting 2016

EUROTOP (2007). Wave overtopping of sea defences and related structures; Manual. Die Küste, Heft 73

Ferreira, O., Dias, J.A., Taborda, R. (2008). Implications of sea-level rise for continental Portugal, Journal of coastal research 24 (2), p. 317-324

Frouin, P. ; Pujos, M.; Watremez, P. (1997). Revue des connaissances sur la zone côtière de Guyane française. Programme National d'Océanographie Côtière.

Gal, Y., Browne, M., Lane, C. (2011). Automatic estimation of nearshore wave height from video timestacks. In Proceedings - 2011 International Conference on Digital Image Computing: Techniques and Applications, DICTA 2011. http://doi.org/10.1109/DICTA.2011.68

Gal, Y., Browne, M., Lane, C. (2014). Long-term automated monitoring of nearshore wave height from digital video. IEEE Transactions on Geoscience and Remote Sensing, 52(6), 3412–3420. http://doi.org/10.1109/TGRS.2013.2272790

Gallop, S., Bryan, K., Coco, G., Stephens, S. (2011). Storm-driven changes in rip channel patterns on an embayed beach. Geomorphology, 127(3-4), 179-188. doi:10.1016/j.geomorph.2010.12.014

Gama, C., Dias, J. A., Ferreira, Ó., Taborda, R. (1994). Analysis of storm surge in Portugal, between June 1986 and May 1988. In Proceedings of Littoral (Vol. 94, pp. 381-387).

Gaughan, M. K. and Komar, P. D. (1975). The theory of wave propagation in water of gradually varying depth and the prediction of breaker type and height. Journal of Geophysical Research, 80(21), 2991-2996. doi:10.1029/jc080i021p02991

González-Jorge, H., Díaz-Vilariño, L., Martínez-Sánchez, J., Riveiro, B., Arias, P. (2015). Wave Run-Up Monitoring on Rubble-Mound Breakwaters Using a Photogrammetric Methodology. Journal of Performance of Constructed Facilities, 30(4), 4015075. http://doi.org/10.1061/(ASCE)CF.1943-5509.0000822

Guedes, R. M. C., Bryan, K. R., Coco, G., Holman, R. A. (2011a). The effects of tides on swash statistics on an intermediate beach. Journal of Geophysical Research: Oceans, 116(4), 1–13. http://doi.org/10.1029/2010JC006660

Guedes, R. M., Calliari, L. J., Holland, K. T., Plant, N. G., Pereira, P. S., Alves, F. N. (2011b). Short-term sandbar variability based on video imagery: Comparison between Time–Average and Time–Variance techniques. Marine Geology, 289(1-4), 122-134. doi:10.1016/j.margeo.2011.09.015

Haller, M. C. and Catalan, P. A. (2009). Remote sensing of wave roller lengths in the laboratory. Journal of Geophysical Research: Oceans, 114(7), 1–19. https://doi.org/10.1029/2008JC005185

Harley, M. D. (2009). Daily to decadal embayed beach response to wave and climate foricing. PhD thesis. School of Civil and Environmental Engineering.. University of New South Wales.

Harley, M. D., Turner, I. L., Short, A. D., Ranasinghe, R. (2011). Assessment and integration of conventional, RTK-GPS and image-derived beach survey methods for daily to decadal coastal monitoring. Coastal Engineering, 58(2), 194-205.

Harley, M. D., Andriolo, U., Armaroli, C., Ciavola, P. (2013). Shoreline rotation and response to nourishment of a gravel embayed beach using a low-cost video monitoring technique: San Michele-Sassi Neri, Central Italy. Journal of Coastal Conservation, 18(5), 551-565. doi:10.1007/s11852-013-0292-x

Hart, C.A. and Miskin, E.A. (1945). Developments in the method of determination of beach gradients by wave velocity. Air survey research paper No. 15, pp. 1-54.

Hartley R. and Zisserman, A.(2003). Multiple View Geometry in Computer Vision, second ed. Cambridge University Press. 665 pp.

Holland, K.T. and Holman, R.A. (1993). The statistical distribution of swash maxima on natural beaches. Journal of Geophysical Research, 98, pp. 10271-10278.

Holland, K.T., Raubenheimer, B., Guza, R. T., Holman, R. A. (1995). Runup kinematics on a natural beach. Journal of Geophysical Research, 100(C3), 4985. http://doi.org/10.1029/94JC02664

Holland, K. T., Holman, R. A. Lippmann, T. C. (1997). Practical use of video imagery in nearshore oceanographic field studies. IEEE Journal of Oceanic Engineering 22, pp. 81–92.

Holland, T.K. (2001). Application of the linear dispersion relation with respect to depth inversion and remotely sensed imagery. IEEE Transactions on Geoscience and Remote Sensing 39 (11), 2060–2071.

Holland, K. T., Vinzon, S. B., Calliari, L. J. (2009). A field study of coastal dynamics on a muddy coast offshore of Cassino beach, Brazil. Continental Shelf Research, 29(3), 503-514. doi:10.1016/j.csr.2008.09.023

Holman, R. A. and Sallenger, A.H.J. (1985). Setup and swash on a natural beach. Journal of Geophysical Research 90, pp. 945–953.

Holman, R. A., Sallenger, A. H., Lippmann, T. C. Haines, J. W. (1993). The application of video image processing to the study of nearshore processes. Oceanography 6(3), pp. 78–85.

Holman, R. A. and Stanley, J. (2007). The history and technical capabilities of Argus. Coastal Engineering, 54(6–7), 477–491. http://doi.org/10.1016/j.coastaleng.2007.01.003

Holman, R., Plant, N., Holland, T. (2013). CBathy: A robust algorithm for estimating nearshore bathymetry. Journal of Geophysical Research: Oceans. http://doi.org/10.1002/jgrc.20199

Holman, R. and Stanley, J. (2013). cBathy bathymetry estimation in the mixed wave-current domain of a tidal estuary. Journal of Coastal Research, Special Issue 65, 1391-1396. doi:10.2112/SI65-235.1

Hoonhout, B., Baart, F., Van Thiel de Vries, J. (2014). Intertidal beach classification in infrared images. Journal of Coastal Research, 70, 657-662. doi:10.2112/si70-111.1

Hoonhout, B. M. and M. Radermacher (2015). Flamingo: a coastal image analysis toolbox, GIT repository, doi:10.5281/zenodo.14596.

Hoonhout, B., Radermacher, M., Baart, F., Van der Maaten, L. (2015). An automated method for semantic classification of regions in coastal images. Coastal Engineering, 105, 1-12. doi:10.1016/j.coastaleng.2015.07.010

Horikawa, K. (1988). Nearshore Dynamics and Coastal Processes, Theory, Measurement and Predictive Models, University of Tokyo Press, Tokyo, Japan.

Horsburgh, K., Losada, I., Vousdoukas, M., Weisse, R., Wolf, J. (2017). Hydrological risk: wave action, storm surge and coastal flooding. In: Poljanšek, K., Marín Ferrer, M., De Groeve, T., Clark, I. (Eds.). Science for disaster risk management 2017: knowing better and losing less. EUR 28034 EN, Publications Office of the European Union, Luxembourg, Chapter 3.6, doi: 10.2788/688605.

Huisman, C. E., Bryan, K. R., Coco, G., Ruessink, B. G. (2011). The use of video imagery to analyse groundwater and shoreline dynamics on a dissipative beach. Continental Shelf Research, 31(16), 1728–1738. http://doi.org/10.1016/j.csr.2011.07.013

Hunt, J.N. (1979). Direct solution of wave dispersion equation J. Waterw., Port, Coastal Ocean Div., American Society Civil Engineering, 105 (4) (1979), pp. 457-459

Huntley, D., Saulter, A., Kingston, K., Holman, R. (2009). Use of video imagery to test model predictions of surf heights. WIT Transactions on Ecology and the Environment, 126, 39–50. https://doi.org/10.2495/CP090041

Iribarren, C. R. and C. Nogales (1949). "Protection des Ports." 17th International Navigation Congress 2: Section II, Communication 31 - 80

Kamphuis, J. W. (1991). Incipient wave breaking. Coastal Engineering, 15(3), 185–203. https://doi.org/10.1016/0378-3839(91)90002-X

Kamphuis, J. W. (2000). Introduction to Coastal Engineering and Management World Scientific, Singapore

Komar, P. (1976). Beach processes and sedimentation. Englewood Cliffs, NJ: Prentice-Hall, Inc.

Kroon, A., and Masselink, G. (2002). Morphodynamics of intertidal bar morphology on a macrotidal beach under low-energy wave conditions, North Lincolnshire, England. Marine Geology 190, 591–608.

Lefebvre, J., Almar, R., Viet, N. T., Uu, D. V., Thuan, D. H., Binh, L. T, Duc, N. V. (2014). Contribution of swash processes generated by low energy wind waves in the recovery of a beach impacted by extreme events: Nha Trang, Vietnam. Journal of Coastal Research, 70, 663-668.

Lippmann, T. C. and Holman, R.A. (1989). Quantification of sand bar morphology: A video technique based on wave dissipation. Journal of Geophysical Research, 94(C1), 995–1011.

Lippmann, T. C. and Holman, R. A. (1990). The spatial and temporal variability of sand bar morphology. Journal of Geophysical Research 95, pp. 11575–11590.

Lippmann, T. C. and Holman, R. A. (1991), Phase speed and angle of breaking waves measured with video techniques, in ‘Kraus, N. (Ed.). Coastal Sediments ’91’.

Lippmann, T. C., Brookins A. H., Thornton, E.B. (1996). Wave energy transformation on natural profiles. Coastal Engineering 27: 1-20

Liu, H., Arii, M., Sato, S., Tajima, Y. (2012). Long-term neasrhore bathyemtry evolution from video imagery: a case study in the Miyazaki coast. Coastal Engineering Proceedings, 1(33), 60. doi:10.9753/icce.v33.sediment.60

Madsen, P.A., Sørensen, O.R., Schäffer, H.A. (1997). Surf zone dynamics simulated by a Boussinesq type model. Part I. Model description and cross- shore motion of regular waves. Coastal Engineering 32, 255–287.

Madsen, A. and Plant, N. (2001). Intertidal beach slope predictions compared to field data. Marine Geology, 173(1-4), 121-139.

Mason, D. C., Gurney, C., Kennett, M. (2000). Beach topography mapping - a comparsion of techniques. Journal of Coastal Conservation, 6(1), 113-124. doi:10.1007/bf02730475

Masselink, G. (1993). Simulating the effects of tides on beach morphodynamics. Journal of Coastal Research. SI 15, 180–197.

Masselink, G., Kroon, A., Davidson-Arnott, R.G.D. (2006). Morphodynamics of intertidal bars in wave-dominated coastal settings — a review. Geomorphology 73, 33–49.

Masselink, G., Hughes, M. G., Knight, J. (2011). Introduction to Coastal Processes and Geomorphology. 2nd edition, London, UK: Hodder Education

Masselink, G., Austin, M., Scott, T., Poate, T., Russell, P. (2014). Role of wave forcing, storms and NAO in outer bar dynamics on a high-energy, macro-tidal beach. Geomorphology, 226, 76-93. doi:10.1016/j.geomorph.2014.07.025

Matias, A., Blenkinsopp, C. E., Masselink, G. (2014). Detailed investigation of overwash on a gravel barrier. Marine Geology, 350, 27-38. doi:10.1016/j.margeo.2014.01.009

Matias, A., Carrasco, A.R., Loureiro, C., Andriolo, U., Masselink, G., Guerreiro, M., Pacheco, A., McCall, R., Ferreira, O., Plomaritis, T.A. (2017). Measuring and modelling overwash hydrodynamics on a barrier island. Proceedings Coastal Dynamics, ASCE, Helsingor, Denmark, 1616-1627.

McCowan, J. (1894). On the Highest Waves of a Permanent Type. Philosophical Magazine, Edinburgh 38(5): 351 - 358.

Mole, M. A., Mortlock, T. R. C., Turner, I. L., Goodwin, I. D., Splinter, K. D., Short, A. D. (2013). Capitalizing on the surfcam phenomenon: a pilot study in regional- scale shoreline and inshore wave monitoring utilizing existing camera infrastructure. Journal of Coastal Research, (65). http://doi.org/10.2112/SI65-242.1

Neumann, B., Vafeidis, A. T., Zimmermann, J., Nicholls, R. J. (2015). Future Coastal Population Growth and Exposure to Sea-Level Rise and Coastal Flooding - A Global Assessment. PLOS ONE, 10(3), e0118571. doi:10.1371/journal.pone.0118571

Nieto, M. A., Garau, B., Balle, S., Simarro, G., Zarruk, G. A., Ortiz, A., Orfila, A. (2010). An open source, low cost video-based coastal monitoring system. Earth Surface Processes and Landforms. http://doi.org/10.1002/esp.2025

Oliveira, L. (2009). Estudo Morfodinâmico e Sedimentar das Praias do Concelho de Sintra. Master Thesis, Universidade de Lisboa, 148 p. (unpublished)

Ortega-Sánchez, M., Fachin, S., Sancho, F., Losada, M. A. (2008). Relation between beachface morphology and wave climate at Trafalgar beach (Cádiz, Spain). Geomorphology, 99(1-4), 171-185. doi:10.1016/j.geomorph.2007.10.013

Orzech, M. D., Thornton, E. B., MacMahan, J. H., O'Reilly, W. C., Stanton, T. P. (2010). Alongshore rip channel migration and sediment transport. Marine Geology, 271(3-4), 278-291. doi:10.1016/j.margeo.2010.02.022

Osorio, A., Medina, R., Gonzalez, M. (2012). An algorithm for the measurement of shoreline and intertidal beach profiles using video imagery: PSDM. Computers & Geosciences, 46, 196-207. doi:10.1016/j.cageo.2011.12.008

Phillips, M. S., Harley, M. D., Turner, I. L., Splinter, K. D., Cox, R. J. (2017). Shoreline recovery on wave-dominated sandy coastlines: the role of sandbar morphodynamics and nearshore wave parameters. Marine Geology, 385, 146-159. doi:10.1016/j.margeo.2017.01.005

Pitman, S., Gallop, S. L., Haigh, I. D., Masselink, G., Ranasinghe, R. (2016). Wave breaking patterns control rip current flow regimes and surfzone retention. Marine Geology, 382, 176-190. doi:10.1016/j.margeo.2016.10.016

Plant, N. G. and Holman, R. A. (1997). Intertidal beach profile estimation using video images. Marine Geology, 140(1-2), 1-24.

Plant, N.G., Holland, K.T., Puleo, J.A. (2002). Analysis of the scale of errors in nearshore bathymetric data. Marine Geology. 191, 71–86. https://doi.org/10.1016/S0025-3227(02) 00497-8.

Plant, N.G., Holland, K.T., Haller, M.C. (2008). Ocean wavenumber estimation from wave- resolving time series imagery. Transactions on Geoscience and Remote Sensing 46, 2644–2658. https://doi.org/10.1109/TGRS.2008.919821.

Plant, N., K. Edwards, J. Kaihatu, J. Veeramony, L. Hsu, K. Holland (2009). The effect of bathymetric filtering on nearshore process model results, Coastal Engineering, 56, 484–493

Poate, T. G., McCall, R. T., Masselink, G. (2016). A new parameterisation for runup on gravel beaches. Coastal Engineering, 117, 176–190. http://doi.org/10.1016/j.coastaleng.2016.08.003

Postacchini, M. and Brocchini, M. (2014). A wave-by-wave analysis for the evaluation of the breaking-wave celerity. Applied Ocean Research, 46, 15–27. http://doi.org/10.1016/j.apor.2014.01.005

Power, H. E., Holman, R. A., Baldock, T. E. (2011). Swash zone boundary conditions derived from optical remote sensing of swash zone flow patterns. Journal of Geophysical Research: Oceans, 116(6). http://doi.org/10.1029/2010JC006724

Price, T. and Ruessink, B. (2008). Morphodynamic zone variability on a microtidal barred beach. Marine Geology, 251(1-2), 98-109. doi:10.1016/j.margeo.2008.02.008

Quartel, S., Addink, E., Ruessink, B. (2006). Object-oriented extraction of beach morphology from video images. International Journal of Applied Earth Observation and Geoinformation, 8(4), 256-269. doi:10.1016/j.jag.2006.01.002

Ranasinghe, R., Symonds, G., Black, K., Holman, R. (2004). Morphodynamics of intermediate beaches: a video imaging and numerical modelling study. Coastal Engineering, 51(7), 629-655. doi:10.1016/j.coastaleng.2004.07.018

Revollo, N. V., Delrieux, C. A., Perillo, G. M. (2016). Automatic methodology for mapping of coastal zones in video sequences. Marine Geology, 381, 87-101. doi:10.1016/j.margeo.2016.08.005

Ribeiro, M. (2017). Headland sediment bypassing processes. PhD thesis. University of Lisbon, 229p

Rigos, A., Tsekouras, G. E., Vousdoukas, M. I., Chatzipavlis, A., Velegrakis, A. F. (2016). A Chebyshev polynomial radial basis function neural network for automated shoreline extraction from coastal imagery. Integrated Computer-Aided Engineering, 23(2), 141-160. doi:10.3233/ica-150507

Ris, R.C., Booij, N., Holthuijsen, L.H. (1999). A third-generation wave model for coastal regions, Part II, Verification, Journal of Geophysical Research, C4, 104, 7667-7681.

Robertson, B. R. D. (2013). Remote Measurement and Analysis of Shallow Water Breaking Wave Characteristics. PhD thesis. University of Guelph, Ontario, Canada

Robertson, B., Gharabaghi, B., Hall, K. (2015). Prediction of Incipient Breaking Wave-Heights Using Artificial Neural Networks and Empirical Relationships. Coastal Engineering Journal, 57(4). http://doi.org/10.1142/S0578563415500187

Rogeiro, J., Gomes, J.L., Jesus, G., Oliveira, A., Rodrigues, M., Azevedo, A., Fortunato, A.B. (2014). WIFF: Water Information Forecast Framework. Proocedings of the 13th International Workshop on Multiscale (Un)-structured mesh numerical ocean modelling – IMUM 2014 (Lisboa, Portugal), 2 pp.

Ruggiero, P., Komar, P.D., McDougal, W.G., Marra, J.J., Beach, R.A. (2001). Wave runup, extreme water levels and the erosion of properties backing beaches. Journal of Coastal Research 17(2):407–419

Ruggiero, P., Holman, R.A., Beach, R.A. (2004). Wave run-up on a highenergy dissipative beach. Journal of Geophysical Research 109(C06025). doi:10.1029/2003JC002160

Ruiz de Alegria-Arzaburu, A. and Masselink, G. (2010). Storm response and beach rotation on a gravel beach, Slapton Sands, U.K. Marine Geology, 278(1-4), 77-99. doi:10.1016/j.margeo.2010.09.004

Salman, A., Lombardo, S., Doody, P. (2004). Living with coastal erosion in Europe: sediment and space for sustainability. Part I - Major findings and policy recommendations of the EUROSION project. Service contract B4-3301/2001/329175/MAR/B3

Salmon, J. E., Holthuijsen, L. H., Zijlema, M., van Vledder, G. P., Pietrzak, J. D. (2015). Scaling depth-induced wave-breaking in two-dimensional spectral wave models. Ocean Modelling, 87, 30–47. https://doi.org/10.1016/j.ocemod.2014.12.011

Sánchez-García, E., Balaguer-Beser, A., Pardo-Pascual, J. E. (2017). C-Pro: A coastal projector monitoring system using terrestrial photogrammetry with a geometric horizon constraint. ISPRS Journal of Photogrammetry and Remote Sensing, 128, 255–273. http://doi.org/10.1016/j.isprsjprs.2017.03.023

Schäffer, H.A., Madsen, P.A., Deigaard, R. (1993). A Boussinesq model for waves breaking in shallow water. Coastal Engineering 20, 185–202.

Schimmels, S., Vousdoukas, M., Wziatek, D., Becker, K., Gier, F., Oumeraci, H. (2012). Wave Run-Up Observations on Revetments With Different Porosities. Coastal Engineering Proceedings; No 33 (2012): Proceedings of 33rd Conference on Coastal Engineering, Santander, Spain, 2012, 1(33), 1–14. http://doi.org/http://dx.doi.org/10.9753/icce.v33.structures.73

Seiwell, H. R. (1946). Military oceanography in tactical operations of World War II. Transactions, American Geophysical Union, 27(5), 677. doi:10.1029/tr027i005p00677

Senechal, N., Abadie, S., Gallagher, E., MacMahan, J., Masselink, G., Michallet, H., Garlan, T. (2011a). The ECORS-Truc Vert'08 nearshore field experiment: Presentation of a three-dimensional morphologic system in a macro-tidal environment during consecutive extreme storm conditions. Ocean Dynamics, 61(12), 2073–2098. http://doi.org/10.1007/s10236-011-0472-x

Senechal, N., Coco, G., Bryan, K. R., Holman, R. A. (2011b). Wave runup during extreme storm conditions. Journal of Geophysical Research: Oceans. http://doi.org/10.1029/2010JC006819

Shand, T. D., Bailey, D. G., Shand, R. D. (2012). Automated Detection of Breaking Wave Height Using an Optical Technique. Journal of Coastal Research, 282, 671-682. doi:10.2112/jcoastres-d-11-00105.1

Short, A. D. (2004). Handbook of beach and shoreface morphodynamics. Chichester: John Wiley & Sons.

Short, A. D. and Trembanis, A. C. (2004). Decadal Scale Patterns in Beach Oscillation and Rotation Narrabeen Beach, Australia—Time Series, PCA and Wavelet Analysis. Journal of Coastal Research, 202, 523-532. doi:10.2112/1551-5036(2004)020[0523:dspibo]2.0.co;2

Silva, A.M.N. (2014). Beach morphodynamics at Nazaré coast using video monitoring. PhD thesis, University of Lisbon, Portugal, 183 pp

Silva, M., Patrício, P., Mariano, A., Morais, M., Valério, M. (2012). Obtenção de Dados LiDAR para as Zonas Costeiras de Portugal Continental. 2as Jornadas de Engenharia Hidrográfica. Lisbon, Portugal (in Portuguese)

Siveira, T. (2017). Geological framework control on beach dynamics. PhD thesis. University of Lisbon, 368p

Simarro, G., Bryan, K. R., Guedes, R. M., Sancho, A., Guillen, J., Coco, G. (2015). On the use of variance images for runup and shoreline detection. Coastal Engineering, 99, 136-147. doi:10.1016/j.coastaleng.2015.03.002

Simarro, G., Ribas, F., Álvarez, A., Guillén, J., Chic, Ò., Orfila, A. (2017). ULISES: An Open Source Code for Extrinsic Calibrations and Planview Generations in Coastal Video Monitoring Systems. Journal of Coastal Research, 335(5), 1217–1227. http://doi.org/10.2112/JCOASTRES-D-16-00022.1

Sobral, F., Pereira, P., Cavalcanti, P., Guedes, R., Calliari, L. (2013). Intertidal bathymetry estimation using video images on a dissipative beach. Journal of Coastal Research, 165, 1439-1444.

Stansby, P.K. and Feng, T. (2005). Kinematics and depth-integrated terms in surf zone waves from laboratory measurement. Journal of Fluid Mechanics 529, 279–310.

Stansell, P. and MacFarlane, C. (2002). Experimental investigation of wave breaking criteria based on wave phase speeds. Journal of Physical Oceanography 32, 1269–1283.

Stive, M.J.F. (1980). Velocity and pressure field of spilling breakers. Proceedings, 17th International Conference on Coastal Engr. ASCE, pp. 547–565.

Stockdon, H. F. and Holman, R. A. (2000). Estimation of wave phase speed and nearshore bathymetry from video imagery. Journal of Geophysical Research, 105033(15), 15–22.

Stockdon, H. F., Holman, R. A., Howd, P. A., Sallenger, A. H. (2006). Empirical parameterization of setup, swash, and runup. Coastal Engineering, 53(7), 573–588. http://doi.org/10.1016/j.coastaleng.2005.12.005

Stockdon, H. F., Thompson, D. M., Plant, N. G., Long, J. W. (2014). Evaluation of wave runup predictions from numerical and parametric models. Coastal Engineering, 92, 1–11.

Stocker, T.F., Qin, D., Plattner, G-K., et al. (2013). Climate Change 2013. The Physical Science Basis. Working Group I Contribution to the Fifth Assessment Report of the Intergovernmental Panel on Climate Change-Abstract for decision-makers (IPCC). Groupe d'experts intergouvernemental sur l'evolution du climat/Intergovernmental Panel on Climate Change-IPCC, C/O World Meteorological Organization, 7bis Avenue de la Paix, CP 2300 CH-1211 Geneva 2 (Switzerland)

Svendsen, I. A. (2006). Introduction to Nearshore Hydrodynamics. Advanced Series on Ocean Engineering. doi:10.1142/5740

Taborda, R. and Dias, J. A. (1992). Análise da sobreelevação do nível do mar de origem meteorológica durante os temporais de Fevereiro/Março de 1978 e Dezembro de 1981. Geonovas, 1, A Geologia e o Ambiente, 89-97.

Taborda, R. and Silva, A. (2012). COSMOS: A lightweight coastal video monitoring system. Computers and Geosciences, 49, 248–255. http://doi.org/10.1016/j.cageo.2012.07.013

Thornton, E.B. and Guza, R.T. (1982). Energy saturation and phase speeds measured on a natural beach. Journal of Geophysical Research 87 (C12), 9499–9508.

Thornton, E.B. and Guza, R.T. (1983). Transformation of wave height distribution. Journal of Geophysical Research 88(C10): 5925-5938.

Thuan, D.H., Binh, L.T., Viet, N.T., Hanh, D.H., Almar, R., Marchesiello, P. (2016) Typhoon Impact and Recovery from Continuous Video Monitoring: a Case Study from Nha Trang Beach, Vietnam. Journal of Coastal Research: Special Issue 75 - Proceedings of the 14th International Coastal Symposium, Sydney, 6-11 March 2016: pp. 263 – 267. https://doi.org/10.2112/SI75-053.1

Tissier, M., Bonneton, P., Almar, R., Castelle, B., Bonneton, N., Nahon, A. (2011). Field measurements and non-linear prediction of wave celerity in the surf zone. European Journal of Mechanics - B/Fluids, 30(6), 635-641. doi:10.1016/j.euromechflu.2010.11.003

Tolman, H. L. (2009). User manual and system documentation of WAVEWATCH III version 3.14. NOAA / NWS / NCEP / MMAB Technical Note 276, 194 pp.+ Appendices

Turner, I. L., Whyte, D., Ruessink, B., Ranasinghe, R. (2007). Observations of rip spacing, persistence and mobility at a long, straight coastline. Marine Geology, 236(3-4), 209-221. doi:10.1016/j.margeo.2006.10.029

Uunk, L., Wijnberg, K., Morelissen, R. (2010). Automated mapping of the intertidal beach bathymetry from video images. Coastal Engineering, 57(4), 461-469. doi:10.1016/j.coastaleng.2009.12.002

Valentini, N., Saponieri, A., Damiani, L. (2017a). A new video monitoring system in support of Coastal Zone Management at Apulia Region, Italy. Ocean and Coastal Management. http://doi.org/10.1016/j.ocecoaman.2017.03.032

Valentini, N., Saponieri, A., Molfetta, M. G., Damiani, L. (2017b). New algorithms for shoreline monitoring from coastal video systems. Earth Science Informatics, 10(4), 495-506. doi:10.1007/s12145-017-0302-x

Van der Meer, J.W. (2011). Design aspects of breakwaters and sea defences. Keynote Lecture, Proc. 5th SCAR, International Short Conference on Applied Coastal Research, Aachen, Germany

Vousdoukas, M. I., Velegrakis, A. F., Dimou, K., Zervakis, V., Conley, D. C. (2009). Wave run-up observations in microtidal, sediment-starved pocket beaches of the Eastern Mediterranean. Journal of Marine Systems, 78(SUPPL. 1), S37–S47. http://doi.org/10.1016/j.jmarsys.2009.01.009

Vousdoukas, M. I., Ferreira, P. M., Almeida, L. P., Dodet, G., Psaros, F., Andriolo, U. Ferreira, Ó. M. (2011). Performance of intertidal topography video monitoring of a meso-tidal reflective beach in South Portugal. Ocean Dynamics, 61(10), 1521-1540.

Vousdoukas, M. I., Wziatek, D., Almeida, L. P. (2012). Coastal vulnerability assessment based on video wave run-up observations at a mesotidal, steep-sloped beach. Ocean Dynamics, 62(1), 123–137. http://doi.org/10.1007/s10236-011-0480-x

Vousdoukas, M. I. (2014). Observations of wave run-up and groundwater seepage line motions on a reflective-to-intermediate, meso-tidal beach. Marine Geology, 350, 52–70. http://doi.org/10.1016/j.margeo.2014.02.005

Vousdoukas, M., Kirupakaramoorthy, T., Oumeraci, H., De la Torre, M., Wübbold, F., Wagner, B., Schimmels, S. (2014). The role of combined laser scanning and video techniques in monitoring wave-by-wave swash zone processes. Coastal Engineering, 83, 150-165.

Williams, W. W. (1947). The Determination of Gradients on Enemy-Held Beaches. The Geographical Journal, 109 (1/3), 76. doi:10.2307/1789903

Williams, A. and Pranzini, E. (2013). Coastal Erosion and Protection in Europe. Routledge, 457 pp., doi:10.4324/9780203128558, 2013

Wolf, P.R., and Dewitt, B.A. (2000). Elements of Photogrammetry: with Applications in GIS. McGraw-Hill, New York.

Wright, L. D., and A. D. Short (1984), Morphodynamic variability of surf zones and beaches: A synthesis, Marine Geology, 56(1–4), 93–118, doi:10.1016/0025-3227(84)90008-2.

Yao, Y., Huang, Z., Monismith, S. G., Lo, E. Y. M. (2013). Characteristics of Monochromatic Waves Breaking over Fringing Reefs. Journal of Coastal Research, 286, 94–104. https://doi.org/10.2112/JCOASTRES-D-12-00021.1

Yoo, J. (2007). Nonlinear Bathymetry Inversion Based on Wave Property Estimation from Nearshore Video Imagery. PhD thesis. Georgia Institute of Technology

Zijlema, M., Stelling, G., Smit, P. (2011). SWASH: An operational public domain code for simulating wave fields and rapidly varied flows in coastal waters. Coastal Engineering, 58(10), 992-1012. doi:10.1016/j.coastaleng.2011.05.015

Zikra, M. (2012). Development of video image analysis methods for estimating bathymetry and the directional wave spectrum in shallow water areas. PhD thesis. Department of Maritime Engineering, Graduate School of Sngineering, Kyushu University, Fukuoka, Japan